THE UNIVERSITY OF SYDNEY

Application of Surrogate Based Optimisation in the Design of Automotive Body Structures

BY

Jianguang FANG

A thesis submitted in fulfilment of the requirements for the degree of Doctor of Philosophy

School of Aerospace, Mechanical and Mechatronic Engineering

Faculty of Engineering & IT

The University of Sydney, Australia

June, 2016

Declaration

This thesis presents original work carried out by Jianguang Fang at the School of Aerospace, Mechanical and Mechatronic Engineering, Faculty of Engineering & IT at the University of Sydney towards the degree of Doctor of Philosophy in Engineering. I hereby declare that this thesis contains no material previously published or written by another person unless where due acknowledgment is given. I give permission for the digital version of my thesis to be made available on the web, via the University's digital research repository, the library catalogue and also through web search engines, unless permission has been granted by the University to restrict access for a period of time.

Name: Jianguang FANG

SID: 430559538

Signed: 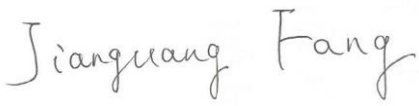

Date: 11-June-2015

ABSTRACT

The rapid development of automotive industry requires manufacturers to continuously reduce the development cost and time and to enhance the product quality. Thus, modern automotive design pays more attention to using CAE analysis based optimisation techniques to drive the entire design flow. This thesis focuses on the optimisation design to improve the automotive crashworthiness and fatigue performances, aiming to enhance the optimisation efficiency, accuracy, reliability, and robustness etc. The detailed contents are as follows:

(1) To excavate the potential of crash energy absorbers, the concept of functionally graded structure was introduced and multiobjective designs were implemented to this novel type of structures. First, note that the severe deformation takes place in the tubal corners, multi-cell tubes with a lateral thickness gradient were proposed to better enhance the crashworthiness. The results of crashworthiness analyses and optimisation showed that these functionally graded multi-cell tubes are preferable to a uniform multi-cell tube. Then, functionally graded foam filled tubes with different gradient patterns were analyzed and optimized subject to lateral impact and the results demonstrated that these structures can still behave better than uniform foam filled structures under lateral loading, which will broaden the application scope of functionally graded structures. Finally, dual functionally graded structures, i.e. functionally graded foam filled tubes with functionally graded thickness walls, were proposed and different combinations of gradients were compared. The results indicated that placing more material to tubal corners and the maximum density to the outmost layer are beneficial to achieve the best performance.

(2) To make full use of training data, multiple ensembles of surrogate models were proposed to maximize the fatigue life of a truck cab, while the panel thicknesses

were taken as design variables and the structural mass the constraint. Meanwhile, particle swarm optimisation was integrated with sequential quadratic programming to avoid the premature convergence. The results illustrated that the hybrid particle swarm optimisation and ensembles of surrogates enable to attain a more competent solution for fatigue optimisation.

(3) As the conventional surrogate based optimisation largely depends on the number of initial sample data, sequential surrogate modeling was proposed to practical applications in automotive industry. (a) To maximize the fatigue life of spot-welded joints, an expected improvement based sequential surrogate modeling method was utilized. The results showed that by using this method the performance can be significantly improved with only a relatively small number of finite element analyses. (c) A multiojective sequential surrogate modeling method was proposed to address a multiobjective optimisation of a foam-filled double cylindrical structure. By adding the sequential points and updating the Kriging model adaptively, more accurate Pareto solutions are generated.

(4) While various uncertainties are inevitably present in real-life optimisations, conventional deterministic optimisations could probably lead to the violation of constraints and the instability of performances. Therefore, nondeterministic optimisation methods were introduced to solve the automotive design problems. (a) A multiobjective reliability-based optimisation for design of a door was investigated. Based on analysis and design responses surface models, the structural mass was minimized and the vertical sag stiffness was maximized subjected to the probabilistic constraint. The results revealed that the Pareto frontier is divided into the sensitive region and insensitive region with respect to uncertainties, and the decision maker is recommended to select a solution from the insensitive region. Furthermore, the

reduction of uncertainties can help improve the reliability but will increase the manufacturing cost, and the tradeoff between the reliability target and performance should be made. (b) A multiobjective uncertain optimisation of the foam-filled double cylindrical structure was conducted by considering randomness in the foam density and wall thicknesses. Multiobjective particle swarm optimisation and Monte Carlo simulation were integrated into the optimisation. The results proved that while the performances of the objectives are sacrificed slightly, the nondeterministic optimisation can enhance the robustness of the objectives and maintain the reliability of the constraint. (c) A multiobjective robust optimisation of the truck cab was performed by considering the uncertainty in material properties. The general version of dual response surface model, namely dual surrogate model, was proposed to approximate the means and standard deviations of the performances. Then, the multiobjective particle optimisation was used to generate the well-distributed Pareto frontier. Finally, a hybrid multi-criteria decision making model was proposed to select the best compromise solution considering both the fatigue performance and its robustness.

During this PhD study, the following ideas are considered innovative:

(1) Surrogate modeling and multiobjective optimisation were integrated to address the design problems of novel functionally graded structures, aiming to develop more advanced automotive energy absorbers.

(2) The ensembles of surrogates and hybrid particle swarm optimisation were proposed for the design of a truck cab, which could make full use of training points and has a strong searching capacity.

(3) Sequential surrogate modeling methods were introduced to several optimisation problems in the automotive industry so that the optimisations are less

dependent on the number of initial training points and both the efficiency and accuracy are improved.

(4) The surrogate based optimisation method was implemented to address various uncertainties in real life applications. Furthermore, a hybrid multi-criteria decision making model was proposed to make the best compromise between the performance and robustness.

Key Words: Engineering optimisation, Sequential surrogate model, Optimisation under uncertainties, Fatigue durability, Crashworthiness, Ensemble of surrogates, Functionally graded structure, Multi-criteria decision making

Contents

Chapter 1 Introduction

1.1 Background

With the rapid development of automotive industry and the advances in mechanical manufacture in China, car makers require reducing development cycle of products, lowering development cost and meanwhile improving the product quality. Especially since China joined WTO in 2001, the automotive sector has been facing increasingly fierce competition and the requirement in the development cycle has been increasingly more critical to meet the market needs. To satisfy the customers' pursuit of individuality, being an integral part of automobiles, bodies always have a shorter development cycle than engines and chassis. Therefore, development ability of bodies plays a rather crucial role to a car maker.

Computer-aided engineering (CAE), widely applied in body design, has been revolutionizing the whole process of the vehicle development[1]. The modern vehicle design process has replaced the old-fashioned manual design process and focuses on the CAE-based optimisation technique for driving product design.

Structural optimisation is to seek optimum design of the predefined objective subjected to a certain constraint. It is one of the most important research topics in structural design, integrating computational mechanics, mathematic programming, computer science and other engineering sciences. With regard to optimisation design of vehicle body structures, various performances have to be taken into account. This thesis mainly focuses on crashworthiness and fatigue durability, which are closely related to vehicle safety.

1.2 Surrogate modelling in engineering optimisation

In engineering optimisation, abovementioned direct coupling method may be inefficient (if not impossible) since iterative nonlinear FE analyses during optimisation usually require

enormous computational costs and take the risk of premature FE failure prior to a proper convergence. As a result, an alternative approach is to use meta-models (or surrogate models) for formulating design criteria in advance of optimisation, which has proven an effective and sometimes unique approach.

Surrogate models aim to establish the explicit relation between design variables and system response, where only a limited number of sampling points are required. To date, most commonly used surrogate models include Polynomial Response Surface (PRS) model, Kriging (KRG) model, artificial neural network (ANN), radial basis function (RBF) and support vector regression (SVR). In order to gain an insight into the selection of metamodels, substantial studies have been done (e.g., [2-10]). For instance, Fang et al. [2] compared quadratic PRS and RBF for fitting nonlinear responses in a frontal collision, and found PRS was able to produce satisfactory approximation models for the energy absorption while RBF models performed better to approximate the maxiamum acceleration. Also, RBF models can yield more accurate optimisation results. Forsberg and Nilsson [4] compared linear PRS and Kriging with the same updating scheme of the region of interest. Kriging was found to be able to improve the sequential behavior of the optimisation algorithm in the beginning of the optimisation process. However, Kriging could be problematic if a constraint was violated after several iterations and linear PRS seemed more easily to find a feasible solution. We can come to a conclusion that the selection of metamodels is case dependent. In other words, no unique metamodel is able to produce the most accurate result for all cases.

In general, it is always expensive computationally to obtain sampling data for developing surrogate models while the cost of surrogate modelling and running optimisation themselves can be negligible. Thus, to make full use of different surrogate models to exploit as much information as possible, concurrent use of multiple surrogate models might be sensible to obtain the most competent solution[9]. In order to take full advantages of different individual

surrogates to extract as much information as possible with a relatively small number of sample points, some researchers have been paying attention to the use of an ensemble of surrogates for different problems. In this regard, Zerpa et al. [11] proposed the ensemble of surrogates to perform the optimisation of alkaline-surfactant-polymer flooding process, where a weighted average model provided the smallest difference between the surrogate estimations and corresponding simulation values compared to other individual surrogates. Goel et al. [12] used an ensemble of surrogates to model the regions with high uncertainty for developing a robust approximation strategy. Acar and Rais-Rohani [13] proposed a new approach to selecting weight factors for an ensemble of surrogates, which treated the determination of weight factors as an optimisation problem thereby minimizing the prediction error metric. Acar [14] also adopted the pointwise cross-validation as a local error measure to construct an ensemble of surrogates. Pan and Zhu[15] adopted the ensemble of surrogate models to optimise the upper structure for improving the roof strength. Zhou et al. [16] formulated an ensemble of surrogates with a more accurate control, in which the weight factors were updated using a recursive process until the ensemble achieved a desirable prediction accuracy. They also employed the ensemble of surrogates to build dual response surfaces for robust parametric design [17].

When performing a surrogate-based optimisation, a basic assumption is that the surrogate model is sufficiently accurate and all we need to do is to find the optimum design using the established surrogate model [18]. However, the surrogate model constructed using initial samples will probably not be accurate in the local region of the optimum. It is common to *exploit* this local region by sequentially positioning additional samples inside. These infill points are then used to update the surrogate model until the optimum converges to the final location properly, which seems to be attractive to more accurately locate a local optimum rather than the true global optimum [18]. On the other hand, *exploring* design space is a

strategy to increase the global accuracy of a surrogate model. It is straightforward to add sequential samples to the sparse regions of design space. If error estimates are available for the surrogate model, those points with large errors can be a candidate for increasing the accuracy of the surrogate. For example, the mean squared error of KRG model can be maximised to determine new sampling points in the framework of sequential optimisation [19, 20].

Considering both *exploration* and *exploitation*, Efficient Global Optimisation (EGO) [21] has also been proposed to add new sampling points iteratively which contribute toward global optimisation. The EGO algorithm uses KRG models because they provide not only the surrogate prediction but also error estimates. Due to the advances of hardware resources, parallel computing has also been studied by some researchers [22, 23]. Another extension of EGO is the multiobjective versions of *EI*, which have also been established recently (e.g., [24], [25], [26]). As the dimension increases, the calculation of EI could be very complicated from the theoretical point of view. Yang et. al [27] proposed to select sequential sampling points from the previous Pareto solutions based on the maximum minimum distance criterion[28], which does not require error information from the surrogate models.

1.3 Structural optimisation with uncertainties

4.2.3 Uncertainty classification in crashworthiness optimisation

Most of the engineering problems involve uncertainties, such as

(1) Manufacturing uncertainties. The uncertainties induced by manufacturing process account for the discrepancy between the nominal design and the real product. They may include parameters such as geometry (thickness, shape) and material properties (Young's modulus, Poisson's ratio, density, yield stress, tangent modulus, etc) [29-31].

(2) Operational uncertainties. These are the uncertainties on the operational conditions

upon crashing, which include occupant mass, impact speed, impact position, barrier's geometries, etc. [30, 32, 33]

(3) Modeling uncertainties. These are related to mathematical and numerical modeling techniques. For example, numerical errors in FEA and uncertainties in surrogate modelling [34-37] should be considered in optimisation.

It must be pointed out that usually a deterministic optimisation tends to push a design toward one or more constraints until the constraints become active, thereby leaving no room for tolerances in modeling, uncertainties, and/or manufacturing imperfections. To overcome such significant limitations of deterministic optimisation, some researchers have employed reliability-based design optimisation (RBDO). In addition to the constraint reliability, the objective robustness is another critical issue of optimisation with uncertainties. That is to say, optimisation algorithms search for a "peak" solution, where even a subtle perturbation in design variables and/or parameters can result in substantial loss of performance, making an "optimum" less meaningful or even misleading. Although RBDO deals with an optimal design that meets reliability constraints, it does not directly control design sensitivity to uncertainties. The robust design optimisation (RDO) aims to tackle the critical issues associated with uncertainty, thereby ensuring performance and quality of design.

Zhang and Liu[38] proposed to use the second-moment method and reliability based design concept as an effective tool for designing vehicular components. Acar 和 Solanki[37] performed the RBDO of vehicle crashworthiness and analysed the effects of reducing various uncertainties on the performance of optimisation design. Song and Lee [39] also adopted RBDO for an automotive knuckle component under different conditions, where a constraint-feasible moving least squares method was used for the meta-modelling of inequality constraint functions. d'Ippolito et al. [40] applied RBDO of fatigue life to a vehicle knuckle considering the variability in the material parameters. Ju 和 Lee[41] used Kriging modelling

with an active constraint strategy to solve the difficulties in implementing the moment method into RBDO. Sinha [31] applied MORBDO to the vehicle crashworthiness design optimisation for side impact, considering both structural crashworthiness and occupant safety, with structural weight and front door velocity under side impact as objectives. Lin et al. [31] developed a systematic approach for identifying the β-Pareto set for bi-objective optimisation problems under random uncertainties for a vehicle design problem. Daskilewicz et al. [42] studied the effects of uncertainty in MOO in the conceptual design of aircraft by demonstrating the changes in the Pareto frontiers due to variability in disciplinary metrics and differences in the formulation of the probabilistic optimisation problem. Deb et al. [43] combined the classical reliability optimisation techniques with evolutionary multi-objective optimisation (EMO) for better handling uncertainties of variables and parameters, in which vehicle design under side-impact problem was investigated. Boessio et al. [44] carried out a fatigue lifetime estimation of commercial vehicles due to loading randomness induced by rough pavement surfaces and performed the structural optimisation by considering the reliability index as a constraint. Grujicic et al. [45] performed RBDO of fatigue durability for ground vehicle suspension system components considering various uncertainties and revealed the importance of considering uncertainties of material properties. Youn et al. [29, 46] proposed a novel RBDO method and demonstrated it with side impact problems.

Some researchers introduced the six sigma design concept in product quality engineering to vehicle crashworthiness optimisation.[32, 33, 47, 48]. Lönn et al. [49] proposed to an RDO method capable of dealing with a large number of design variables and successfully applied it to an aluminium profile subjected to axial crushing. Zhang et al. [34] proposed to concurrently consider parameter uncertainty and model uncertainty, which was proven effective by two mathematical examples and a vehicle crashworthiness problem.

1.4 Optimisation of vehicle body structures

1.4.1 Crashworthiness optimisation

Vehicle crash brings about increasing concern from socioeconomic aspects. Each year vehicle crash leads to some 1.2 million deaths and many more injuries worldwide, becoming one of the biggest public health problems facing modern society. Taking USA, the most motorized country, as an example, the crash induced fatality has remained a high level, though certain reduction, over the past decade (Fig. 1), leading to the direct annual cost of US$277 billion, equivalent to nearly $900 per head or 1.9% of real Gross Domestic Product (GPD) of the country [50]. With rapid motorization in many developing countries, the magnitude of this problem is likely to continue growing. As per the statistical data from the authority[51], there was 58,539 deaths and 213,724 injuries in 198,394 road traffic accidents in 2013 in China, leading to a direct economic loss of 1.039 billion RMB.

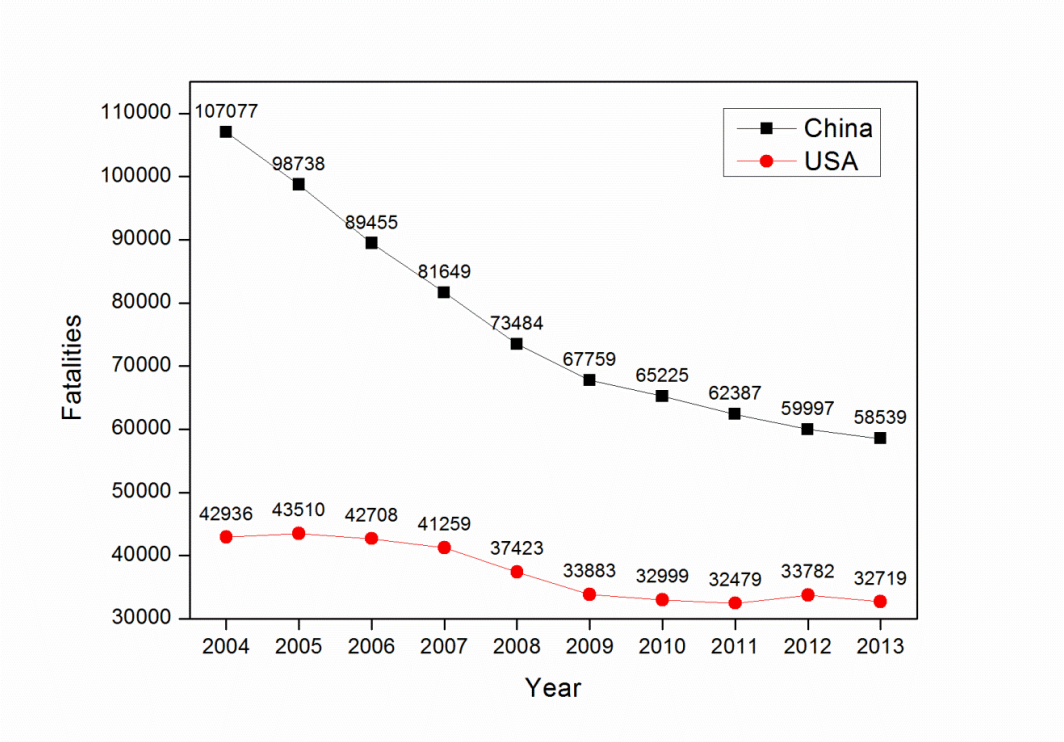

Fig. 1.1 Fatalities caused by motor vehicle crashes [50, 51]

Real-world loading conditions of crashworthiness optimisation mainly include front crash, side crash and rollover in the literature. For example, Liao et al. [52] implemented stepwise regression models to optimise the crashworthiness performance under the full front and 40% offset front impacts, where the vehicle mass, acceleration, and intrusion were taken as objectives. Wang et al.[53] used a probability-based least square SVR modelling technique to optimise the front substructure, where the impact force against the rigid wall was the objective while constraining the structural mass and energy absorption. Su et al. [54] approximated the static responses such as the stiffness and strength using PRS models and the impact responses such as intrusion were approximated using hybrid RBF models; based on a multi-island generic algorithm, the mass and stiffness were optimised simultaneously as the objectives while the stress and intrusion were taken as the constraints. Based on the non-dominated sorted genetic algorithm, Bojanowski and Kulak[55] optimised the bus beam structures to enhance the rollover and side impact safety and lightweight requirement. To improve the rollover safety in accidents, Pan and Zhu[15] utilised multiple surrogate models to optimise the crush strength of the roof structure. Gao et al. [56] optimised key components of a bus to reduce the acceleration of the centroid and the structural mass, based on the ECE R66 regulation.

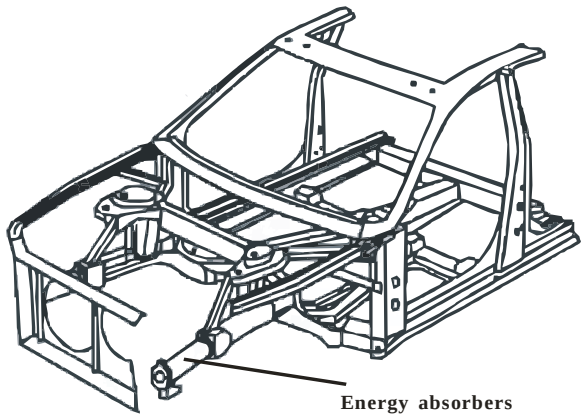

Fig. 1.2 Energy absorbers in automobile/train structures [57]

In reality, front impact contributes 67% of all types of impact accidents and is the most frequent impact form [58]. In this case, longitudinal rails are the most investigated components (Fig. 1.2), as they can absorb up to 50 percent of the kinetic energy of the vehicle upon the occurrence of a full frontal collision [59]. For example, Soto [60] employed topology optimisation to design frontal longitudinal rails. Cho et al. [61] adopted homogenisation method to determine the locations of the triggers, in order to induce the axial folding mode and thus to maximise the energy absorption in a front impact. Zhang et al. [62] explored a lightweight design for the front rails based on the design of experiments and response surface models. In vehicular systems, bumpers are expected to protect the pedestrian and passengers when a frontal crash occurs. The bumper should have a relatively low stiffness for the purpose of protecting pedestrians. On the other hand, FMVSS requires a strong bumper system to avoid large intrusion to the passenger compartment. Shin et al. [63] optimised the vehicle bumper system for the mass and crashworthiness requirements. Belingardi et al. [64] optimized the cross-sectional shape, wall thickness and transverse curvature of the E-Glass pultruded bumper and they achieved comparable energy absorption with steel and E-Glass fabric bumpers but better progressive failure mode with reduced peak load. Gao et al. [65] proposed a two-stage design procedure for bumpers based on the hybrid cellular automaton and Kriging methods. In addition, though side impact only contributes 28% of the accidents, it brings out a higher death rate (34% of the causalities). In the side impact, side structures such as A and B pillars play an irreplaceable role in protecting the passengers and driver. For example, Hanssen et al. [66] optimized an A-pillar structure with metal foam insert and the result improved the energy absorption by 30% at the cost of an only 3% mass increase. Marklund and Nilsson [67] optimised a B-pillar structure and achieved a 25% mass decrease without sacrificing the safety requirement. Pan et al. [68] optimized a TWB based B-pillar structure to

minimize the weight subject to the crashworthiness constraints of vehicular roof crush and side impact.

With regard to the component level, researchers have been continuously devising novel crashworthy materials and structures, aiming at lay a solid foundation for their application in the automotive engineering.

Alexander [69] pioneered research on the axial crushing for thin cylindrical shells and derived a closed-form analytical formula for calculating average crushing force. Then, experimental and theoretical studies by Wierzbicki and Abramowicz [70], Abramowicz and Jones [71, 72] and others carried on the studies on the axial crushing of tubes subjected to static and dynamic loads. More recently, thin-walled tubes with various sections have been investigated for crashworthiness, such as circular[73-80], polygonal[49, 81-89], conical/ tapered[90-98] and hat[99-102], to seek for optimal designs.

Generally, the number of angular elements (corners) in a tubal cross-section largely determines the energy absorption and crashing behaviours [70, 103]. It is therefore expected to design thin-walled tubes with multiple cells and internal webs for achieving better energy-absorbing characteristics. Crashworthiness optimisation was also introduced to the design of multi-cell configurations [20, 104-111].

Foam-filled structures have aroused increasing interest in the automotive industry for their extraordinary lightweight and energy absorption capacity. The presence of the foam-filler materials in thin-walled structures helps improve crashing stability and collapse modes, thereby increasing the overall crashworthiness [112-114]. However, the crashworthiness performance was found to be highly dependent on the foam density and geometrical configurations [115-117]. To address this issue, optimisation techniques were used to select best possible combination of tube geometry and foam density in both simple tubes (e.g., [118-124])

and complex structures (e.g., [66, 125-127]). Similarly, thin-walled structures filled with honeycomb core have also been investigated in the literature [128-130].

Increasing attention has been paid to lightweight of the vehicle for a range of demanding environment associated issues, e.g. material usage and fuel consumption. To maximize the functionality of material, substantial efforts have been devoted to the applications of proper tailor-welded blanks (TWB) structures. Automobile engineers can "tailor" the location of stamping so that the desire of specific material properties and/or thickness allocation can be achieved in a more efficient way [131]. Crashworthiness optimisation of TWB structures often aims to seek the best partition of different materials and thickness of each blank for both lightweighting and crash behaviours. The inner door panel [132, 133], B-pillar [68, 133] and frontal rail [134] are some typical examples for TWB structures adopted in vehicles.

One option to achieve lightweight design is to replace heavy metallic materials with light composites. Although most composite materials display little plastic characteristics, properly designed composite materials could absorb more energy per unit mass than the conventional metals [64, 78, 130, 135-137].

To tailor the crashworthiness performance, functionally-graded materials and structures, such as functionally graded foam-filled structures [10, 138-141] and structures with a functionally graded thickness [10, 142, 143], are more attracted increasing attention recently. The proposal of using such novel structures and materials provides the designer with more flexible solutions for crashworthiness, and meanwhile it gives the optimisation a new mission to design the best gradient. The relevant content will be discussed in more detail in Chapter 3.

1.4.2 Fatigue optimisation

During the usage of a car, the body are always subjected to a cyclic load due to the roughness of the road. The fatigue phenonminon is a strength issue caused by this cyclic load.

Generally, there are two types of methods assessing the fatiue life of a structure, i.e. the experimental and theoretical methods[58]. The conventional experimental method directly measures the fatigue life in the real or similar situation situation. The theoretical method analyses the fatigue performance by an established model based on the material property and applied load information.

The vehicle fatigue experments can be divided into three types, namely road test, proving gound test and in-door bench test. The in-door bench test is revelutionising the development of the fatigue performance while the out-door tests (the first two types) used to play an important role at the early time. In the 1970s, test system supliers MTS and Schenck developed their road simulator systems. Guan and Du et al. [144] developed the first road simulor of China based on the remote parameter control technique. The researchers in Tongji University significantly reduced the development cycle by conducting accelerated fatigue tests for vehicle components; they also investigated the quantitive correlation between the typical roads in China and test tracks in the proving ground of Shanghai Volkswagen and thus obtained the accurate fatigue prediction of a sedan car[145-147].

Finite element analysis based fatigue simulation started to be used in 1920. Compared to the experiment method, the simulation method can provide the detailed contour of the fatigue distribution. As such, the week part can be predicted at the design stage and thus aviod the unreasonable structural design. Therefore, the simulation method has become a powerful tool in the morden vehicle development, as it is able to reduce the number of physical prototypes. In this regard, Wannenburg et al. [148] presented a fatigue equivalent static load (FESL) method to assess the numerical durability of heavy vehicle structures. Koh [149] performed fatigue analysis of a vehicular steering link to prevent fatigue failure. He et al. [150] explored the failure causes in a damper spring of passenger car, in which the fatigue life prediction was carried out with the measured strain signals and local strain-life method. These works signify

urgency of developing design procedure for improving durability and fatigue life of vehicles. Sun and Lu [151] analysed the fatigue life of a body by combining finite element analysis and the power spectrum density method. Gao et al. [152] analysed the critical parts and fatigue life for a fuel-cell bus based on the transient stress history.

As the dynamic load is extremely difficult to handle during the optimisation process, most of the work in the automotive literature was focused on adopting one of the following optisation strategies[153]:

(1) static response optimisation: this straregy uses a series of static laods[154-156], which can reflet the extreme values of the loading history, to carry out the optimisation. Though static response optimisation has been well developed, applying this strategy to a dynamically loaded component could lead to overweight, unsafe and unreliable design.

(2) frequency response optimisation: the principle of this strategy is to move away the natural frequncy of the dynamically loaded structure from the maximum frequency of the loads so as to prevent the resonance[157-160]. The optimality of the design obtained from this strategy cannot be guaranteed because the real information of the loading condition is not taken into account.

(3) Quasi-static response optimisation: this strategy uses the fatigue life of the most critical location as a constraint in the optimisation process. The inexpensive quasi-static analysis was used for the sake of computational efficiency[161, 162]. Again, the quasi-static load cannot account for the history information of the real load. Furthermore, the constraint of the fatigue life on a specific location cannot guarantee the optimum design for the whole structure, since the most damaged locate could change during the optimisation process.

More recently, fatigue optimisation has been widely used in control arms [45, 163-166], knuckles [39, 40], wheels [167, 168] and body structures [44, 169, 170]. Zhu et al. [169] performed fatigue analysis of the body for a sports utility vehicle and performed topological optimisation of the

spot weld location in the critical region by using the homogenization method to improve its durability. Boessio et al. [44] carried out a fatigue lifetime estimation of commercial vehicles due to loading randomness induced by rough pavement surfaces and performed the structural optimisation by considering the reliability index as a constraint.

Note that the fatigue analysis depends on the history of the dynamic loading and it always needs an intensive simulation to extract a dynamic response. To address this issue, metamodel-based structural optimisation techniques have been playing an increasingly important role in vehicular design. In this regard, Hsu and Hsu [167] solved a weight reduction problem of aluminum disc wheels under constraints of fatigue life through a sequential neural network surrogate approximation. Lee and Jung [171] developed a KRG metamodel for optimizing a connecting rod subjected to a certain fatigue life. Ho et al. [172] developed a quadratic PRS model to improve a crankshaft rolling process for durability. Bayrakceken et al. [170] conducted a multiobjective optimisation for a passenger car's body, where ANN was used to model the fatigue life. Kaya et al. [173] re-designed a failed vehicle component subjected to cyclic loading by combining topology optimisation with PRS based shape optimisation. Song et al. [165] adopted the PRS and KRG surrogate models to optimize a control arm by considering strength and durability performance.

1.5 Research problems

It can be concluded for the review of literature that structural optimisation in vehicle structure has been achieved fruitful research outcomes and played an essential role in accelerating the development and reducing the development cost. However, the following problems still exist:

(1) To excavate the potential of crashworthiness, various novel structures have been proposed, among which funtionally graded structures are a representive. Then, is it possible to integrate functionally graded structures with other configurations? Can functionally graded

structure apply to multiple loading scinarios to widen the application scope? Can the tube with a funtionally graded thickness be combined with functionally graded foam to achieve preferable crashworthiness performance? Finally, how to design the gradients for the functionally graded structures and materials?

(2) There is no report available on the use of an ensemble of surrogate models in fatigue optimisation. Can the ensemble of surrogate models be used for fatigue optimisation and what is the effectiveness of using this tenique in fatigue optimisation?

(3) What advantages does the EGO have in practical engineering problems and why does it have such advantages? How to implementate the sequential surrogate based optmisation for a multiobjective optimisation problem?

(4) There is few studies on the microstructural uncertainty of the foam-filled structures. How does this uncertainty affect the results of crashworthiness optimisation?

(5) For specific engineering design case, how to make a decision considering the unceratinty?

1.6 Thesis structure

Based on a couple of industrial projects, this thesis investigates the surrogate modelling method and its application in the vehicle body design, aiming to improve the effectiveness and efficiency of fatigue and crashworthiness optimisation and to enhance the accuracy, reliability and robustness of the optimisation design. Fig. 1.3 outlines the structure of the thesis and the contents are as follows:

Chapter1 Introduction. This chapter first introduces the backgound and significance of this study. Then, the state of the art is systematically reviewed, including surrogate based engineering optmisation, structural optimisation under uncertainty, and optimisation of body structures. Last, the research problems to be addressed in this thesis are pointed out.

Chapter 2 Theory of surrogate-based engineering optimisation. This chapter

introduces the relevant theories in surrogate-based optimisation, including design of experiments, surrogate modelling, and particle swarm optimisation algorithms, laying the theretical foundation for the later chapters.

Chapter 3 crashworthiness optimisation for functionally graded structures based on surrogate modeling. A series of novel crashworthy structures is introduced to the design of energy absorbers from the bio-inspired perspective. The multiobjective particel swarm optimisation algorithm is used to conducted the crashworthiness optimisation for multi-cell tubes with a functionally graded thickness under the axial crushing, functionally graded foam-filled tubes under the bending and doubly graded structures, respectively. The purpose is to develop the advanced energy absorbers to push the vehicle safety to a new level.

Chapter 4 Fatigue optimisation of a truck cab based on the ensemble of surrogates. This chapter proposed to use the ensmeble of surrogate models to optimise the fatigue life of a truck cab, in order to make full use of the information of training points and excavate the potential of multiple surrogate models. Meanwhile, this chapter proposes a hyrid particle swarm optimisation algorithm to address the optimisation problem by integrating the standard particle swarm optimisation algorithm with the sequential quadratic programming so that the premature issue of the standard particle optimisaiton can be avoided.

Chapter 5 Sequential surrogate based optimisation and its application to body structures. To allieviate the depedence of optimisation results on the number of initial training points and to improve the efficiency and accuracy of the optimisation, sequential surrogate based optimisation is proposed to handle practical problems in the automotive engineering. The EI-based optimisation method was employed to enhance the fatigue performance of a spot weled joint; the multiobjective sequential optimisation is applied to a crashworthiness design of a foam-filled bitubal structure.

Chapter 6 Uncertainty-based optimisation and its application to vehicle body

structures. To account for the uncertainties in material properties and geometries, uncertainty-based optimisation is proposed to address three engineering problems. First, the analysis response surface and design response surface models are used to maximise the vetical sag stiffness and minimise the mass of a vehicle door subjected to the probabilistic constraint. The effects of reducing the uncertainty and improving the desired reliability level are analysed to guide the practical design. Second, a multiobjective optimisation under uncertainty is conducted based on the multiobjective particle swarm optimisation and Monte Carlo simulation. The study compares the optimisation results between the deterministic and non-deterministic optimisations and analyses the effects of the weight on the mean and standard deviation of the performances on the optimisation results. Third, considering the uncertainty in the material property, the multiobjective optimisation of a truck cab is investigated. The concept of the general dual surrogate models is introduced to approximate the mean and standard deviation of the fatigue life and then the multiobjective robust optimisation is conducted based on the established dual surrogate models and the multiobjective particle swarm optimisation algorithm. A hybrid decision making model is proposed to select the most appropriate solution from the Pareto front, which makes a best tradeoff between the fatigue performance and the robustness.

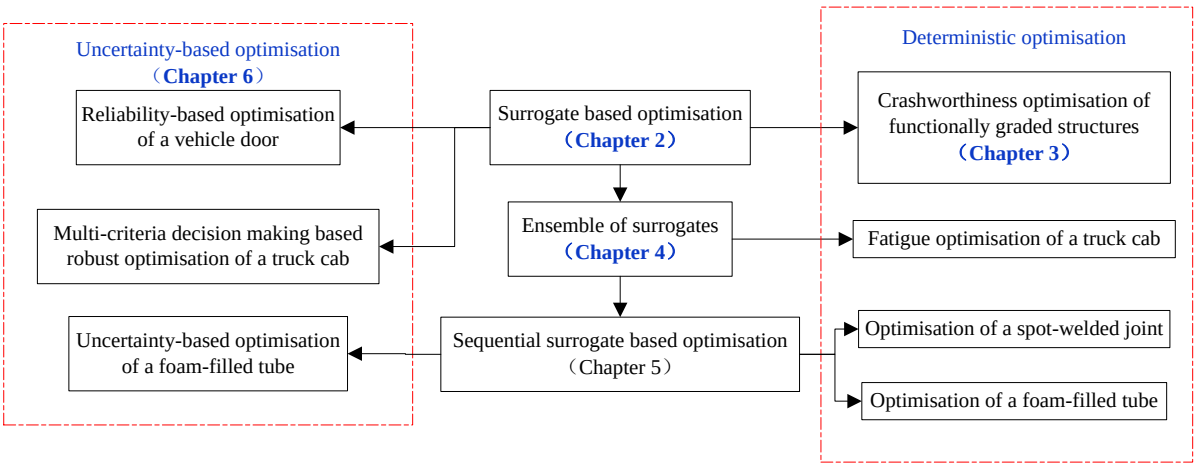

Fig. 1.3 Structure of the thesis

Chapter 2 Theory of surrogate-based engineering Optimisation

In engineering optimisation of complex systems, surrogate modelling has been widely used as a powerful tool. Surrogate models are established mathematical models between design variable inputs and response outputs based on a limited number of sample data. The mathematical models can replace the high-fidelity simulations during the optimisation iteration. Fig. 2.1 displays the optimisation procedure of using surrogate models and the details will be introduced in this chapter.

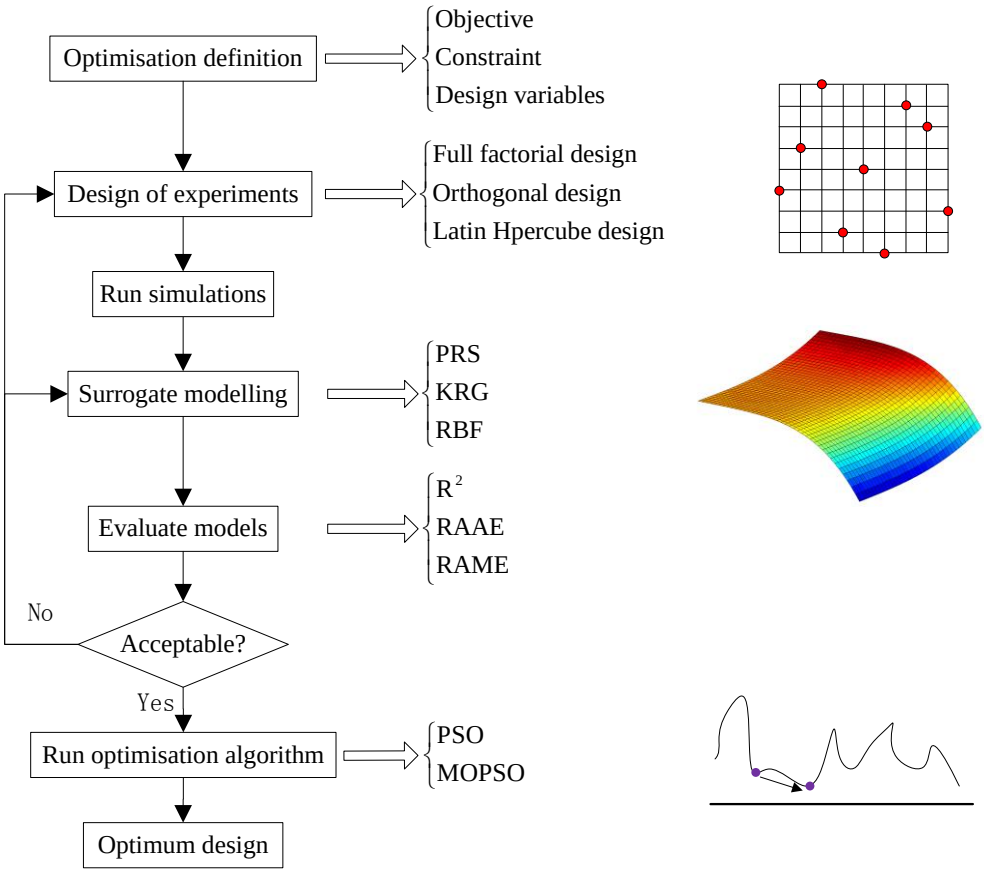

Fig. 2.1 Procedure of surrogate based optimisation

2.1 Definition of the optimisation problem

The optimisation problem can be defined as:

$$\begin{cases} \min \ \ y=\left(f_1(\mathbf{x}), f_2(\mathbf{x})..., f_M(\mathbf{x}) \right) \\ s.t. \ \ g(\mathbf{x}) \le 0 \end{cases} \tag{2.1}$$

where $\mathbf{x}$ is the vector of design variables and $f_i(\mathbf{x})$, i=1,2,…,M is the objective function, $g(\mathbf{x}) \le 0$ is the constraint function. When M>1, Eq. (2.1) is a multiobjective optimisation problem; otherwise, it is a single objective optimisation problem。

2.2 Design of experiments

Based on probability theory and mathematical statistics, Design of Experiments (DoE) can guide to scientifically select sampling points in the design space so that these points can reflect the characteristics of the design space as much as possible.

2.2.1 Full factorial design

A full factorial design contains all possible combinations of all factors at all levels. It contains the most amount of information, providing the main effect of each factor and the interaction effect between the factors. Assume n factors with m_1, m_2, ..., m_n levels (discrete values) respectively, and then $m_1 \times m_2 \times ... \times m_n$ experiments are required to be conducted for the full factorial design. The major drawback of the full factorial design is that when the numbers of the factors and/or the levels are large, the number of the experiments can be prohibited for the practical implementation. For example, the full factorial design with 11 factors and 2 levels needs 2^{11}=2048 experiments.

2.2.2 Orthogonal array desgin

Table 2.1 Orthogonal array $L_{12}(2^{11})$

Exp No.	Factor

	1	2	3	4	5	6	7	8	9	10	11
1	1	1	1	1	1	1	1	1	1	1	1
2	1	1	1	1	1	2	2	2	2	2	2
3	1	1	2	2	2	1	1	1	2	2	2
4	1	2	1	2	2	1	2	2	1	1	2
5	1	2	2	1	2	2	1	2	1	2	1
6	1	2	2	2	1	2	2	1	2	1	1
7	2	1	2	2	1	1	2	2	1	2	1
8	2	1	2	1	2	2	2	1	1	1	2
9	2	1	1	2	2	2	1	2	2	1	1
10	2	2	2	1	1	1	1	2	2	1	2
11	2	2	1	2	1	2	1	1	1	2	2
12	2	2	1	1	2	1	2	1	2	2	1

Different from a full factorial design, orthogonal array design is a fractional factorial design. A fractional factorial experiment is a certain fractional subset of the full factorial set of experiments, carefully selected to maintain orthogonality (independence) among the various factors and certain interactions. It is this orthogonality that allows for independent estimation of factor and interaction effects from the entire set of experimental results.

In the orthogonal array $L_A\left(m^n\right)$, L denotes the orthogonal array and A is the number of the rows (i.e. the number of the experiments), m is the number of the levels and n is the number of the factors. Table 2.1 is the $L_{12}\left(2^{11}\right)$ orthogonal array.

Orthogonal arrays are characterised by their orthogonality. In Table 2.1, if the levels (1, 2) are converted to (-1, 1), then the vectors of the 1st and 2nd factors $\mathbf{x}_1$= (-1，-1，-

1，-1，-1，-1，1，1，1，1，1，1), $\mathbf{x}_2$= (-1，-1，-1，1，1，1，-1，-1，-1，1，1，1), and thus we can obtain $\mathbf{x}_1\mathbf{x}_2^T$=0. The orthogonality means: 1) the levels of a factor appear the same times in the orthogonal array, which makes the experimental results at different levels are comparable; 2) the ordered pairs formed by the rows restricted to any two columns are all the possible ordered pairs of the two-element set (full factorial design).

The orthogonal array design with 11 factors and 2 levels only needs 12 experiments, far more than 2018 of the full factorial design. However, it will be still cost-prohibitive for the cases of a large number of factors and levels.

2.2.3 Optimal Latin Hypercube design

Another class of experimental design which efficiently samples large design spaces is the Latin Hypercube design. The Latin Hypercube design is a space-filling design as shown in Fig. 2.2b. An advantage of using Latin Hypercubes over Orthogonal Arrays (Fig. 2.1a) is that more points and more combinations can be studied for each factor. The Latin Hypercube technique allows the designer total freedom in selecting the number of designs to run as long as the number of experiments is larger than that of the factors. With this technique, the design space for each factor is uniformly divided for all factors. These levels are then randomly combined to specify *m* points defining the design matrix (each level of a factor is studied only once). A drawback to the Latin Hypercubes is that, in general, they are not reproducible since they are generated with random combinations. In addition, as the number of points decreases the chances of missing some regions of the design space increases.

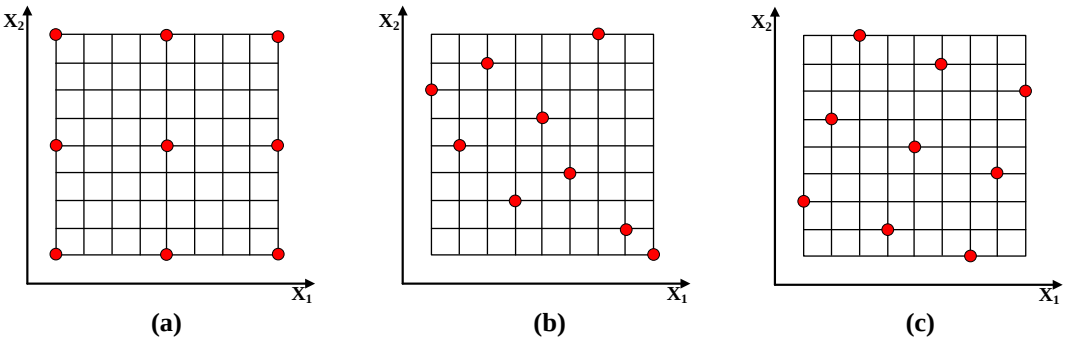

Fig. 2.2 Comparison of DoEs：(a)Orthogonal array(b)Latin Hypercube(c)Optimal Latin Hypercube

An optimal Latin Hypercube design is a modified Latin Hypercube, in which the combination of factor levels for each factor is optimized, rather than randomly combined. The goal of this optimisation process is to design a matrix in which the points are spread as evenly as possible within the design space defined by the lower and upper level of each factor. As shown in Fig. 2.2c, the optimal Latin Hypercube design can inherit the merit of the Latin Hypercube design and overcome its drawback of failing to capture some regions of the design space. The following three commonly used optimality criteria can be used to construct an optimal Latin Hypercube design: [174]

1) Maximin distance criterion, i.e., to maximise the minimum in-site distance as follows

$$\max\left[\min_{1\le i,j\le n, i\ne j} d\left(\boldsymbol{x}_i,\boldsymbol{x}_j\right)\right] \tag{2.2}$$

$d\left(\boldsymbol{x}_i,\boldsymbol{x}_j\right)$ is the distance between $\mathbf{x}_i$ and $\mathbf{x}_j$

$$d\left(\boldsymbol{x}_i,\boldsymbol{x}_j\right)=d_{ij}=\left[\sum_{k=1}^{m}\left|x_{ik}-x_{jk}\right|^{t}\right]^{1/t},\ t=1\text{ or }2 \tag{2.3}$$

2) Entropy criterion

$$\min \ -\log|\boldsymbol{R}| \tag{2.4}$$

$\boldsymbol{R}$ is the correlation function of the experimental matrix:

$$\boldsymbol{R}_{ij} = \exp\left[\sum_{k=1}^{m} \theta_k \left|x_{ik} - x_{jk}\right|^t\right], 1 \le i, j \le n; 1 \le t \le 2 \tag{2.5}$$

where θ_k is the correlation coefficient。

3) Centered L2 discrepancy criterion)

The Lp discrepancy is a measure of non-uniformity of a design. Among Lp discrepancy, L2 discrepancy is used most frequently since it can be expressed analytically and is much easier to compute.：

$$\begin{aligned} CL_2(\boldsymbol{x})^2 = &\left(\frac{13}{12}\right)^2 - \frac{2}{n}\sum_{i=1}^{n}\prod_{k=1}^{m}\left(1+\frac{1}{2}\left|x_{ik}-0.5\right|-\frac{1}{2}\left|x_{ik}-0.5\right|^2\right) \\ &+\frac{1}{n^2}\sum_{i=1}^{n}\sum_{j=1}^{n}\prod_{k=1}^{m}\left(1+\frac{1}{2}\left|x_{ik}-0.5\right|+\frac{1}{2}\left|x_{jk}-0.5\right|-\frac{1}{2}\left|x_{ik}-x_{jk}\right|\right) \end{aligned} \tag{2.6}$$

2.3 Theory of Surrogate modelling

As demonstrated in Fig. 2.3, for an optimisation problem with the design variables (inputs) x_1 and x_2 and the response (output) y, nine sampling points are generated first using the DoE technique in Section 2.2; then the response are extracted from simulations; finally, the surrogate model $\hat{y}$ is established to replace the real response y in the subsequent optimisation.

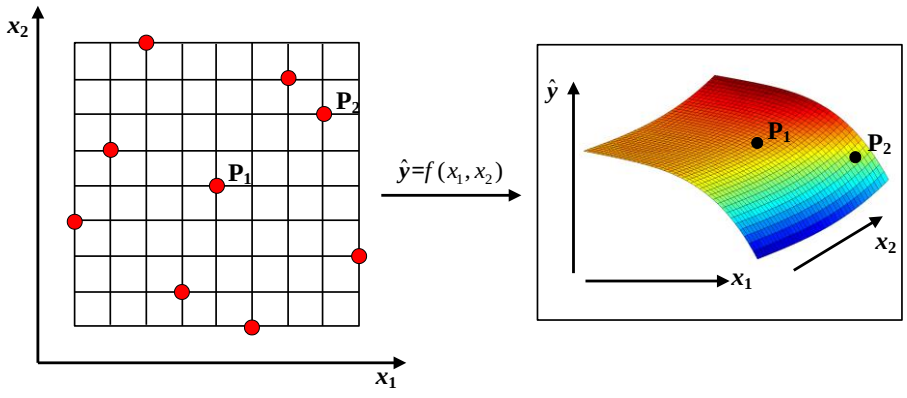

(a) (b)

Fig. 2.3 Construction of surrogate models: (a) sampling points; (b) surrogate models

2.3.1 Response surface method model

The response surface method (RSM) was originally proposed to analyze the results of physical experiments and create empirically-based analytical models for the observed response values. The RSM postulates a model as

$$y(\mathbf{x}) = f(\mathbf{x}) + \varepsilon \tag{2.7}$$

where $y(\mathbf{x})$ is the unknown function of interest, $f(\mathbf{x})$ is a known basis function of design variable $\mathbf{x}$, and ε is the residual error which is assumed to be normally distributed with mean zero and variance σ^2. The individual errors, ε_i at each observation points, are also assumed to be independent and distributed consistently.

In many cases, the polynomial basis functions are found rather effective, and the corresponding RSM is named as polynomial response surface (PRS) methods. For example, a quadratic PRS model can be expressed as [175],

$$\hat{y}(\mathbf{x}) = b_0 + \sum_{i=1}^{n} b_i x_i + \sum_{i=1}^{n} b_i x_i^2 + + \sum_{i=1}^{n-1} \sum_{j=i+1}^{n} b_{ij} x_i x_j \tag{2.8}$$

where b_0, b_i and b_{ij} are the unknown coefficients, x_i is the *i*-th design variable, and *n* is the total number of design variables. These unknown coefficients can be

determined through the least square regression by minimizing the squared sum of the deviations of predicted value $\hat{y}(\mathbf{x})$ from the actual value $y(\mathbf{x})$.

Note that the minimum number of FEA runs for a quadratic PRS model should be $(n+1)\times(n+2)/2$ in order to obtain the unknown coefficients, which implies the number of design variables could be critical. To address this issue, stepwise regression [32, 33, 52, 176] can be implemented to screen the terms in PRS which have a relatively little contribution to the design criteria.

2.3.2 Radial basis function model

The radial basis function (RBF) model was developed for scattered multivariate data interpolation by using a series of basis functions that are symmetric and centered at each sampling point. Radial basis functions are typically formulated as [177]:

$$\hat{y}(\mathbf{x}) = \sum_{j=1}^{m} c_j p_j(\mathbf{x}) + \sum_{i=1}^{n_s} \lambda_i \phi(r(\mathbf{x}, \mathbf{x}_i)) \tag{2.9}$$

where m is the number of the polynomial terms, c_j is the coefficient for polynomial basis function $p_j(\mathbf{x})$. λ_i is the weighed coefficient, $r(\mathbf{x}, \mathbf{x}_i)$ is the Euclidean distance expressed in terms of $\|\mathbf{x} - \mathbf{x}_i\|$. $\varphi(r)$ is the radial basis function, for which most commonly used include Gaussian, thin plate spline, multiquadric, inverse quadric function, etc, given in Table 2.2.

Table 2.2 Commonly used radial basis functions

	Basis function
Thin-plate spline function	$\varphi(r) = r^2 \log(cr^2),\ 0 \le c \le 1$
Gaussian function	$\phi(r) = e^{-cr^2},\ c > 0$

Multiquadric function	$\varphi(r)=\sqrt{r^2+c^2}\ ,\ 0\le c\le 1$
Inverse quadric function	$\varphi(r)=\dfrac{1}{r^2+c^2}\ ,\ 0\le c\le 1$

To solve those undetermined parameters c_j and λ_i, the orthogonality conditions are used without loss of generality,

$$\sum_{i=1}^{n_s}\lambda_i p_j(\mathbf{x}_i)=0, \qquad \text{for} \qquad j=1,2,\cdots,m$$

(2.10)

Combining Eqs. (4) with (5) in a matrix form gives

$$\begin{bmatrix}\mathbf{\Phi} & \mathbf{P}\\ \mathbf{P}^{\mathbf{T}} & \mathbf{0}\end{bmatrix}\begin{bmatrix}\boldsymbol{\lambda}\\ \mathbf{c}\end{bmatrix}=\begin{bmatrix}\mathbf{y}\\ \mathbf{0}\end{bmatrix} \tag{2.11}$$

in which matrices $\mathbf{\Phi}$ and $\mathbf{P}$ are determined by the sampling point values of both the radial basis function and the polynomial basic function, respectively.

2.3.3 Kriging (KRG) model

The Kriging (KRG) model was originally developed for mining and geostatistical applications involving spatially and temporally correlated data. The Kriging model comprises a global model and a localized departure [178]:

$$y(\mathbf{x})=f(\mathbf{x})+Z(\mathbf{x}) \tag{2.12}$$

where $y(\mathbf{x})$ is the unknown function of interest, $f(\mathbf{x})$ is the known approximation (usually polynomial) function, and $Z(\mathbf{x})$ represents a stochastic parameter with mean zero, variance σ^2, and nonzero covariance. The $f(\mathbf{x})$ term is similar to a polynomial response surface, providing a global model of the design space, often taken as a constant β. $Z(\mathbf{x})$ provides localized deviations. The covariance matrix of $Z(\mathbf{x})$ is given as:

$$Cov[Z(\mathbf{x}^i), Z(\mathbf{x}^j)] = \sigma^2 \mathbf{R}[R(\mathbf{x}^i, \mathbf{x}^j)] \tag{2.13}$$

where $\mathbf{R}$ is a correlation matrix defined by Gaussian correlation function $R(\mathbf{x}^i, \mathbf{x}^j)$ as follows:

$$R(\mathbf{x}_i, \mathbf{x}_j) = \exp\left[-\sum_{k=1}^{n_{dv}} \theta_k \left| \mathbf{x}_k^i - \mathbf{x}_k^j \right|^2 \right] \tag{2.14}$$

where n_{dv} is the number of design variables, θ_k is the unknown correlation parameter used to fit the model, and $\mathbf{x}_k^i$ and $\mathbf{x}_k^j$ are the kth components of sample points $\mathbf{x}^i$ and $\mathbf{x}^j$, respectively. From Eqs. (2.13) and (2.14), the correlation function approaches 1 when $\mathbf{x}^i$ and $\mathbf{x}^j$ are very closed to each other while correlation function approaches 0 when $\mathbf{x}^i$ and $\mathbf{x}^j$ are far away from each other. In addition, the larger the θ_k the smaller the correlation function (Fig. 2.4).

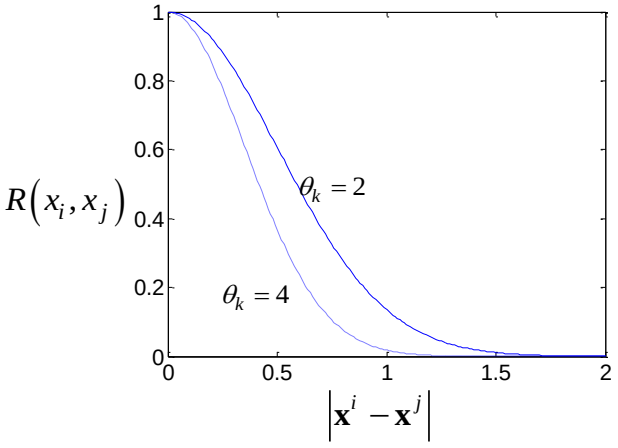

Fig. 2.4 Correlation function

Then, predicted estimates, $\hat{y}(\mathbf{x})$, of the response $y(\mathbf{x})$ at untried points are given by:

$$\hat{y}(\mathbf{x}) = \hat{\beta} + \mathbf{r}^T(\mathbf{x})\mathbf{R}^{-1}\left(\mathbf{y} - \mathbf{f}\hat{\beta}\right) \tag{2.15}$$

where $\mathbf{y}$ is the response vector and $\mathbf{f}$ is a column vector that is filled with ones when

$f(\mathbf{x})$ is taken as a constant. $\mathbf{r}^T(\mathbf{x})$ is a correction vector that implies how close between sample points and untried points

$$\mathbf{r}^T(\mathbf{x}) = \left[R(\mathbf{x}, \mathbf{x}^1), R(\mathbf{x}, \mathbf{x}^2), ..., R(\mathbf{x}, \mathbf{x}^{n_s}) \right]^T \tag{2.16}$$

$\hat{\beta}$ is the general least square estimator given as follows:

$$\hat{\beta} = (\mathbf{f}^T \mathbf{R}^{-1} \mathbf{f})^{-1} \mathbf{f}^T \mathbf{R}^{-1} \mathbf{y} \tag{2.17}$$

The estimate of the variance of the sample data from the global model is

$$\hat{\sigma}^2 = \frac{\left(\mathbf{y} - \mathbf{f}\hat{\beta}\right)^T \mathbf{R}^{-1} \left(\mathbf{y} - \mathbf{f}\hat{\beta}\right)}{n_s} \tag{2.18}$$

For calculating θ_k in Eq. (2.14), the maximum likelihood estimates are used by solving the following maximization problem over the interval $\theta_k > 0$,

$$\max\left(-\frac{n_s \ln\left(\hat{\sigma}^2\right) + \ln|\mathbf{R}|}{2} \right) \tag{2.19}$$

where both $\hat{\sigma}^2$ and $|\mathbf{R}|$ are the functions of θ_k.

Kriging models can also predict the mean squared error at any point of the design space:

$$\hat{s}^2(\mathbf{x}) = \hat{\sigma}^2 \left\{ 1 - [\mathbf{f}^T(\mathbf{x}) \ \mathbf{r}^T(\mathbf{x})] \begin{bmatrix} \mathbf{0} & \mathbf{F}^T \\ \mathbf{F} & \mathbf{R} \end{bmatrix}^{-1} \begin{bmatrix} \mathbf{f}(\mathbf{x}) \\ \mathbf{r}(\mathbf{x}) \end{bmatrix} \right\} \tag{2.20}$$

The reader can refer to [178] for more details about the Kriging moel techique.

2.3.4 Error metrics for surrogate modelling

As surrogate models are just the approximations of the real system response, their accuracies need to be validated before they can be used to replace the real response during the optimisation. Commonly-used error metrics are summarised in Table 2.3, where y_i denotes the exact function value for assessment point *i*, $\hat{y}_i$ is the

corresponding surrogate value. $\bar{y}$ is the mean of y_i, N_v is the number of the confirmation sampling points. Apparently, a larger value of R-square and a smaller value of the other metrics are preferred.

Table 2.3 error metrics for surrogate modelling

Metrics	Expression
R^2	$R^2 = 1 - \frac{\sum_{i=1}^{N_v}(y_i - \hat{y}_i)^2}{\sum_{i=1}^{N_v}(y_i - \bar{y})^2}$
Root-mean-square error(RMSE)	$RMSE = \sqrt{\frac{1}{N_v}\sum_{i=1}^{N_v}(y_i - \hat{y}_i)^2}$
Relative average absolute error(RAAE)	$RAAE = \frac{\sum_{i=1}^{N_v}\lvert y_i - \hat{y}_i\rvert}{\sum_{i=1}^{N_v}\lvert y_i - \bar{y}\rvert}$
Relative maximum absolute error(RMAE)	$RMAE = \frac{\max\{\lvert y_i - \hat{y}_1\rvert, \ldots, \lvert y_i - \hat{y}_{N_v}\rvert\}}{\sum_{i=1}^{N_v}\lvert y_i - \bar{y}\rvert / N_v}$
Maximum relative error(e_{max})	$e_{\max} = \max_{i\in\{1,\ldots,N_v\}}\left(\frac{\lvert y_i - \hat{y}_i\rvert}{\lvert y_i\rvert}\right)$
Average relative error(e_{avg})	$e_{avg} = \frac{1}{N_v}\sum_{i=1}^{N_v}\frac{\lvert y_i - \hat{y}_i\rvert}{\lvert y_i\rvert}$

2.4 Particle swarm optimisation algorithm

2.4.1 Single-objective particle swarm optimisation algorithm

Particle swarm optimisation (PSO) algorithm [179] is a relatively new heuristic approach inspired by the choreography of a bird flock. In the standard PSO, every particle is treated as a point in a *d*-dimensional design space which adjusts its "flying" according to its own and other particles' flying experience. Meantime, each particle keeps track of its position in the solution space in terms of the fitness value achieved

by this particle so far, in which this fitness value is named as personal best (pBest). Another best fitness value that is tracked by PSO is the best value obtained by the whole swarm up to now, and it is called global best (gBest). The operation of PSO is by gradually changing the velocity of each particle toward its pBest and gBest positions at each time step. The update of velocity and position can be done as [180]:

$$\mathbf{v}_i(t+1) = \mathbf{v}_i(t) + r_1 c_1(\mathbf{p}_i(t) - \mathbf{x}_i(t) + r_2 c_2(\mathbf{p}_g(t) - \mathbf{x}_i(t))) \quad (2.21)$$

$$\mathbf{x}_i(t+1) = \mathbf{x}_i(t) + \mathbf{v}_i(t+1) \quad (2.22)$$

where $\mathbf{v}_i(t+1)$ and $\mathbf{x}_i(t+1)$ are the velocity and position of particle i at $(t+1)$th iterations respectively, $\mathbf{p}_i(t)$ is the particle position of pBest$_i(t)$, $\mathbf{p}_g(t)$ is the particle position of gBest(t), c_1 and c_2 are the acceleration factors, r_1 and r_2 are the uniformly distributed random numbers between 0 and 1. The algorithmatic procedure of PSO is as follows:

(1). Initialise the PSO parameters, such as population size, acceleration factors, maximum generation;

(2). Randomlise $\mathbf{x}_i$ and $\mathbf{v}_i$ and calculate the fitness value $f(\mathbf{x}_i)$; set the interation number t=0 and $\mathbf{p}_i = \mathbf{x}_i$, and find the optimum position $\mathbf{p}_g$.

(3) Update the particle velocities using Eq. (2.21).

(4) Update the particle positions according to Eq. (2.22) and calculate the fitness function value. If $f(\mathbf{x}_i) \le f(\mathbf{p}_i)$, then $\mathbf{p}_i = \mathbf{x}_i$; otherwise $\mathbf{p}_g = \mathbf{x}_i$.

(5) Check if the termination criteria are met: if so terminate the optimisation process, otherwise $t = t+1$ and return to Step (3).

2.4.2 Multi-objective Particle Swarm Optimisatioin

As an extended version of PSO, the multiobjective particle swarm optimisation (MOPSO) algorithm is characterized by fast convergence and well-distributed Pareto

frontier compared with other multiobjective optimisation algorithms such as NSGA-II [52, 181, 182]. Note that MOPSO has been employed successfully to solve a series of design problems, such as sheet metal forming and crashworthiness with foam filled structures [10, 183, 184]

The objective functions in a multiobjective optimisation problem are always conflicting and one can obtain a set of optmal solutions that cannot be further improved without sacrificing at least one of the objectives. These solutions are called non-dominated solutions or Pareto optimal solutions. Different from a single-objective optimisation that seeks a single optimum subjected to the constraint function, the multiobjective optmisation aims to acquire the Pareto solution set. A standard multiobjective optimisation can be writtern as:

$$\min y=\left(f_1(x), f_2(x)..., f_n(x)\right) \qquad (2.64)$$

$$s.t.\ g_i(x)\le 0, h_i(x)=0 \qquad (2.65)$$

$f_i(x)$, i=1,2,…,n is the objective functions, $g_i(x)\le 0$ denotes the inequality constraints and $h_i(x)=0$ represents the equality constraints. The Pareto dominance means that $\mathbf{x}^0$ dominates $\mathbf{x}^1$ ($\mathbf{x}^0 < \mathbf{x}^1$) if and only if Eq. (2.23) is satisfied.

$$\begin{cases} f_i\left(\mathbf{x}^0\right) \le f_i\left(\mathbf{x}^1\right), & i=1,2,\ldots,m \\ f_i\left(\mathbf{x}^0\right) < f_i\left(\mathbf{x}^1\right), & \exists i \in \{1,2,\ldots,m\} \end{cases} \qquad (2.23)$$

All the Pareto solutions comprise the Pareto solution set:

$$P_S=\left\{\boldsymbol{x}^0 \middle| \exists \boldsymbol{x}^1 > \boldsymbol{x}^0\right\} \qquad (2.24)$$

The values of the Pareto solution set in the objective sapace comprise the Pareto front P_F:

$$P_F=\left\{ f(\boldsymbol{x})=\left(f_1(\boldsymbol{x}), f_2(\boldsymbol{x}),\ldots, f_m(\boldsymbol{x})\right) \middle| \boldsymbol{x}\in P_S\right\} \qquad (2.25)$$

The multiobjective particle swarm optimisation algorithm proposed by Coello et al. [181] is as follows:

(1). Initialise the position of each particle $POP[i]$.

(2). Initialise the velocity of each parcle $VEL[i] = 0$.

(3). Evalute each of the particles in *POP* andstore the positions of the particles that represent non-dominated vectors in the repository REP.

(4). Generate hypercubes of the search space explored so far, and locate the particles using hypercubes as a coordinate system where each particle's coordinates are defined according to the values of its objective functions.

(5). Initialize the memory of each particle $PBEST[i] = POP[i]$.

(6). If the maximum number of the cycles has not been reached, continue to execute the following steps.

(7). Update the velocity of each particle $VEL[\mathrm{i}]=W\times VEL[i]+R1\times(PBEST[i]-POP[\mathrm{i}])+R2\times(REP[h]-POP[i])$, where W is the inertial weight,$R1$ and $R2$ random numbers between 0 and 1 and $REP[h]$ is a value taken from the repository.

(8). Update the position of each particle $POP[i]= POP[i]+ VEL[i]$.

(9). Maintain the particles within the search space in case they go beyond their boundaries.

(10). Evaluate each of the particles in *POP*.

(11). Upadate the contents of REP and the geographical representation of the particles.

(12). Increment the loop counter.

It can be seen that the main procedures of the multiobjective particle swarm optmisation algorithm include the update of the external repository, the selection of the global best and the update of the local bests, and the boundary treatment etc. [181]

2.5 Summary

This chapter introduced the whole process of the surrogate based optimisation,which is widely used in engineering optimisation. First, commonly-used DoE techiniques were introduced and discussed. Second, polynomial response surface, radial basis function and Kriging models are introduced together with the error metrics for assessing the surrogate models. Last, the single- and multi-objective particle swarm optimisation algorithms were introduced.

Chapter 3 Crashworthiness optimisation for functionally graded structures based on surrogate modeling

3.1 Introduction to functionally graded structures

Recently, functionally graded materials (FGMs), where microstructural details are spatially varied through a non-uniform pattern, are drawing increasing attention attributable to their tailored multifunctional behaviors. These advanced materials with engineered gradients of composition, structure or specific properties in the preferred direction/orientation are superior to homogeneous materials made of the same constituents and uniform geometry. For FGMs, the resultant mechanical properties such as Young's modulus, Poisson's ratio, shear modulus and material density can vary in preferred directions [185]. In nature, FGM structures widely exist, from bamboos (Fig. 3.1a) [186] and cuttlebone consisting of horizontal lamellae separated by vertical pillars [187] (Fig. 3.1b), to the spongy trabecular bone [188]. In the biomimetic context, the gradient concept has been taken into account in a wide range of engineering applications, where optimal use of materials is essential, e.g. functionally graded piezoelectric materials [189], dental implants [190], heat exchanger [38], and novel concrete structures [191], etc. To further improve the crashworthiness of foam-filled thin-wall structures, graded foam material and tube wall thickness have shown certain benefits. In this respect, functionally graded foam (FGF) materials [10, 138-141], where foam density varies continuously in a predefined form, have been attempted to replace uniform foam fillers.

Furthermore, to improve the utilization of wall materials functionally graded thickness (FGT) was proposed, in which the Tailored Rolling Blanks (TRB) technology

has been used to produce sheet metal for continuously changing wall thickness [192]. In this regard, Sun et al. [143] first explored the crushing characteristics of FGT square tubes and found that FGT tube is superior to its uniform counterpart in overall crashing behaviors. More recently, Li et al. [193] compared the novel FGT tube with the conventional tapered tube for withstanding oblique impacting, and found that FGT tube is more beneficial within a given spatial constraint. These studies showed that the column with a graded wall thickness is more preferred than with a uniform thickness for its stable load-deformation responses and reduced risk of global buckling.

The functionally graded structures provide us with a novel approach to crashworthiness design [194] and the gradient design widens the application of structural optimisation. This chapter will conduct optimisation design for various novel functionally graded structures and materials, aiming to develop more advanced energy absorption.

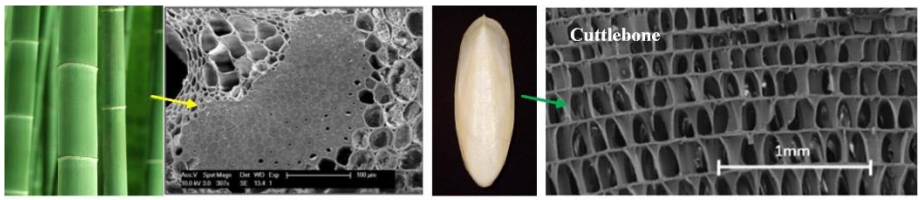

Fig. 3.1 Examples of FGMs in nature and engineering (a) bamboo (b) cuttlebone and SEM image of the transverse cross section of cuttlebone.

3.2 Crashworthiness and multiobjective optimisation of functionally graded multi-cell tubes

Typically, severe deformation with combined bending and membrane deformation takes place near the corners of tubes [195]. Thus, the number of corner elements on a tube's cross-section largely influences the energy absorption and crashing behaviors [70, 103]. It is expected to devise some sophisticated multi-cells and internal webs for

achieving better energy-absorbing characteristics. In this regard, Kim [195] proposed a new cross-section configuration with four square cells at the tubal corners for enhancing energy absorbing capacity. Zhang et al. [196] and Zhang and Cheng [197] derived a closed-form formula for the mean crushing force of multi-cell sections based upon tubal folding mechanism. Later, Alavi Nia and Parsapour [198] corrected Zhang's formula for unequally sized multi-cell tubes. To maximize energy absorption and minimize peak force, Hou et al. [199] adopted response surface method (RSM) to optimize single, double, triple and quadruple cell sectional columns. Qi et al. [95] compared the crashing behaviors of singe-cell straight, single-cell tapered, multi-cell straight and multi-cell tapered tubes, and they found the last one performs the best under oblique impact loading. Song and Guo [200] compared the windowed and multi-cell square tubes under axial and oblique loading. Tang et al. [201] devised a multi-cell circular column and verified its superiority to the conventional square structure. Zhang and Zhang [202] studied the quasi-static axial crushing of multi-cell stub columns with different sectional configurations. Tran et al. [203] developed theoretical solutions to mean horizontal force and mean bending moment for multi-cell square tubes under oblique impact loading. Bai et al. [204] conducted low speed compressive tests on hexagonal multi-cell structures and developed a new analytical model to predict the mean crushing strength. Liu et al. [205] investigated the crashworthiness of automotive front rails with various cross-sections and found the multi-cell section with double vertical internal stiffeners can absorb more energy than other configurations. Hong et al. [206] revealed that multi-cell tubes with triangular lattices enable to have mean crushing forces 60-103% higher than single-cell tubes. The common

features of these abovementioned studies are to increase the number of cells or devise novel cellular configurations with uniform wall thickness for enhancing crashworthiness.

The above-mentioned studies tried to increase the cell number or devise novel multi-cell tubes, while the tube thickness was uniform. On the other hand, is it possible to design transverse gradients to place more material the corners for excavating the potential of multi-cell structures? With this idea in mind, this section will conduct crashworthiness analysis and multiobjective optimisation based on surrogate modelling.

3.2.1 Numerical modelling

3.2.1.1 Geometrical description

The structure analysed herein is a five-cell tube with a functionally graded wall thickness (Fig. 3.2a). The length of this tube is H= 200 mm, and its cross-section dimension is $L \times L$= 75 mm ×75 mm. Fig. 3.2b depicts the graded thickness configuration in the cross section. Due to geometrical symmetry, the cross section is defined in three characteristic regions in this study, i.e., exterior walls of corner-cells (Region I), the exterior wall of the middle connector of corner cells (Region II) and inner ribs (Region III). Thus, the total numbers of these characteristic regions in the FGT tube are eight, four and eight, respectively. Each region is self-symmetric and assumed to has its own thickness gradient by following Eq. (3.1):

$$t_i(x_i, n_i) == t_{\max} - (t_{\max} - t_{\min})(\frac{x_i}{l_i})^{10^{n_i}} \qquad i = 1, 2, 3 \tag{3.1}$$

where $t_{\min}$ and $t_{\max}$ are the minimum and maximum wall thicknesses, respectively. In this study, $t_{\min}$ =0.7 mm and $t_{\max}$ = 2.0 mm are adopted. x_i and l_i are the distances shown

in Fig. 3.2b. n_i denotes the corresponding gradient parameter that governs the thickness variation ($-1 \leq n_i \leq 1$). Thus, Fig. 4 shows thickness variation *vs* normalized distance with different values of n_i. The thickness decreases as x_i increases and the gradient function changes from convex to concave, while n_i varies from negative to positive.

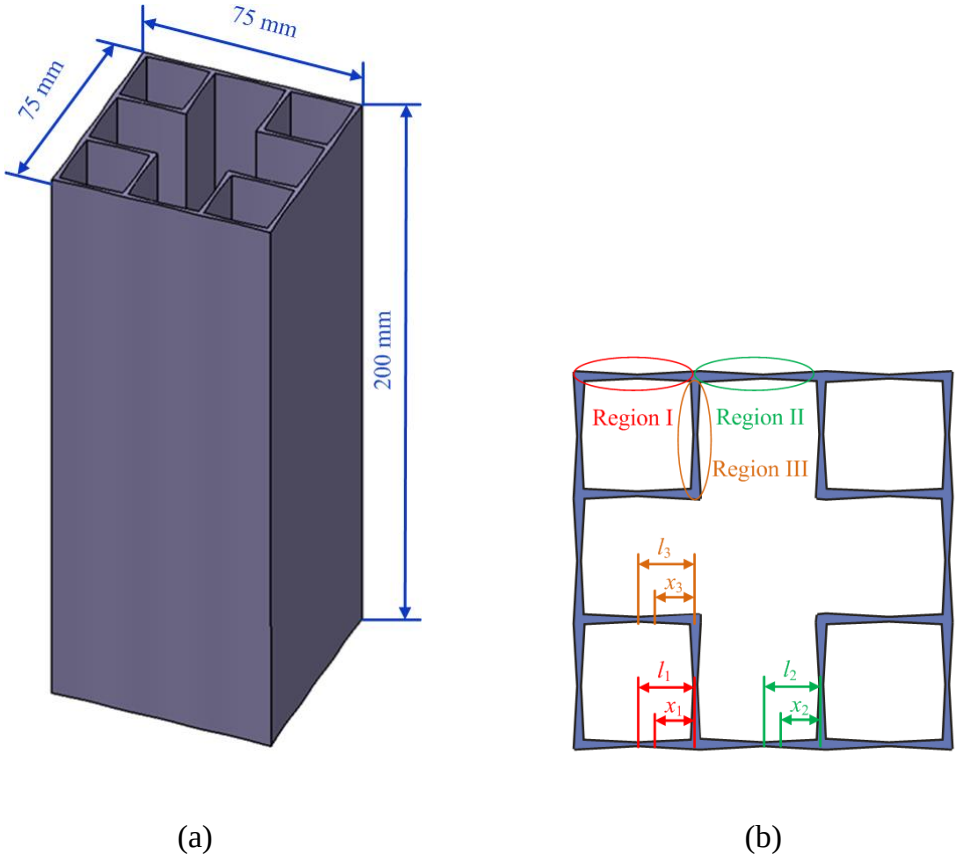

(a) (b)

Fig. 3.2 Configuration of FGT multi-cell tube: (a) 3D view; (b) 2D cross-sectional view

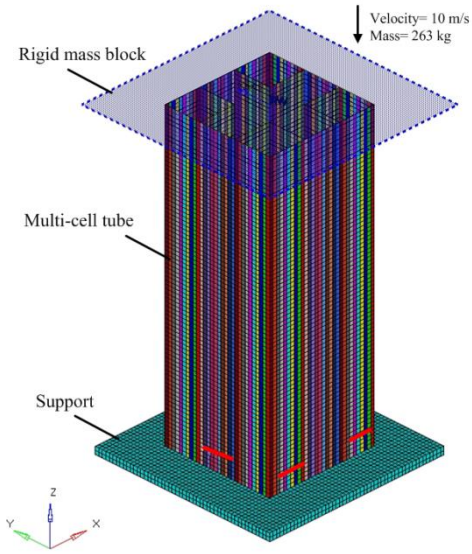

Fig. 3.3 Finite element model of FGT multi-cell tube.

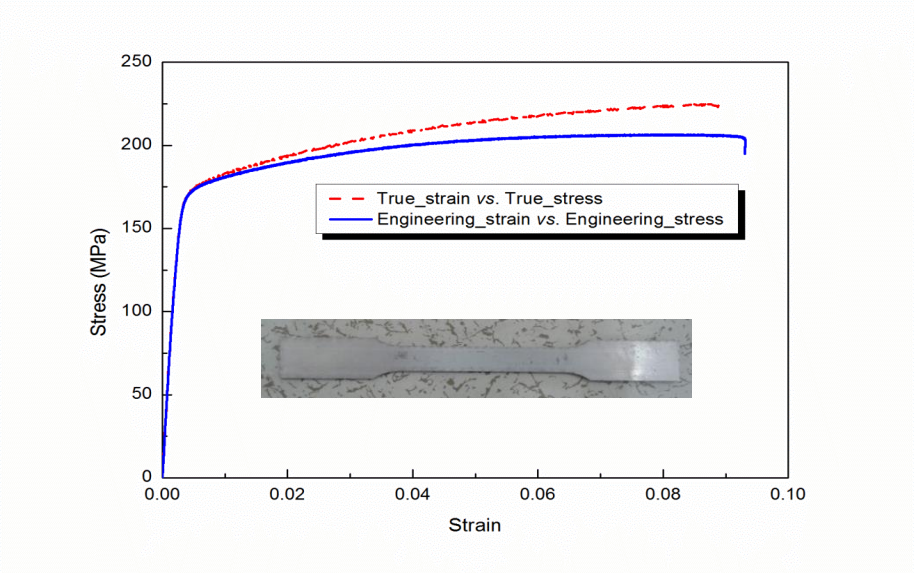

Fig. 3.4 Tensile specimen and stress-strain curves of AA6063-T5.

3.2.1.2 Finite element (FE) model

To investigate the crashworthiness of multi-cell tubes, the FE models were created. The tube was loaded by a rigid mass block of 263 kg with an initial axial velocity of 10 m/s. In order to initiate a stable and progressive crushing, indentation triggers were

introduced in the FE models [207, 208]. Small indentations on the corner-cell regions and connecting walls (refer to Fig. 3.3) near its distal end were used as triggers, which facilitate the FE model to more easily develop progressive folding mode. The triggers are placed at a certain distance from the distal end of the tube, which is approximately the half wavelength of one fold, and the depth of triggers are set to 0.2mm [202].

In this study, the numerical models were developed using explicit non-linear finite element code LS-DYNA. The Belytschko-Lin-Tsay reduced integration shell elements with five integration points through the thickness were employed to model the tubes. To model thickness variation more realistically, we attempted to assign different thicknesses to each of the four nodes of the shell elements in line with Eq. (3.1). Stiffness-based hourglass control was employed to avoid spurious zero energy deformation modes and reduced integration was used to avoid volumetric locking. "*RIGID WALL" was used to model the interaction between the impacting mass block and tube (Fig. 3.3). The interface between the tube and rigid support was modeled as an "automatic node to surface" contact. The "automatic single surface" contact was prescribed to the tube to avoid interpenetration during folding deformation. The static and dynamic frictional coefficients were taken as 0.2 and 0.3, respectively [209].

The tube was modeled through a piecewise linear elastic-plastic behavior with strain hardening (material model 24 in LS-DYNA). The thin wall material was aluminum alloy AA6063-T5 with the density =2700 kg/m^3, Poisson's ratio =0.3, and Young's modulus =70 GPa. The material model was considered insensitive to strain rate but defined as non-linear isotropic work hardening in the plastic region [10, 184]. The obtained stress - strain curve through our in-house tensile tests is provided in Fig. 3.4.

In order to determine the size of elements, a convergence test was carried out to minimize the effect of mesh refinement on the accuracy of numerical analysis, thereby maintaining reasonable balance with computational cost. The shell element size of 2×2 mm^2 was found to be sufficient to simulate the multi-cell tubes, which were used throughout the present study. According to the above description, the 3D FE model of the multi-cell tube with functionally graded thickness is shown in Fig. 3.3.

3.2.1.3 Validation of FE modeling

As a newly introduced structure, the FE model of FGT multi-cell tube cannot be directly validated as the experimental data have not yet been reported adequately and there has been no physical specimen available for the experiment. Nevertheless, FGT multi-cell tube becomes a conventional multi-cell tube with uniform thickness wall when $t_{min} = t_{max}$ in Eq. (3.1). It is thus possible to validate the modeling results in this special case. Fig. 3.5 shows the drop-hammer impacting testing. Figs. 3.6a and b display the deformation patterns of two specimens and Fig. 3.6c presents FEA results under the same impacting conditions. As shown in these pictures, these four corner-celled regions and the connecting walls of such a multi-cell tube undergo in-extensional deformation. As expected, the first fold starts from the dedicated triggers, and then followed by successive folds. Clearly, the simulated collapse modes are almost the same as those obtained by the experimental tests.

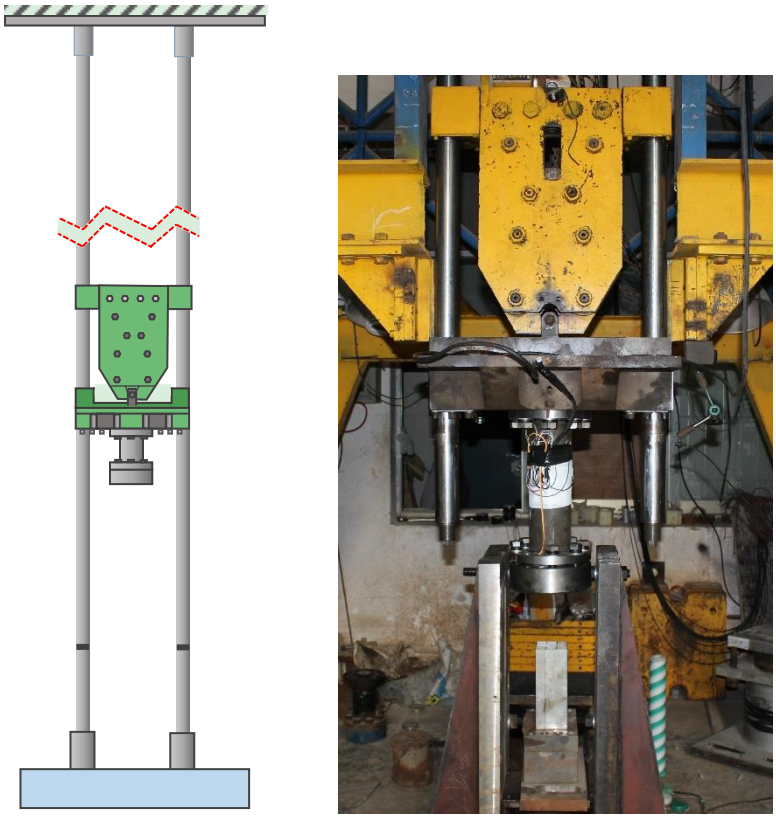

Fig. 3.5 Dynamic impacting experimental set-up.

(a)

(b)

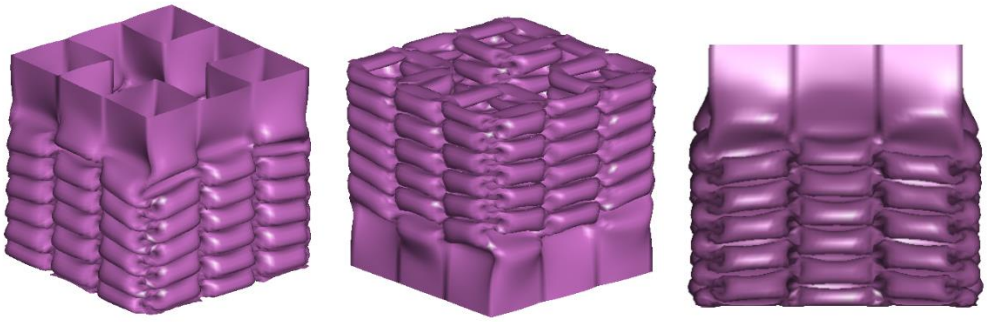

(c)

Fig. 3.6 Comparison of deformation modes between experimental and numerical results: (a) Dynamic axial impacting testing 1; (b) Dynamic axial impacting testing 2; (c) Numerical results

Fig. 3.7 shows the correlation of the force-displacement response and energy absorption curves between the experiment and simulation. It is found the crashing force of FE prediction follows the same trend of the experiment data. Crashing force in FE simulation exhibits a lower value in the first peak but experiences slightly higher values of the rest of peaks during the subsequent folding. Such discrepancy may be due to the trigger placements in the FE model which actually weaken the initial stiffness of the tube and consequently decrease the first peak force in the simulation. In addition, the existence of imperfections in the physical specimen can also be other reason, which is however

very difficult to be considered properly in FE modeling. The energy curve from the FE simulation agrees fairly well with the experimental data of the first specimen but has a slightly higher discrepancy with that of the second specimen due to its instability of deformation as shown in Fig. 3.7b. Overall, the numerical modeling technique adopted here is considered sufficiently accurate and will be extended to the subsequent study.

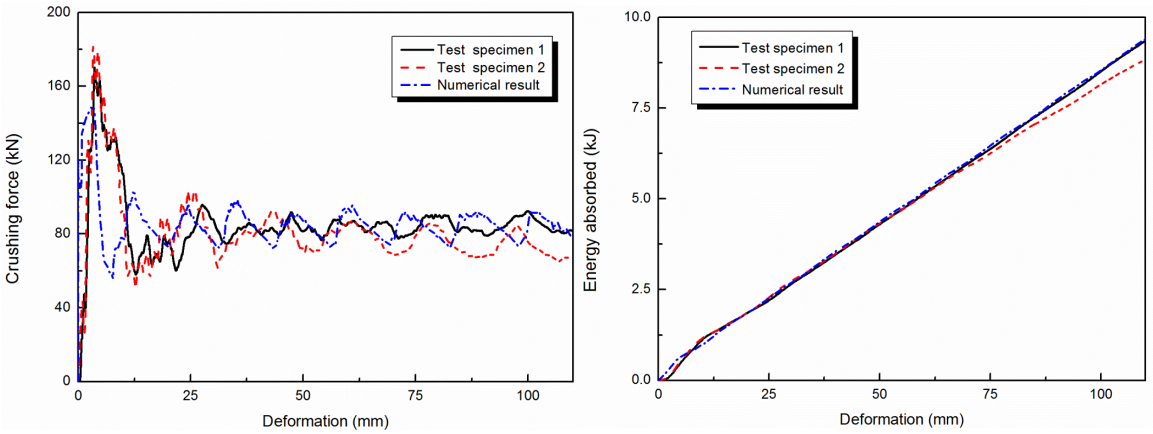

(a) (b)

Fig. 3.7 Comparison of experimental and numerical results. (a) Crushing force (b) Energy absorption

3.2.2 Numerical analysis of crashworthiness

3.2.2.1 Effect of thickness gradients

To investigate the influence of thickness gradients on the crashworthiness performances, sampling points were generated uniformly over the 3D space of gradient parameters n_1, n_2 and n_3 by using full factorial design with five levels for each of gradient parameters. Numerical analyses were then performed for all the sampling points and 3D response surfaces (RS) of crashworthiness indicators were plotted in Figs. 10-13. From Fig. 10, it can be observed that the F_{max} increases monotonically with the increase of n_1,

$n_{2,}$ and n_3. This is mainly because that with increases in the gradient parameters the intermediate thicknesses (between t_{min} and t_{max}) in the corresponding region increases (as shown in Fig. 4), leading to strengthening the tube structure. As such, the values of *EA* and *SEA* become higher as a result of increases in gradient parameters (Figs. 11 and 12). Besides, it is generally advantageous to increase the gradient parameters for yielding a higher *CFE* as shown in Fig. 13. While increasing the gradient parameters seems an effective way to absorb more energy, it would result in an undesirable increase in F_{max}.

3.2.2.2 Comparison of FGT and UT multi-cell tubes

To compare the crashworthiness of FGT multi-cell tubes and their counterparts with uniform thickness (UT), we also plot the response surfaces of UT structures in Figs. 10-13. Each UT multi-cell tube is considered to have the same mass as the corresponding FGT tube by assigning the uniform thickness as follows,

$$\begin{aligned} t_u &= \frac{1}{40L}\left(16\int_0^{L/6} t_1(x_1,n_1)dx_1 + 8\int_0^{L/6} t_2(x_2,n_2)dx_2 + 16\int_0^{L/6} t_3(x_3,n_3)dx_3\right) \\ &= 0.4(t_{max} - \frac{t_{max}-t_{min}}{10^{n_1}+1}) + 0.2(t_{max} - \frac{t_{max}-t_{min}}{10^{n_2}+1}) + 0.4(t_{max} - \frac{t_{max}-t_{min}}{10^{n_3}+1}) \end{aligned} \tag{3.2}$$

From Fig. 3.9 when n_3 = -1 (lowest), the FGT tubes have slightly larger values in F_{max} than the UT tubes at the majority of the design domain. However, when n_3 increases, the F_{max} of FGT tubes becomes lower than that of UT tubes at a larger portion of the space. When n_3 = 1, the FGT tubes have a lower F_{max} over the whole design domain. Overall, no significant difference in F_{max} is observed between the FGT and UT structures, and the FGT tubes become more advantageous over their counterparts when gradient parameters have a greater value. As for the *SEA*, the FGT tubes can always outperform

the UT tubes as displayed in Fig. 3.10. The largest improvement of using the FGT structures appears in the corners regions with $n_1 = n_2 = -1$, which pushes the intermediate thicknesses (in-between t_{min} and t_{max}) toward t_{min}, thereby achieving the most efficient use of material. Nevertheless, the amount of energy absorption is the lowest in this region

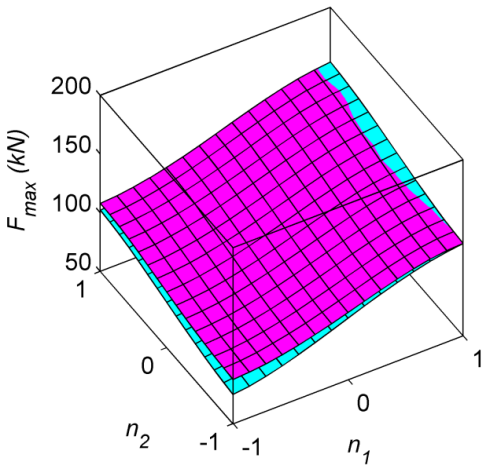

(a)

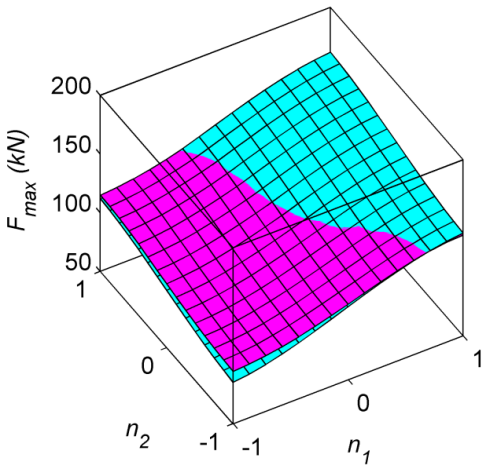

(b)

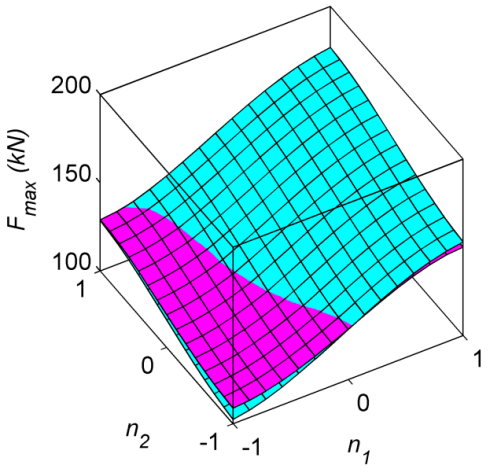

(c)

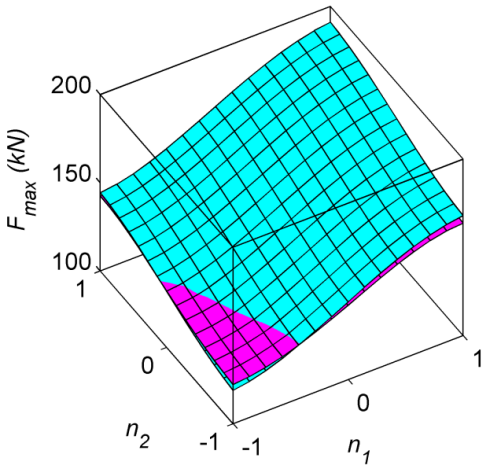

(d)

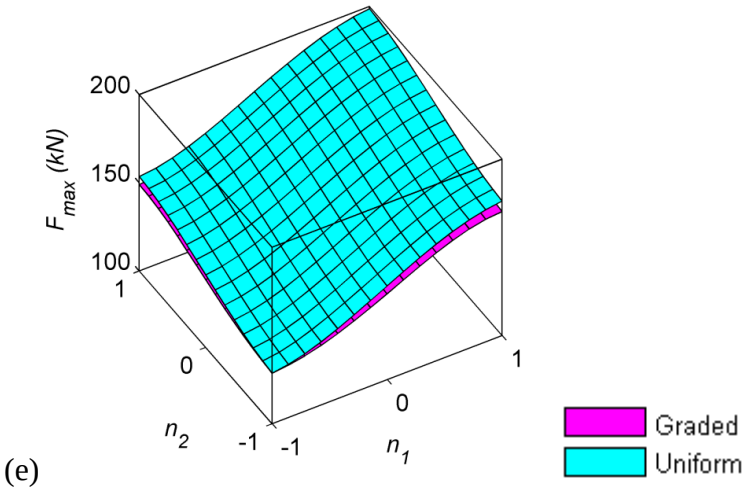

(e)

Fig. 3.9 3D response surfaces of F_{max}. (a)n_3=-1; (b)n_3=-0.5; (c)n_3=0; (d)n_3=0.5; (e)n_3=1.

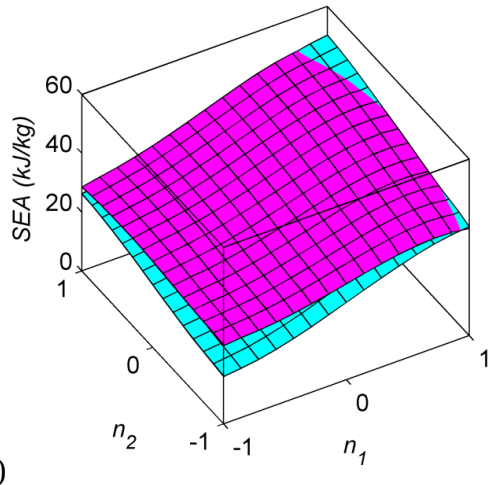

(a)

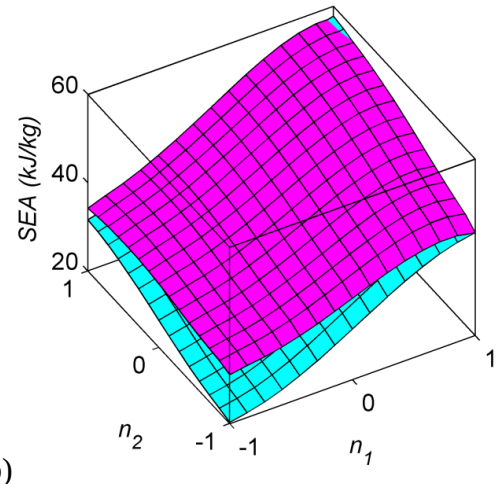

(b)

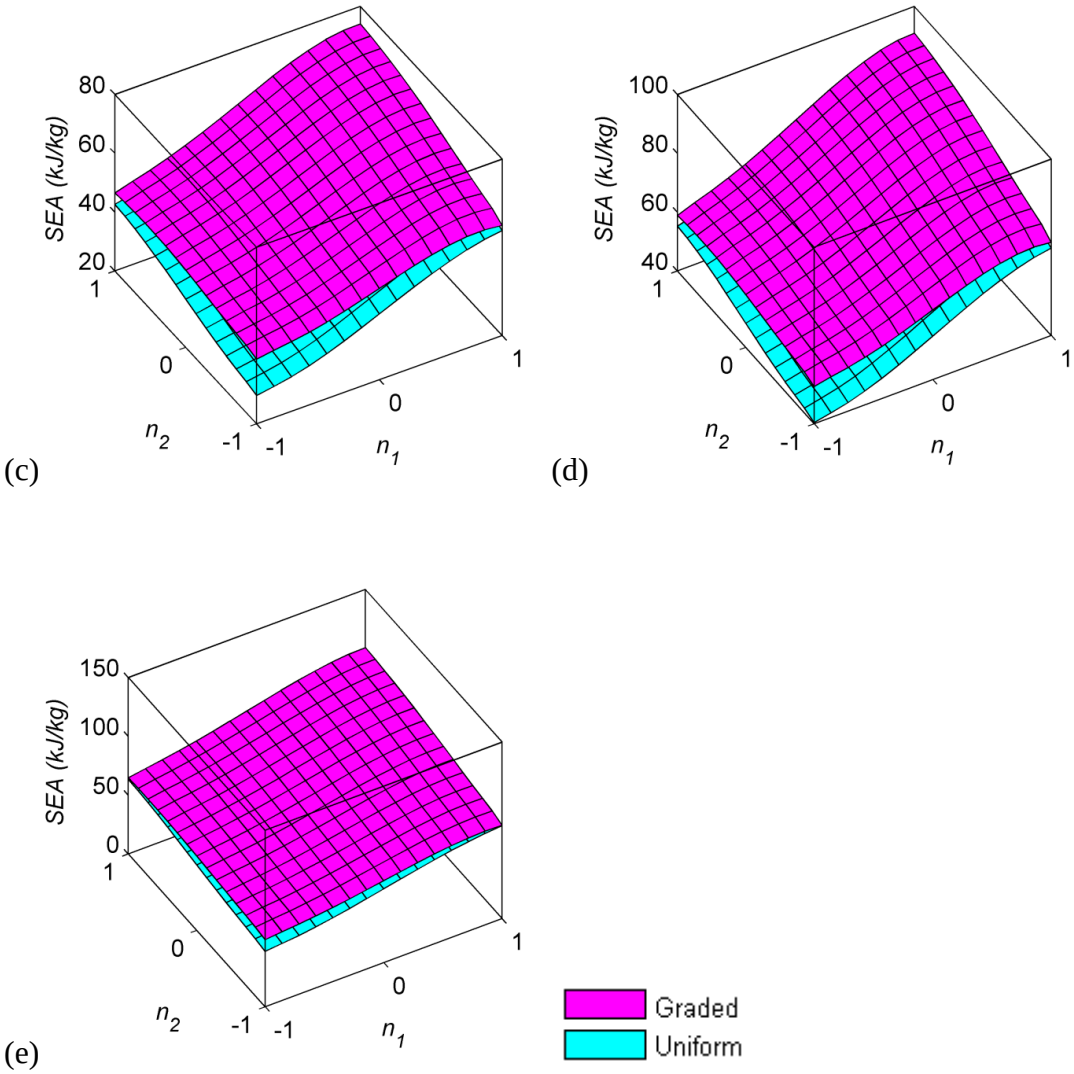

Fig. 3.10 3D response surfaces of *SEA*. (a)n_3=-1; (b)n_3=-0.5; (c)n_3=0; (d)n_3=0.5; (e)n_3=1.

3.2.3 Multiobjective optimisation for FGT multi-cell tubes

3.2.3.1 Definition of optimisation problem

From the above parametric analysis, while it has been clear that the gradient parameters largely affect the crashworthiness of FGT multi-cell tubes, it remains unknown how to determine these gradients for achieving best possible performances, which is the main task of the rest of this study. As an energy absorber, the tube structure

is expected to absorb as much impact energy per unit mass as possible. Thus, *SEA* should be an objective function to be maximized. Furthermore, F_{max} of the structure is another indicator to the safety of occupants, to be minimized. Therefore, we formulated the multiobjective optimisation problem in Eq. (3.3), aiming to seek for the optimum gradient configurations with these two design criteria.

$$\begin{cases} \min & F_{max}, \text{-}SEA \\ s.t. & -1 \le n_1, n_2, n_3 \le 1 \end{cases} \tag{3.3}$$

For comparison, we conducted the optimisation for the corresponding UT structures as well, in which the gradient parameters in the corresponding FGT tube are taken as the design variables *indirectly* (Figs. 10-13).

3.2.3.2 Response surface models

In practice, metamodeling starts with the sampling data at some training points. In this study, the sampling points presented in Section 3 were used to approximate the *EA* and $F_{\max}$. Ten additional points were generated randomly in the design space to examine the accuracies of different orders of RSMs. Table 3.1 summarizes the results of accuracy assessment. Clearly, the values of R^2 are all close to 1 and the values of e_{max} and e_{avg} are within 8%. However, it was found that there is no single order of response surface model suitable for all the crashworthiness indicators and the RSM may not necessarily become more accurate when a higher order model is chosen. Thus, the orders of RSMs were selected with boldface highlighted in Table 3.1 for the subsequent optimisations, and their expressions are given in Eqs. (3.4)-(3.7), where superscripts G and U represent the FGT and UT multi-cell tubes, respectively. the *SEA* can be calculated by Eq.(3.8), where A and ρ are the total area of walls and the density of aluminum, respectively.

$$F_{\max}^{G}(n_1,n_2,n_3) = 139.1685 + 30.9810n_1 + 15.8719n_2 + 30.0639n_3 + 2.5652n_1n_2 + 1.0136n_2n_3 + 0.1619n_1n_3 + 1.3747n_1^2 + 0.0349n_2^2 - 1.4471n_3^2 - 9.3238n_1^3 - 4.7640n_2^3 - 9.4350n_3^3 - 1.6451n_1^4 - 0.9291n_2^4 + 0.8931n_3^4 \quad (3.4)$$

$$EA^{G}(n_1,n_2,n_3) = 9.0425 + 2.4678n_1 + 1.0898n_2 + 3.1922n_3 - 0.1656n_1n_2 + 0.4656n_2n_3 + 0.3625n_1n_3 - 0.2101n_1^2 + 0.1873n_2^2 - 0.1899n_3^2 - 0.8143n_1^3 - 0.3686n_2^3 - 1.0464n_3^3 \quad (3.5)$$

$$F_{\max}^{U}(n_1,n_2,n_3) = 140.8515 + 33.6084n_1 + 17.0421n_2 + 33.6088n_3 - 1.4080n_1n_2 - 0.5853n_2n_3 - 1.5313n_1n_3 - 0.0483n_1^2 - 0.5854n_2^2 - 1.4089n_3^2 - 8.8679n_1^3 - 4.6089n_2^3 - 8.8682n_3^3 - 0.7749n_1^4 - 0.0064n_2^4 + 0.7759n_3^4 \quad (3.6)$$

$$EA^{U}(n_1,n_2,n_3) = 7.7913 + 2.9216n_1 + 1.4414n_2 + 2.9212n_3 + 0.0705n_1n_2 + 0.0839n_2n_3 + 0.1398n_1n_3 + 0.0276n_1^2 + 0.0839n_2^2 + 0.0709n_3^2 - 0.7895n_1^3 - 0.3851n_2^3 - 0.7891n_3^3 \quad (3.7)$$

$$SEA^{G(U)}(n_1,n_2,n_3) = EA^{G(U)} / (t_u \cdot A \cdot \rho) \quad (3.8)$$

Table 3.1 Modelling accuracy of response surface models

		Order	R^2	$e_{\max}$	e_{avg}
Gradient	*EA*	Linear	0.9734	5.80%	2.61%
		Quadratic	0.9844	6.81%	2.41%
		Cubic	**0.9929**	**3.75%**	**1.55%**
		Quartic	0.9917	3.97%	1.66%
	$F_{\max}$	Linear	0.9859	6.23%	1.56%
		Quadratic	0.9845	6.55%	1.60%
		Cubic	0.9986	1.36%	0.49%
		Quartic	**0.9987**	**1.29%**	**0.46%**
Uniform	*EA*	Linear	0.9914	10.38%	2.38%
		Quadratic	0.9904	11.70%	2.41%

		Cubic	**0.9995**	**1.43%**	**0.62%**
		Quartic	0.9994	1.70%	0.63%
	F_{max}	Linear	0.9870	7.63%	1.69%
		Quadratic	0.9890	7.10%	1.56%
		Cubic	0.9992	0.82%	0.40%
		Quartic	**0.9993**	**0.74%**	**0.37%**

3.2.3.3 Optimisation results

Fig. 3.11 compares Pareto frontiers of the FGT and UT multi-cell tubes. The Pareto optimal frontiers provide designers with a wide spectrum of solutions over the design space for selection. Specifically, if the designers wish to pay more attention to *SEA*, the solutions at the top left corner should be selected. But if the designers would like to emphasize more on F_{max}, the solutions at the bottom right corner should be considered. Most importantly, when optimized conventional UT tubes are replaced by the optimized FGT tubes, the Pareto frontier indicates considerably better performance in both F_{max} and *SEA*. That is to say that the FGT multi-cell tubes enable to enhance *SEA* and lower F_{max} concurrently.

Fig. 3.12 depicts the distribution of Pareto optimum solutions of the FGT multi-cell tubes in the design space. To achieve a wide range of crashworthiness performances, each of the design variables (i.e., gradient parameters) spreads over their corresponding dimensions of the design space. Interestingly, all of the optimums are located around the diagonal line of $n_1 = n_2$, which indicates that similar values of gradient parameters in the outer walls are more likely to yield optimal performance. Moreover, the optimums also have values of $n_3 > n_1$ and $n_3 > n_1$, which indicates stronger internal ribs improve the performance of the FGT multi-cell tubes.

In real-life applications, F_{max} is often required to be controlled under a certain level for concerning occupant's safety. In this study, if we constrain $F_{max} \leq 150$ kN for a

quantitative comparison between FGT and UT multi-cell structures, the optimal solutions can be simply selected from the intersection between Pareto frontiers and the horizontal line of F_{max} =150 kN. Table 3.2 lists the two specific optimums, where the surrogate models were also checked against the FE analyses. It is seen that the RS model can predict the actual performance with fairly high accuracy. Furthermore, while these two designs develop the same first peak force (F_{max}), the crashing force of the FGT multi-cell tube maintains at a higher level overall during the subsequent deformation seen in Fig. 3.13, where the shaded area between these two curves is the additional energy absorbed by the FGT structure. As a result, the *SEA* of the FGT increases to 58.94 kJ/kg by 19.51%.

Table 3.2 Optimal solutions ($F_{max} \leq 150$ kN).

		UT	FGT
n_1		0.0206	0.1105
n_2		0.0690	-0.0622
n_3		0.2152	0.2899
F_{max} (kN)	Eq. (3.4)/ (3.6)	149.78	150.00
	FE	150.88	150.20
	Error	-0.73%	-0.13%
SEA (kJ/ kg)	Eq. (3.8)	45.41	54.69
	FE	45.75	56.67
	Error	-0.73%	-3.50%

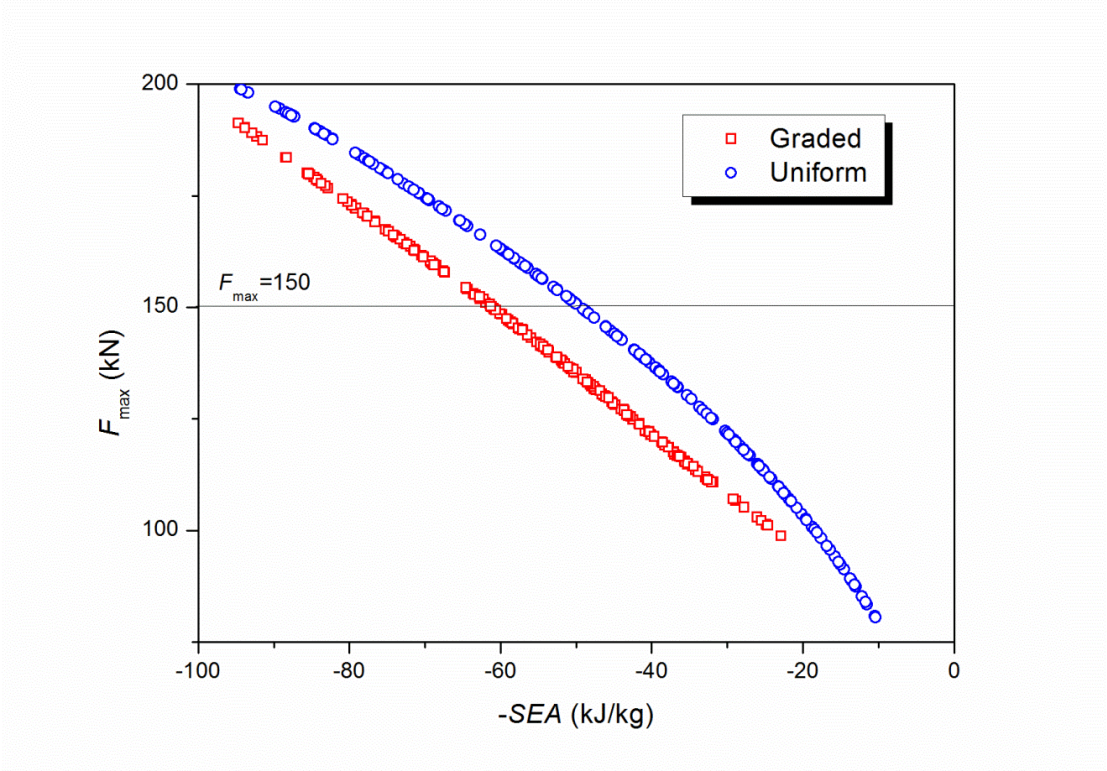

Fig. 3.11 Pareto frontiers of FGT and UT multi-cell tubes.

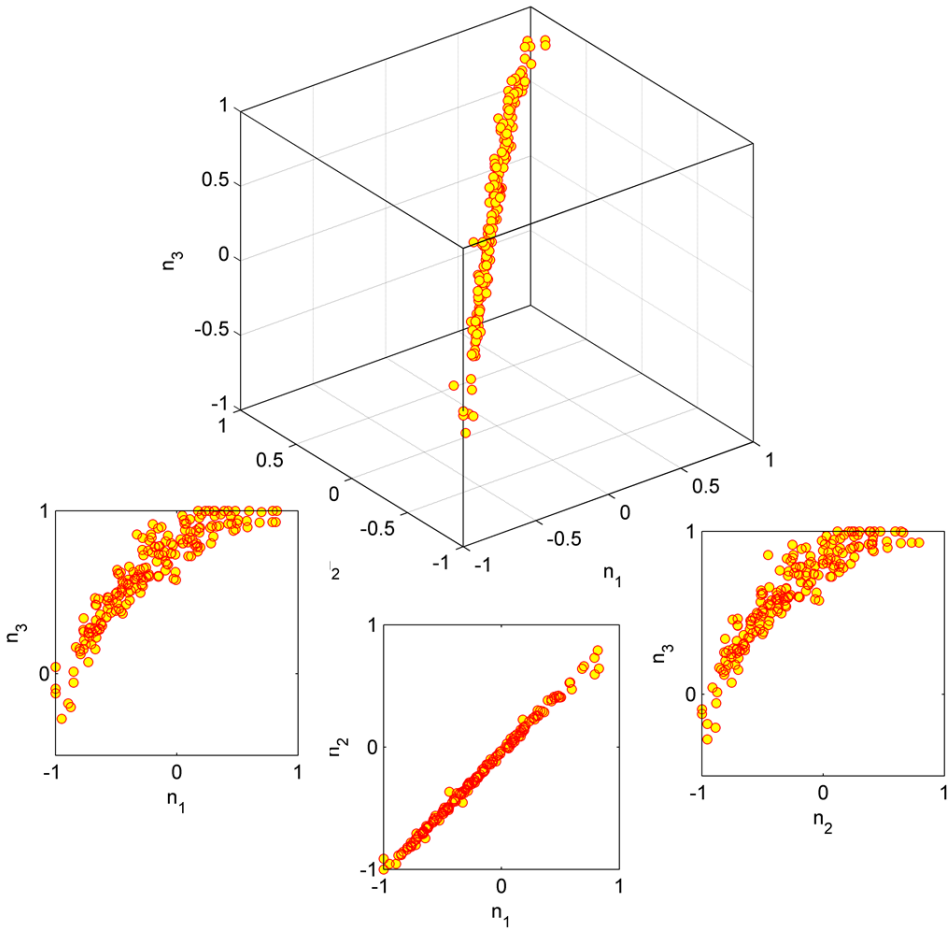

Fig. 3.12 Distribution of Pareto solutions of FGT multi-cell tubes.

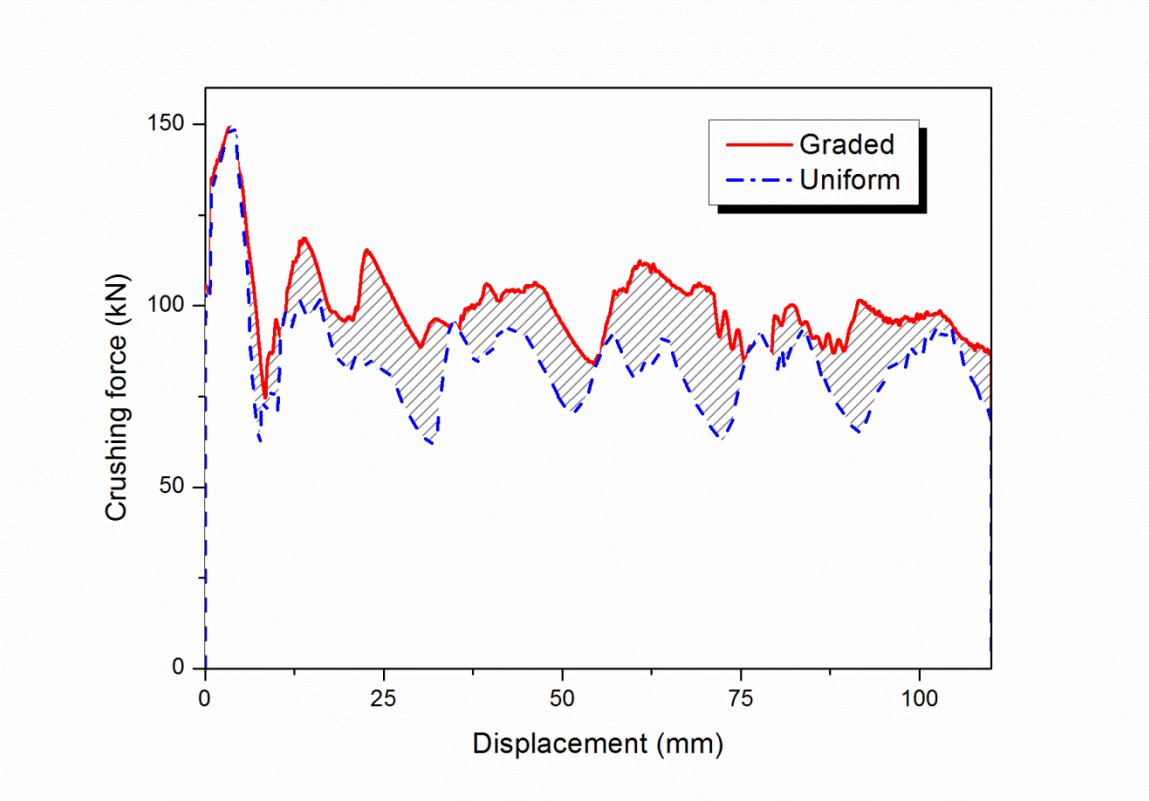

Fig. 3.13 Crushing force of optimal strucuture

3.3 Crashworthiness and multiobjective optimisation of functionally graded foam-filled tubes

In vehicular systems, bumpers are expected to protect the driver and passengers when a frontal crash occurs. The collision energy is absorbed by the bumpers subjected to bending condition. Likewise, side door beams or B-pillars are required to provide enough load-carrying capacity in the event of side impact. Therefore, it is of significance to investigate the bending behavior of thin-walled structures under lateral impact. Recently, cellular materials, especially metallic foams have aroused increasing attention for extraordinary energy absorption capacity and lightweight potential in the automotive industry. The inclusion of lightweight foam-fillers into thin-walled sections has proven an

effective way to help increase the load-carry capacity and energy absorption. In this regard, several studies have been conducted on bending behavior of foam-filled thin-walled structures. For example, Santosa and Wierzbicki [210] pointed out that filling aluminum honeycomb or foam core is preferable to thickening the column wall in order to enhance the energy-absorbing efficiency. Shahbeyk et al. [211] concluded that aluminum foam filling can significantly change the bending behavior in terms of energy absorption and deformation patterns. Zarei and Kröger [212] found that the filled column can absorb the same energy as the optimal empty column with a 28.1% lower weight. Guo and Yu [213] studied the dynamic response of foam-filled double cylindrical tubes under three-point bending experimentally and numerically.

The above-mentioned studies are mainly restricted to uniform foam (UF) filled thin-walled structures. To the authors' best knowledge, however, previous studies on FGF-filled thin-walled structures did not take into account the bending behavior under lateral impact, which is a significant crashworthiness performance for thin-walled structures. To date, some advanced technologies have been available to fabricate the functionally graded materials and structure for a devised gradient under laboratory conditions [214-217]. It will promote the development of advanced energy absorbers to investigate the novel functionally graded foam-filled structures.

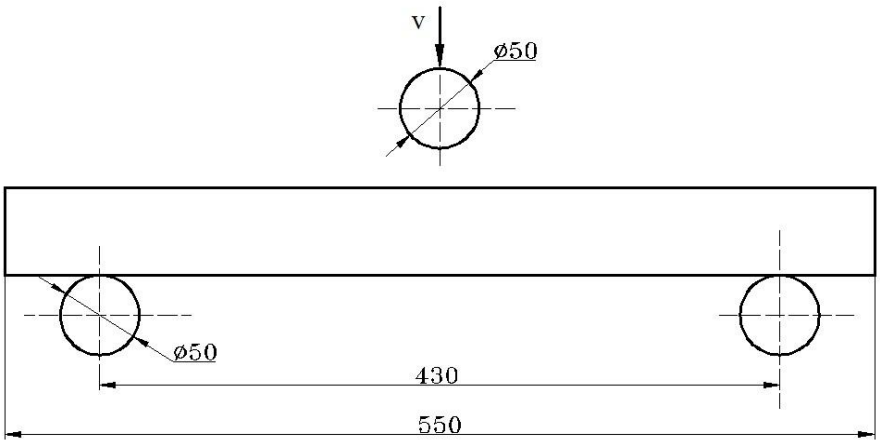

(a)

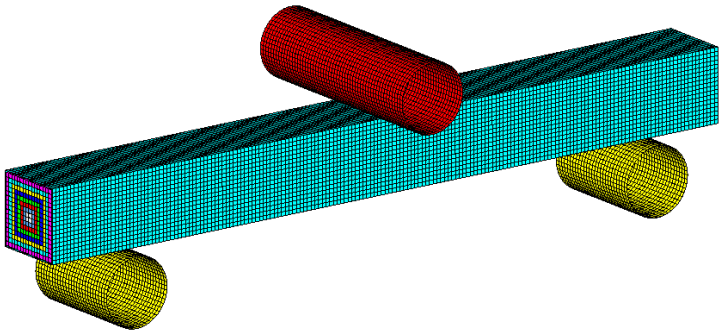

(b)

Fig. 3.14 Square column with graded foam-filler: (a) Schematic, and (b) Finite element model.

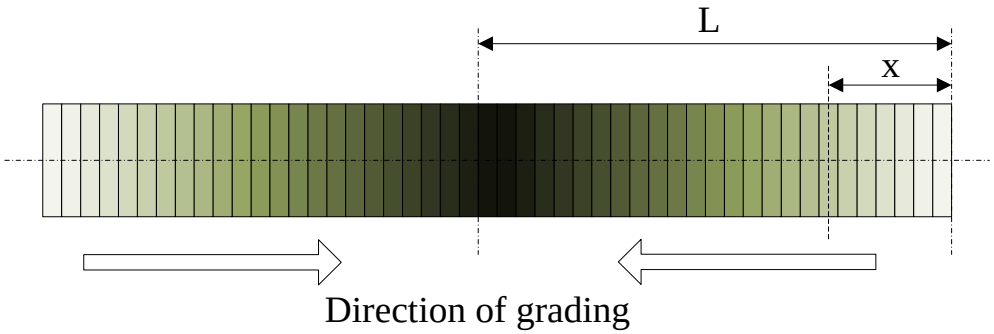

Fig. 3.15 Schematic showing grading patterns in the axial direction.

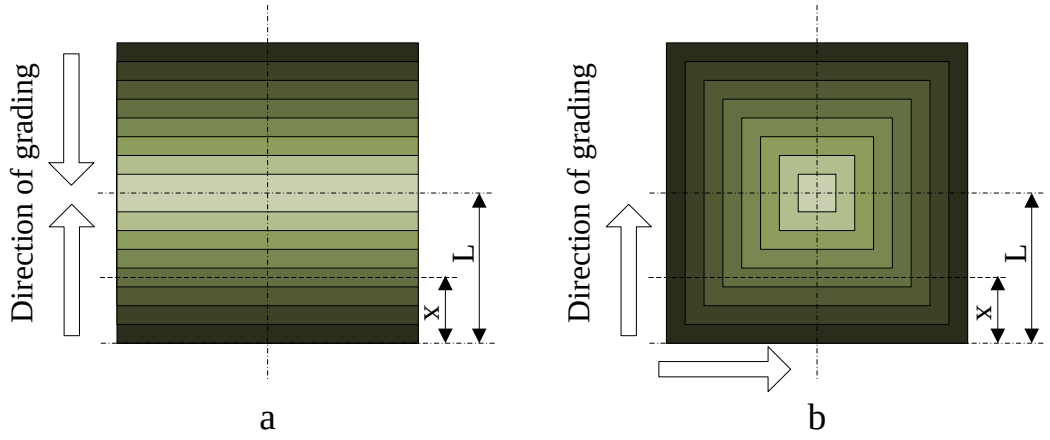

Fig. 3.16 Schematic showing grading patterns in the transverse direction.

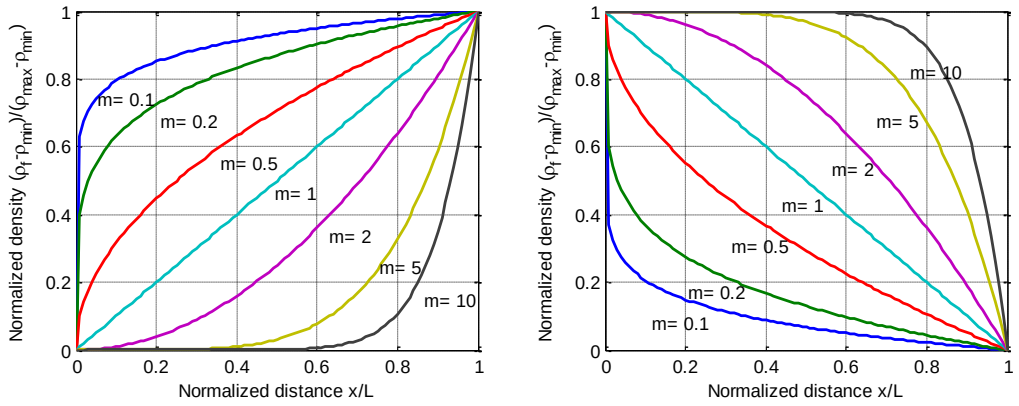

(a) (b)

Fig. 3.17 Variation of foam density *vs* normalized distance: (a) ascending gradient pattern, and (b) descending gradient pattern.

3.3.1 Numerical modeling

The structure analyzed herein is a functionally graded foam (FGF) filled thin-walled square column subjected to lateral impact loading (Fig. 3.14). The length of the column is 550 mm, and the side length of the section is 55 mm. The foam-filled column lays on two cylindrical supports, and the span and diameters are 430 mm and 50 mm respectively. A

cylindrical punch with a diameter of 50 mm and a mass of 128 kg impacts onto the column at an initial velocity of v=4.4 m/s in the mid-span.

3.3.1.1 Modeling of functionally graded foam

In this study, both axial and transverse FGF materials are considered, where the foam is discretized to several layers and in each layer the density is uniform. Fig. 3.15 depicts the grading pattern for the axial FGF, whose density changes along the axis and has symmetry about the mid-span plane of the column. Figs. 3.16a and 3.16b display the grading patterns for the transverse FGF, where the foam density changes along the height direction of the column section and is symmetrical about the horizontal mid-plane, and along the two directions of the column section respectively. The density gradient is determined by the following power-law functions:

$$\rho_f(x,m)=\begin{cases}\rho_{\min}+(\rho_{\max}-\rho_{\min})(\dfrac{x}{L})^m & \text{for an ascending pattern}\\ \rho_{\max}-(\rho_{\max}-\rho_{\min})(\dfrac{x}{L})^m & \text{for a descending pattern}\end{cases} \tag{3.9}$$

where $\rho_{\min}$ and $\rho_{\max}$ are the minimum and maximum densities, respectively. x and L represent the distances shown in Figs. 3.15 and 3.16. m denotes the gradient exponent parameter that governs the variation of foam density. Figs. 3.17a and 3.17b show the variation of foam density along the grading direction for ascending and descending pattern respectively. In our case of bending column to be explained in detail, the column has a large bending deformation at the contact area with the punch while other parts undergo a rigid body rotation. Since the strong interaction between the column wall and FGF has a positive influence on the energy absorption characteristics, the large stiffness of foam is expected at the large deformation area [218]. That is to say, the outermost layer

should have the maximum density for transverse FGF and the middle layer for axial FGF in our specific case. Accordingly, the ascending pattern is selected for the axial FGF and the descending pattern for the two types of transverse FGF.

In an ideal functionally graded continuous model, the foam should be divided into an infinite number of layers. In the FE framework, the minimum depth of layer would be equal to the size of each shell element, which would, however, lead to very costly computational time. Furthermore, increasing the number of layers could increase the risk of numerical instability in the model resulting from the use of smaller element sizes. The model selected to represent the material behavior of aluminum foam filler is Deshpande-Fleck foam (Material Model 154) which has been implemented as a user subroutine in LS-DYNA. The model was proposed by Deshpande and Fleck [219], in which the yield criterion of foam material is defined as follows:

$$\Phi = \hat{\sigma} - \sigma_y \leq 0 \tag{3.10}$$

where σ_y is the yield stress and the equivalent stress $\hat{\sigma}$ is given as:

$$\hat{\sigma}^2 = \frac{1}{[1+(\alpha/3)^2]}[\sigma_e^2 + \alpha^2 \sigma_m^2] \tag{3.11}$$

where σ_e is the von Mises effective stress and σ_m the mean stress. Parameter α controlling the shape of the yield surface is a function of the plastic Poisson's ratio ν_p, given as:

$$\alpha^2 = \frac{9(1-2\nu_p)}{2(1+\nu_p)} \tag{3.12}$$

It is easily derived from Eq. (3.12) that $\alpha = 2.12$ when $\nu_p = 0$. The strain hardening rule is implemented in this material model as:

$$\sigma_y = \sigma_p + \gamma \frac{\hat{\varepsilon}}{\varepsilon_D} + \alpha_2 \ln\left[\frac{1}{1-(\hat{\varepsilon}/\varepsilon_D)^{\beta}}\right] \tag{3.13}$$

where $\hat{\varepsilon}$ is equivalent strain, σ_p, α_2, γ, β and ε_D are the material parameters and can be related to the foam density as

$$\begin{cases} (\sigma_p, \alpha_2, \gamma, \frac{1}{\beta}, E_p) = C_0 + C_1 \left(\frac{\rho_f}{\rho_{f0}}\right)^{\kappa} \\ \varepsilon_D = -\ln\left(\frac{\rho_f}{\rho_{f0}}\right) \end{cases} \tag{3.14}$$

where ρ_f is the foam density and ρ_{f0} the density of the base material. C_0, C_1 and κ are the constants as listed in Table 3.3.

Table 3.3 Material parameters for aluminum foam [220, 221].

	σ_p (MPa)	α_2 (MPa)	$1/\beta$	γ (MPa)	E_p (MPa)
C_0 (MPa)	0	0	0.22	0	0
C_1 (MPa)	720	140	320	42	0.33e6
κ	2.33	0.45	4.66	1.42	2.45

3.3.1.2 Validation of the numerical model

More details about the numerical modelling can be found in [10]. To evaluate the validation of the simulation models, the empty column with the same dimension was first investigated under the same loading condition. Figs. 3.18 and 3.19 display the comparison of crash behavior between experiment [212] and simulation, in terms of impact force versus punch displacement curve and deformation pattern respectively. It can be seen that the force versus displacement curve of simulation is able to capture the true bending behavior, and the deformation pattern of simulation also agrees with that of the

experiment. Furthermore, the simulation model of the foam-filled column was also validated experimentally. From Eq. (3.9), it is obvious that the functionally graded foam (FGF) will become a uniform foam (UF) when the parameter *m* equals to 0. Thus, the validation of the developed finite element model of FGF filled column can be verified against the experimental data of the UF filled column. From Figs. 3.20 and 3.21, the simulation results agree fairly well with the corresponding experimental results [212]. As a result, the FE models are considered accurate and effective for the subsequent parametric analysis and design optimisation.

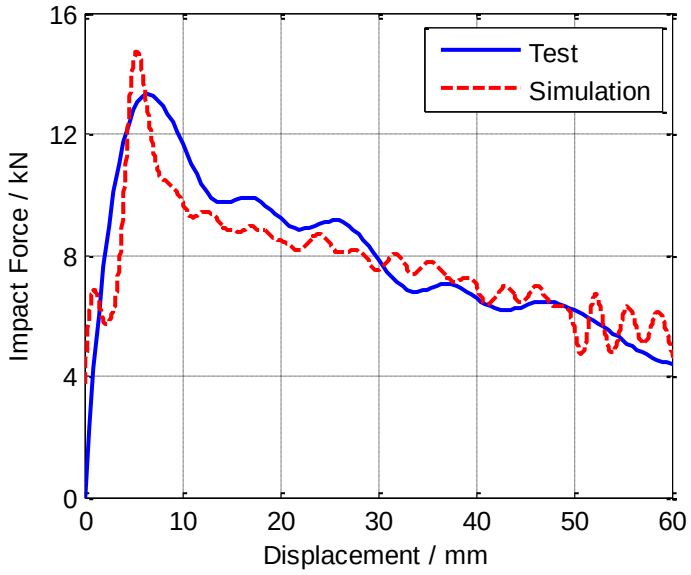

Fig. 3.18 Experimental [212] and numerical impact force curves for the empty column.

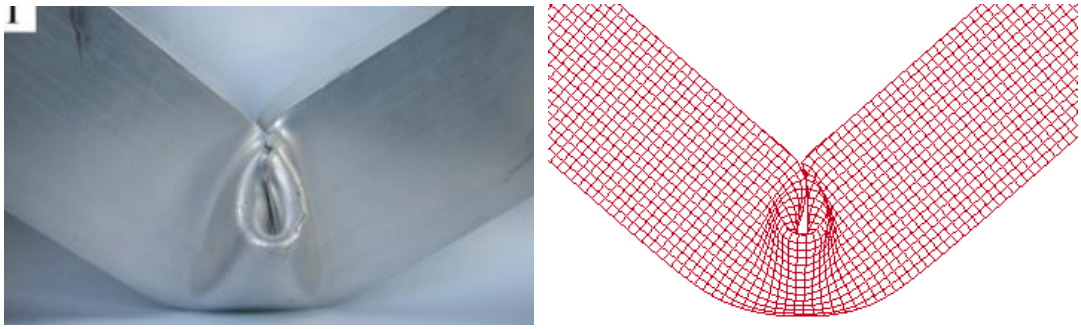

(a) (b)

Fig. 3.19 (a) Experimental [212], and (b) numerical deformation patterns for the empty column.

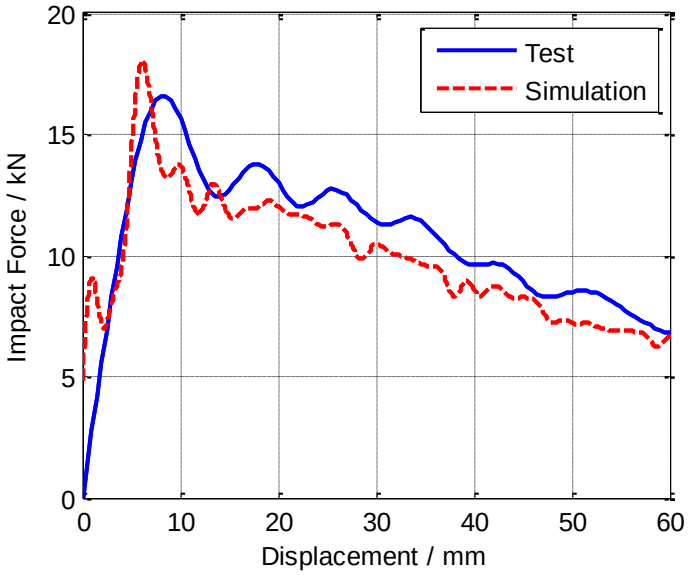

Fig. 3.20 Experimental [212] and numerical impact force curves for the foam-filled column.

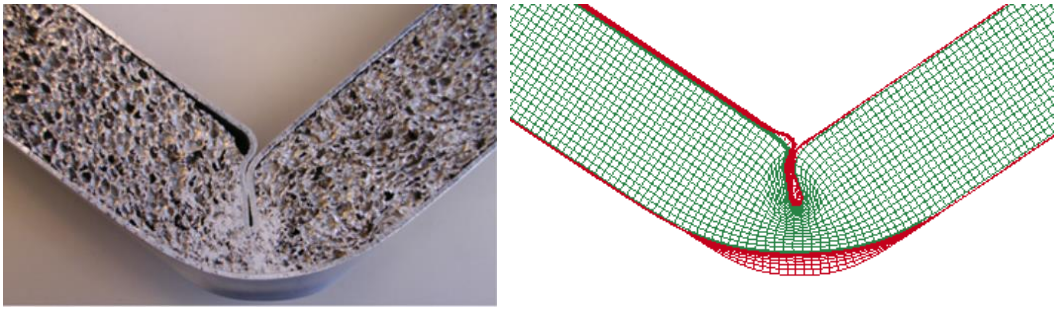

(a) (b)

Fig. 3.21 (a) Experimental [212], and (b) numerical deformation patterns for the foam-filled column.

3.3.2 Parametric study

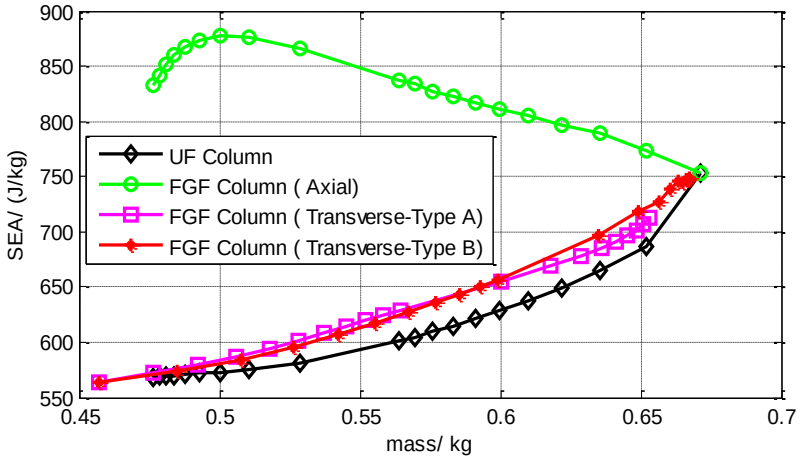

(a)

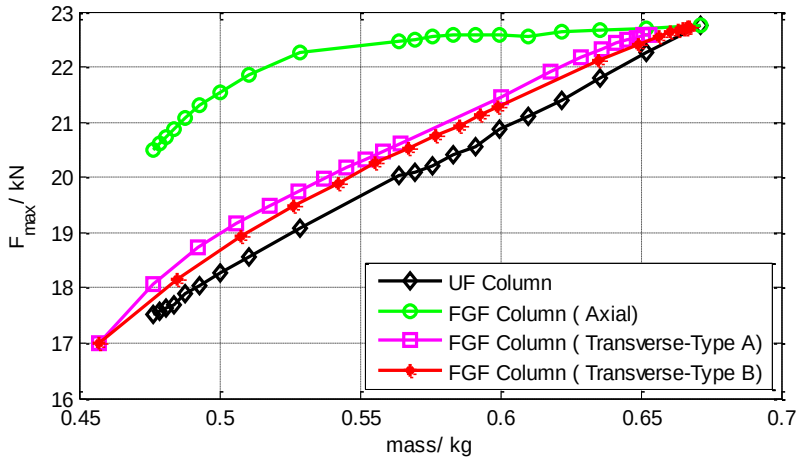

(b)

Fig. 3.22 Comparison of crashworthiness performance between UF and FGF filled columns: (a) *EA*, (b) *SEA*, (c) F_{max} and (d) *CFE*.

3.3.2.1 Effect of density grading

In order to compare the energy absorption characteristics of UF and FGF filled columns, numerical simulations were implemented based on the finite element models of the FGF columns with different values of gradient exponent parameter *m*. In each case,

the other parameters were fixed: $\rho_{\min}$ = 0.20 g/cm^3, $\rho_{\max}$ = 0.50 g/cm^3, σ_y= 227 MPa and t = 2.0 mm (t denotes the wall thickness). Since the total mass of the FGF column was varied, the UF columns of the same weight as the corresponding FGF columns were selected for comparing the crashworthiness. The equivalent foam density of UF columns is calculated as follows,

$$\rho_{eqv} = \sum_{i=1}^{N_G} \rho_i / N_G \tag{3.15}$$

where N_G denotes the total number of layer of axial FGF, and ρ_i is the density of the ith layer.

Figs. 3.22a and b depict the crashworthiness performance in terms of *EA* and *SEA* respectively. For all types of columns, the larger the mass is the more energy the column absorbs. Furthermore, the FGF filled columns, especially the axial FGF filled ones, can absorb more energy than the UF counterparts with the same mass. For the transverse FGF and UF filled columns, the *SEA* increases monotonically when the mass increases. On the other hand, for the axial FGF filled columns, the *SEA* increases up to a peak value and then decreases with the increase of mass. Most importantly, the improvement of the FGF filled columns over the corresponding UF filled columns in *SEA* can be achieved. Considering the grading direction, the axial FGF filled columns seem much more promising than the transverse FGF filled ones in terms of *EA* and *SEA*, which may be because that the axial grading can focus dense foam at the region of severe deformation (mid-span part of the column) more efficiently.

Figs. 3.22c and d compare the F_{max} and *CFE* of the UF and FGF filled columns, respectively. Generally, the axial FGF columns have the largest values of F_{max} and *CFE* under the same mass while the UF columns have the lowest values. While FGF columns

can indeed produce larger SEA than UF counterparts, they would lead to larger F_{max} , which is also an essential indicator for the safety of the occupants.

Note that all the crashworthiness criteria of UF and FGF columns converge to the same value when the mass increases. This is because that all the columns turn out to be a UF column with the maximum foam density of 0.50 g/cm^3 when their masses increase up to the maximum value 0.67 kg.

To further explore the effect of the parameters of foam material and thin wall on the bending behavior of the FGF filled column, we will conduct parametric analysis below by taking the axial FGF column as an example.

3.3.2.2 Effect of density range

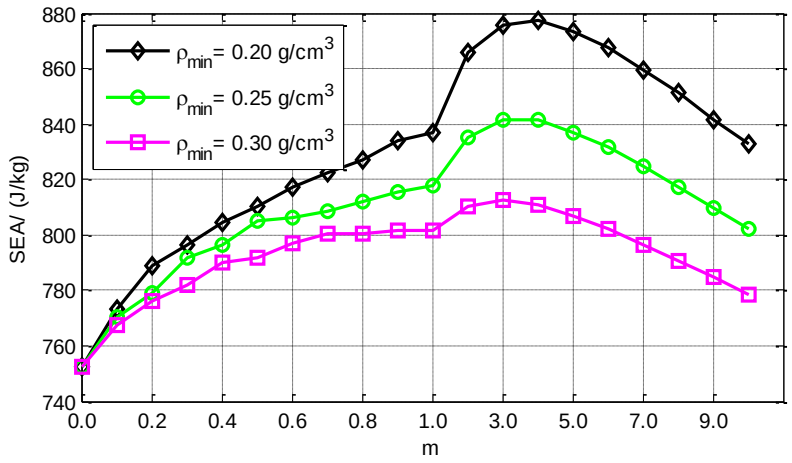

(a)

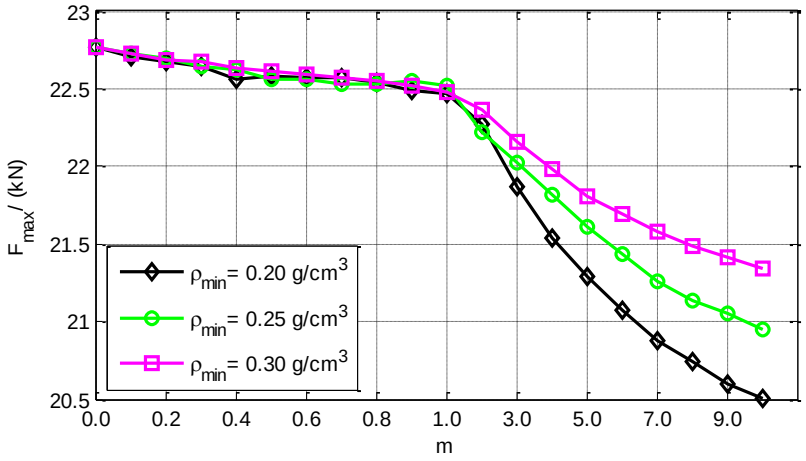

(b)

Fig. 3.23 Variation of crashworthiness performance due to density range: (a) *SEA*, (b) F_{max}

In order to explore the effect of foam density range ($\Delta\rho = \rho_{max} - \rho_{min}$) on the crashworthiness of FGF filled columns, the value of ρ_{min} was varied with 0.20, 0.25 and 0.30 g/cm^3 while the ρ_{max} = 0.50 g/cm^3, t =2.0 mm and σ_y =227 MPa. Figs. 3.23a- d display the *EA*, *SEA*, F_{max} and *CFE* of axial FGF filled columns at different values of grading exponent parameter m. Note that the density range ($\Delta\rho$) has a noticeable implication on crashworthiness performance. Specifically, large values of $\Delta\rho$ (small values of ρ_{min}) help improve *SEA*, although it could have a negative effect on *EA*. Besides, large values of $\Delta\rho$ (small values of ρ_{min}) could lead to small values of *CFE* while it is able to reduce the values of F_{max}.

It should be noted that the crashworthiness performance is closely related to the value of m. When m increases for axial FGF filled columns with ascending grading pattern, the intermediate foam density (between ρ_{min} and ρ_{max}) decreases (as shown in Fig. 3.17a), leading to the reduction of strengthening the effect of the foam filler. As a result,

the F_{max}, *CFE*, and *EA* decrease monotonically with the increased *m*. On the other hand, the *SEA* first increases and then decreases with the increased *m* when the mass is taken into account.

3.3.2.3 Effect of wall thickness

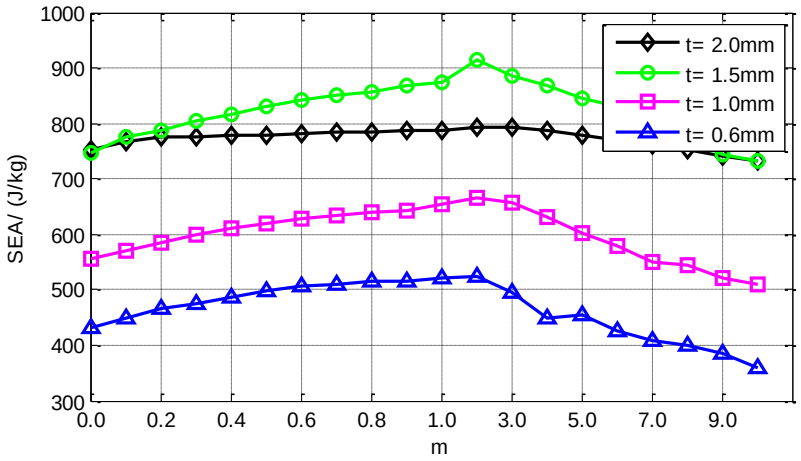

(a)

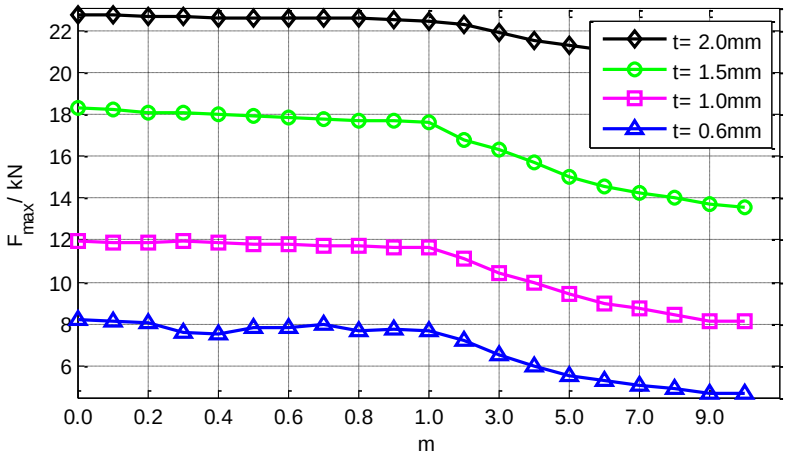

(b)

Fig. 3.24 Variation of crashworthiness performance due to wall thickness(a) *SEA*, (b) F_{max}

In addition to the foam material, the column wall can also affect the crash behavior

of the FGF filled columns. We varied the wall thickness with t= 0.6, 1.0, 1.5 and 2.0 mm while fixing other parameters (i.e., ρ_{max}= 0.5 g/cm^3, ρ_{min}= 0.2 g/cm^3, σ_y= 227 MPa), to quantify the effect on *SEA* and F_{max}. Froom Fig. 3.24a, the SEA values with t= 1.5 mm are preferable, which are larger than those with a thicker wall (t= 2.0 mm) and thinner walls (t= 1.0 and 0.6 mm). From Fig. 3.24b, it is found effective to reduce the F_{max} by thinning the wall directly.

3.3.2.4 Effect of wall yielding stress

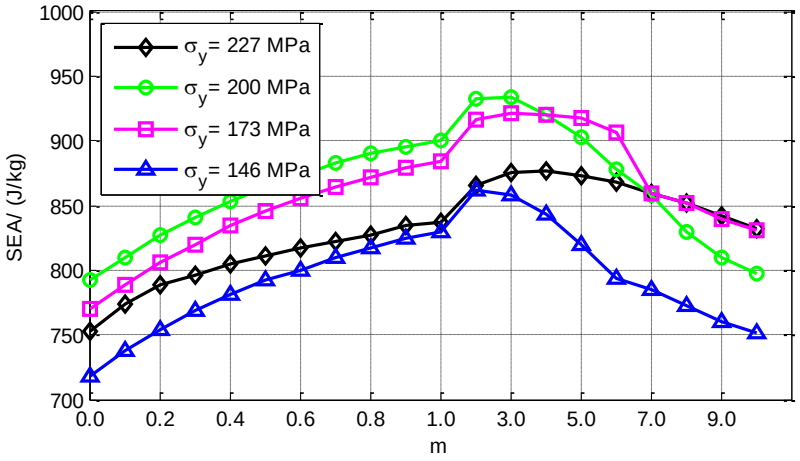

(a)

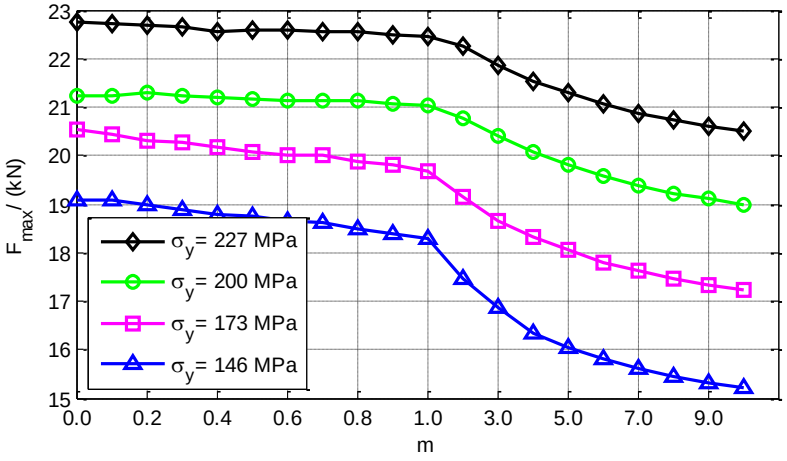

Fig. 3.25 Variation of crashworthiness performance due to wall thickness: (a) *SEA*, (b)

F_{max}.

The yielding stress was varied with σ_y = 146, 173, 200 and 227 MPa while ρ_{max}= 0.5 g/cm^3, ρ_{min}= 0.2 g/cm^3, t= 2.0 mm. Fig. 3.25 depicts the change of crashworthiness criteria due to the variation of σ_y. When m≤ 4.0, the axial FGF filled columns with σ_y= 200 MPa can obtain the largest SEA values. When 4< m< 7, the FGF columns σ_y= 173MPa absorb the most energy in all the columns. When m≥ 7, the FGF columns with σ_y= 173 and 227 MPa have the equal SEA values. For F_{max}, the columns with σ_y= 227 MPa perform worst while the columns with σ_y= 146MPa behave best. Therefore, the columns with low σ_y are preferred in terms of the F_{max}. However, this conflicts with the requirements of *SEA* by causing the smallest values of the *SEA*.

To be brief, FGF filled columns perform better in *SEA*, while worse in F_{max} than its UF counterparts. Besides, the parameters including grading exponent m, density range ($\Delta\rho$), and wall thickness (t) and yielding stress (σ_y) could largely affect the crashworthiness of FGF filled columns.

3.3.3 Multiobjective optimisation for functionally graded foam filled tubes

3.3.3.1 Definition of optimisation problem

While the effect of various parameters on crashworthiness behavior has been explored, it remains unknown how to design specific best designs for FGF filled thin-wall column. Furthermore, the F_{max} fails to be reduced by using FGF filled columns although the *SEA* is able to be increased in the parametric study. Therefore, we formulate the multiobjective optimisation problems for UF and FGF filled columns in Eq. (3.16) and Eq. (3.17) respectively, aiming to simultaneously enhance the two design criteria. In FGF problem, the densities of foam can be varied by taking m as a design variable when ρ_{max}=

0.5 g/cm^3, ρ_{min}= 0.2 g/cm^3, while in UF problem the density itself is taken as a design variable.

$$\begin{cases} \min & F_{max}, \text{-}SEA \\ s.t. & 0.6\,\text{mm} \le t \le 2.0\,\text{mm} \\ & 0.2\,\text{g/cm}^3 \le \rho_f \le 0.5\,\text{g/cm}^3 \\ & 140\,\text{MPa} \le \sigma_y \le 230\,\text{MPa} \end{cases} \tag{3.16}$$

$$\begin{cases} \min & F_{max}, \text{-}SEA \\ s.t. & 0.6\,\text{mm} \le t \le 2.0\,\text{mm} \\ & 0 \le m \le 10 \\ & 140\,\text{MPa} \le \sigma_y \le 230\,\text{MPa} \end{cases} \tag{3.17}$$

3.3.2.2 Results and discussion

It is difficult to derive analytical objective functions mathematically for the *SEA* and F_{max} that involve highly nonlinear contact-impact and large deformation mechanics. As an alternative, surrogate modeling techniques have proven effective and been widely implemented in crashworthiness design. The optimal Latin Hypercube sampling is implemented to generate training points. Then the Kriging surrogate models are established to approximate the functions of *SEA* and F_{max}.

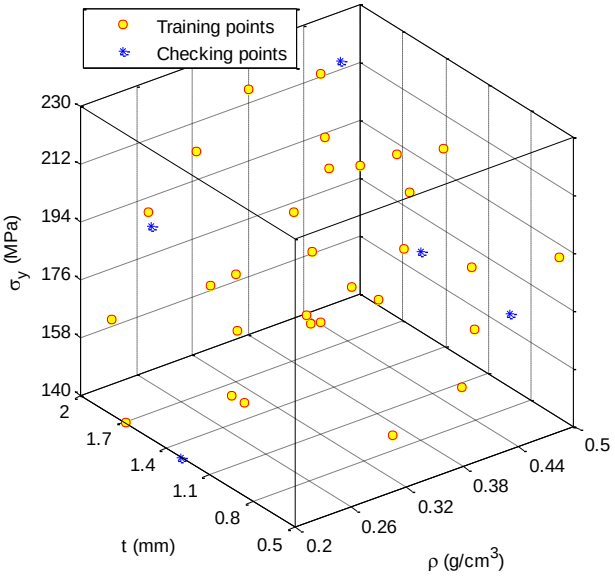

Fig. 3.26 Training points and checking points for the UF filled column.

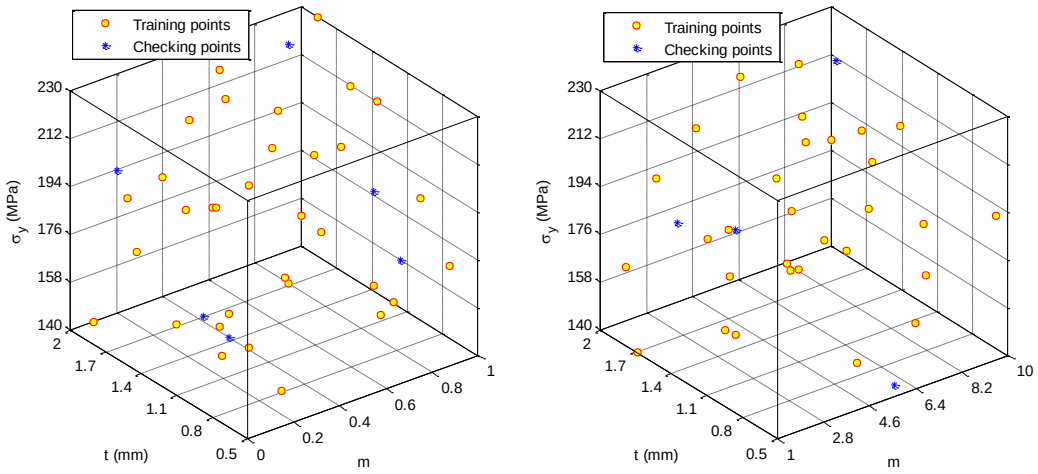

(a) (b)

Fig. 3.27 Training points and checking points for the FGF filled columns: (a) 0≤m≤1, and (b) 1≤m≤10.

Table 3.4 Accuracy Assessment of Kriging models.

			R^2	e_{max}	e_{avg}
UF column		F_{max}	0.9985	0.0271	0.0170
		SEA	0.9792	0.0476	0.0288
FGF column (Axial)	0≤m<1	F_{max}	0.9992	0.0298	0.0114
		SEA	0.9998	0.0086	0.0040
	1≤m≤10	F_{max}	0.9992	0.0189	0.0071
		SEA	0.9980	0.0252	0.0138
FGF column (Transverse-Type A)	0≤m<1	F_{max}	0.9996	0.0242	0.0087
		SEA	0.9520	0.0589	0.0267
	1≤m≤10	F_{max}	0.9890	0.0701	0.0394
		SEA	0.9866	0.0489	0.0209
FGF column (Transverse-Type B)	0≤m<1	F_{max}	0.9999	0.0077	0.0048
		SEA	0.9431	0.0604	0.0248
	1≤m≤10	F_{max}	0.9973	0.0266	0.0156
		SEA	0.9998	0.0046	0.0020

Figs. 3.26, 3.27a and 3.27b display the training points and checking points over the design space for the UF column, FGF columns with 0≤m≤1 and FGF columns with 1≤m≤10 respectively. Table 3.4 lists the results of accuracy assessment. It can be seen that the values of R^2 are all close to 1 and the values of e_{max} and e_{avg} are within 8%, indicating the Kriging models can be considered accurate adequately to replace the high-fidelity finite element analyses.

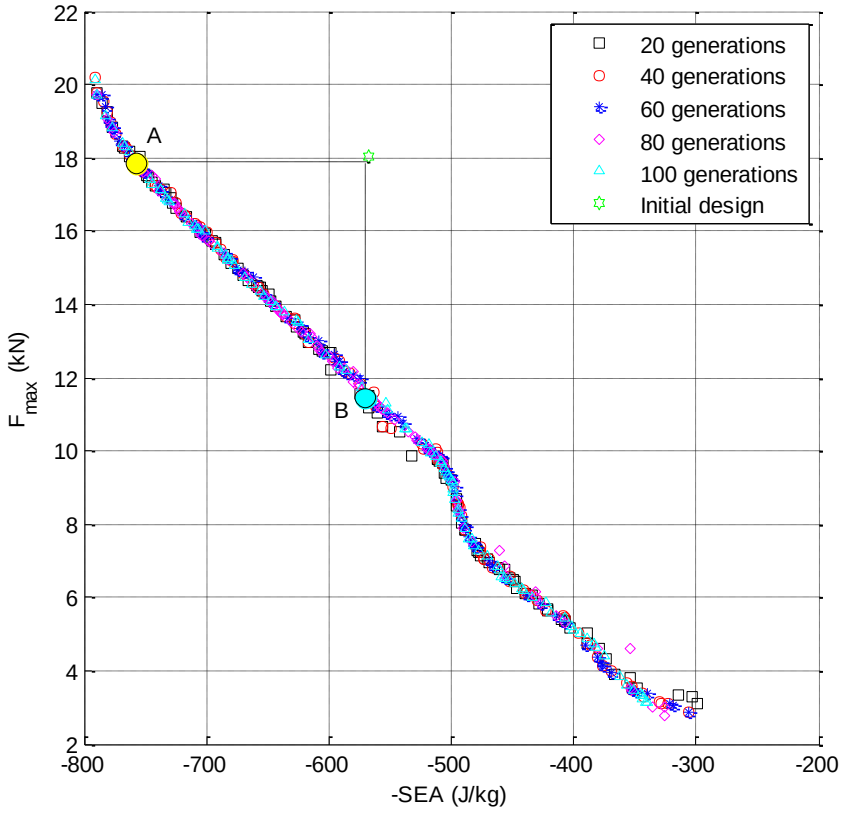

Fig. 3.28 Pareto frontiers of different generations for the UF filled column.

Fig. 3.28 depicts the Pareto frontiers of different generations of the multiobjective optimisation for the UF column. Obviously, after 100 generations the Pareto frontier converges adequately. The Pareto optimal frontier provides designers with a set of solutions over the Pareto space for design selection. Specifically, if the designers pay more attention to *SEA*, the solutions at the top left corner will be selected. While if the designers emphasis on F_{max}, the solutions at the bottom right corner will be considered. To be compared with the optimized solution in the objective space, the initial design is also signified in Fig. 3.28. It can be seen that optimum A improves the *SEA* when maintaining the F_{max}, while optimum B reduces the F_{max} when maintaining the *SEA*, in

comparison to the initial design. The optimums between A and B can simultaneously reduce the F_{max} and increase the *SEA*.

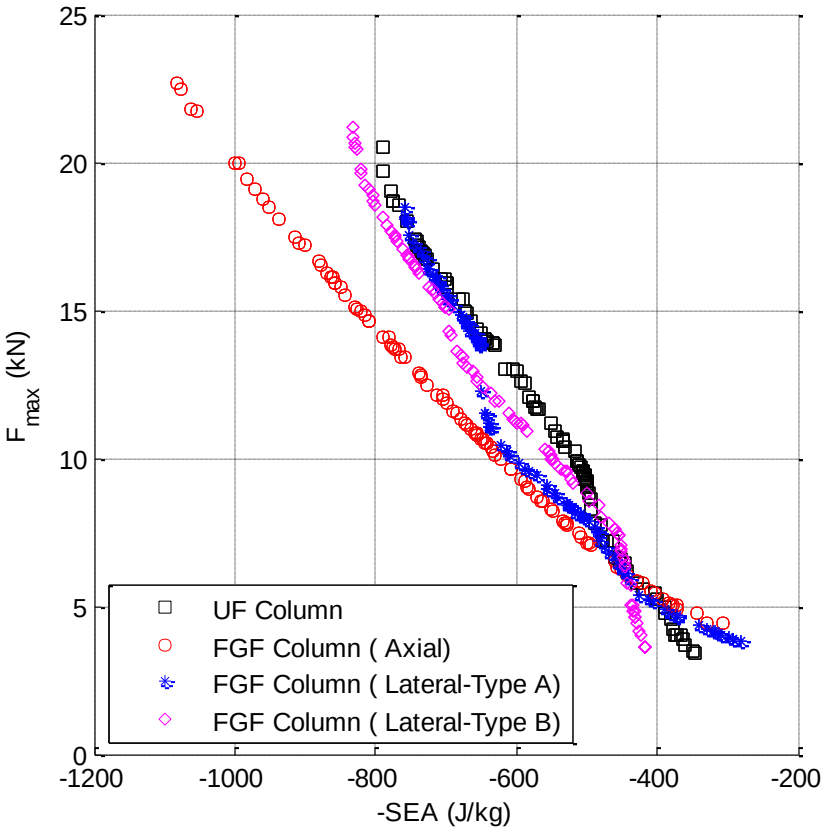

Fig. 3.29 Comparison of Pareto frontiers of UF filled column and FGF filled columns.

To compare the results of UF and FGF columns, their Pareto frontiers are plotted in Fig. 3.29 together. Similar to the Pareto frontier for the UF column, the Pareto frontiers of FGF filled columns present a series of solutions over the Pareto space, while parametric study just analyzes the effect of various parameters on crashworthiness performances and produces no specific optimal solution. Surprisingly, when UF is replaced with FGF, the Pareto frontiers move towards the direction representing the better performance both in *SEA* and F_{max}, except for those at the bottom right corner. That is to say, the FGF columns are able to increase the *SEA* and reduce the F_{max} simultaneously, which was not found in

the parametric study.

Tables 3.5 list the four optimal solutions for each column, which are selected from the corresponding Pareto solutions subject to the constraint F_{max}≤14kN. It can be seen that all the solutions have acceptable errors by comparing finite element analysis (FEA) results with Kriging values. The *SEA* values validated by FEA of the two types of transverse FGF filled columns are very close, indicating they have the equal effect on crashworthiness. Furthermore, optimisation on the axial FGF column produces the largest *SEA* value under the same level of $F_{\max}$.

Table 3.5 Optimal solutions (under the constraint of $F_{max} \leq 14$ kN).

		UF	Axial FGF	Transverse FGF	
				Type A	Type B
m (rho (kg/cm$^{3)}$)		0.46	5.69	4.37	0.90
t (mm)		1.44	1.52	1.24	1.37
σ_y (Mpa)		166.55	199.34	225.70	219.33
F_{max} (kN)	Kriging	13.99	13.84	13.86	14.00
	FEA	13.79	13.80	14.13	14.54
	Error	1.48%	0.32%	-1.89%	-3.75%
SEA (J/ kg)	Kriging	643.74	778.7	654.09	688.64
	FEA	613.80	777.23	673.52	683.08
	Error	4.88%	0.19%	-2.88%	0.81%

3.4 Crashworthiness and multiobjective optimisation of functionally graded foam-filled tubes with a functionally graded thickness

This section tries to integrate two kinds of gradients, i.e. functionally graded foam and functionally graded thickness, to achieve more competent crashworthiness.

3.4.1 Numerical modelling

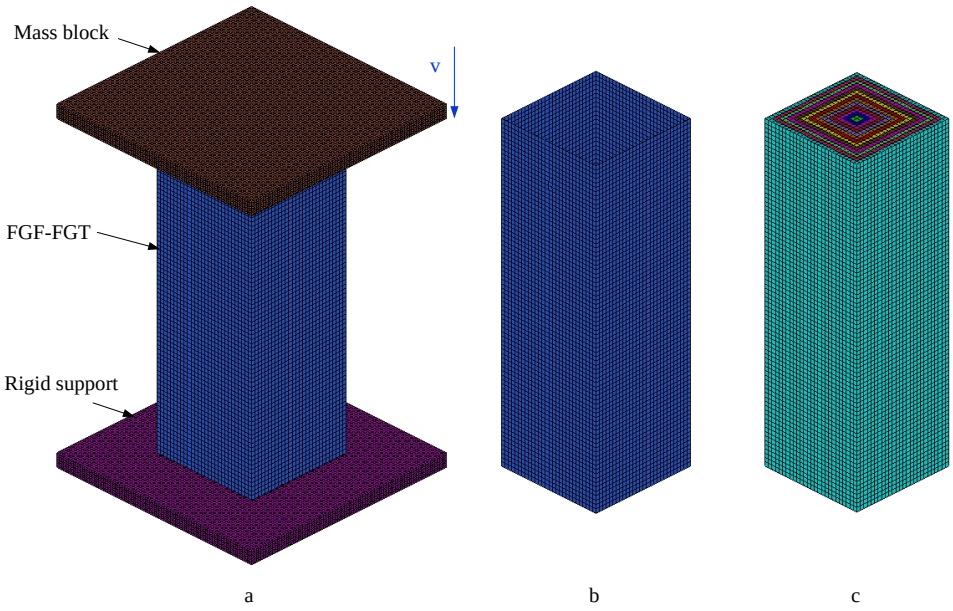

Fig. 3.30 Finite element model for (a) crashing analysis of FGF-FGT structure, (b) FGT tube and (c) FGF

The structure analysed herein is an FGF-FGT structure subjected to axial impact loading (Fig. 3.30). The continuous FGF was discretized with a limited number of discrete layers, and within each layer, the foam density was regarded uniform. Fig. 1 depicts the grading patterns for the FGF, and the foam density can be determined by the following power-law functions:

$$\rho_f(x,m_1)=\begin{cases}\rho_{\min}+(\rho_{\max}-\rho_{\min})(\dfrac{x}{L_{\mathrm{f}}})^{10^{n_1}}, & \text{ascending pattern}\\ \rho_{\max}-(\rho_{\max}-\rho_{\min})(\dfrac{x}{L_{\mathrm{f}}})^{10^{n_1}}, & \text{descending pattern}\end{cases} \tag{3.18}$$

where $\rho_{\min}$ and $\rho_{\max}$ are the minimum and maximum densities, respectively. n_1 denote the gradient parameters that govern the variation of foam density. x and L_{f} are the distances shown in Fig. 3.31. Figs. 3.31a and b show the variation of foam density for ascending and descending pattern, respectively. The square tube considered herein is fabricated with functionally graded thickness (FGT) sheet, where the thickness gradient was determined by the following power-law functions [143]:

$$t(x,m_2)=\begin{cases}t_{\min}+(t_{\max}-t_{\min})(\dfrac{x}{L_{\mathrm{t}}})^{10^{n_2}}, & \text{ascending pattern}\\ t_{\max}-(t_{\max}-t_{\min})(\dfrac{x}{L_{\mathrm{t}}})^{10^{n_2}}, & \text{descending pattern}\end{cases} \tag{3.19}$$

where $t_{\min}$ and $t_{\max}$ are the minimum and maximum thicknesses, respectively. In this study, $t_{\min}$ =0.6 mm and $t_{\max}$ = 1.5 mm are adopted. x and L_{t} are the distances shown in Fig. 3.31b. n_2 denote the gradient parameters that govern the thickness variation. The length of the column is L_{a}=240 mm, and the section of the tube and foam filler are $L_{\mathrm{t}}\times L_{\mathrm{t}}$ = 80 mm×80 mm and $L_{\mathrm{f}}\times L_{\mathrm{f}}$ = 78 mm×78 mm, respectively. The bottom surface of the foam-filled column is attached to the rigid support, and a block with a mass of 600 kg impacts onto the top surface at an initial velocity of v=15 m/s. According to gradient combinations of FGF and FGT, four different configurations of FGF-FGT structures are considered in this study, as listed in Table 3.6. The related FE modelling and its experimental validation can be found in [222].

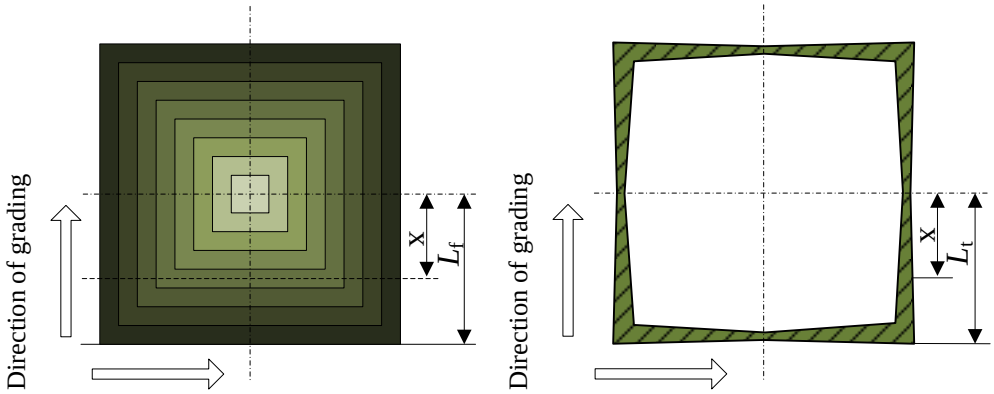

(a) (b)

Fig. 3.31 Schematic showing grading pattern: (a) foam; (b) wall thickness

Table 3.6 Types of FGF-FGT structures.

Type	FGF pattern	FGT pattern
AF-AT	ascending	ascending
AF-DT	ascending	descending
DF-AT	descending	ascending
DF-DT	descending	descending

3.4.2 Crashworthiness analysis

In this study, the optimial Latin Hypercube sampling approach was first used to generate 20 sample points for both functionally graded and uniform structures. Then, the finite element (FE) simulation results at these sample points were obtained to construct the PRS models for F_{max} and *SEA*. To evaluate the accuracy of those metamodels with the different orders, 5 checking points were sampled randomly in the design space. Table 3.7 lists the assessment results of the accuracy metrics and the orders of PRS models were selected with boldface highlight for the subsequent optimisations.

Table 3.7 Accuracy assessment of PRS models.

	Responses	*Order*	R^2	*RAAE*	*RMAE*
AF-AT	F_{max}	Linear	0.9174	0.2016	0.4895
		Quadratic	0.9043	0.2734	0.4691
		Cubic	**0.9420**	**0.2062**	**0.3993**
		Quartic	0.9176	0.2255	0.5165
	SEA	Linear	0.7826	0.4242	0.7251
		Quadratic	0.8750	0.2613	0.6592
		Cubic	0.9270	0.2212	0.4723
		Quartic	**0.9644**	**0.1586**	**0.3117**
AF-DT	F_{max}	Linear	0.9974	0.0457	0.0740
		Quadratic	**0.9987**	**0.0240**	**0.0628**
		Cubic	0.9985	0.0340	0.0563
		Quartic	0.9965	0.0433	0.1007
	SEA	Linear	0.9745	0.1367	0.2168
		Quadratic	**0.9981**	**0.0358**	**0.0590**
		Cubic	0.9979	0.0425	0.0617
		Quartic	0.9920	0.0655	0.1475
DF-AT	F_{max}	Linear	0.9220	0.2525	0.3645
		Quadratic	**0.9991**	**0.0186**	**0.0578**
		Cubic	0.9971	0.0458	0.0791
		Quartic	0.9979	0.0398	0.0718
	SEA	Linear	0.9274	0.2638	0.3491
		Quadratic	**0.9959**	**0.0529**	**0.0992**
		Cubic	0.9927	0.0745	0.1185

		Quartic	0.9801	0.1170	0.2046
DF-DT	F_{max}	Linear	0.9761	0.1279	0.2452
		Quadratic	0.9771	0.1297	0.2392
		Cubic	**0.9888**	**0.0979**	**0.1429**
		Quartic	0.9839	0.1261	0.1425
	SEA	Linear	0.9216	0.2297	0.4468
		Quadratic	0.9565	0.1981	0.2899
		Cubic	**0.9674**	**0.1786**	**0.2145**
		Quartic	0.9581	0.1982	0.2699
Uniform	F_{max}	Linear	0.7724	0.4228	0.6910
		Quadratic	0.8945	0.2697	0.5004
		Cubic	0.8990	0.3149	0.3725
		Quartic	**0.9407**	**0.2389**	**0.2898**
	SEA	Linear	0.9710	0.1355	0.2972
		Quadratic	0.9986	0.0314	0.0489
		Cubic	**0.9991**	**0.0258**	**0.0494**
		Quartic	0.9990	0.0271	0.0515

By relating n_1 and n_2 to equivalent t and ρ_f, the response surfaces for the transverse FGF-FGT and uniform structures are plotted together in Figs. 3.32-3.35. From Figs. 3.32 and 3.33, the FGF-FGT structures with AF (ascending foam gradient) - AT (ascending wall thickness gradient) as well as AF (ascending foam gradient) - DT (descending wall thickness gradient) configurations enhance the *SEA* clearly, but also increasing the $F_{\max}$ marginally. From the perspective of energy absorption, the AF-AT, and AF-DT structures

seem to be the good choices though a higher crushing force could have a somewhat negative effect on occupant safety.

On the other hand, the response surfaces for the DF (descending foam gradient) - AT and DF-DT structures are shown to intersect with the equivalent uniform structures and there is no noticeable difference observed in most of the design space. Besides, it can be seen that for all the four different configurations, the gradient of foam density (n_1) is more critical to the tube's crashing behaviors than the gradient of wall thickness (n_2). That is to say that when n_1 varies from -1 to 1 under the same value of n_2, more changes in F_{max} and *SEA* arise than the situation when n_2 varies from -1 to 1 under the same value of n_1.

For different gradient configurations, the relationships of crashing behaviors to n_1 and n_2 are different. For example, the F_{max} of AF-AT increases with the decreased n_1 and n_2 (Fig. 3.34b), whilst that of DF-DT increases with the increased n_1 and n_2 (Fig. 3.35b). This is because, for the ascending patterns, the decrease in n_1 and n_2 represents the increase of foam density and wall thickness on average, whereas for the descending patterns the changing trend is opposite.

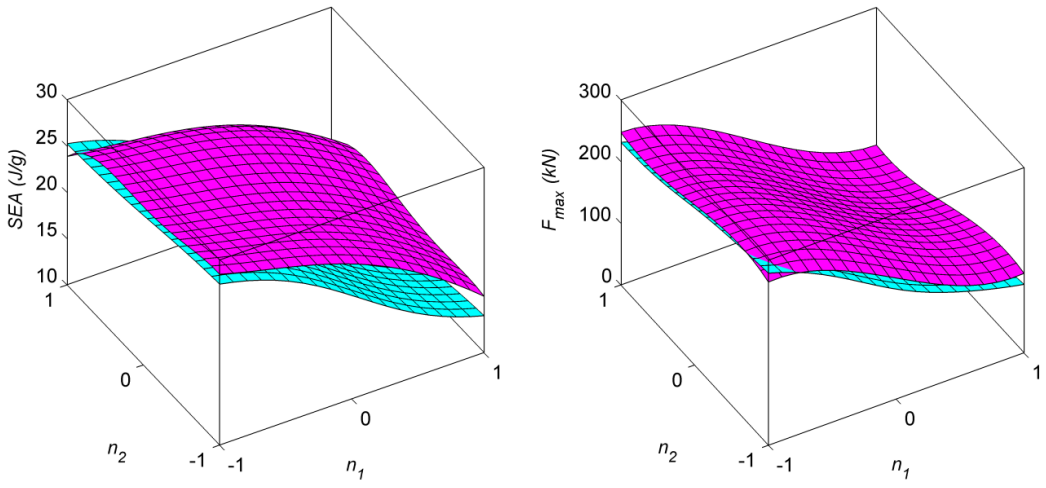

(a) (b)

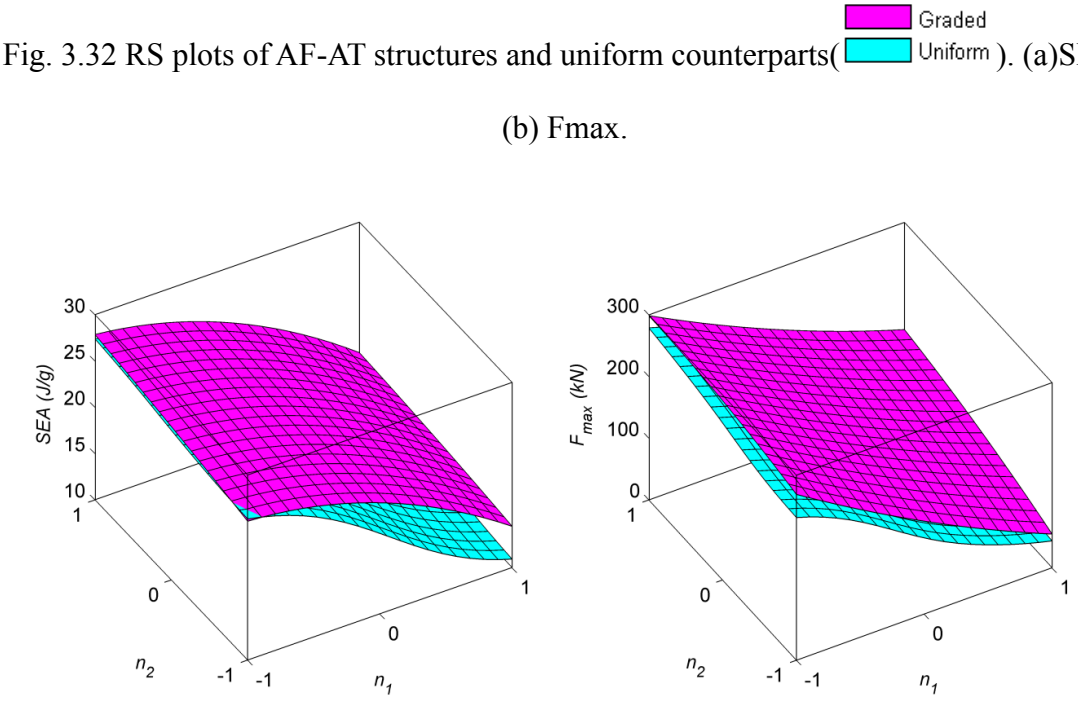

(a) (b)

Graded
Uniform

Fig. 3.32 RS plots of AF-AT structures and uniform counterparts( ). (a)SEA, (b) Fmax.

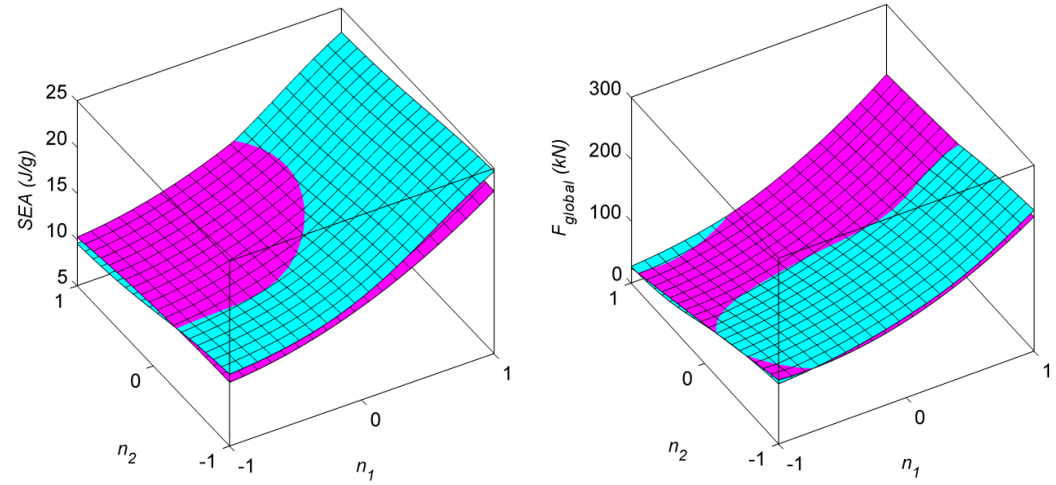

(a) (b)

Graded
Uniform

Fig. 3.33 RS plots of AF-DT structures and uniform counterparts( ). (a)SEA, (b) Fmax.

Fig. 3.34 RS plots of DF-AT structures and uniform counterparts (Graded Uniform). (a)SEA, (b) Fmax.

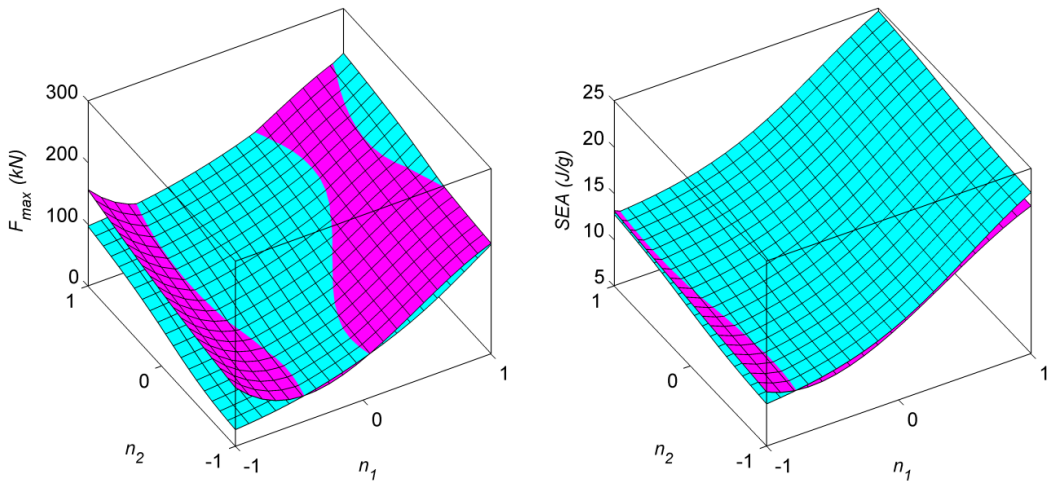

(a) (b)

Fig. 3.35 RS plots of DF-DT structures and uniform counterparts(Graded Uniform). (a)SEA, (b) Fmax.

3.4.3. Multiobjective optimisation of doubly graded tubes

3.4.3.1 Definition of optimisation problem

In this study, the optimisation for FGF-FGT structure is formulated in terms of the gradient exponent parameters n_1 and n_2 as follows:

$$\begin{cases} \min & \{F_{\max}(n_1, n_2), -SEA(n_1, n_2)\} \\ s.t. & -1 \le n_1 \le 1 \\ & -1 \le n_2 \le 1 \end{cases} \tag{3.20}$$

For comparison, we also define the optimisation problem for uniform structures as:

$$\begin{cases} \min & \{F_{\max}(\rho_f, t), -SEA(\rho_f, t)\} \\ s.t. & 0.2\,\text{g/cm}^3 \le \rho_f \le 0.5\,\text{g/cm}^3 \\ & 0.6\,\text{mm} \le t \le 1.5\,\text{mm} \end{cases} \tag{3.21}$$

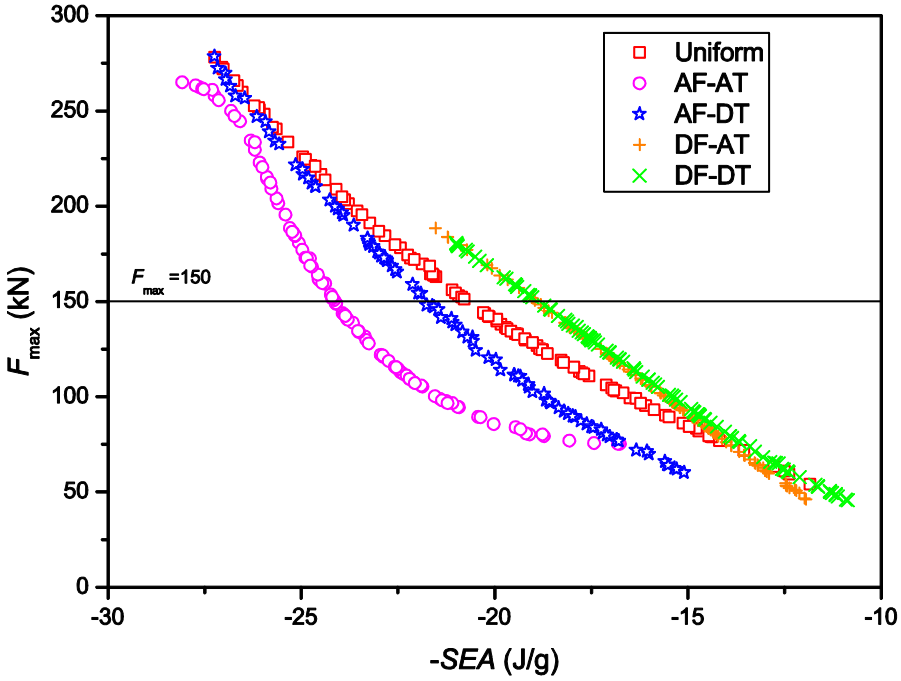

Fig. 3.36 Pareto frontiers for FGF-FGT and uniform structures.

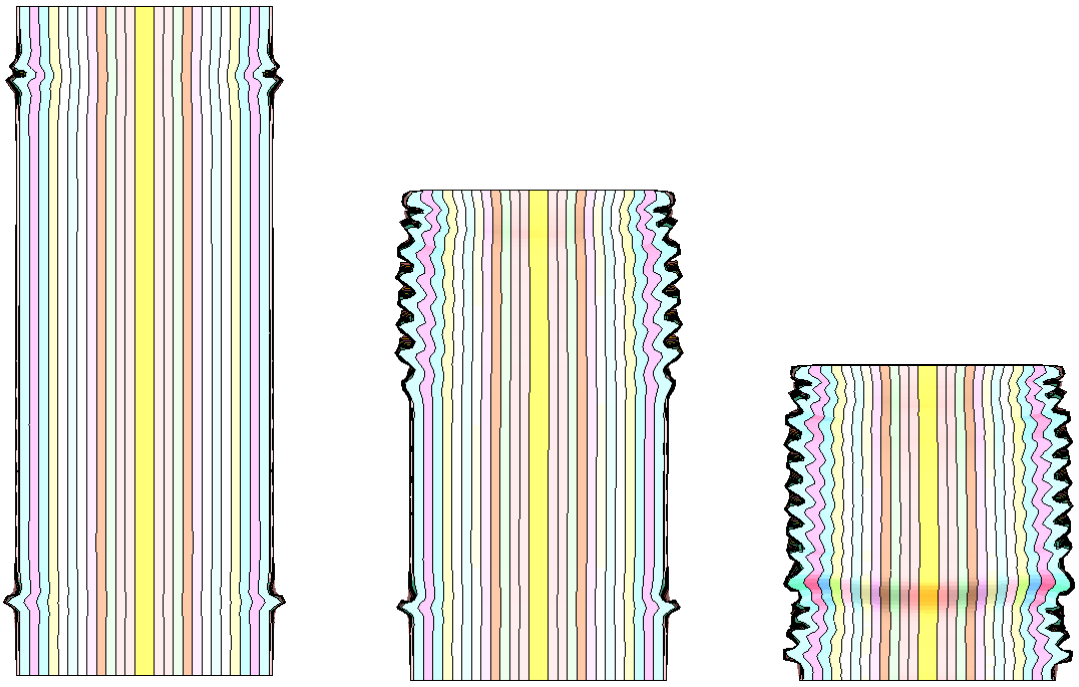

(a)

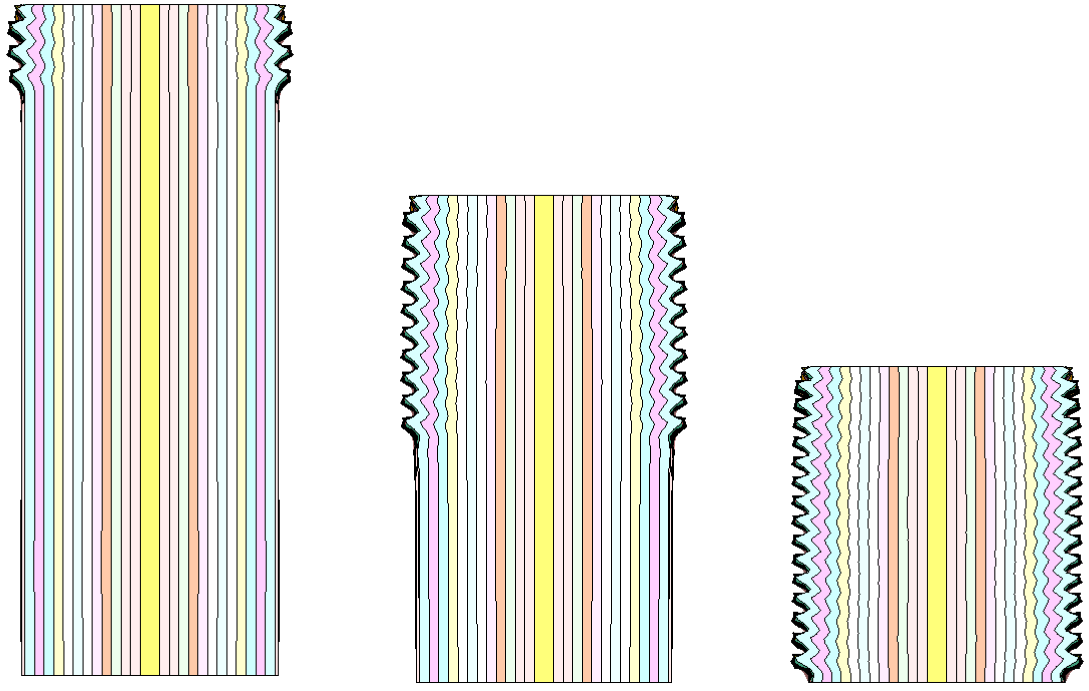

(b)

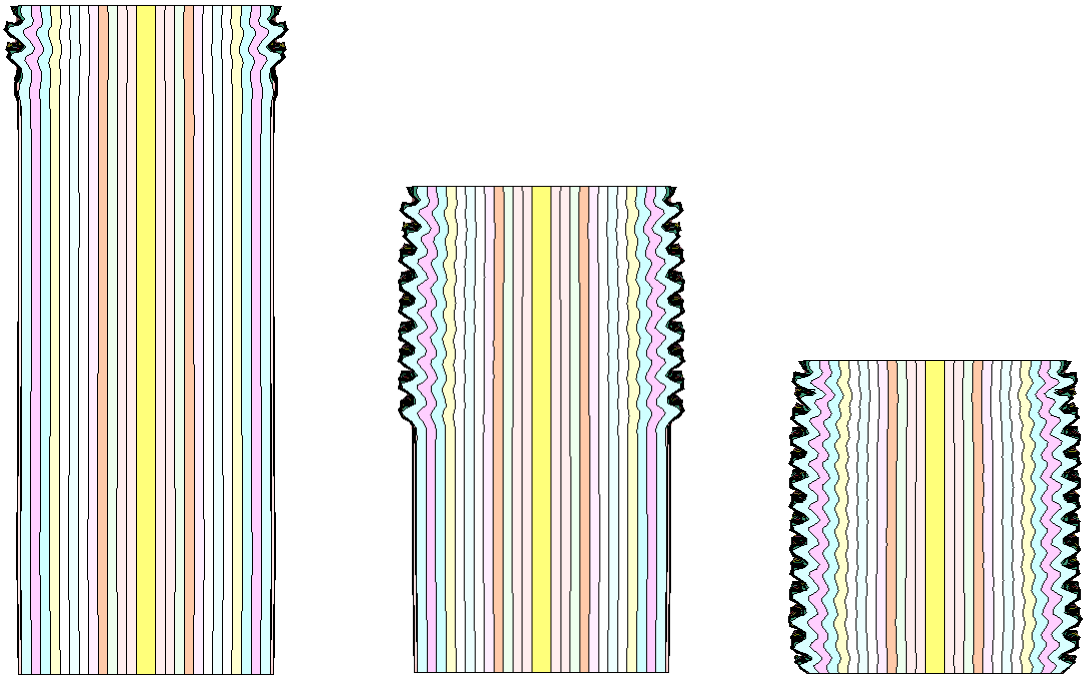

(c)

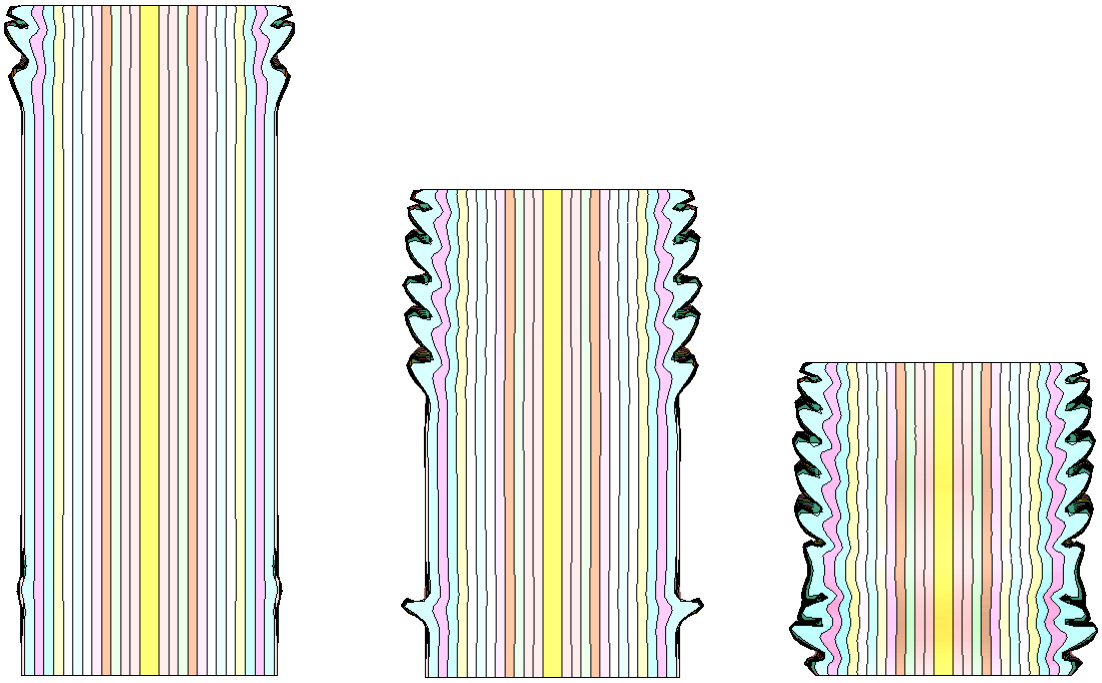

(d)

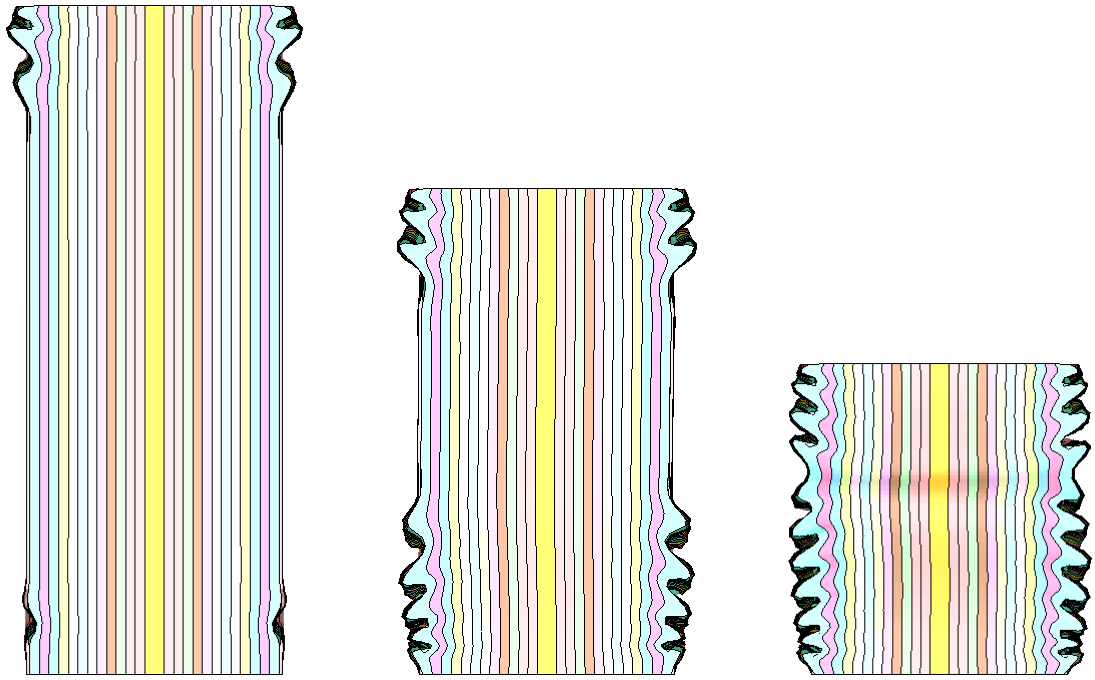

(e)

Fig. 3.37 Deformation patterns of FGF-FGT and uniform structures. (a) Uniform; (b) AF-AT; (c) AF-DT; (d) DF-AT; (e) DF-DT;

3.4.3.2 Optimisation results

Fig. 3.36 depicts the Pareto frontiers of multiobjective optimisations for the uniform and FGF-FGT structures with different gradient configurations. The Pareto frontiers of AF-AT and AF-DT structures locate on the lower-left of the uniform counterpart, indicating that these FGF-FGT structures are advantageous over the uniform structure. That is to say that the AF-AT and AF-DT structures are able to produce a lower F_{max} under the same *SEA* or to achieve a higher *SEA* under the same F_{max}. It can also be seen that thanks to the ascending transverse wall thickness, the Pareto frontier of AF-AT structures moves further towards the direction representing even better performance, compared to the AF-DT structures. Note that these two structures also make different

contributions to energy absorption, which might be because that it is more efficient to place tube material to the corners than the middle parts [223]. On the contrary, DF-AT and DA-DT structures perform worse than the uniform structures as the majority of their Pareto solutions are in the upper-right region in relation to the uniform solutions in the objective space. If the F_{max} is constrained no higher than 150 kN, the corresponding optimum for each structure can be easily selected from the Pareto solution set and the results are listed in Table 3.8. It can be observed that if the uniform structures are replaced by the AF-AT and AF-DT structures, the *SEA* values can be improved by 14.62% (from 20.25 J/g to 23.021 J/g) and 6.27% (to 21.52 J/g) respectively.

Table 3.8 Optimal solutions

		Uniform	AF-AT	AF-DT	DF-AT	DF-DT
n_1 (ρ_f (kg/cm3))		ρ_f = 0.6976	n_1= 0.0954	n_1= 0.1163	n_1= 0.6407	n_1= 0.6670
n_2(t (mm))		t = 4.2623	n_2= 0.6108	n_2= - 0.7748	n_2= 0.3472	n_2= - 0.9098
F_{max} (kN)	PRS	147.70	148.33	146.94	148.40	147.25
	FEA	152.54	147.35	146.18	146.14	145.91
	Error	-3.17%	0.67%	0.52%	1.54%	0.92%
SEA (J/ g)	PRS	20.55	24.06	21.65	18.81	18.68
	FEA	20.25	23.21	21.52	19.47	18.84
	Error	1.45%	3.69%	0.59%	-3.42%	-0.85%

Furthermore, the deformation modes of these five optimums are compared in Fig. 3.37 (axial sectional view). Interestingly, the uniform, DF-AT, and DT-DT structures are found to crush at both the upper and lower parts in the beginning, leading to uneven sizes of lobes at the end of the deformations. Conversely, the AF-AT and AF-DT structures develop the progressive deformation with the even size of lobes from top to bottom progressively. As a result, these two structures can be made of full use to absorb more energy under the same value of F_{max}. The reason for different deformation patterns probably lies in the interactive effect between the tube wall and the outmost foam layer. The ascending foam density (with the highest density in the outmost layer) seems to be preferred for helping produce a more stable deformation. In other words, the strong interaction between the wall and foam has a positive influence on stability and energy absorption characteristics [218]. Overall, the transverse gradient plays an important role in enhancing crashworthiness performance, and the ascending patterns in both wall thickness and foam density are more competent than the other configurations.

3.5 Summary

To excavate the potential of crash energy absorbers, the concept of functionally graded structure was introduced and multiobjective designs were implemented to this novel type of structures. First, note that the severe deformation takes place in the tubal corners, multi-cell tubes with a lateral thickness gradient were proposed to better enhance the crashworthiness. The results of crashworthiness analyses and optimisation showed that these functionally graded multi-cell tubes are preferable to a uniform multi-cell tube. Then, functionally graded foam filled tubes with different gradient patterns were analyzed and optimized subject to lateral impact and the results demonstrated that these

structures can still behave better than uniform foam filled structures under lateral loading, which will broaden the application scope of functionally graded structures. Finally, dual functionally graded structures, i.e. functionally graded foam filled tubes with functionally graded thickness walls, were proposed and different combinations of gradients were compared. The results indicated that placing more material to tubal corners and the maximum density to the outmost layer are beneficial to achieve the best performance.

Chapter 4 Fatigue optimisation of a truck cab using ensembles of surrogates

As one of the key factors in determining the performance, safety and durability, fatigue life has drawn significant attention in automotive engineering ranging from key components to entire vehicle. To improve the fatigue life, metamodel-based structural optimisation techniques have been playing an increasingly important role in vehicular design. In this regard, Lee and Jung [171] developed a Kriging (KRG) metamodel for optimizing a connecting rod subjected to a certain fatigue life. Ho et al. [172] developed a quadratic polynomial response surface (PRS) model to improve a crankshaft rolling process for durability. Bayrakceken et al. [170] conducted a multiobjective optimisation for a passenger car's body, where the artificial neural network (ANN) was used to model the fatigue life. Kaya et al. [173] re-designed a failed vehicle component subjected to cyclic loading by combining topology optimisation with PRS based shape optimisation. Song et al. [165] adopted the PRS and KRG surrogate models to optimize a control arm by considering strength and durability performance.

Note that these different surrogate models often provide rather a different modeling accuracy and design outcomes. It remains unclear which surrogate model is most suitable for any particular case; therefore, there are a number of comparative studies on different surrogate schemes in order to determine a most appropriate model [224-227]. In general, obtaining sampling data for developing surrogate is always more expensive computationally. In order to take full advantages of different individual surrogates to extract as much information as possible with a relatively small number of sample points, an ensemble of surrogates has been paid attention and proven a more promising method for different problems[11, 13, 16, 228]. This study will extend it for modeling the fatigue life

of a truck cab so that the optimisation can be performed for a better durability performance.

4.1 Theory of ensemble of surrogates

For a specific problem, if all the individual surrogates constructed from sampling data through high-fidelity simulations happen to have the same accuracy, then a straightforward form of the ensemble would be a simple weighted average surrogate (SWS), i.e., the same weight factors will be allocated to the individual surrogate functions. However, this special case can hardly appear as some surrogates may have better accuracy than the others. Thus, different weights should be placed on different individual surrogates to improve overall accuracy. Using the weighting technique, the ensemble of different surrogates can be formulated as [229] :

$$\hat{y}_{Ens}(\mathbf{x}) = \sum_{i=1}^{M} \omega_i(\mathbf{x}) \hat{y}_i(\mathbf{x}) \tag{4.1}$$

where $\hat{y}_{Ens}(\mathbf{x})$ denotes the predicted response by the ensemble of surrogates, M is the number of individual surrogates in the ensemble, $\hat{y}_i(\mathbf{x})$ and $\omega_i(\mathbf{x})$ are the predicted response and the corresponding weight factor of the ith surrogate, respectively. The weight factors in Eq. (4.1) are usually satisfied:

$$\sum_{i=1}^{M} \omega_i(\mathbf{x}) = 1 \tag{4.2}$$

Determination of proper weight factors associated with individual surrogates can be based upon global and/or local measures [12, 14]. This paper will focus on the global measure, in which the weight factors are treated as a constant in the entire design space

(i.e. $\omega_i(\mathbf{x}) = \omega_i$). Commonly-used global error metric with a generalized mean square cross-validation error (GMSE) [13] is implemented as,

$$GMSE = \frac{1}{N}\sum_{k=1}^{N}(y^k - \hat{y}_{Ens}^k)^2 \tag{4.3}$$

where N is the number of sampling points, y^k is the true response at $\mathbf{x}^k$ and $\hat{y}_{Ens}^k$ is the corresponding predicted value from the ensemble of surrogates constructed by using all but the kth design point (i.e., leave-one-out cross-validation strategy).

a) Goel et al. [12] proposed a heuristic weight scheme, namely the prediction-sum-of-squares-based weighted average surrogate (PWS) as follows:

$$\begin{aligned} \omega_i &= \omega_i^* \Big/ \sum_{j=1}^{N} \omega_j^* \\ \omega_i^* &= (E_i + \alpha\bar{E})^{\beta} \\ \bar{E} &= \frac{1}{N}\sum_{i=1}^{N} E_i \end{aligned} \tag{4.4}$$

where E_i is the generalized mean square cross-validation error (GMSE) of the ith surrogate with $\alpha < 1$ and $\beta < 0$. α and β are used to control the importance of $\bar{E}$ and E_i. Goel et al. suggested $\alpha = 0.05$ and $\beta = -1$ [12].

b) Viana et al. [230] proposed to select the weight factors following an approach to minimizing the mean square error as follows:

$$\boldsymbol{\omega} = \frac{\mathbf{C}^{-1}\mathbf{1}}{\mathbf{1}^T\mathbf{C}^{-1}\mathbf{1}}, \quad C_{ij} = \frac{1}{T}e_i^T e_j, \tag{4.5}$$

where **1** is the identity matrix, and the elements of the mean square error matrix **C** can be calculated from. T is the number of training points and e_i is the prediction error estimator of the ith surrogate.

c) Acar and Rais-Rohani [13] proposed an optimal weighted surrogate (OWS) by selecting the weight factors using optimisation:

$$\begin{cases} \min \ \ Err[\hat{y}_{Ens}(\omega_i)] \\ s.t. \ \sum_{i=1}^{N} \omega_i = 1 \end{cases} \tag{4.6}$$

where $Err()$ is the error metric that measures the accuracy of the ensemble $\hat{y}_{Ens}$.

The difference between the last two is that Acar and Rais-Rohani's approach obtains the weights through an optimisation process, while Viana's approach obtains the weights through an analysis expression [16]. However, both approaches have exactly the same solution [16].

4.2 Hybrid Particle Swarm Optimisation Algorithm

When particles are exploring the search space, if some particle finds the current best position, the others will fly toward it. If the best position is a local optimum, particles may not explore over again in the search space. In consequence, the algorithm will be trapped into a local optimum, which is also called premature convergence. A higher dimensional function can be easier to appear this phenomenon. To overcome this drawback, a hybrid method that integrates the standard PSO procedure with a gradient search algorithm called SQP is implemented in this paper. In the beginning, PSO has more possibilities to explore a large space and therefore the agents are freer to move and

sit on different valleys. The best value of all the agents will be taken as the starting point for the SQP algorithm, in which it will be tuned. Thus, the possibility of obtaining a global minimum from more local optima increases. The search will continue until a termination criterion is satisfied. This new hybrid PSO method has proven more effective and efficient for solving the economic dispatch problem compared with other methods [231]. In the hybrid PSO algorithm, PSO is the main optimizer and SQP serves as a tuner for refining the solution of PSO, as follows:

Step 1: Initialize swarm population with random positions and velocities (set t=1)

Step 2: If the maximum iterations or convergence criteria are not satisfied, then

For i =1 to NOP (number of particles)

Calculate fitness value;

Update velocity and position (Eq. (2.21) and (2.22) respectively);

Calculate $\boldsymbol{pBest}_i(t)$;

If $\boldsymbol{pBest}_i(t) < \boldsymbol{pBest}_i(t-1)$ then

Run SQP with $\mathbf{p}_i(t)$ as the initial point;

Replace $\boldsymbol{pBest}_i(t)$ with the newly obtained optimum;

Update $\boldsymbol{gBest}(t)$;

Step 3: $t=t+1$ and return to Step 2

4.3 Fatigue simulation and its experimental validation

4.3.1 Theories for fatigue simulation

4.3.2.1 Local strain-life fatigue analysis

The local strain-life fatigue analysis is based on the cyclic stress-strain curve of the material. This method has the following assumption: if a component made of the same material experiences the same strain history of the standard specimen at the most dangerous location, then it has the same fatigue life of the standard specimen. To acquire the fatigue life of the fatigue life, one should follow this procedure (as in Fig. 4.1): (1) identify the most dangerous location; (2) calculate the nominal stress history; (3) calculate the local strain spectrum; (4) determine the $\varepsilon - N$ curve; (5) predict the fatigue life based on the cumulative damage rule (Miner's rule).

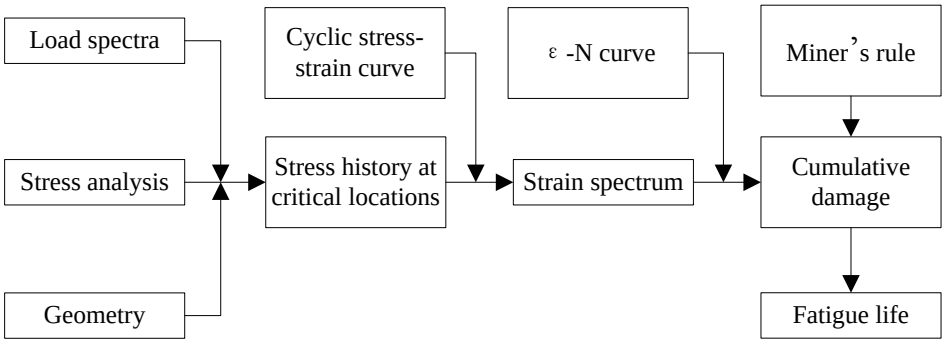

Fig. 4.1 Fatigue prediction of using the local strain-life method

. The strain-life (ε-N) curve is expressed by the classical Coffin-Manson equation as follows:

$$\varepsilon_a = \varepsilon_{ea} + \varepsilon_{pa} = \frac{\sigma'_f}{E}(2N_f)^b + \varepsilon'_f(2N_f)^c \tag{4.7}$$

where $\sigma_f^{'}$, b, $\varepsilon_f^{'}$ and c are fatigue strength, fatigue strength exponent, fatigue ductility coefficient and fatigue ductility exponent, respectively. The relation between the fatigue life and the elastic strain component ε_{ea}, plastic strain component ε_{pa} and total strain ε_a is displayed in Fig. 4.2.

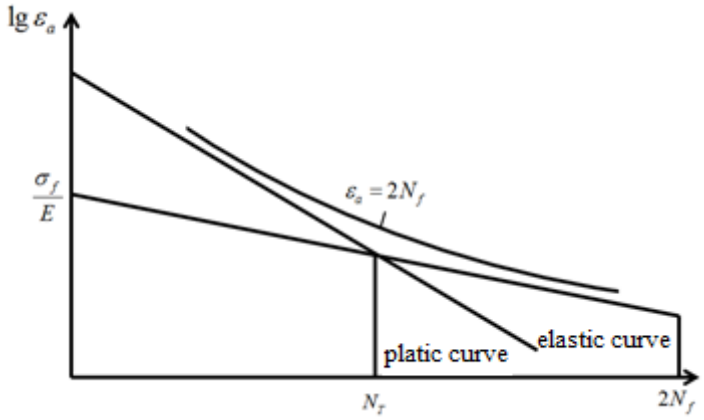

Fig. 4.2 Coffin-Manson equation

To account for the mean stress effect, Eq. (4.8) can be used

$$\varepsilon_a = \frac{(\sigma_f' - \sigma_m)}{E}(2N_f)^b + \varepsilon_f'(2N_f)^c \tag{4.8}$$

where σ_m is the mean stress.

4.3.2.2 cumulative damage model

The so-called damage is the microstructural change of the material at the crack initiation stage and the crack formation and propagation at the later stage. When the stress is higher than the fatigue limit, the damage caused by one cycle is $1/N_f$. $n_f$cycles of the constant-amplitude stress lead to the damage of the cycle ration n_f / N_f. The damage D of a variable-amplitude stress can be calculated as Eq. (4.9)

$$D = \sum_{i=1}^{l} n_{fi} / N_{fi} \tag{4.9}$$

where l is the level number of the variable-amplitude stress, n_{fi} is the cycle number at the i^{th} level and N_{fi} is the corresponding fatigue life.

When the cumulative damage reaches the critical value D_f, i.e. $D = \sum_{i=1}^{l} n_{fi} / N_{fi} = D_f$, the failure will occur. The Miner's rule is based on the assumption: the component reaches its fatigue life when the energy absorbed reaches the maximum. If the maximum value is W and the energy absorbed in n_{fi} cycles is W_i, then one can obtain the following relation:

$$\frac{W_i}{W} = \frac{n_{fi}}{N_f} \tag{4.10}$$

Thus, assuming that the component is loaded by m stress levels (δ_1, δ_2, ... δ_m), the fatigue life under these levels are N_{f1}, N_{f2}, ... N_{fm} and the cycle numbers are n_{f1}, n_{f2}, ... n_{fm} respectively, if the damage

$$D = \sum_{i=1}^{l} n_{fi} / N_{fi} = 1 \tag{4.11}$$

then the energy absorbed by the component reaches the maximum value and the failure occurs. Eq. (4.11) is the mathematical expression of the Miner's rule.

4.3.2 Simulation model

Fig. 4.3 displays the finite element analysis (FEA) model of a truck cab using the commercial FEA code MSC.NASTRAN. The panels are modeled with CQUAD and CTRIA surface element, and their material property is assigned linear elastic material

model MAT1. The cab is subjected to a torsional cyclic load at the rear body mounts when the front body mounts are fixed. As shown in Fig. 4.3, the forces F_1, F_2 form the torsional moment, and its amplitude and frequency of two load cases are listed in Table 4.1 according to our previous studies [98, 232].

Table 4.1 Load specifications for fatigue assessment

Case No.	*Cycles*	*Amplitude*	*Frequency*
1	0- 86,000	5 kN·m	1 Hz
2	86,000- 200,000	5 kN·m	2 Hz

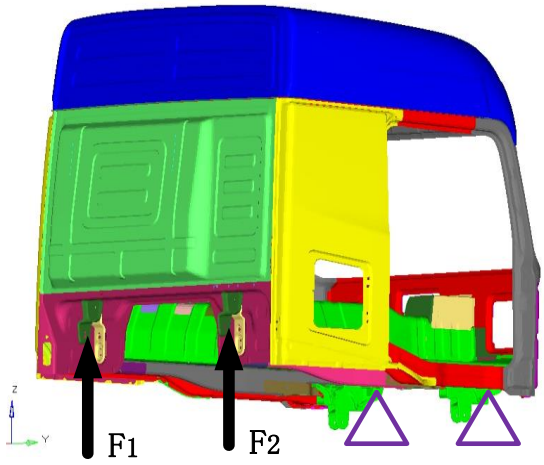

Fig. 4.3 Finite element model

4.3.2 Experimental validation

In order to validate the FE model, the modal and static stiffness experiments were conducted as shown in Figs. 4.4 and 4.5 prior to the fatigue test. The corresponding simulations were performed under the same conditions and the correlation results were list in Table 4.2. It can be noted that the simulation models had satisfactory accuracies by correlating to the physical experiments.

Fig. 4.4 Modal test

Fig. 4.5 Stiffness test

The fatigue test was conducted on a four-post test bench and the test facility is the IST vehicle vibration test system (Fig. 4.6), including the hydraulic pump (Fig. 4.7), excitation cylinder, electro-hydraulic servo system (Fig. 4.8), 8800 control system (Fig. 4.9), TWR (Time Waveform Replication) system and SCHENCK kraftaufnehmer bi-diretional force transducer (±25kN) (Fig. 4.10).

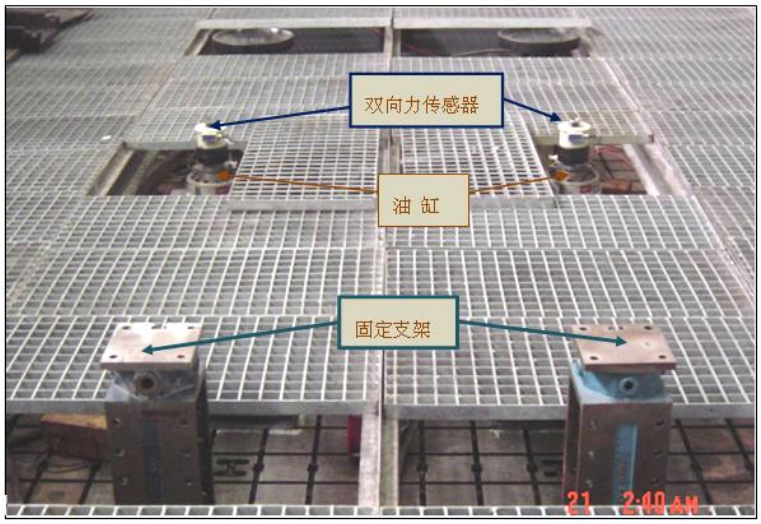

Fig. 4.6 vehicle vibration test system

Fig. 4.7 Hydraulic pump

Fig. 4.8 electro-hydraulic servo system

Fig. 4.9 8800 control system

Fig. 4.10 Bi-directional force transducer

Fig. 4.11 Truck cab in the fatigue test

The study subject is a truck cab together with front and rear mounts as shown in Fig. 4.11. The cab was connected to the test bench at the four mounting points and all the degrees of freedom were fixed except for the rotation about the y axis at the front points and the rotation about the x axis at the rear points.

In the fatigue experiment (Fig. 4.12b), we checked every 30 minutes for the first load case and every 10 minutes for the second load case if there were visible cracks on the surface of sheets. The fatigue life was the cumulative number of load cycles when the first crack was detected. Note that as a large engineering structure, the cab can probably continue to mostly or partially fulfill its function even after some small cracks appear. Nevertheless, it is difficult to quantify this ability. As a result, a visible crack might be a good choice to assess the fatigue life. From Fig. 4.42, the simulation and test have the same fatigue failure location, i.e., the upper region of the front left pillar. And it can be seen that the fatigue life is also comparable between the simulation and experimental test as summarized in Table 4.2.

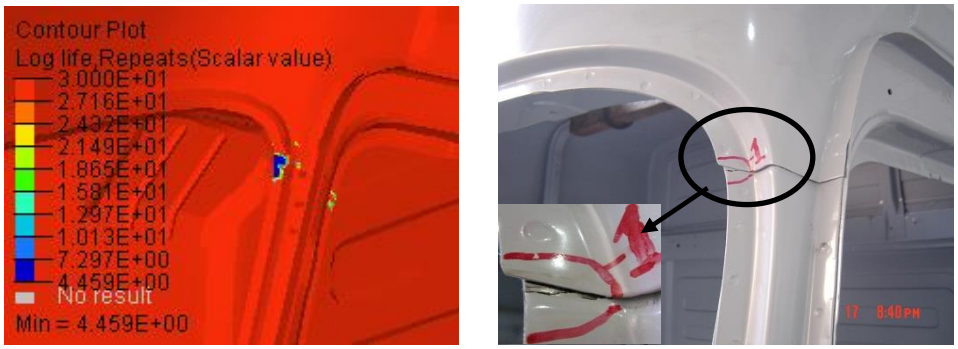

a) b)

Fig. 4.12 Failure location: a) Simulation; b) Experiment

Table 4.2 Comparison between the simulation and physical tests

	Simulation	Experiment

Torsional frequency	20.06 Hz	19.94 Hz
Bending frequency	29.64 Hz	28.47 Hz
Static stiffness	2689 KN·m/rad	2476 KN·m/rad
fatigue life (log)	4.46	4.60

4.4 Fatigue optimisation for a truck cab

4.4.1 Definition of optimisation problem

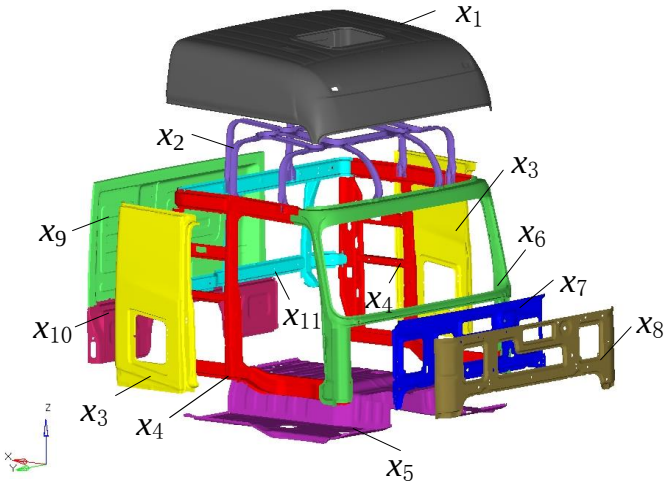

Fig. 4.13 Illustration of design variables

In this study, we aimed to maximize the fatigue life of the cab without increasing the mass. Thus, the optimisation problem can be formulated mathematically as,

$$\begin{cases} \min \ -F(\mathbf{x}) \\ s.t. \ \ m(\mathbf{x}) \le 475.20\text{kg} \\ \quad \mathbf{x}_L \le \mathbf{x} \le \mathbf{x}_U \\ \quad \mathbf{x}=[x_1, x_2, \ldots, x_{11}] \end{cases} \tag{4.12}$$

where $F(\mathbf{x})$ and $m(\mathbf{x})$ are the log of fatigue life and mass of the cab structure. Fig. 4.13 presents 11 thickness design variables whose ranges are all from 0.6 mm to 2.0 mm in this study. The surrogate model is to construct an approximate function from a series of

sampling points, which are typically determined using design of experiment (DoE) methods. In this study, 100 sets of sampling data were generated using the Optimal Latin Hypercube sampling (OLHS) approach. Since the mass of the cab follows a linear relationship to the panel thicknesses, $m(\mathbf{x})$ is thus fitted by a linear function of the thickness variables. In this study, the individual PRS, RBF and KGR surrogates were adopted in the ensembles for $F(\mathbf{x})$. After constructing the surrogates, the next step was to search for an optimal solution. The standard and hybrid PSO algorithms were utilized to run the optimisation for investigating their searching capacities with different surrogate models.

4.4.2 Results and Discussions

For a comparative study, the abovementioned three individual surrogates (PRS, RBF and KRG) and three ensembles (SWS, PWS and OWS) were constructed and used to run the optimisation. To assess the modeling accuracy of these six different surrogate schemes, 10 new validation points are also generated using the OLHS approach here.

The assessment results are compared in Table 4.3. Overall, the ensembles outperformed the individual surrogates in terms of these three metrics. The OWS model performed the best of all these six models, followed by PWS. KRG is the most accurate model of three individual models. Besides, the comparison showed that actually any of these surrogate models is sufficiently accurate for prediction of the fatigue life. Nevertheless, the following study will show why we need to examine the optimisation with these different surrogate models.

Table 4.3 Accuracy assessment of surrogates

Surrogates		Accuracy metrics		
		R^2	RMSE	RMAE
Individual	PRS	0.9624	0.1345	0.4154
	RBF	0.9546	0.1480	0.4232
	KRG	0.9877	0.0768	0.2538
Ensemble	AWS	0.9845	0.0866	0.2525
	SWS	0.9883	0.0755	0.2307
	OWS	**0.9903**	**0.0686**	**0.1944**

Tables 4.4 and 4.5 summarize the optimal solutions using the standard and hybrid PSO algorithms, respectively; and Tables 4.6 and 4.7 list their corresponding fatigue results from the surrogate prediction and direct durability simulation at each optimum. Interestingly, x_6 was pushed to the upper limit in all optimisations, indicating that this thickness variable is of the most critical effect on the cab's fatigue life. Compared to the baseline design (as in Table 4.2), all the obtained optima did improve the fatigue life markedly without increasing (actually even decreasing) the mass.

Table 4.4 Optimal solutions using the standard PSO based on different surrogates

Design variables	Original	Optimum					
		PRS	KRG	RBF	SWS	PWS	OWS
x_1	0.9	0.95	0.61	0.87	1.22	0.74	1.02
x_2	1.5	1.21	1.88	0.72	1.95	0.61	1.03
x_3	0.9	1.17	0.61	0.77	0.61	1.88	0.80
x_4	1.5	1.18	2.00	1.86	1.95	0.60	1.43

x_5	1.0	0.93	0.60	0.64	0.65	0.60	0.64
x_6	1.5	**2.00**	**1.99**	**1.94**	**1.98**	**1.98**	**1.98**
x_7	1.5	1.33	0.60	1.96	0.66	1.84	1.97
x_8	1.7	1.23	0.61	1.90	0.64	2.00	1.40
x_9	0.9	1.15	0.61	0.68	0.62	0.66	0.87
x_{10}	1.2	1.17	0.60	1.35	0.66	1.04	1.37
x_{11}	1.5	1.30	0.64	1.83	0.62	1.94	1.77

Table 4.5 Optimal solutions using hybrid PSO based on different surrogates

Design variables	Original	Optimum					
		PRS	KRG	RBF	SWS	PWS	OWS
x_1	0.9	0.60	0.98	0.83	1.43	0.60	1.08
x_2	1.5	2.00	1.23	0.73	2.00	0.60	1.08
x_3	0.9	0.60	1.15	0.74	0.60	2.00	0.80
x_4	1.5	2.00	1.16	2.00	2.00	0.60	1.51
x_5	1	0.60	0.96	0.60	0.60	0.60	0.60
x_6	1.5	**2.00**	**2.00**	**1.95**	**2.00**	**1.95**	**1.99**
x_7	1.5	0.60	1.33	2.00	0.60	2.00	2.00
x_8	1.7	0.60	1.25	2.00	0.60	2.00	1.22
x_9	0.9	0.60	1.08	0.60	0.60	0.60	0.73
x_{10}	1.2	0.60	1.17	1.31	0.60	0.60	1.37
x_{11}	1.5	0.60	1.28	2.00	0.60	2.00	1.79

Table 4.6 Optimisation results using standard PSO based on different surrogates

Surrogates		Fatigue life (log)			Mass (kg)
		Prediction	Simulation	Error	
Individual	PRS	6.9161	5.0349	37.36%	474.84
	RBF	5.5056	4.8655	13.16%	425.38
	KRG	5.1674	**5.1599**	0.15%	474.54
Ensemble	SWS	5.3802	4.9860	7.90%	464.30
	PWS	5.2295	**5.1870**	0.82%	441.60
	OWS	5.1385	5.1059	0.64%	473.68

Table 4.7 Optimisation results using hybrid PSO based on different surrogates

Surrogates		Fatigue life (log)			Mass (kg)
		Prediction	Simulation	Error	
Individual	PRS	7.0744	4.8831	44.88%	425.37
	RBF	5.5135	5.0371	9.46%	475.20
	KRG	5.1770	**5.1806**	-0.07%	475.20
Ensemble	SWS	5.4682	5.0199	8.93%	475.20
	PWS	5.3026	**5.2163**	1.65%	427.97
	OWS	5.1423	5.0834	1.16%	475.20

From Table 4.6, of the individual surrogates, the KRG-based standard PSO provided the longest fatigue life and the highest modeling accuracy (the lowest error of 0.15%) at the optimal point. In contrast, the PRS-based standard PSO gave the highest modeling

error (37.36%) and attains a worse optimum (5.0349) though it succeeded to seek a better value of surrogate prediction (6.9161) than KRG. In general, the ensembles of surrogates had considerably better performance than the individual surrogates from both the prediction accuracy and optimum obtained. From Table 4.6, of the three ensembles, PWS yielded the best fatigue performance, which also outperformed the best individual surrogate (KRG in this study) with a fatigue life increase of 9297 ($=10^{5.1870}-10^{5.1599}$) cycles.

For the same surrogate, the hybrid PSO converged to an optimum better than the standard PSO (comparing Tables 4.6 with 4.7). It is noted that almost all optima validated by the direct fatigue simulation using the hybrid PSO outperformed those using the standard PSO. Overall, the hybrid PSO appeared preferable for the both individual surrogates and ensembles of surrogates in order to enhance the optimisation performance.

Traditionally, the researchers prefer to select a so-called accurate surrogate model by assessing its error metrics prior to optimisation. However, our comparative study demonstrated that the method may not be ideal sometimes. If one relies only on the error metrics R^2, RMAE and RMSE in this case (Table 4.3), the OWS model should be chosen to run optimisation. Unfortunately, the best OWS accuracy metrics failed to obtain the best optimum (Tables 7 and 8). On the contrary, the SWS model succeeded to obtain the most competent optimum, though it behaved worse than OWS in all the three accuracy metrics. Therefore, the most accurate model does not necessarily ensure the best optimisation. This is because the optimisation algorithms require assessing relative improvement (PSO) and/or gradient information (SQP), which will largely depend on the

mathematical nature of different surrogate functions. As a result, the resulted optima could be fairly different. Unlike the traditional methods, we suggest here using multiple ensembles of surrogates for seeking the optimum simultaneously and then select the best of all, because the computational cost of surrogate modeling and subsequent optimisation is negligible compared to full scale simulation analysis in engineering applications.

The same experimental test was conducted on the optimised design, and the detalis of the fatigue cracks were summarised in Table 4.8 together with the results of the initial design.

Table 4.8 Fatigue results of physical experiments before and after optimisation

Case No.	Before optimisation		After optimisation	
	Cumulative cycles	Crack locations	Cumulative cycles	Crack locations
1	40607	Upper region of left front pillar		No detected damage
	51593	Upper region of left front pillar		
	60900	Upper region of right front pillar		
2	100743	Upper region of left front pillar	104034	Upper region of right front pillar
	113872	Upper region of right front pillar	118941	Upper region of right front pillar
	189812	Upper region of right front pillar		

4.5 Summary

To make full use of training data, multiple ensembles of surrogate models were proposed to maximize the fatigue life of a truck cab, while the panel thicknesses were taken as design variables and the structural mass the constraint. Meanwhile, particle swarm optimisation was integrated with sequential quadratic programming to avoid the premature convergence. The results illustrated that the hybrid particle swarm optimisation

and ensembles of surrogates enable to attain a more competent solution for fatigue optimisation.

Chapter 5 Sequential surrogate based optimisation and its applications to body structures

In engineering optmisation, the conventional one-step sampling method cannot nececsarily obtain a real optimum because the accuracy of the surrogate model can hardly be guranteed, though it is able to reduce the compuational cost. Enven if the ensemble of surrogate models in Chapter 4 is used, the optimum might not be validated by the simulation. Thus, the conventional method to construct models largely depends on the number of the initial sampling points: if the number is small, the established surrogate model may be not accurate enough; if the number is large, it may lead to a heavy compuational burden. However, before the surrogate is constructed, due to the lack of *a priori* knowledge, the proper number ofsampling points is difficult to decide. To achieve the independence of optimisation on the number of sampling points, it is necessary to adaptively add sequential points and update the surrogate model until the optimisation process is converged. The flowchart of sequential surrogate based optimisation is shown in Fig. 5.1.

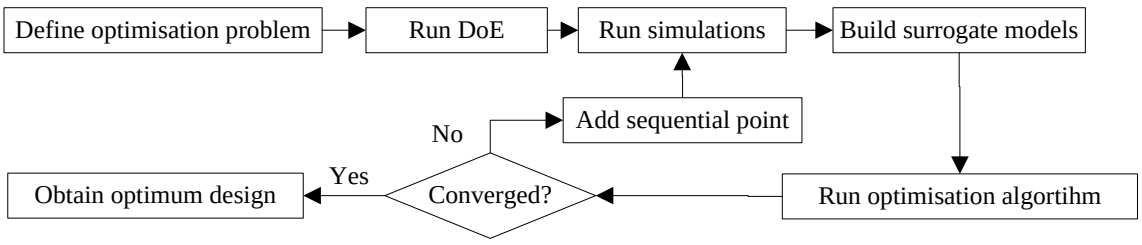

Fig. 5.1 Sequential surrogate based optimisation

5.1 Sequential surrogate based optimisation

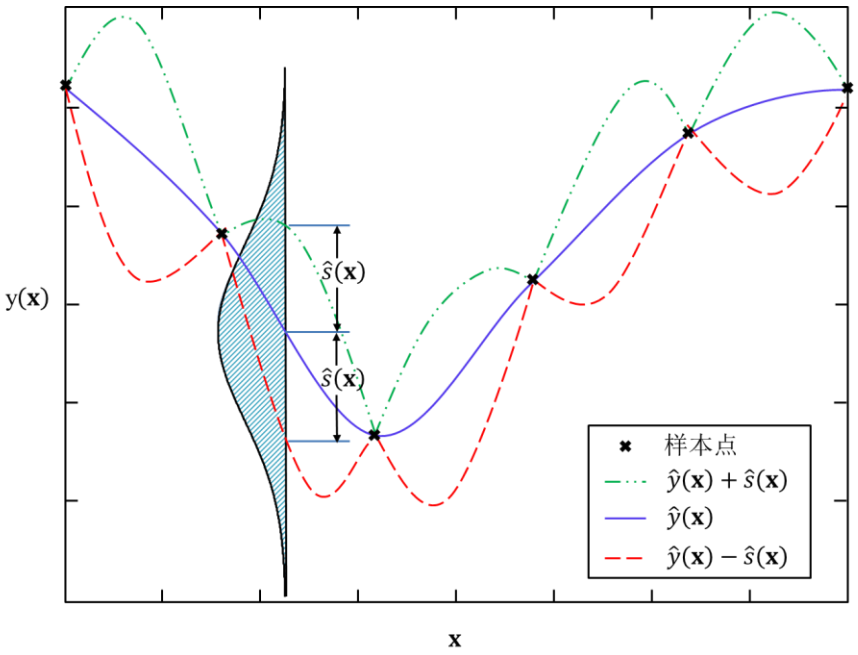

Fig. 5.2 Prediction of Kriging models

5.1.1 Sequential surrogate modelling in single objective optimisation

In practice, it is expected to only *exploit* local regions by sequentially positioning sample points in the neighborhood of the optimum. However, to *explore* design space may be necessary to increase the global accuracy of a metamodel by adding sequential samples to the sparse regions of the design space.

As introduced in Chapter 2, the Kriging model allows predicting two important parts of response, (1) an approximation to the objective ($\hat{y}(\mathbf{x})$ in Eq. (2.15)); and (2) an estimate of the mean squared error (MSE, i.e. $\hat{s}^2(\mathbf{x})$ as in Eq. (2.20)) at the untried point. The former provides local information and the latter involves the uncertainty of the prediction value. A Statistical Lower Bound (SLB) function based on both of them can be formulated as [233]:

$$y_{\mathrm{SLB}}(\mathbf{x}) = \hat{y}(\mathbf{x}) - \xi \cdot \hat{s}(\mathbf{x}) \tag{5.1}$$

Thus, the training points in this study are generated in a sequential and adaptive manner by minimizing the merit function defined in Eq. (5.1). The weight factor ξ can be used to increase or decrease the influence of the error term. If ξ = 0, the new training points equal the optima of the prediction $\hat{y}(\mathbf{x})$. If $\xi = \infty$, the new training points are added in a space-filling manner. In general, when insufficient information is gathered to construct an accurate metamodel, heavier weight ξ should be prescribed. When the accuracy of the metamodel improves, more weight should be placed on the optimisation of the metamodel. Fig. 5.3 displays the SLB function, where $f_{\min}$ is the minimum value of the existing training points. The SLB function has multiple minima and the global one is always selected as the sequential point.

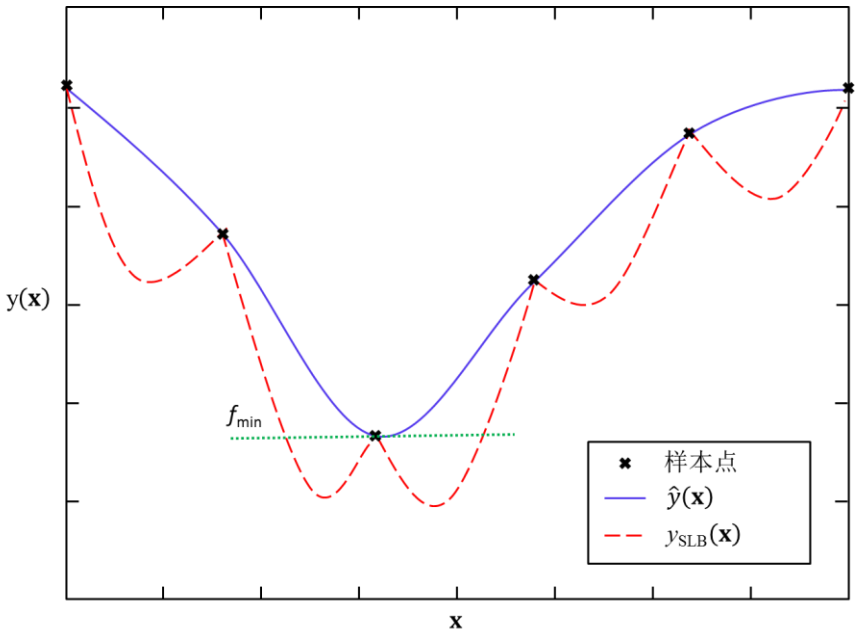

Fig. 5.3 SLB function

The Efficient Global Optimisation (EGO) approach was proposed by Schonlau [21].

This method starts by defining Improvement I:

$$I = \begin{cases} f_{\min} - y & \text{if } y < f_{\min} \\ 0 & \text{otherwise} \end{cases} \tag{5.2}$$

where $f_{\min}$ is the lowest objective function value obtained during previous iterations and y is a possible new outcome of a function evaluation. Clearly, if $y < f_{\min}$, the situation has improved. Assuming a normal distribution, the Expected Improvement can be obtained:

$$E(I) = \int_{-\infty}^{f_{\min}} (f_{\min} - y)\varphi(y)dy \tag{5.3}$$

where $\varphi(y)$ is the normal probability density function. Now y can be replaced by the Kriging prediction value $\hat{y}(\mathbf{x})$ and Eq. (5.3) can be rewritten to:

$$E(I) = (f_{\min} - \hat{y}(\mathbf{x}))\Phi\left(\frac{f_{\min} - \hat{y}(\mathbf{x})}{\hat{s}(\mathbf{x})}\right) + \hat{s}(\mathbf{x})\phi\left(\frac{f_{\min} - \hat{y}(\mathbf{x})}{\hat{s}(\mathbf{x})}\right) \tag{5.4}$$

where $\phi(\cdot)$ and $\Phi(\cdot)$ denote the probability density and the cumulative distribution functions of the standard normal distribution. The first term in Eq. (5.4) is the difference between the current minimum and the predicted value multiplied by the probability that $Y(\mathbf{x})$ is smaller than $f_{\min}$, and is, therefore, large where $\hat{y}(\mathbf{x})$ is likely smaller than $f_{\min}$. The second term is the standard deviation of $Y(\mathbf{x})$ multiplied by the probability that $y(\mathbf{x})$ is equal to $f_{\min}$. This term is large where there is the high uncertainty of the prediction (probably far away from the existing samples as the Kriging model goes exactly through them). Schonlau[38] proposed to maximize *E(I)* to yield the point promising the Maximum Expected Improvement (MEI). From Fig. 5.4, maximisation of the EI function can balance the local exploitation and global exploration. Compared with Eq. (5.1), Eq. (5.4) does not have to predefine the weight factor and can quantify the expected value of the improvement.

To summarize, sequential surrogate based single objective optimisation can be conducted by the following procedure:

(1) Define the optimisation problem: design variables $\mathbf{x}^L \le \mathbf{x} \le \mathbf{x}^U$, objective function $y(\mathbf{x})$ and constraint function $g(\mathbf{x}) \le 0$;

(2) Generate initial training points $\mathbf{X}=\{\mathbf{x}_1, \mathbf{x}_2, ..., \mathbf{x}_n\}$ using the optimal Latin Hypercube design;

(3) Run simulations to obtain the real responses $\mathbf{Y}=\{\mathbf{y}_1, \mathbf{y}_2, ..., \mathbf{y}_n\}$ and $\mathbf{G}=\{g_1, g_2, ..., g_n\}$ at the training points;

(4) Calculate the optimum of the existing training points, $f_{min}= \min(y_1, y_2, ..., y_n)$;

(5) Employ Kriging modelling to approximate the response function $\hat{y}(\mathbf{x})$ and its mean square error $\hat{s}^2(\mathbf{x})$ and the objective function $\hat{g}(\mathbf{x})$;

(6) Establish the $EI(\mathbf{x})$ defined in Eq. (5.4) and maximizing it to obtain the sequential sample point;

(7) Check if the convergence criteria of the optimisation process are met:

If not, then let $n= n+1$ and run the simulation to extract y_n by taking the sequential point in Step 6 as $\mathbf{x}_n$; if so, conduct the optimisation based on $\hat{y}(\mathbf{x})$ and $\hat{g}(\mathbf{x})$ and terminate the whole process.

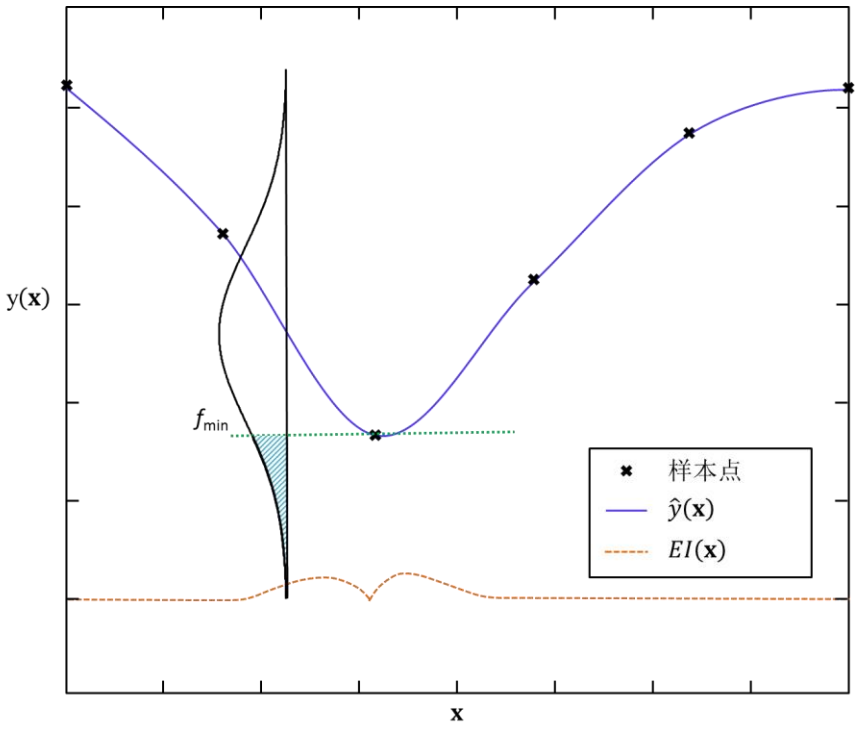

Fig. 5.4 Schemetic of the maximum EI method

5.1.2 Sequential surrogate modelling in multiobjective optimisation

Yang et al. [27] proposed a framework of sequential surrogate modelling in multiobjective optimisation, namely Adaptive Approximation in Multiobjective Optimisation (AAMO). In this framework, a multiobjective optimisation algorithm is used for generating Pareto frontier. Out of the Pareto solutions, a few points are selected for reconstructing the metamodels according to maximum distance design criterion [28]. That is to say that at each iteration the minimum distance from each Pareto solution to existing training points is calculated and then N_{add} points having the remotest distances are chosen to add to the training point set for refitting the metamodels. Then, the Pareto optimality of Pareto solutions is checked with the updated Kriging models and the remaining verified solutions are inserted into the initial generation of a multiobjective optimisation algorithm for the next iteration. If the difference of the number of solutions

before and after being checked are slight (e.g., 5% of the number of total solutions), AAMO is regarded convergent adequately. In other words, a small difference represents the metamodels have already approximated the true functions sufficiently well around the Pareto solutions, and thus the Pareto frontier becomes fairly reliable.

As Yang et al. [27] pointed out, however, AAMO may fail in finding out the respective optimum of two objectives (e.g. if m= 2 in Eqs. (1) and (2)) located at both ends of Pareto curve. It is because Pareto solutions to be compared with the optimum at the end are placed on only one side, while an optimum in the middle of Pareto curve has such Pareto solutions on both sides. The failure in finding out the extreme Pareto solutions leads to less chance to get additional sample points near the regions in the design space and to obtain a sufficient accuracy for metamodels in these regions. To address this limitation of AAMO, Yang et al. [27] proposed a combined AASO-AAMO method. This strategy is intended to enhance the accuracy of the metamodels at above-mentioned extreme regions by conducting two AASOs for seeking the respective optimums, separately, which will be used herein. The flowchart of AAMO-AASO is shown in Fig. 5.5 and the detailed procedure is as follows:

(1) Define the optimisation problem: design variables $\mathbf{x}^L \leq \mathbf{x} \leq \mathbf{x}^U$, objective function $y(\mathbf{x})$ and constraint function $g(\mathbf{x}) \leq 0$;

(2) Generate initial training points $\{\mathbf{x}_1, \mathbf{x}_2, ..., \mathbf{x}_n\}$ using the optimal Latin Hypercube design;

(3) Run simulations to obtain the real responses $\mathbf{Y}=\{\mathbf{y}_1, \mathbf{y}_2, ..., \mathbf{y}_n\}$ and $\mathbf{G}=\{g_1, g_2, ..., g_n\}$; at the training points;

(4) Construct the surrogate models $\hat{\mathbf{y}}(\mathbf{x})$ 和 $\hat{g}(\mathbf{x})$;

(5) Run *m* single objective optimisations to generate solutions $\mathbf{Q}=\{\mathbf{w}_1, \mathbf{w}_2,...,\mathbf{w}_m\}$;

(6) Run multiobjective optimisation to generate Pareto solution set $\mathbf{P}_0 = \{\mathbf{z}_1, \mathbf{z}_2, ..., \mathbf{z}_N\}$;

(7) Select N_{add} points from $\mathbf{P}_0$ based according to maximum distance design criterion;

(8) Let $\mathbf{X}_{add}= \{\mathbf{x}_1^{'}, \mathbf{x}_2^{'}, ..., \mathbf{x}_{Nadd}^{'}\} \cup \{\mathbf{w}_1, \mathbf{w}_2, ..., \mathbf{w}_m\}$, and run simulation to extract responses $\{\mathbf{y}_1^{'}, \mathbf{y}_2^{'}, ..., \mathbf{y}_{Nadd+m}^{'}\}$ 和 $\{\mathbf{g}_1^{'}, \mathbf{g}_2^{'}, ..., \mathbf{g}_{Nadd+m}^{'}\}$;

(9) Let $\mathbf{X} = \mathbf{X} \cup \mathbf{X}_{add}$, $\mathbf{Y} = \mathbf{Y} \cup \mathbf{Y}_{add}$, $\mathbf{G} = \mathbf{G} \cup \mathbf{G}_{add}$, and update $\hat{\mathbf{y}}(\mathbf{x})$ and $\hat{g}(\mathbf{x})$;

(10) Check the Pareto optimality of $\mathbf{P}_0$ based on the updated $\hat{\mathbf{y}}(\mathbf{x})$ and $\hat{g}(\mathbf{x})$, and add the verified points to the new Pareto solution set $\mathbf{P}_{new} = \{\mathbf{z}_1^{'}, \mathbf{z}_2^{'}, ..., \mathbf{z}_{Nnew}^{'}\}$;

(11) Check if the difference of the numbers of optimal solutions in $\mathbf{P}_0$ 和 $\mathbf{P}_{new}$ is small enough: If so, the optimisation process converges and $\mathbf{P}_{new}$ is the final Pareto solution set; otherwise, return to Step 5.

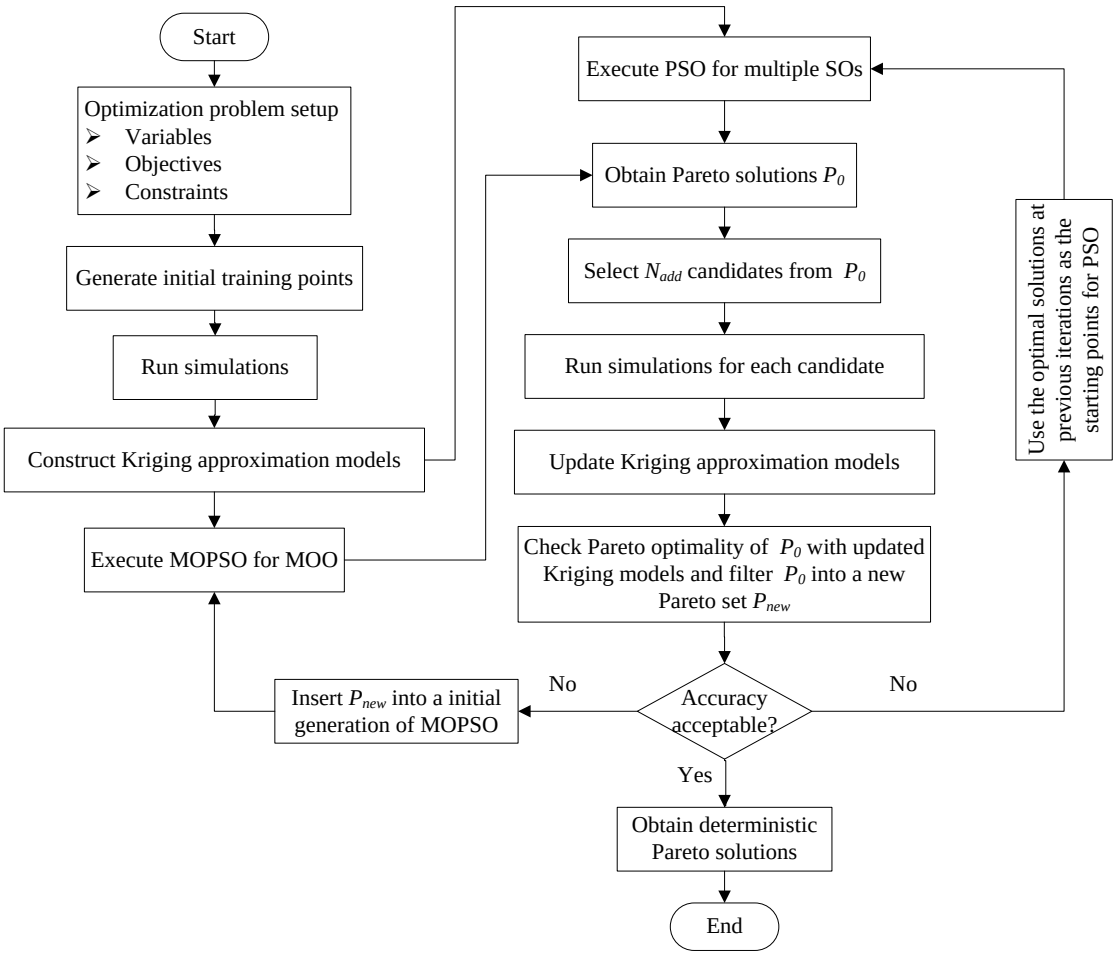

Fig. 5.5 AAMO-AASO procedure

5.2 EI based sequential optimisation of spot-welded joints

Automotive bodies as many other structures are composed of metal sheets joined by spot welds. There are about 4,000- 6,000 spot welds in a typical Body in White (BIW). Because spot weld joints provide localized connection and thus lead to high stress concentration in the joined plates, any improper design may result in excessively high stresses and premature failure [234]. Among these failure modes, fatigue is the most failure mode. It is imperative for automotive engineers to understand fatigue behavior of spot-welded joints under fluctuating loads. In this regard, numerical techniques have been

developed to carry out the predictive tasks such as design, analysis and evaluation. For example, Deng et al. [235] studied the mechanical behavior of spot welds under tensile-shear and symmetric coach-peel loading conditions using finite element analysis (FEA). Pan and Sheppard [236] presented a strain-based approach which could predict the fatigue life of mixed-thickness spot welds well based on empirical fatigue life data and FEA. Mahadevan and Ni [237] developed a damage tolerance reliability analysis method for automotive spot-welded joints using a three-dimensional finite element (FE) model. Wang and Shang [238] carried out elasto-plastic FEA for a single spot tensile-shear spot weld and predicted the low-cycle fatigue life. Ertas et al. [239] took into account the material nonlinearity, local plastic deformations around the welds during loading and the residual stress and strain after unloading in FEA. Based on the predicted stress and strain states, fatigue lives were calculated and compared to experimental results. Tovo and Livieri [240] adopted an implicit gradient approach to investigate the fatigue strength of spot welds, where the material was assumed linear elastic and an effective stress for the fatigue life estimation was considered as a transformation of the maximum principal stress field.

Zhang and Taylor [241] pointed out that the fatigue indictors could be a complex function of spot weld positions, even in the simple two-spot case. In addition, the fatigue indictors may be very sensitive to the design parameters such as the spot weld positions. For these reasons, the design optimisation of spot-welded structures could be very helpful and beneficial in engineering applications. In this regard, Zhang and Taylor [241] introduced an umbrella model of spot welds and the radial stresses around a spot weld into the optimisation process of fatigue life. Chae et al. [242] proposed an optimal design

system for spot welding locations in shell structures, where an h-version of adaptive meshing scheme based on background mesh was implemented. Ertas and Sonmez [243] integrated the design optimisation procedure with commercial software ANSYS to minimize the maximum Von Mises stress, where the Nelder-Mead simplex method was used to change the locations iteratively. Later, they also applied this procedure to find the optimal locations of spot welds and the optimal overlapping length of the joined plates to maximize fatigue life for a number of cases [234].

These above-mentioned studies on optimisation of spot-welded joints are restricted to directly coupling numerical simulation with an optimisation algorithm, which is commonly regard as not an efficient way since traditional optimisation usually need to call for a lot of finite element analysis results. To address this issue, the technique of meta-models or surrogate models appears effective to replace costly simulations for optimisation. This section aims to further enhance the optimisation efficiency by combining surrogate modelling with the sequential sampling strategy.

5.2.1 Finite element modeling

The spot-welded structure studied herein was a tensile-shear joint of two plates, whose geometry is depicted in Fig. 5.6. The dimensions of the plates are 100×50×1.0 mm, their overlapping length is 50 mm, and the diameters of the spot welds are 4 mm. For obtaining accurate results of stress and strain states developed in the structure, commercial FEA software ANSYS was utilized. A 3D ten-node tetrahedral solid element (SOLID 92) was used for the plates. This element has plasticity, stress stiffening, large deflection, and large strain capabilities. Each spot weld set consisted of a beam element and two node-to-surface MPC contact pairs. The nugget was modeled using a two-node

beam element (BEAM 188), which linked the spot weld surfaces. Each contact pair has only one contact element (CONTA175) which is defined by the associated spot weld node. The target element elements (TARGE170) were formed by a group of surface nodes lying within the search radius, which was set four times the spot weld radius. Six constraint equations were generated for each spot weld surface (i.e., each contact pair) by the software capacity to couple the motion of contact nodes to the motion of the target node in an average sense.

In addition to the contact condition, non-linearity in material property and geometry deformation were also considered in this study. The basic material property was generated on the basis of the engineering stress vs. strain through:

$$\begin{cases} \sigma = S(1+e) \\ \varepsilon = \ln(1+e) \end{cases} \tag{5.5}$$

where S and e are engineering stress and strain respectively, and σ and ε are the true stress and strain respectively. The engineering stress vs. strain curve for the basic plates was depicted in Fig. 5.7, and the elastic properties were set E= 207 GPa and v= 0.25. Because the nugget develops low stress, its material model was selected as linearly elastic. As heat treatment does not cause an appreciable change in elastic modulus and Poisson's ratio, their magnitudes were considered to remain about the same throughout the specimen despite melting during the formation of the nugget.

The boundary condition of the FE model is shown in Fig. 5.8. All of six translational and rotational degrees of freedom were constrained at one end. The other end was subjected to uniformly distributed in-plane loads in the x- and y-direction (1000 N and 250 N respectively), while the displacement was prevented in the z-direction. Due to high stress concentration, much smaller elements were used around the spot-weld nuggets in

comparison to those of the base metal as shown in Fig. 5.9.

Figs. 5.10a and b show equivalent stress distribution (in terms of Mega Pascal) over the inner surfaces of the lower and upper sheets, respectively. High stresses develop at regions on the inner surfaces of the sheets close to the peripheries of the spot welds because load transfer in a spot-weld nugget mainly occurs through the material near the boundary of the nugget, whist the central region of the nugget bears relative low stresses.

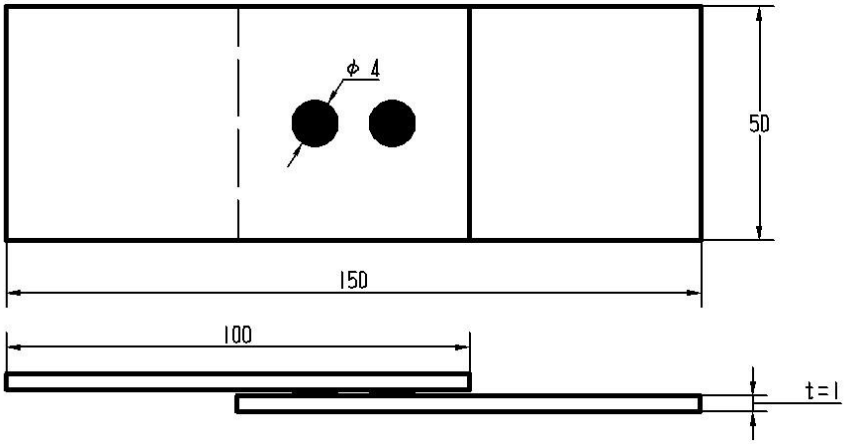

Fig. 5.6 Geometry of the TS specimen.

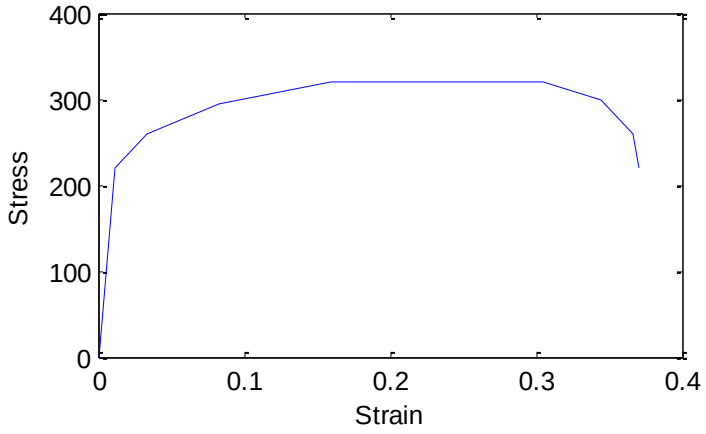

Fig. 5.7 Engineering stress-strain curve.

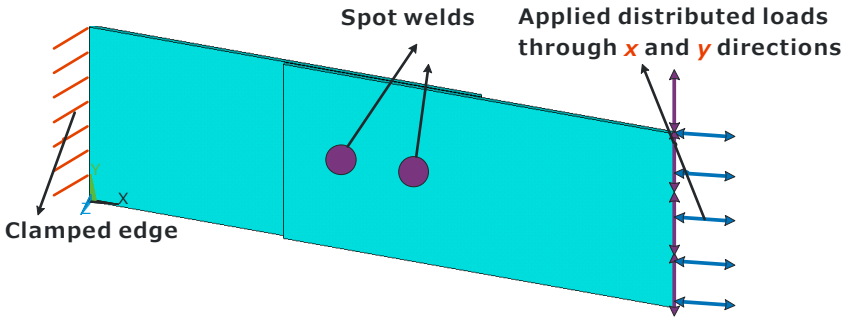

Fig. 5.8 Boundary conditions.

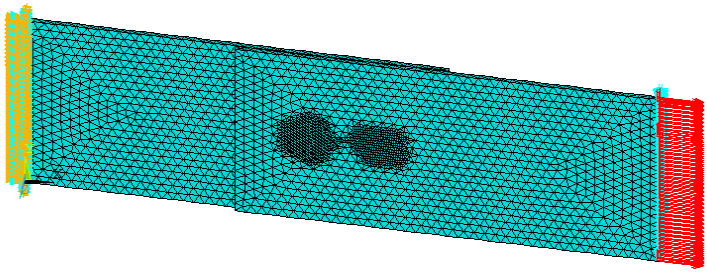

Fig. 5.9 Finite element model.

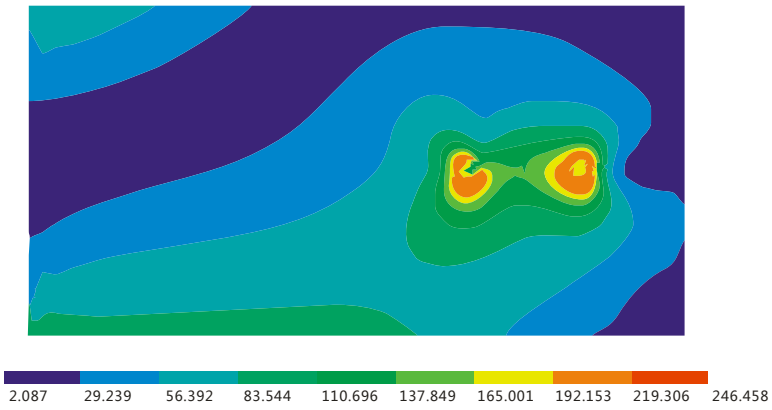

(a)

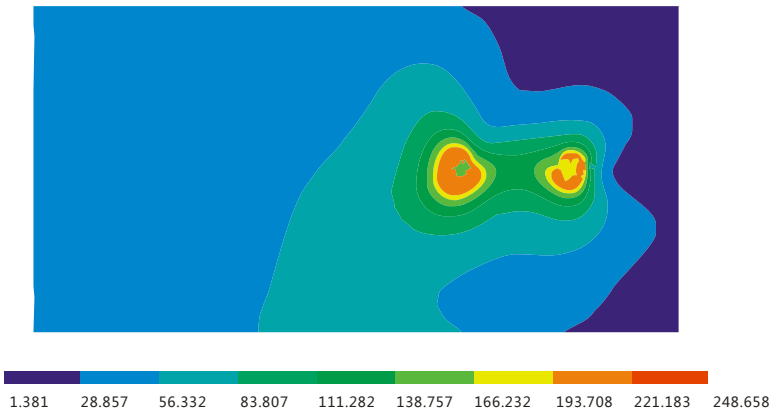

(b)

Fig. 5.10 Von Mises stress distrubition on inner surfaces of the initial design: (a) lower sheet; (b) upper sheet.

5.2.2 Description of optimisation problem

In this paper, we aim to maximize the fatigue life for a spot-welded structure. The absolute maximum principal strain theory of multi-axial fatigue failure proposed by Ellyin and Valaire [244] states that similar fatigue lives will be achieved when the maximum principal strains are the same. Pan and Sheppard [236] also drew the similar conclusion that the maximum principal strain is able to correlate well with fatigue life for a spot-welded joint. Hence, the maximum principal strain was used as the objective to characterize the fatigue behavior of spot welds in this study.

The spot welds should be allocated properly to avoid interfering with each other and getting close to the plate boundaries. That is to say, the design should conform to the standards related to weld-to-weld spacing and weld-to-edge distance. According to American Welding Society, the distance between an edge and the center of a spot weld should be greater than one spot weld diameter. Besides, the distance between the centers of the spot welds should be greater than twice the spot-weld diameter as recommended by

the industry. As a result, the mathematical problem to be optimized regarding the spot weld locations can be formulated as:

$$\begin{cases} \min \varepsilon_1 \\ s.t.\ D=\sqrt{(x_1-x_2)^2+(y_1-y_2)^2} \geq 2d \\ \quad 50+d \leq x_1, x_2 \leq 100-d \\ \quad d \leq y_1, y_2 \leq 50-d \end{cases} \tag{5.6}$$

where ε_1 denotes the maximum principal strain, D represents the distance between the spot welds, d is the diameter of the spot weld (herein d=4), x_1 and y_1 are the center coordinates in the x- and y- direction for the first spot weld respectively, and x_2 and y_2 for the second spot weld respectively.

5.2.3 Results and discussions

Table 5.1 Initial DoE points and their FEA results.

No.	x_1	y_1	x_2	y_2	ε_1	D
1	54.00	14.77	88.46	19.08	0.00230	34.73
2	55.08	42.77	74.46	32.00	0.05778	22.17
3	56.15	16.92	72.31	21.23	0.02341	16.72
4	57.23	32.00	58.31	27.69	-	4.44
5	58.31	13.69	76.62	40.62	0.00951	32.57
6	59.38	8.31	85.23	13.69	0.00170	26.40
7	60.46	39.54	86.31	11.54	0.00518	38.11
8	61.54	34.15	71.23	12.62	0.02314	23.61
9	62.62	18.00	90.62	42.77	0.00768	37.38
10	63.69	30.92	62.62	35.23	-	4.44

11	64.77	22.31	63.69	16.92	-	5.50
12	65.85	12.62	57.23	41.69	0.01500	30.32
13	66.92	7.23	73.38	37.38	0.00545	30.83
14	68.00	44.92	68.00	44.92	-	0.00
15	69.08	24.46	59.38	4.00	0.00459	22.64
16	70.15	26.62	84.15	14.77	0.01945	18.34
17	71.23	35.23	82.00	30.92	0.22667	11.60
18	72.31	4.00	55.08	15.85	0.00468	20.91
19	73.38	38.46	69.08	5.08	0.00683	33.66
20	74.46	11.54	93.85	8.31	0.00180	19.66
21	75.54	33.08	54.00	34.15	0.06039	21.57
22	76.62	6.15	77.69	25.54	0.00513	19.42
23	77.69	19.08	80.92	18.00	-	3.41
24	78.77	27.69	66.92	22.31	0.05791	13.01
25	79.85	10.46	92.77	26.62	0.00357	20.69
26	80.92	36.31	94.92	7.23	0.00369	32.27
27	82.00	46.00	79.85	38.46	-	7.84
28	83.08	25.54	56.15	6.15	0.00340	33.18
29	84.15	29.85	96.00	33.08	0.07518	12.28
30	85.23	15.85	64.77	39.54	0.01403	31.30
31	86.31	21.23	78.77	46.00	0.02269	25.89
32	87.38	37.38	60.46	9.38	0.00353	38.84
33	88.46	41.69	89.54	28.77	0.15530	12.97

34	89.54	5.08	87.38	10.46	-	5.80
35	90.62	43.85	75.54	20.15	0.01949	28.09
36	91.69	23.38	91.69	36.31	0.06770	12.93
37	92.77	9.38	61.54	23.38	0.00249	34.22
38	93.85	20.15	65.85	29.85	0.00567	29.63
39	94.92	40.62	70.15	43.85	0.06428	24.98
40	96.00	28.77	83.08	24.46	0.04458	13.62

Table 5.2 Sequential DoE points and their FEA results.

No.	x_1	y_1	x_2	y_2	ε_1	D
1	96.00	45.52	71.27	14.21	0.00635	39.90
2	96.00	43.85	70.59	15.04	0.00656	38.41
3	67.67	4.35	84.99	46.00	0.00569	45.10
4	85.15	46.00	73.62	12.74	0.00635	35.20
5	59.24	27.39	93.75	6.94	0.00255	40.11
6	63.90	28.14	91.20	7.98	0.00315	33.94
7	96.00	4.00	67.02	32.88	0.00305	40.92
8	96.00	6.49	66.05	31.64	0.00286	39.11
9	82.35	4.00	91.88	19.27	0.00209	18.00
10	96.00	22.72	54.00	27.39	0.00311	42.26
11	96.00	19.21	60.29	27.56	0.00301	36.68
12	76.27	5.40	96.00	37.39	0.00318	37.58
13	85.93	4.00	71.79	27.90	0.00346	27.77

14	54.00	46.00	62.63	25.34	0.07214	22.39
15	96.00	6.53	84.58	23.02	0.00249	20.06
16	87.22	6.04	86.09	22.93	0.00256	16.93
17	61.31	4.00	76.80	42.62	0.00410	41.62
18	59.60	4.00	77.62	41.94	0.00406	42.00
19	54.00	45.94	54.42	19.86	0.04015	26.09
20	54.00	14.47	96.00	9.71	0.00165	42.27
21	82.52	4.00	96.00	30.18	0.00289	29.45
22	55.10	6.16	93.72	13.94	0.00166	39.39
23	54.00	46.00	64.24	26.85	0.09402	21.71
24	56.11	5.44	88.18	12.34	0.00164	32.80

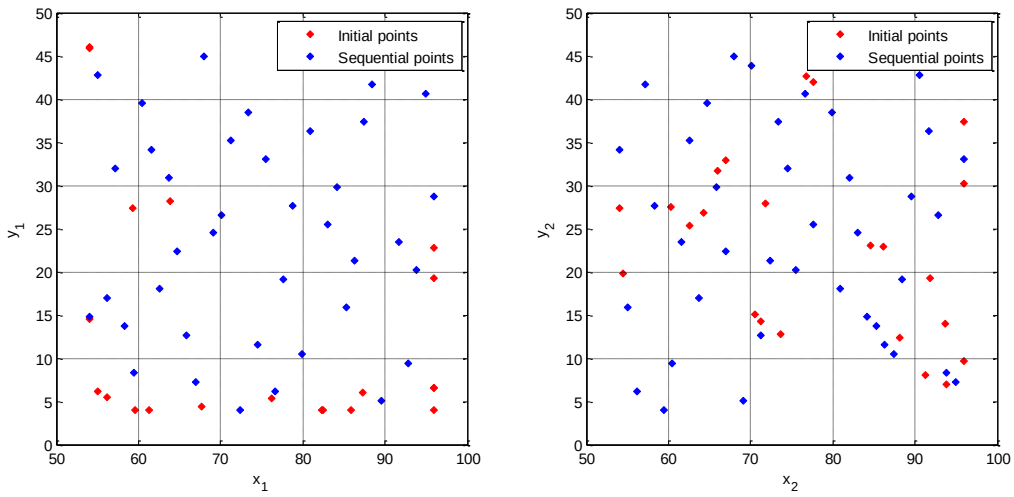

Fig. 5.11 Distribution of DoE points.

Table 5.1 lists the initial DoE sample points generated using OLHS, and its size is chosen 10 times the number of the variables (i.e. 40). Fig. 5.11 displays the distribution of the sample points over the design space. From which, it is easily found that the initial DoE points are generated evenly. Therefore, these sample points can extract the overall

trend of the objective and lay a foundation for obtaining a global optimum in the subsequent optimisation process.

From Table 5.1, 7 points violate the distance constraint and thus are not further submitted to the analyzer (ANSYS) for calculating stress and strain states. After generating the initial DoE points, the iterations of sequential sampling begin to work according to Fig.1, and the majority of the newly points are located on the boundary of the design space as shown in Fig. 5.11. This is because large prediction uncertainties existing in those areas, and adding sample points there can effectively enhance the expected improvement. Finally, after 12 iterations the process becomes converged. Table 5.2 provides the iteration history of the sequential sampling, where the constraint is actually inactive during the whole iterations and the objective has a lower average value compared to that of the initial samples.

Overall, the FEA is executed 57 times for yielding the global optimum in our proposed optimisation process. The resulting maximum principal strain is reduced significantly compared to the initial design (as listed in Table 5.3), which indicates the fatigue life can be improved considerably through optimisation. Besides, the optimal locations are fairly different from the initial, signifying the importance of optimisation. The first spot weld moves to one corner of the overlapping square area of sheets, and the second one also moves to the boundary of this area.

To validate the effectiveness of our proposed method, the conventional optimisations directly coupling with FEA model were also done and the results are also list in Table 5.3, where the Nelder-Mead simplex method and sequential quadratic programming (SQP) were adapted for comparison. It is known that the selection of starting point can affect the

optimisation results when using the two algorithms. Because the objective is a complex function of spot weld positions, it is difficult to choose the starting point according to the engineering experience. Thus, the initial design is used as the starting point for both Nelder-Mead method and SQP. From Table 5.3, we can see both the two directly coupling methods converge to local minima near the initial design, although SQP calls fewer FEA than SKO. They might be able to find a global optimum by executing the algorithms many times starting from different initial points. However, it will definitely increase the computational time and cost significantly. On the other hand, our proposed method enables to find more optimal locations for spot welds in terms of the fatigue life with a relatively low computational burden.

Table 5.3 Initial design, optimum obtained from SKO and comparison with other methods.

	Initial design	SKO	Simplex	SQP
x_1	67.00	55.10	63.45	67.21
y_1	25.00	6.16	28.53	25.12
x_2	84.00	93.72	86.53	84.44
y_2	25.00	13.94	44.65	25.11
ε_1	0.0396	0.00165	0.0262	0.0251
No. of FEA	-	57	79	34

5.3 AAMO-AASO based optimisation for foam-filled bitubal structures

Here we construct accurate Kriging models using the combined AASO-AAMO method and conduct multiobjective optimisation for a foam-filled bitubal structure.

5.3.1 Finite element modeling

The structure analyzed herein is a foam-filled thin-walled cylindrical tube subjected to an axial impact loading (Fig. 5.12). The bitubal arrangement, consisting of outer and inner walls with foam filler in between, is adopted in the tube. The length of the tube is 250 mm, the diameters of outer and inner tubes are 50 mm and 25 mm respectively. The foam-filled tube impacts onto the rigid wall at an initial velocity of v=15 m/s. To generate sufficient kinetic energy similarly to vehicle crashing, an additional mass block of 400kg is attached to the top free end.

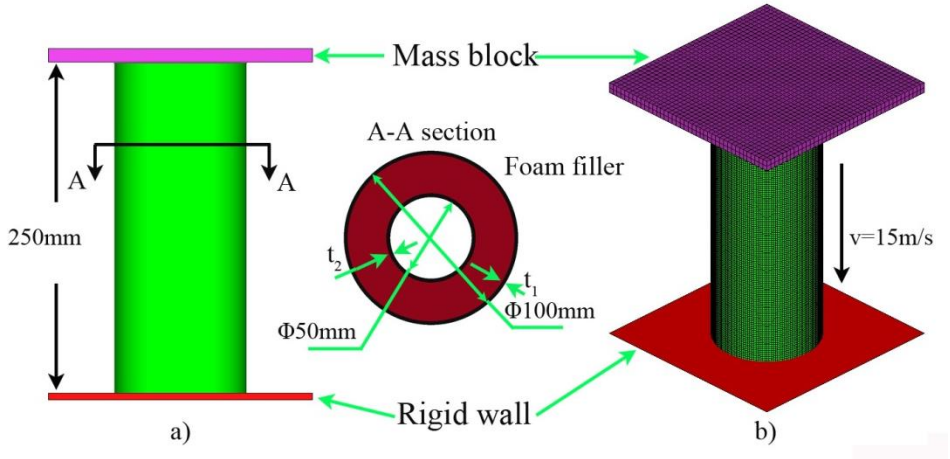

Fig. 5.12 Bitubal tube with foam-filler: (a) Schematic (b) Finite element model.

Table 5.4 Strain hardening data for AA6060-T4 [114].

Plastic strain (%)	plastic stress (MPa)
0.0	80
2.4	115
4.9	139
7.4	150
9.9	158

12.4	167
14.9	171
17.4	173

The tube was modeled through a piecewise linear elastic-plastic behavior with strain hardening (material model 24 in LS-DYNA). The thin wall material is aluminum alloy AA6060-T4 with the following mechanical properties: density =2700 kg/m^3, Poisson's ratio =0.3, Young's modulus =68.2 GPa, and initial yielding stress =80 MPa [114]. To accurately define the hardening characteristic in the FE model, the pairs of the plastic strain and true stress were specified as in Table 5.4 [114]. As the aluminum is insensitive to the strain rate, the rate-dependent effect was neglected in the FE modeling. The other details about finite element modelling can be found in [245].

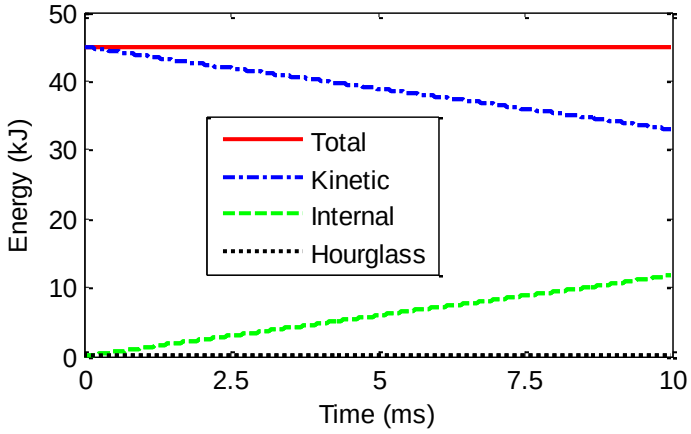

Fig. 5.13 Kinetic, internal, total and hourglass energy of the foam-filled tube (t_1= 0.8 mm, t_2= 1.5mm, ρ_f = 0.42 g/cm^3)

After a convergence study, mesh sizes 2×2 mm^2 and 2.5×2.5×2.5 mm^3 are determined for the tubes and foam are, respectively. Fig. 5.13 plots the kinetic, internal,

total and hourglass energies during the crashing process of a foam-filled tube under dynamic loading. It is easily seen that the decrease in kinetic energy is almost equal to the increase in internal energy, and the total energy remains nearly unchanged. The hourglass energy is less than 1% of the system internal energy. Note that the amount of hourglass energy is also a good indicator to the estimation of mesh quality, which typically should be less than 5% of the internal energy of the system to overcome the hourglass problem [246]. Therefore, the mesh size used here is considered adequate to capture the crashing details of the foam filled thin-walled tube.

In addition to the above-mentioned energy evaluation, the FE modeling approach is further validated by comparing the FEA results with the experimental data in the literature. The compressive test results of foam-filled cylindrical double tubes were reported in [247]. To use the same testing conditions given in the reference, the foam-filled structure is modelled as the length of 90 mm, sectional diameters of the outer and inner tubes are 38 mm and 22 mm, respectively; and the thicknesses are 1.6 mm and 1.4 mm respectively. The correlation results are summarized in Table 5.5. It is seen that all the simulation results agree well with the corresponding experimental results [247]. From the comparisons, the numerical modelling technique adopted here is considered accurate and effective for the subsequent design optimisation.

Table 5.5 Result comparisons between simulations and physical tests.

	Simulation	Experiment	Difference
Specific energy absorption	16.7 J/g	17.0 J/g	-1.76%
Deformation distance	53.6 mm	50.4 mm	6.35%

5.3.2 Definition of optimisation problem

In this study, we aim to maximize *SEA* and simultaneously minimize F_{max} while constraining F_{avg} no lower than a predefined level. The outer wall thickness t_1, inner wall thickness t_2 and foam density ρ_f are taken as the design variables, which range from 0.6 to 3.0 mm, from 0.6 to 3.0 mm and from 0.2 to 0.6 g/cm^3, respectively.

The MOO problem can be formulated mathematically as follows:

$$\begin{cases} \min & \{-SEA,\ F_{max}\} \\ s.t. & F_{avg} \geq 85 \text{ kN} \\ & 0.6 \text{ mm} \leq t_1, t_2 \leq 2.0 \text{ mm} \\ & 0.2\text{g/cm}^3 \leq \rho_f \leq 0.6\text{g/cm}^3 \end{cases} \tag{5.7}$$

Its corresponding two single optimisations used in AASO can be respectively defined as follows.

(1) SEA maximization:

$$\begin{cases} \min & -SEA \\ s.t. & F_{avg} \geq 85 \text{ kN} \\ & 0.6 \text{ mm} \leq t_1, t_2 \leq 2.0 \text{ mm} \\ & 0.2\text{g/cm}^3 \leq \rho_f \leq 0.6\text{g/cm}^3 \end{cases} \tag{5.8}$$

(2) F_{max} minimization:

$$\begin{cases} \min & F_{max} \\ s.t. & F_{avg} \geq 85 \text{ kN} \\ & 0.6 \text{ mm} \leq t_1, t_2 \leq 2.0 \text{ mm} \\ & 0.2\text{g/cm}^3 \leq \rho_f \leq 0.6\text{g/cm}^3 \end{cases} \tag{5.9}$$

5.3.3 Results and discussions

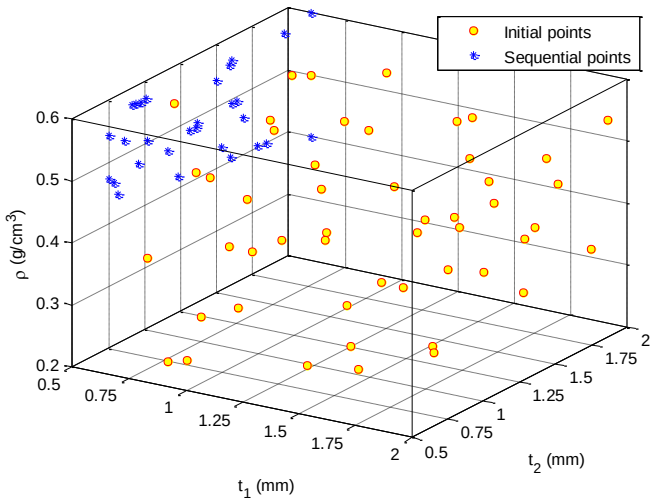

Fig. 5.14 Training points.

In this paper, the optimal Latin Hypercube sampling (OLHS) is implemented to generate initial sample data. Then, the combined AASO-AAMO is used to sequentially update the Kriging models until the deterministic Pareto frontier becomes stable.

Table 5.6 Design matrix for initial sample points.

No.	t_1 (mm)	t_2 (mm)	ρ (g/cm^3)	F_{max} (kN)	*SEA* (J/g)	F_{avg} (kN)
1	0.60	1.20	0.44	108.76	13.66	82.66
2	0.63	1.00	0.58	236.01	19.70	151.61
4	0.69	1.09	0.22	37.02	7.71	29.81
5	0.71	1.83	0.53	196.42	17.64	140.29
6	0.74	1.34	0.39	89.97	12.12	70.78
7	0.77	0.74	0.20	31.55	6.59	22.99
8	0.80	1.71	0.40	104.76	13.09	84.29
9	0.83	0.94	0.48	138.24	14.64	97.77

No.	t_1 (mm)	t_2 (mm)	ρ (g/cm^3)	F_{max} (kN)	*SEA* (J/g)	F_{avg} (kN)
10	0.86	1.46	0.58	247.52	19.72	171.34
11	0.89	1.14	0.34	70.21	10.48	56.38
12	0.91	1.23	0.54	201.39	17.52	138.94
13	0.94	0.60	0.23	39.52	7.29	28.83
14	0.97	0.91	0.28	56.98	8.82	41.69
15	1.00	1.77	0.47	157.82	14.86	113.11
16	1.03	1.43	0.35	82.94	11.13	66.03
17	1.06	1.51	0.52	192.40	16.46	133.55
18	1.09	0.66	0.42	102.27	12.21	75.50
19	1.11	1.69	0.24	66.13	9.69	50.04
20	1.14	1.94	0.31	92.63	11.23	69.50
21	1.17	1.63	0.59	274.51	19.61	187.67
22	1.20	0.80	0.60	265.80	19.63	174.00
23	1.23	1.26	0.27	68.29	9.29	48.73
24	1.26	1.06	0.40	97.61	11.87	77.49
25	1.29	0.89	0.22	56.85	8.06	36.67
26	1.31	2.00	0.49	169.37	15.29	131.50
27	1.34	0.63	0.45	126.77	13.20	91.78
28	1.37	0.86	0.51	182.67	15.25	120.79
29	1.40	1.74	0.36	106.97	11.94	83.38
30	1.43	0.97	0.25	69.45	8.87	45.80
31	1.46	1.29	0.31	87.70	10.32	62.60

No.	t_1 (mm)	t_2 (mm)	ρ (g/cm^3)	F_{max} (kN)	*SEA* (J/g)	F_{avg} (kN)
32	1.49	1.80	0.27	93.11	10.72	66.50
33	1.51	1.60	0.37	109.51	12.06	86.15
34	1.54	1.37	0.21	75.80	9.25	48.56
35	1.57	1.49	0.56	232.06	17.52	168.69
36	1.60	1.91	0.32	109.77	11.59	81.29
37	1.63	0.71	0.26	73.28	9.01	48.21
38	1.66	1.57	0.46	168.53	14.17	119.98
39	1.69	1.03	0.45	141.00	13.24	103.42
40	1.71	1.97	0.41	153.08	13.28	110.50
41	1.74	1.31	0.54	240.25	16.37	153.77
42	1.77	1.11	0.38	115.61	11.74	85.05
43	1.80	0.69	0.57	252.51	17.19	160.46
44	1.83	1.54	0.30	105.80	10.92	74.37
45	1.86	1.66	0.50	200.30	15.35	145.57
46	1.89	0.83	0.29	93.36	10.03	62.31
47	1.91	1.89	0.33	124.08	11.90	90.79
48	1.94	1.17	0.49	177.92	14.73	132.93
49	1.97	1.40	0.43	141.41	13.20	111.53
50	2.00	1.86	0.55	254.48	16.94	181.69

Table 5.7 Design matrix for sequential sample points

Iteration		t_1 (mm)	t_2 (mm)	ρ (g/cm^3)	F_{max} (kN)	*SEA* (J/g)	F_{avg} (kN)
1	1	0.61	1.51	0.49	158.49	16.07	112.79
	2	0.60	1.48	0.52	168.61	17.19	125.95
	3	0.60	1.45	0.52	177.99	17.20	125.55
	4[a]	0.60	2.00	0.40	101.68	13.65	86.32
	5[b]	0.60	2.00	0.60	287.75	21.31	192.82
2	1	0.61	1.19	0.52	177.19	17.20	122.49
	2	0.60	1.16	0.51	156.37	16.45	113.20
	3	0.60	1.20	0.51	166.17	16.61	115.56
3	1	0.62	1.41	0.44	119.57	13.94	87.79
	2	0.61	1.36	0.46	127.13	14.71	95.67
	3	0.61	0.99	0.50	150.78	16.07	107.17
4	1	0.64	1.75	0.60	275.59	21.21	188.00
	2	0.61	1.67	0.43	126.01	14.07	90.57
	3	0.60	1.63	0.43	121.52	13.96	88.40
5	1	0.62	1.40	0.59	241.25	20.52	169.88
	2	0.60	1.45	0.59	256.93	20.67	171.88
	3	0.64	1.28	0.58	240.63	19.84	158.88
6	1	0.60	0.76	0.60	252.42	22.82	179.80
	2	0.61	0.80	0.60	268.89	22.84	181.38
	3	0.60	0.85	0.60	246.42	20.83	162.14
7	1	0.60	0.60	0.50	138.05	15.71	98.38

	2	0.61	0.64	0.47	116.72	14.19	83.78
	3	0.60	0.63	0.49	130.33	15.18	93.17
8	1	0.60	0.60	0.57	205.08	19.10	136.12
	2	0.60	0.70	0.55	179.30	17.98	124.71
	3	0.60	0.78	0.60	249.78	21.01	163.02
9	1	0.60	0.80	0.50	146.00	16.05	104.36
	2	0.60	0.86	0.53	178.59	17.36	119.91
	3	0.61	1.06	0.45	110.73	13.96	85.15

a, b: Sequential points by AASO

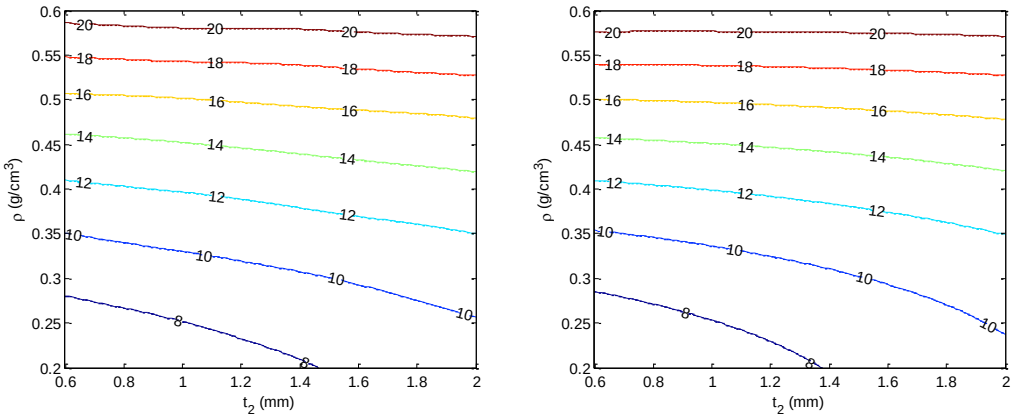

a) before combined AASO-AAMO b) after combined AASO-AAMO

Fig. 5.15 Contours of Kriging models for *SEA*.

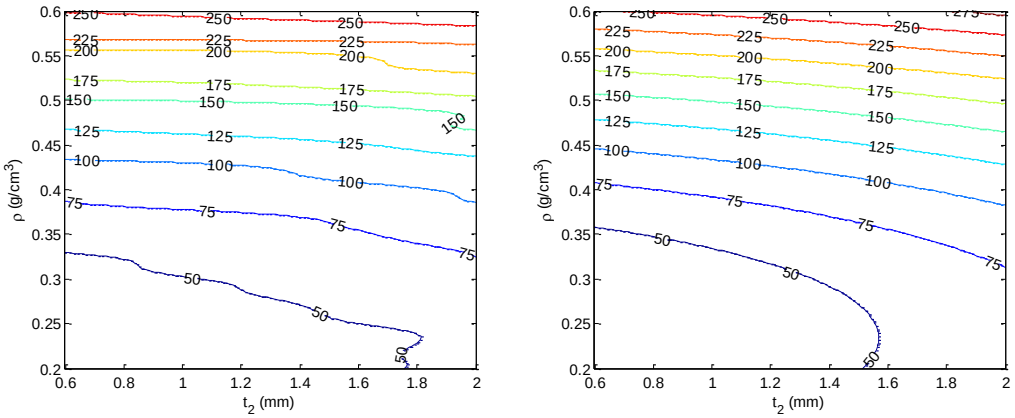

a) before combined AASO-AAMO b) after combined AASO-AAMO

Fig. 5.16 Contours of Kriging models for F_{max}.

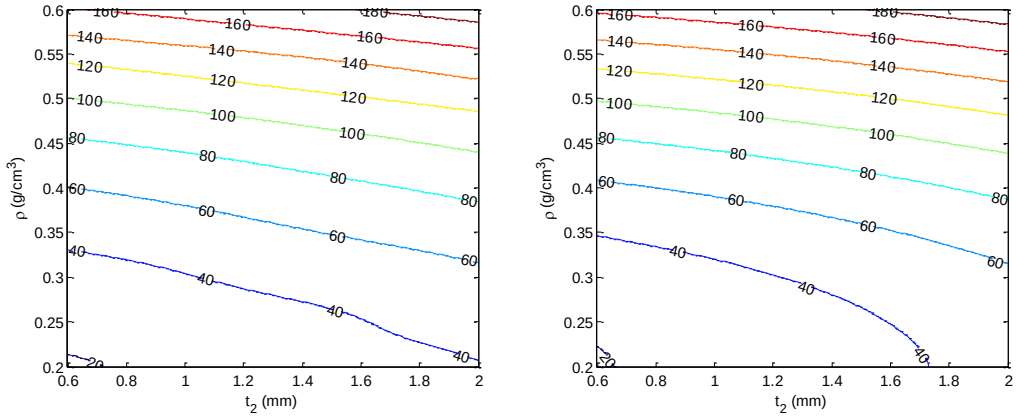

a) before combined AASO-AAMO b) after combined AASO-AAMO

Fig. 5.17 Contours of Kriging models for F_{avg}.

In this study, the sample size of the initial training points is 50. After 9 iterations of combined AASO-AAMO the Pareto frontier is found stable adequately, i.e. the decrease in the number of Pareto solutions through the Pareto optimality checking is lower than 5 (the total number of Pareto solutions is specified as 100) according to the convergence criteria of 5%. Fig. 5.14 exhibits the training points during the entire process including 50 initial points and 29 sequential points, and Tables 5.6 and 5.7 list the details of these

sample data. It can be found that OLHS tends to provide space-filling and uniformly distributed training points in the interior of the design domain. To contrast, all the 29 Pareto solutions generating during the iterations are located on the boundary of the design space representing the thinnest outer walls (i.e., t_1 = 0.6 mm). This is probably attributed to that the thinnest outer wall is capable of achieving the weakest peak impact force and simultaneously the highest energy absorption efficiency.

Figs. 5.15-5.17 depict the contours of the Kriging models before and after combined AASO-AAMO for *SEA*, F_{max} and F_{avg} respectively (when t_1= 0.6 mm). For F_{max}, the Kriging model changes significantly after iterations; whilst for *SEA* and F_{avg}, the Kriging models are refined relatively slightly. Besides, *SEA*, F_{max} and F_{avg} are more sensitive with respect to foam density (ρ_f) than inner wall thickness (t_2). More importantly, the two objectives *SEA* and F_{max} have almost the same trend (i.e., a larger *SEA* means a larger F_{max}), indicating the requirement of performing a multiobjective optimisation, where a larger *SEA* and smaller F_{max} are the target design.

Fig. 5.18 plots the comparison of the obtained Pareto frontiers before and after iterations (i.e., Iteration 0 and 9 respectively). After 9 iterations the Pareto frontier actually moves towards the origin in the objective space. This is because the updated accurate Kriging models yield true optimal solutions, which are even more competent than the results obtained from the initial Kriging models. Overall, by combined AASO-AAMO, the Kriging models are refitted repeatedly to achieve high accuracies.

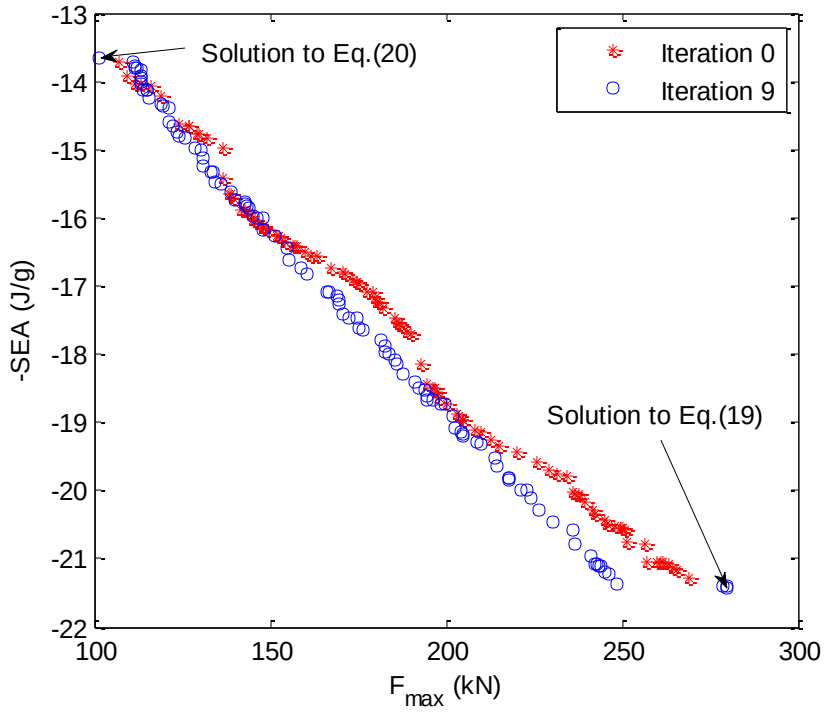

Fig. 5.18 Comparison of Pareto frontiers before and after combined AASO-AAMO.

5.4 Summary

As the conventional surrogate based optimisation largely depends on the number of initial sample data, sequential surrogate modeling was proposed to practical applications in automotive industry. (a) To maximize the fatigue life of spot-welded joints, an expected improvement based sequential surrogate modeling method was utilized. The results showed that by using this method the performance can be significantly improved with only a relatively small number of finite element analyses. (c) A multiojective sequential surrogate modeling method was proposed to address a multiobjective optimisation of a foam-filled double cylindrical structure. By adding the sequential points and updating the Kriging model adaptively, more accurate Pareto solutions are generated.

Chapter 6 Engineering optimisation under uncertainties

Most (if not all) real-life engineering problems involve some degree of uncertainties in loading conditions, material properties, geometries, manufacturing tolerances and actual usage, etc. It must be pointed out that usually a deterministic optimisation tends to push a design toward one or more constraints until the constraints become active, thereby leaving no room for accommodating various uncertainties. Therefore, reliability-based optimisation, which aims to seek a reliable optimum by converting the deterministic constraints into probabilistic counterparts representing that probability of failure is restricted to a pre-specified level, has been widely applied to engineering problems. As shown in Fig. 6.1a, let $\mathbf{x}_d$ represent the deterministic optimum and $\mathbf{x}_{re}$ represent the reliable optimum in the design space (x_1-x_2 space), which is divided into infeasible and feasible regions by the constraints. Since the deterministic optimum $\mathbf{x}_d$ is located on the boundary of the constraint, it may fall to the infeasible region when uncertainties present. On the other hand, the reliable optimum $\mathbf{x}_{re}$ moves away to create a gap from the boundary of the constraint so that it can still be within the feasible region when uncertainties present.

Moreover, traditional design likely leads to a large scatter of optimal performance to accommodate uncertainties, which may not only cause significant fluctuations from the desired performance, but also increase life-cycle costs, including inspection, repair and other maintenance expenses. Thus, the concept of robust design optimisation (RDO) is to reduce the scatter of the structural performance without eliminating the source of uncertain variability. This approach has drawn increasing attention for solving real-world

problems recently. As shown in Fig. 6.1b, let the x-axis represent the uncertain parameter, e.g. random design variable and other noise factors, and the vertical axis represents the value of an objective function $f(\mathbf{x})$ to be minimized. Of these two optimal solutions x_1 and x_2 as pointed, x_2 is considered more robust as a variation of $\pm\Delta\mathbf{x}$ in the design variable and/or noise factor does not alter the objective function too much ($\Delta f_{ro} << \Delta f_d$). On the contrary, $\mathbf{x}_d$ appears highly sensitive to the parametric perturbation and often cannot be recommended as a design in practice, even though it has a better nominal value than $\mathbf{x}_{ro}$. It is noted that a robust-based optimisation places more emphasis on the stability of the objective, while a reliability-based optimisation pays more attention to the feasibility of the constraint.

This chapter mainly introduces the uncertainty based optimisation methodologies and their applications in body structures. The results from different design cases will reveal the effect of the constraint reliability on the optimisation result, the effect of the objective robustness on the optimisation result and the decision-making method in the context of uncertainties.

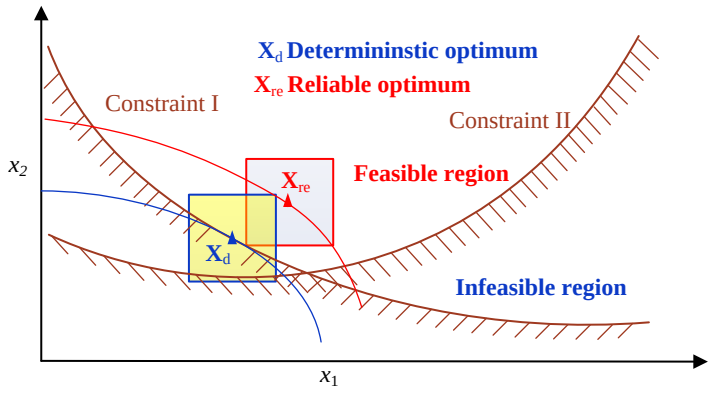

(a) Reliability based optimisation (RBO)

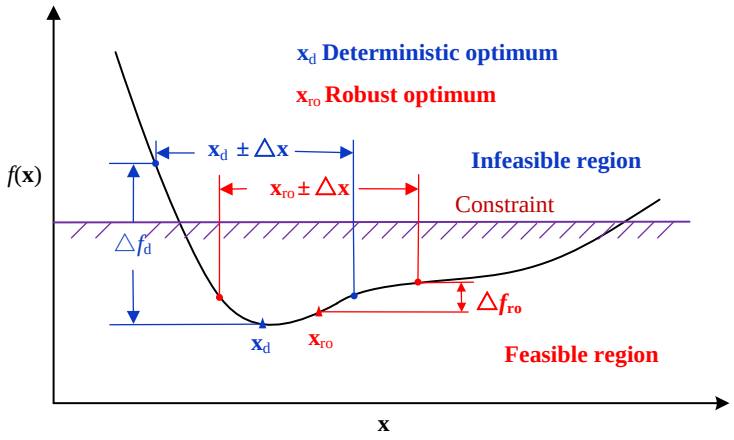

(b) Robust design optimisation (RDO)

Fig. 6.1 Illustrations of design optimisation with uncertainties (a) RBO and (b) RDO

6.1 Methodology of uncertainty based optimisation

6.1.1 Definition of uncertainty based optimisation

6.1.1.1 Reliability-based optimisation (RBO)

To create room for accommodating uncertainties, reliability-based optimisation (RBO) has been adopted in crashworthiness problems. A general RBO problem can be written as:

$$\begin{cases} \min \ \ f(\mathbf{x}) \\ s.t. \ \ P(\mathbf{g}(\mathbf{x}) \le 0) \ge R_t \\ \qquad \mathbf{x}_L \le \mathbf{x} \le \mathbf{x}_U \end{cases} \tag{6.1}$$

R_t denotes the reliability level and $P(\cdot)$ stands for the probability function.

6.1.1.2 Robust design optimisation (RDO)

It is commonly accepted that a robust design was firstly presented by Japanese engineer Genichi Taguchi, who developed the Taguchi method to improve the quality of manufactured goods and makes the product performance less sensitive to variations of variables beyond the control of designers. A general RDO problem can be formulated mathematically as:

$$\begin{cases} \min & F\left(\mu_f(\mathbf{x}), \sigma_f(\mathbf{x})\right) \\ s.t. & g(\mathbf{x}) \le 0 \\ & \mathbf{x}^L \le \mathbf{x} \le \mathbf{x}^U \end{cases} \tag{6.2}$$

where $\mu_f(\mathbf{x})$ and $\sigma_f(\mathbf{x})$ are the mean and standard deviation of the objective, respectively.

6.1.1.3 Reliability-based robust design optimisation (RBRDO)

To enhance the design in both reliability and robustness, RBO and RDO can be combined and referred to as reliability-based robust design optimisation (RBRDO), which can be formulated as:

$$\begin{cases} \min & F\left(\mu_f(\mathbf{x}), \sigma_f(\mathbf{x})\right) \\ s.t. & P(g(\mathbf{x}) \le 0) \ge R_t \\ & \mathbf{x}^L \le \mathbf{x} \le \mathbf{x}^U \end{cases} \tag{6.3}$$

6.1.2 Uncertainty quantification

6.1.2.1 Monte Carlo simulation

The problems defined in Eqs. (22)-(25) involve a procedure to obtain the values of probabilistic objective and constraint. One of the robust yet simple approaches could be Monte Carlo simulation (MCS). Based on the theory of large numbers, the Monte Carlo simulation allows determining an estimate of the probability of success as follows,

$$P(g(\mathbf{x}) \le 0) = \frac{1}{Q}\sum_{i=1}^{Q} I(\mathbf{x}) \tag{6.4}$$

where Q is the total number of MCS and $I(\mathbf{x})$ is an indicator function defined as

$$I(\mathbf{x}) = \begin{cases} 1 & if\ g(\mathbf{x}) \le 0 \\ 0 & if\ g(\mathbf{x}) > 0 \end{cases} \tag{6.5}$$

Note that in Eq. (6.4), Q independent sets of design variables are obtained from sampling techniques on the basis of the probability distribution for each random variable. Thus, MCS is also referred to as sampling-based method [248]. MCS is also a conventional method of quantifying robustness, allowing determining the means and standard deviations of objectives in Eqs. (23)- (25).

$$\begin{cases} \mu_f(\mathbf{x}) \cong \dfrac{\sum_{i=1}^{N} f(\mathbf{x}_i)}{N} \\ \sigma_f^2(\mathbf{x}) \cong \dfrac{1}{N-1}\sum_{i=1}^{N}\left(f(\mathbf{x}_i) - \mu_f(\mathbf{x})\right)^2 \end{cases} \tag{6.6}$$

If the $\mathbf{x}_i$ is independent, the laws of large numbers allow us to achieve any degree of accuracy by increasing Q. The error of estimating the nominal value is a random variable with standard deviation of

$$err = \frac{\sigma_f(\mathbf{x})}{\sqrt{Q}} \tag{6.7}$$

The error is, therefore, unrelated to the problem dimension (i.e., the number of design variables), which is very appealing for large-scale problems. And it is proportional to $1/\sqrt{Q}$, which means that the improvement of accuracy by one order will require 100 times more samples. This expensive computation is prohibitive in the application for complex and highliy nonlinear problems.

On the other hand, the minimum sampling size required for the desired reliability level R_t as suggested by Tu and Choi [249] is:

$$Q = 1/(1-R_t) \tag{6.8}$$

The above equation indicates that for a 10% estimated probability of failure; about 100 structural evaluations are required with some confidence on the first digit of failure prediction. To verify an event having a 1% failure probability; about a 1000 structural analyses are required, which usually would also be too expensive.

To apply MCS to crashworthiness optimisation, the use of metamodels has been advocated by many researchers (e.g., [33, 37, 48, 245, 250-253]). The metamodeling approach makes it possible to evaluate function values a very large number (millions) of times around each design point at a relatively low computational cost.

6.1.2.2 Dual response surface methodology (DRSM)

Following Vining et al.'s work [254], dual response surface models (DRSM) have been used in crashworthiness (e.g., [47, 49]) in which two response surfaces are created, one for the mean and another for the variance or standard deviation of a response. Two types

of variables are considered in such a system: design (controllable) variables and noise (uncontrollable) variables. For constructing DRSM, the cross product array (Table 6.1) needs to be generated, where design variables are arranged in an inner array while random variables in an outer array. In each set of design variables, the simulation is repeated several times to capture the mean and standard deviation. Then, they are approximated as the functions with respect to the design variables using metamodeling techniques, which can be used in the optimisation.

Table 6.1 Cross product array

				Outer array (ramdom variables)				
				z_1	-1	-1	-1	-1
				z_2	-1	-1	1	1
Inner	x_1	x_2	x_3	z_3	-1	1	-1	1
array	-1	-1	-1		y_{11}	y_{12}	y_{13}	y_{14}
(design	-1	0	0		y_{11}	y_{12}	y_{13}	y_{14}
variables)	-1	1	1		⋮	⋮	⋮	⋮
	0	-1	0		⋮	⋮	⋮	⋮
	0	0	1		⋮	⋮	⋮	⋮
	0	1	-1		⋮	⋮	⋮	⋮
	1	-1	1		y_{71}	y_{72}	y_{73}	y_{74}

6.2 Reliability-based optimisation for a vehicle door

As an indispensable assembly of an automotive body, the door serves as a key

supporting component for functional accessories and sound insulation in occupant compartment. Poor performances of a door will lead to lots of functional problems such as bad sealing, abnormal sounds and severe intrusion in crashing. Consequently, structural design and optimisation of a vehicle door have become one of the major concerns in the automotive industry. For example, Shin et al. [255] presented a design procedure by integrating topology, shape and size optimisation and design of experiments to develop door structure with better performances in terms of stiffness and natural frequency. Song and Park [256] exploited multi-disciplinary optimisation (MDO) to include various disciplinary analyses with a weight reduction of a door by using a tailored blank. Lee and Kang [257] combined the Kriging interpolation method with a simulated annealing algorithm to the design of a frontal door. Zhu et al. [132] presented an integrated approach using finite element analysis, an artificial neural network, and a genetic algorithm for the optimal design of an inner door panel. Cui et al. [258] adopted a multi-material configuration in the lightweight design by combining a multiobjective genetic algorithm with an artificial neural network.

These above-mentioned studies on structural optimisation for a vehicle door are restricted to deterministic optimisation, in which all design variables and parameters involved are regarded certain. Nevertheless, structural optimisation for a vehicle door considering the uncertainty has received limited attention in the literature.

6.2.1 Finite element modeling

As a critical and independent component assembled to the vehicle body, the door structure requires a high stiffness to carry out its functions. Similarly to the literature [5], the finite element analysis (FEA) models of a vehicle door, subjected to three load

conditions, were established as illustrated in Fig. 6.2. The finite element models are established to run using the commercial FEA code MSC.NASTRAN. The panels are modeled with CQUAD and CTRIA surface element. The panel materials are assigned steel, which is modeled with a linear elastic material model MAT1. For connection, PSOLID and CWELD elements are used to model the glue and weld spots, respectively. The entire FEA model has 89,043 elements and 546,912 degrees of freedom. For both upper and lower lateral stiffness, as shown in Fig. 6.2(a) and (b), the hinges are fully restrained except for roll rotation and the latch is fully restrained, and at the same time two y-directional forces (F_1 = F_2 = 200 N) are applied to the lower and upper location respectively. For vertical sag stiffness, as shown in Fig. 6.2(c), the hinges are fully restrained except for roll rotation and a vertical force (F_3 = 750 N) is applied at the latch that is fixed in the lateral translation. The stiffness is evaluated in terms of the displacements at the loading point, using finite element method. In addition, load condition 4 is defined to perform modal analysis with the free-free boundary condition to calculate the door's first natural frequency.

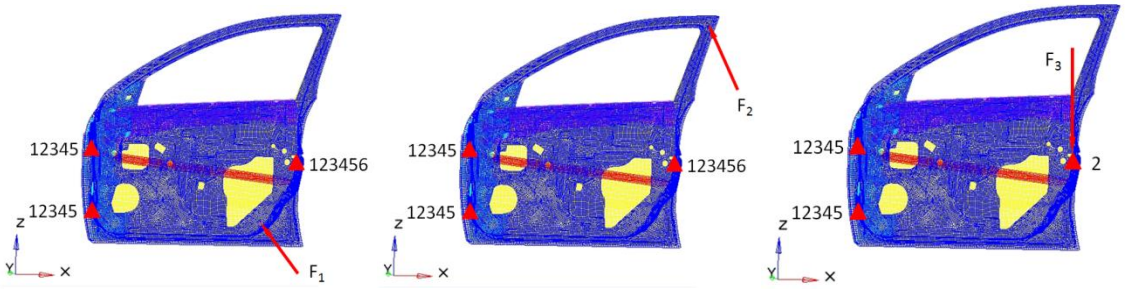

(a) lower lateral (b) upper lateral (c) vertical sag

Fig. 6.2 Loading conditions for stiffness analyses of the vehicle door structure

Although computer aided engineering allows promoting the development of a vehicle door to a considerable extent, the numerical models still need to be verified before making use of them. In this regard, it is critical to validate the simulation results by using some physical tests prior to an effective design optimisation. In this study, the validation of FEA model was conducted by comparing the simulation results with the corresponding experimental results. Fig. 6.3 shows the setups of physical tests, whose four loading conditions are identical to the simulations. The correlation results are summarized in Table 6.2. It is found that all the results of the simulations agree very well with the corresponding experimental results. As a result, the FE models are considered accurate and effective for the subsequent design optimisation.

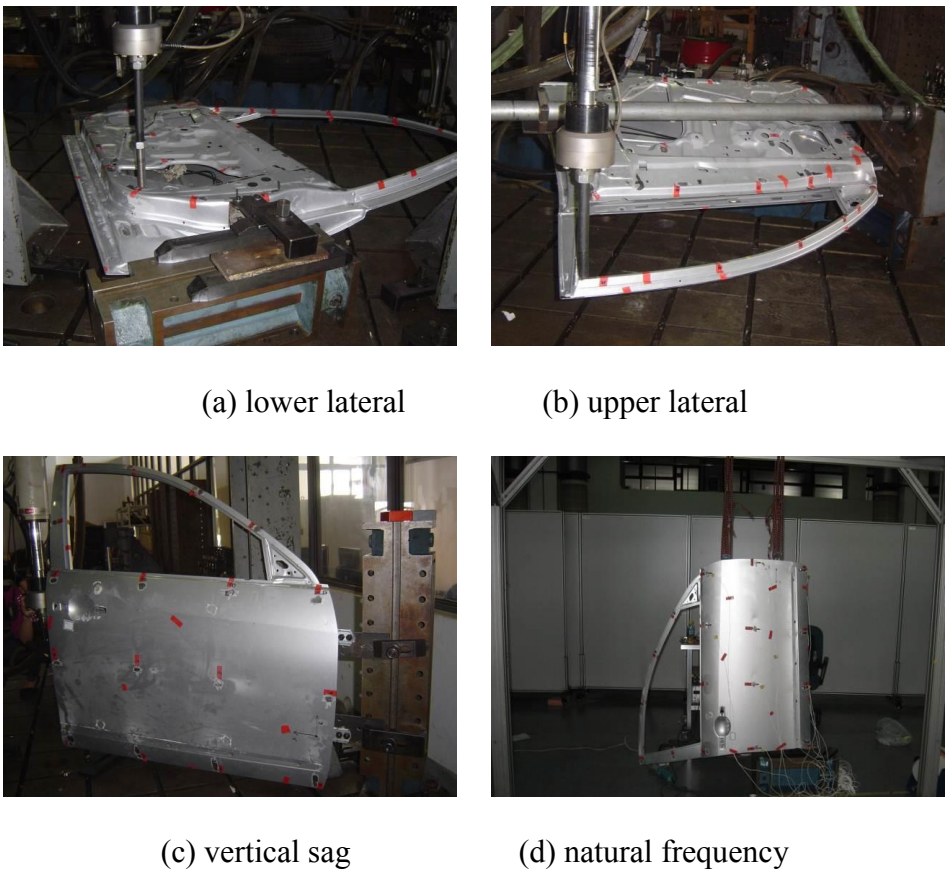

(a) lower lateral (b) upper lateral

(c) vertical sag (d) natural frequency

Fig. 6.3 Experimental tests of the door stiffness

Table 6.2 Result comparison between simulations and physical tests

	Simulation	*Experiment*	*Difference*
mass $f_1(\mathbf{x})$	22.13 kg	22.20 kg	-0.32%
vertical sag $f_2(\mathbf{x})$	4.49 mm	4.53 mm	-0.88%
natural frequency $g_1(\mathbf{x})$	40.45 Hz	40.71 Hz	-0.64%
upper lateral $g_2(\mathbf{x})$	2.86 mm	2.83 mm	1.06%
lower lateral $g_3(\mathbf{x})$	1.67 mm	1.68 mm	-0.60%

6.2.2 Definition of optimisation problem

6.2.2.1 Probabilistic sufficiency factor

In this study, two sets of response surfaces are established, which are referred to the analysis response surface (ARS) and design response surface (DRS), respectively [259]. ARS can replace the FE simulations of the door stiffness for optimisation. Despite the use of ARS, the evaluation of the probabilistic constraint is still computationally costly during the optimisation process. Thus, DRS is established to approximate the probabilistic constraint PSF which is obtained from MCS based on ARS at each DoE sampling point. The probability of success ($P(g_j(\mathbf{x}) \le 0)$ as defined by Eq. (6.1)) is not a unique form of probabilistic constraints and can be transformed into other forms, such as reliability index and probabilistic sufficiency factor (PSF) [259, 260]. It has proven that PSF has a higher accuracy for establishing design response surface (DRS).

The constraints of any deterministic design optimisation can be typically expressed as,

$$\begin{cases} g(\mathbf{x}) \le 0 \\ g(\mathbf{x}) = g_r(\mathbf{x}) - g_t(\mathbf{x}) \end{cases} \tag{6.9}$$

where $g_r(\mathbf{x})$ and $g_t(\mathbf{x})$ represent the response and corresponding target (upper limit), respectively.

In deterministic optimisation, the constraint can be reformulated as $s(\mathbf{x}) \geq 1$, where $s(\mathbf{x})$ denotes the safety factor defined as,

$$s(\mathbf{x}) = s_L(\mathbf{x}) = \frac{g_t(\mathbf{x})}{g_r(\mathbf{x})} \tag{6.10}$$

In this study, for the upper lateral stiffness of the vehicle door, the displacement at the loading point has an upper limit of 2.86 mm, if the corresponding value of a design is 2.90 mm, then the safety factor is 0.986 (=2.86/2.90).

For an optimisation problem with a lower limit, the safety factor can be defined as,

$$s(\mathbf{x}) = s_U(\mathbf{x}) = \frac{g_r(\mathbf{x})}{g_t(\mathbf{x})} \tag{6.11}$$

In this study, the first natural frequency of the vehicle door has a lower limit of 40.45 Hz, if the corresponding value of a design is 41.00 Hz, then the safety factor is 1.014 (= 41.00/40.45).

In RBDO, the corresponding constraint can be transformed into the probabilistic expression as:

$$P(s(\mathbf{x}) \geq 1) \geq R_t \tag{6.12}$$

Probabilistic sufficiency factor can be thus defined as the value of the safety factor that has a reliability level of R, and it is the solution to

$$P(s(\mathbf{x}) \geq PSF) = R_t \tag{6.13}$$

PSF can be easily calculated using MCS. The safety factors for the Q samplings are ranked in an ascending order and have such a sequence as $\{s_1, s_2, ..., s_N\}$, $s_m < s_{m+1}$. Then, the PSF can be obtained from Eq. (6.14).

$$PSF = s_k \tag{6.14}$$

where $Q(1-R)-1 < k \le Q(1-R)$.

When the optimisation problem has multiple (p) constraints, the most critical safety constraint is calculated as PSF:

$$PSF = \min_{j=1}^{p}(s_{k,j}) \tag{6.15}$$

Note that $PSF \ge 1$ means that the reliability level is equal to or higher than the target and thus the design meets or exceeds the prescribed safety requirement. Therefore, it can replace the constraints in Eq. (6.1).

6.2.2.2 Optimisation procedure

Of all the stiffness indices, vertical sag stiffness can largely influence operation condition of door's opening and closing, and thus, it is closely relevant to customers' subjective perception towards the product quality. Therefore, the vertical sag stiffness is maximized and at the same time, the structural mass is minimized, while maintaining certain levels of other stiffness indices. The multiobjective optimisation problem for door structure is thus more specifically formulated as a standard form in terms of design variables, objectives, and constraints as follows:

$$\begin{cases} \min & F(\mathbf{x}) = \left[f_1(\mathbf{x}),\, f_2(\mathbf{x}) \right] \\ s.t. & \begin{cases} g_1(\mathbf{x}) \ge 40.45 \\ g_2(\mathbf{x}) \le 2.86 \\ g_3(\mathbf{x}) \le 1.67 \\ \mathbf{x}^L \le \mathbf{x} \le \mathbf{x}^U \end{cases} \end{cases} \tag{6.16}$$

The reliability-based optimisation problem can be defined by converting the deterministic constraints into $PSF \ge 1$:

$$\begin{cases} Min & F(\mathbf{x}) = [\, f_1(\mathbf{x}),\, f_2(\mathbf{x})] \\ s.t. & \begin{cases} PSF \geq 1 \\ \mathbf{x}^L \leq \mathbf{x} \leq \mathbf{x}^U \end{cases} \end{cases} \tag{6.17}$$

In this study, thicknesses of six panels in Fig. 6.4 are selected as the designs variables. It is assumed that variations of these designs variables are normally distributed [261, 262] and their ranges and coefficients of variation (CoVs) are listed in Table 6.3. The whole procedure of the door design is summarized in Fig. 6.5.

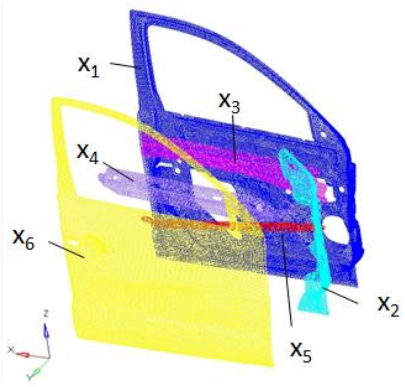

Fig. 6.4 Design variables

Table 6.3 Variable information

Design variables	Upper bounds	Lower bounds	CoVs
Inner panel (x_1)	0.7 mm	1.5 mm	0.03
Hinge reinforcement (x_2)	0.7 mm	1.5 mm	0.03
Inner reinforcement (x_3)	0.7 mm	1.5 mm	0.03
Outer reinforcement (x_4)	0.7 mm	1.5 mm	0.03
Side impact beam (x_5)	0.7 mm	1.5 mm	0.03
Outer panel (x_6)	0.7 mm	1.5 mm	0.03

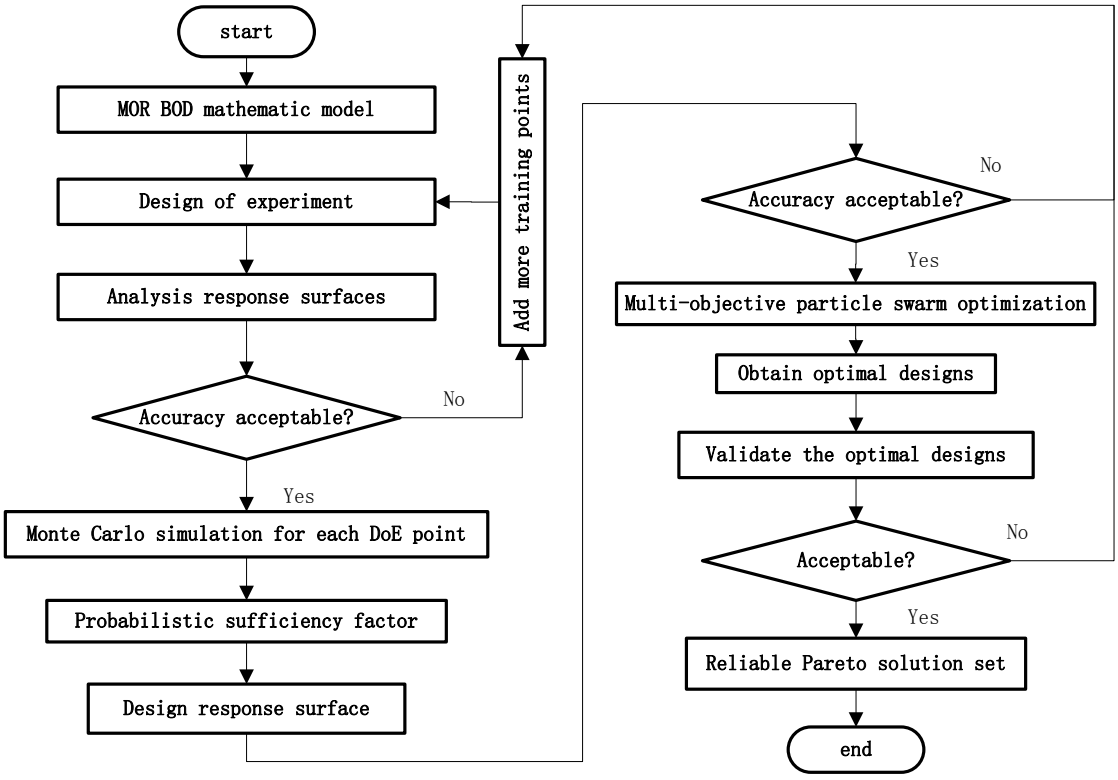

Fig. 6.5 Flowchart of the optimisation procedure for a vehicle door

6.2.3 Results and discussion

6.2.3.1 Results of MORBDO

Since the mass of the door has a linear relationship of the panel thicknesses, the first-order polynomial response surface is employed to model it. For the stiffness indices, polynomial response surface models will be used by comparing the modeling accuracy. Regarding the sample size of training points, Kaufman et al. [263] found 1.5 times of the number of the model coefficients, which means 42 training points in this study, are needed to obtain reasonably accurate quadratic polynomial surface models for 5-variable problems. Thus, a total of 50 training points is generated using the OLHS technique to construct the ARS. Additional 10 validation points are used to assess the accuracy of the

metamodels constructed. The assessments of the accuracy are summarized in Table 6.4. It shows that no single response surface model is suitable for all of the stiffness indices. The quadratic response surface models are considered most suitable for the first natural frequency and vertical sag stiffness, whilst the cubic and quartic response surface models are chosen for lower and upper lateral stiffness, respectively.

Table 6.4 Accuracy assessment for different polynomial response surfaces

responses	*order*	R^2	*RAAE*	*RMAE*
natural frequency	Linear	0.9886	0.0893	0.2594
	Quadratic	**0.9995**	0.0163	**0.0460**
	Cubic	0.9995	**0.0154**	0.0536
	Quartic	0.9991	0.0238	0.0633
vertical sag	Linear	0.8746	0.2468	1.4272
	Quadratic	**0.9821**	**0.0967**	0.4976
	Cubic	0.9774	0.1209	**0.4197**
	Quartic	0.9596	0.1610	0.4670
upper lateral	Linear	0.9459	0.1868	0.7627
	Quadratic	0.9962	0.0475	0.2183
	Cubic	0.9990	0.0239	0.0998
	Quartic	**0.9993**	**0.0236**	**0.0565**
lower lateral	Linear	0.9663	0.1491	0.5527
	Quadratic	0.9980	0.0362	0.1326
	Cubic	**0.9995**	**0.0176**	**0.0473**
	Quartic	0.9995	0.0197	0.0484

PSF	Linear	0.9981	0.0368	0.1032
	Quadratic	**0.9985**	**0.0317**	**0.0821**
	Cubic	0.9981	0.0353	0.1063
	Quartic	0.9981	0.0368	0.1032

Using the MCS integrated with descriptive sampling technique, the value of PSF at each DoE sampling point can be attained. In this paper, the sample size of descriptive sampling is chosen a value of 1000, 5000 and 10000 respectively. It is found that the values of PSF for 5000 and 10000 descriptive samples are practically the same. Therefore, 10000 samples are regarded adequate for calculating PSF. Following the PSF sampling, the DRS of PSF is established and its accuracy assessment result is also shown in Table 6.4. Apparently, the quadratic response surface model behaves best so that it is applied to the subsequent optimisation.

To compare MORBDO with the deterministic MOO, the corresponding Pareto frontiers are plotted in Fig. 6.6 together, where the reliability level for MORBDO is 95%. Similarly to the deterministic MOO, MORBDO presents a series of solutions over the Pareto space. However, as the uncertainties of the design variables are taken into account, the MORBDO Pareto frontier significantly differs from MOO's. Interestingly, it is noted that of these 100 design points, the deterministic MOO provides only 45 reliable solutions, whose PSFs are greater than 1, while MORBDO yields 94 reliable solutions and the PSFs of the remaining 6 solutions are smaller than but very close to 1. Therefore, the conclusion can be drawn that although the objective performances are sacrificed (i.e., the mass is increased and/or vertical sag stiffness is weakened), the constraint reliability increases significantly through MORBDO.

MOO provides 45 reliable solutions as mentioned above. It is noted that this number of reliable solutions is near 50% of all solutions and such a 50-50 value is expected for a deterministic optimisation without considering safety/knockdown factor. This validates the accuracy of ARS to a certain extent. For MORBDO, the results have 6% of unreliable designs, which implies that there are small errors when using DRS to predict the probabilistic constraint. Overall, the RS models used here have satisfactory accuracy for the optimisations and thus no more sample points are needed to improve the RS models.

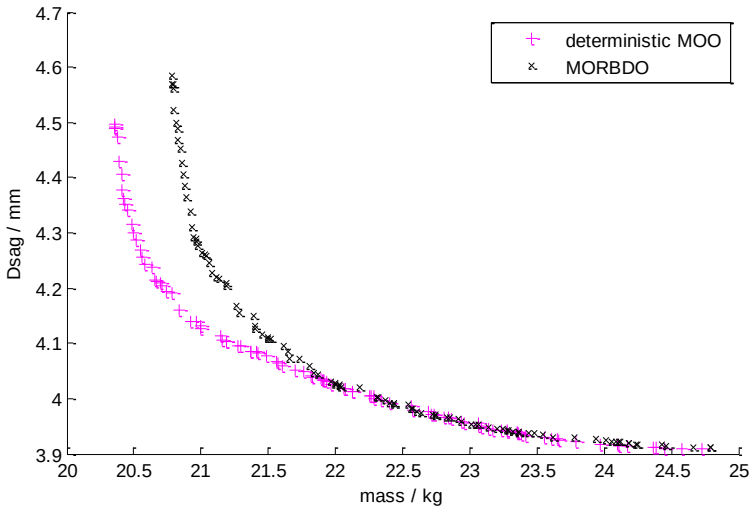

Fig. 6.6 Comparison of MORBDO and deterministic MOO results

Again from Fig. 6.6, the Pareto solution can be divided into two regions: sensitive region when mass < 22kg and insensitive region when mass > 22kg. In the insensitive region, the shapes of the two Pareto frontiers of deterministic MOO and MORBDO almost coincide. The majority of the above-mentioned 45 reliable solutions to the deterministic MOO are actually located in this insensitive region. In the sensitive region, however, due to consideration of uncertainties, the MORBDO Pareto frontier moves toward right within the feasible region, thus its Pareto becomes clearly worse than MOO.

In other words, the mass needs to be sacrificed in order to accommodate the randomness of design variables in MORBDO, in which those 55 unreliable MOO solutions are due to a more sensitive effect of the uncertainties on the objectives.

Furthermore, it is noted that of these 100 Pareto optimal solutions to MORBDO, 70 solutions, which are located in the sensitive region, have the lowest reliability in the lower lateral stiffness and lie on its constraint boundary. The remaining 30 solutions, which are located in the insensitive region, have the lowest reliability in the first natural frequency and they are away from the constraint boundary. Accordingly, we can draw some conclusions as follows. Firstly, each constraint tends to play an unequal role in MORBDO, the order of constraint criticality in this specific optimisation problem is lower lateral stiffness > natural frequency > upper lateral stiffness. Secondly, there is a definite linkage between the sensitivity of the regions and the constraint criticality. Specifically, in the region with a lower mass the constraints are critical that make this region relatively more sensitive. In contrast, in the region with a higher mass, all of the constraints do not actually take effect, the Pareto optimal frontier is dominated by the objectives so that this region becomes insensitive.

Note that the above information of sensitive and insensitive regions can be very useful which will enable the decision-makers to choose a solution from a relatively insensitive region of the Pareto frontier whenever possible.

6.2.3.2 Effects of reducing the uncertainty and improving the desired reliability level

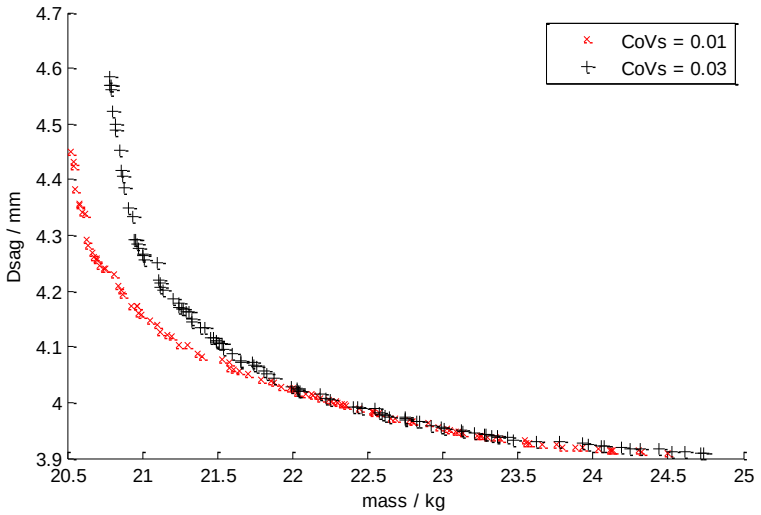

Fig. 6.7 Result comparison of different uncertainty

Fig. 6.7 plots the MORBDO Pareto frontiers with two values of CoVs= 0.01 and 0.03, respectively. As CoVs decrease, the Pareto frontier approaches the deterministic MOO counterpart, which indicates that less sacrifice is needed to achieve a reliable solution. In other words, a better vertical sag stiffness performance can be achieved with the same mass if reduce the uncertainty, and vice versa. Nevertheless, as the uncertainty reduces, the manufacturing cost may increase dramatically due to quality control in practical applications.

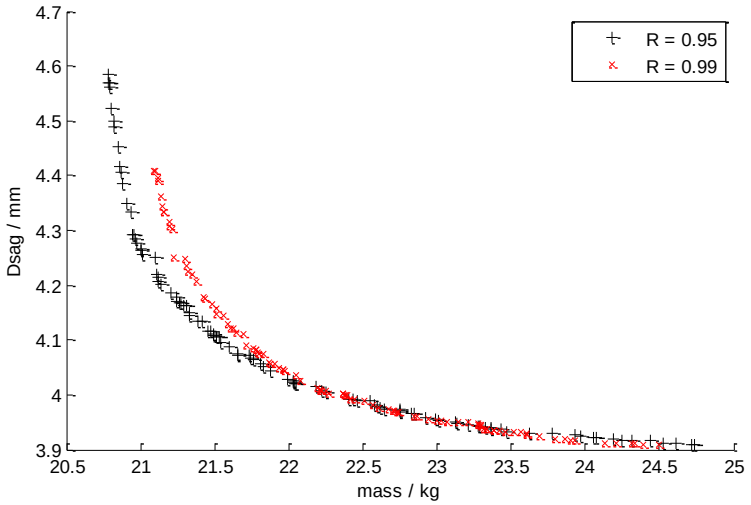

Fig. 6.8 Result comparison of different reliability target

Fig. 6.8 presents the comparison of the MORBDO Pareto frontiers with two target reliability levels of R = 0.95 and 0.99, respectively. As the reliability level increases, the Pareto frontier moves further inward the feasible region in the Pareto space. This means that the performances drop as a result of improvement of reliability. Practically, a compromise should be made between the objective performances and the desired reliability level.

6.3 Reliability-based robust optimisation for a foam-filled tube

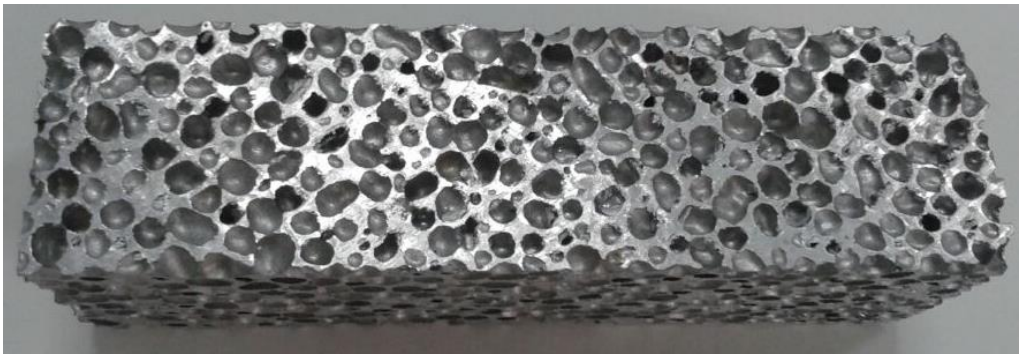

Fig. 6.9 Microstructure of metal foam

Regarding the uncertainty existing in metal foams, Reyes et al. [221] pointed out that as a cellular material, the foam has unevenly distributed pores generated randomly, whose sizes are also varying (as shown in Fig. 1). This will definitely lead to the variation of foam density. Moradi [264] claimed that greater randomness of shape and size of voids could be inevitably introduced into metal foams during the manufacturing process compared to solid metal, resulting in more uncertainty of performance indicators. Randrianalisoa et al. [261] found that the presence of cell randomness could decrease the thermal conductivity of cellular materials. Besides the foam density, thickness and dimension of tubes always come with certain manufacturing errors. For these reasons, the nature of crashworthiness optimisation for foam filled thin-walled structures is indeed nondeterministic, which involves some degree of uncertainties. Unfortunately, there are very few studies available to deal with the uncertainties in the optimisation procedure for crashworthiness design of foam filled thin-walled structures to the author's best knowledge. Based on Section 5.3, the maximum force and energy absorption are optimised with consideration of the uncertainty in the foam and tube wall. The weight factor is introduced to consider the tradeoff between the nominal performance and the standard deviation.

6.3.1 Definition of the optimisation problem

In Section 5.4, We constructed accurate Kriging models using combined AASO-AAMO and generate Pareto solutions for deterministic design. Now, we are going to formulate the deterministic MOO to a MORDO by considering the uncertainties. For clarification, the whole MORDO procedure for the crashworthiness optimisation for foam-filled thin-wall structures is summarized in Fig. 6.10.

The robust objective functions in Eq.(6.3) can be re-written as a weighted sum of the mean and standard deviation (Table 6.5), where λ denotes the weight for emphasizing either the mean or the standard deviation, μ_{fi}^{*} stands for the target for the *i*th objective mean.

Table 6.5 Expression of the objective.

Objective type	Expression
Minimization	$F_i\left(\mu_{fi}(\mathbf{x}),\sigma_{fi}(\mathbf{x})\right)=\lambda\mu_{fi}(\mathbf{x})+(1-\lambda)\sigma_{fi}(\mathbf{x})$
Maximization	$F_i\left(\mu_{fi}(\mathbf{x}),\sigma_{fi}(\mathbf{x})\right)=-\lambda\mu_{fi}(\mathbf{x})+(1-\lambda)\sigma_{fi}(\mathbf{x})$
Target	$F_i\left(\mu_{fi}(\mathbf{x}),\sigma_{fi}(\mathbf{x})\right)=\lambda\left\lvert\mu_{fi}(\mathbf{x})-\mu_{fi}^{*}\right\rvert+(1-\lambda)\sigma_{fi}(\mathbf{x})$

In general mechanical design, a normal distribution is widely assumed and often used in accounting for uncertainties of the design variables [261, 262]. The coefficients of variation of each design variable for considering parameter uncertainties are 0.01 herein. When taking into account the uncertainties, the MORDO problem can be written as:

$$\begin{cases} \min & -\lambda\mu(SEA)+(1-\lambda)\sigma(SEA) \\ & \lambda\mu(F_{max})+(1-\lambda)\sigma(F_{max}) \\ s.t. & \mathrm{P}(F_{avg}\geq 85\ \mathrm{kN})\geq 0.90 \\ & 0.6\ \mathrm{mm}\leq t_1,t_2\leq 2.0\ \mathrm{mm} \\ & 0.2\mathrm{g/cm}^3\leq\rho_f\leq 0.6\mathrm{g/cm}^3 \end{cases} \tag{6.18}$$

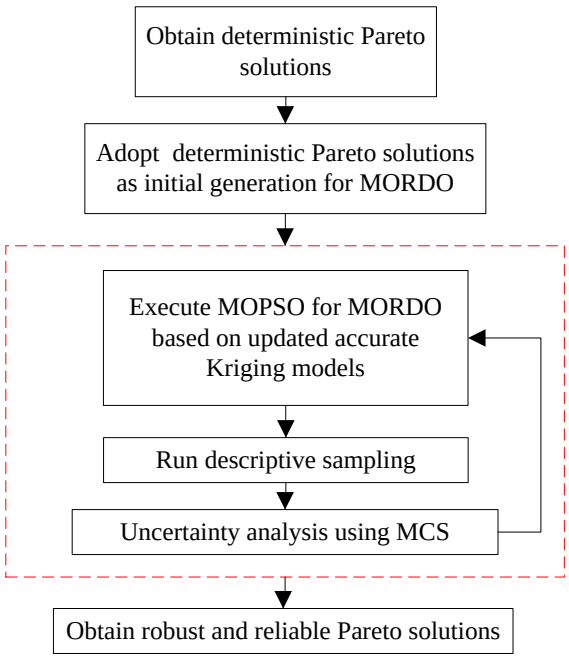

Fig. 10 Flowchart of the proposed procedure

6.3.2 Results and discussion

When the uncertainties of the foam density and wall thicknesses are considered, the Pareto solutions move towards the right to the positions indicating a thicker inner wall (larger t_2 values) in the feasible region ($F_{avg} \geq 85$kN) as plotted in Fig. 6.11. When more emphasis is placed on the means of the objectives, i.e., by taking a larger value of weight factor λ, the solutions move further and have larger values for t_2.

Fig. 6.12 shows that the MOSRDO Pareto frontier of the means of the performances (i.e. *SEA* and F_{max}) moves further inward the feasible region in the objective space, compared to the deterministic counterpart. In order to accommodate the randomness of design variables in MOSRDO, the performances have to be sacrificed, i.e. *SEA* should be decreased and/or F_{max} be increased compared to the deterministic optimisation. Moreover, the larger the value of λ, the further the Pareto frontier moves. This means that the

performances would drop as a result of improvement in robustness. Consequently, the robustness and performances should be compromised in practice, which was also revealed in the previous research [47].

Figs. 6.13(a) and (b) exhibit the relationship between the mean and standard deviation for F_{max} and *SEA* respectively. Interestingly, under the same nominal performance the variation of the optima can be much smaller when the uncertainties are imposed in the optimisation, and more weight on the standard deviations leads to more stable Pareto optima. Therefore, MOSRDO is capable of reducing the performance fluctuations of Pareto solutions with respect to the uncertainties.

Fig. 6.14 presents the effect of the desired reliability level prescribed before optimisation on the MOSRDO results, where the weight factor is set as λ= 0.10. Surprisingly, the Pareto frontiers for the three values of reliability level (i.e., R = 0.90, 0.95 and 0.99) almost coincide. To have an insightful understanding, let us look at Fig. 10 again. It can be seen only a few MOSRDO Pareto solutions lie on the boundary of the constraint. As a result, the reliability constraint is inactive to the majority of the Pareto solutions. In other words, the MOSRDO Pareto solutions are insensitive to the change of reliability level in this specific design case.

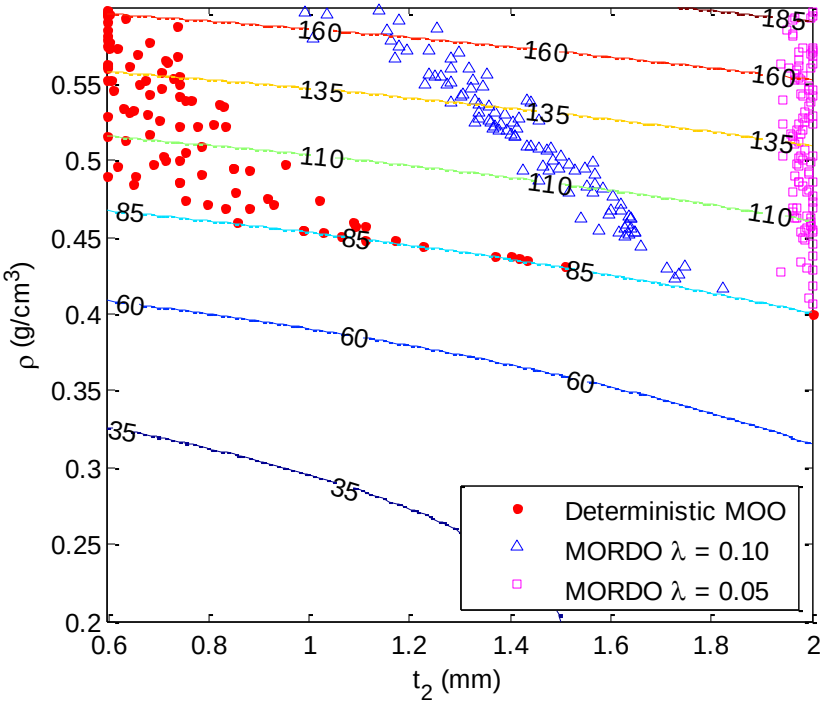

Fig. 6.11 Pareto solutions of deterministic and robust optimisations (t_1= 0.6 mm).

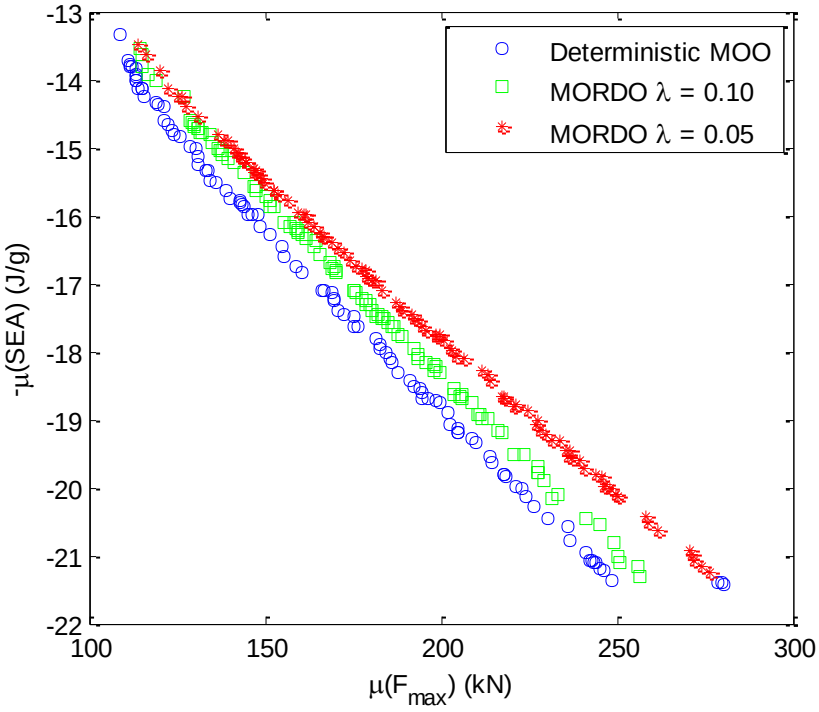

Fig. 6.12 Pareto frontiers of the mean value of deterministic and robust optimisations.

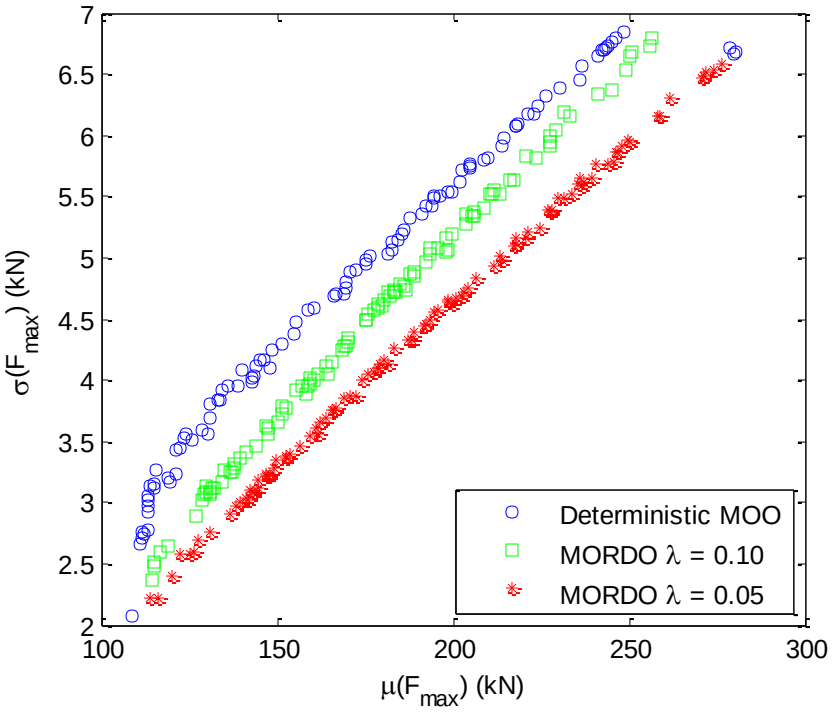
σ(F_max) (kN)
μ(F_max) (kN)
Deterministic MOO
MORDO λ = 0.10
MORDO λ = 0.05

(a)

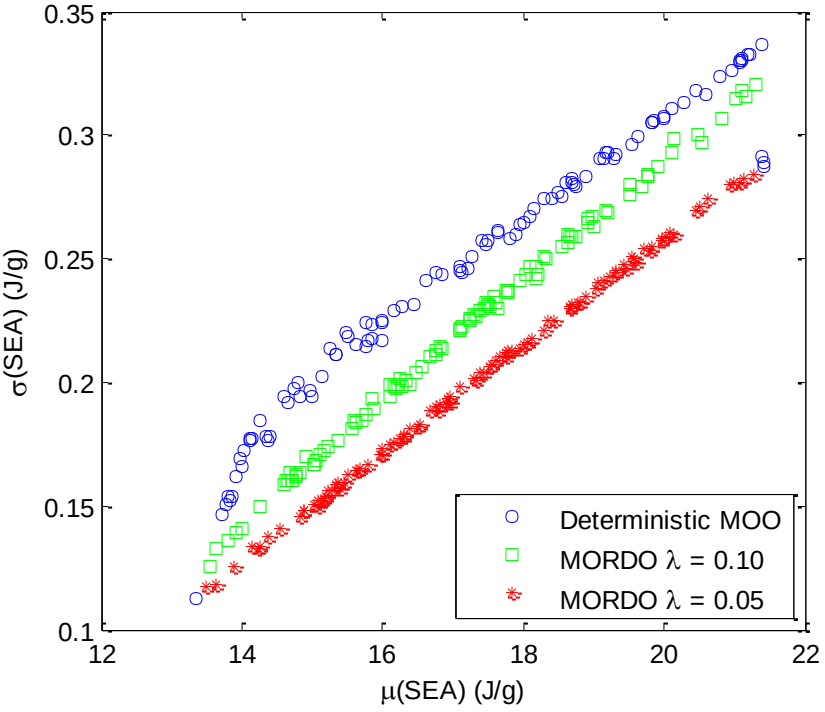
σ(SEA) (J/g)
μ(SEA) (J/g)
Deterministic MOO
MORDO λ = 0.10
MORDO λ = 0.05

(b)

Fig. 6.13 Standard deviation versus the mean of deterministic and robust optimisations: (a)F_{max}, (b)SEA.

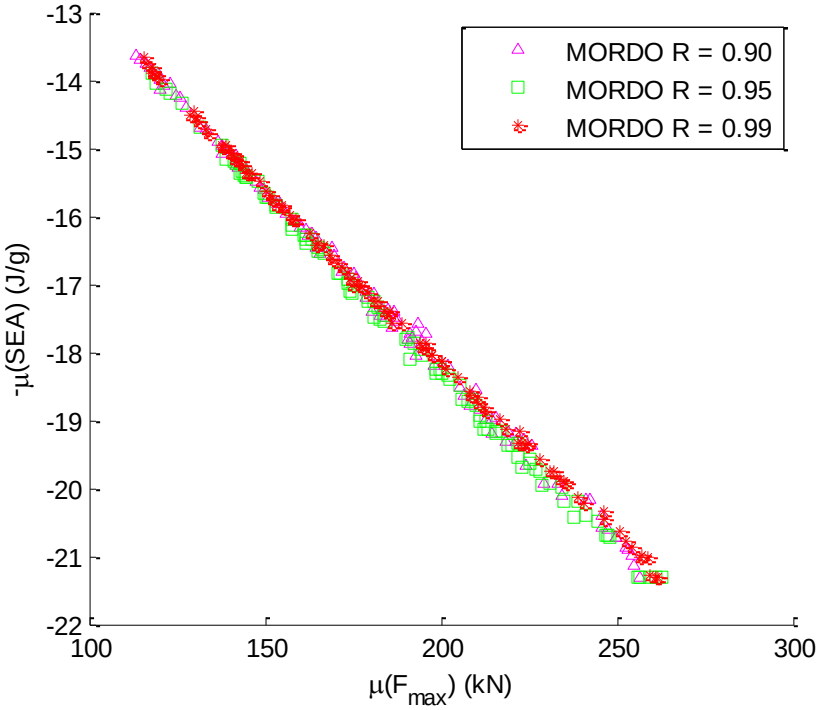

Fig. 6.14 Pareto frontiers of mean value under different reliability levels.

As the multiobjective optimisation can provide a wide spectrum of designs for selection, we checked four optimal solutions for different levels of F_{max} and the results are list in Tables 6.6-6.9. In these tables, the means and standard deviations of FEA results are calculated by stochastic FEA, which is done by randomly changing the values of design variables with descriptive sampling (sample size = 10). Note that the standard deviations have relatively large errors while the mean values of the optima agree fairly well with the FEA results. This is probably because only 10 FE models around each optimum were analysed in this study for computational cost and insufficient FEA samples may not be able to capture the standard deviations adequately.

Overall, the robust designs also provide the designers with the better solutions with

smaller variations while the performances are just weakened slightly. For example, compared to the deterministic design, the robust design with λ =0.05 under $F_{max} \leq$ 120 kN can reduce the standard deviation by 42.82% for the *SEA* and 30.35% for the F_{max} while reducing the mean of the *SEA* by only 2.23%. Besides, when more emphasis is placed on the standard deviations by reducing λ from 0.10 to 0.05, the standard deviation is decreased from 0.1214 to 0.0884 for the *SEA* and from 3.89 to 2.84 for the F_{max}, representing more robust to the uncertainties in foam density and wall thicknesses.

It is also found that at the optimal points, the errors of the means by the deterministic optimisation are generally higher than those of the robust designs. This is probably because the robust optimisations push the design to a *flatter* area so that the performances have less difference around the optimum when uncertainties present, while the deterministic optimisation obtains the design at a *sharper* area. Thus, it is easier for the robust optimisations to attain an accurate FEA mean value against the Kriging value by using only a limited number of simulations.

Note that MOSRDO needs additional computational cost, as it requires a more accurate metamodel and extra uncertainty analyses during the optimisation. Nevertheless, the authors think that it is worth making extra efforts to achieve more practical designs. The adaptive metamodeling technique has already enhanced the efficiency largely, by iteratively fitting the functions of performance indicators with a limited number of sample data. Based on the established Kriging models, uncertainty analyses can be accomplished in a very limited time. Besides, in the long run, the rapid development of computational capacity could make it possible to run simulations of more complex problems in a fast way.

Table 6.6 Comparison between deterministic and robust MOO designs ($F_{max} \leq 120$kN).

Description				Deterministic	Robust (λ =0.10)	Robust (λ =0.05)
Variables	t_1 (mm)			0.60	0.61	0.64
	t_2 (mm)			1.11	1.75	2.00
	ρ (g/cm^3)			0.46	0.43	0.42
Objectives	*SEA* (J/g)	μ(*SEA*)	Kriging	14.36	14.01	13.88
			FEA	14.32	14.14	14.00
			%error	0.27	-0.90	-0.88
		σ(*SEA*)	Kriging	0.1766	0.1397	0.1247
			FEA	0.1546	0.1214	0.0884
			%error	14.20	15.08	41.03
	F_{max} (kN)	$\mu(F_{max})$	Kriging	119.42	119.30	120.16
			FEA	118.03	120.33	120.67
			%error	1.18	-0.85	-0.42
		$\sigma(F_{max})$	Kriging	3.2061	2.6311	2.3565
			FEA	4.0773	3.8943	2.8432
			%error	-21.37	-32.44	-17.12
Constraints	F_{avg} (kN)	$\mu(F_{avg})$	Kriging	89.12	91.13	92.31
			FEA	89.05	91.73	92.27
			%error	0.08	-0.65	0.04
		Reliability		100%	100%	100%

Table 6.7 Comparison between deterministic and robust MOO designs ($F_{max} \leq 160$kN).

Description				Deterministic	Robust (λ =0.10)	Robust (λ =0.05)
Variables	t_1 (mm)			0.61	0.61	0.60
	t_2 (mm)			0.60	1.50	2.00
	ρ (g/cm^3)			0.52	0.50	0.48
Objectives	*SEA* (J/g)	μ(*SEA*)	Kriging	16.75	16.22	15.96
			FEA	16.52	16.19	15.92
			%error	1.41	0.22	0.24
		σ(*SEA*)	Kriging	0.2454	0.1996	0.1722
			FEA	0.2211	0.1755	0.1423
			%error	10.96	13.74	20.98
	F_{max} (kN)	$\mu(F_{max})$	Kriging	158.65	159.27	159.52
			FEA	153.70	154.43	163.06
			%error	3.22	3.13	-2.17
		$\sigma(F_{max})$	Kriging	4.5476	3.9923	3.5510
			FEA	5.0443	4.0361	3.8131
			%error	-9.85	-1.08	-6.87
Constraints	F_{avg} (kN)	$\mu(F_{avg})$	Kriging	110.56	115.37	117.75
			FEA	107.27	113.98	115.55
			%error	3.07	1.22	1.90
	Reliability			100%	100%	100%

Table 6.8 Comparison between deterministic and robust MOO designs ($F_{max} \leq 200$kN).

Description				Deterministic	Robust (λ =0.10)	Robust (λ =0.05)
Variables	t_1 (mm)			0.63	0.61	0.63
	t_2 (mm)			0.74	1.31	2.00
	ρ (g/cm^3)			0.55	0.54	0.52
Objectives	*SEA* (J/g)	μ(*SEA*)	Kriging	18.74	18.31	17.76
			FEA	18.37	18.38	17.68
			%error	2.01	-0.38	0.47
		σ(*SEA*)	Kriging	0.2799	0.2497	0.2094
			FEA	0.2718	0.2135	0.2342
			%error	2.97	16.93	-10.60
	F_{max} (kN)	μ(F_{max})	Kriging	199.86	199.44	199.74
			FEA	197.36	201.49	198.00
			%error	1.27	-1.02	0.88
		σ(F_{max})	Kriging	5.5363	5.1842	4.6122
			FEA	9.4082	7.6381	5.1818
			%error	-41.15	-32.13	-11.00
Constraints	F_{avg} (kN)	μ(F_{avg})	Kriging	135.61	138.71	142.86
			FEA	131.32	138.72	140.25
			%error	3.27	-0.01	1.86
		Reliability		100%	100%	100%

Table 6.9 Comparison between deterministic and robust MOO designs ($F_{max} \leq 240$kN).

Description				Deterministic	Robust (λ =0.10)	Robust (λ =0.05)
Variables	t_1 (mm)			0.60	0.60	0.61
	t_2 (mm)			0.60	1.16	2.00
	ρ (g/cm^3)			0.59	0.58	0.56
Objectives	*SEA* (J/g)	μ(*SEA*)	Kriging	20.78	20.47	19.60
			FEA	20.55	20.38	19.59
			%error	1.12	0.44	0.02
		σ(*SEA*)	Kriging	0.3237	0.3000	0.2495
			FEA	0.3162	0.2692	0.2535
			%error	2.37	11.44	-1.56
	F_{max} (kN)	μ(F_{max})	Kriging	236.64	240.94	239.49
			FEA	235.63	240.07	236.00
			%error	0.43	0.36	1.48
		σ(F_{max})	Kriging	6.5595	6.3354	5.6688
			FEA	6.8376	6.6828	5.5559
			%error	-4.07	-5.20	2.0306
Constraints	F_{avg} (kN)	μ(F_{avg})	Kriging	156.25	162.36	167.02
			FEA	153.45	162.05	166.48
			%error	1.83	0.19	0.32

	Reliability	100%	100%	100%

6.4 Multi-criteria decision making based robust fatigue Optimisation for a Truck Cab

It appears that the performance and robustness of the optimum tend to conflict with each other and often a tradeoff needs to be made appropriately in the design [265, 266]. Herein we proposed a two-stage optimisation procedure to optimise the fatigue life of the truck cab. First, the dual surrogate models were established to approximate the mean and standard deviation of the fatigue life and then run the multiobjective particle swarn optimisation algorithm to generate the Pareto front. Then, a hybrid multi-criteria decision-making model was proposed to select the best compromised solution from the Pareto solutions.

6.4.1 Multiobjective robust optimisation

6.4.1.1 Definition of optimisation problem

As mentioned above, the possible formulations of a robust design optimisation can be mathematically presented in Eqs. 6.19-6.22, where $F_\mu(\mathbf{x})$ and $F_\sigma(\mathbf{x})$ are the mean value and standard deviation functions of fatigue life, and F_μ^* and F_σ^* are their ideal optimums.

$$\text{Design 1: } \begin{cases} \min \ -F_\mu(\mathbf{x}) \\ s.t. \ \ F_\sigma(\mathbf{x}) \le F_{\sigma 0} = 0.050 \\ \qquad \mathbf{x}_L \le \mathbf{x} \le \mathbf{x}_U \end{cases} \tag{6.19}$$

$$\text{Design 2: } \begin{cases} \min \ F_\sigma(\mathbf{x}) \\ s.t. \ \ F_\mu(\mathbf{x}) \ge F_{\mu 0} = 4.70 \\ \qquad \mathbf{x}_L \le \mathbf{x} \le \mathbf{x}_U \end{cases} \tag{6.20}$$

$$\text{Design 3: } \begin{cases} \min \ -\alpha \dfrac{F_\mu(\mathbf{x})}{F_\mu^*} + (1-\alpha)\dfrac{F_\sigma(\mathbf{x})}{F_\sigma^*}; \ \ 0 \le \alpha \le 1 \\ s.t. \ \ \mathbf{x}_L \le \mathbf{x} \le \mathbf{x}_U \end{cases} \tag{6.21}$$

$$\text{Design 4: } \begin{cases} \min \ (-F_\mu(\mathbf{x}), F_\sigma(\mathbf{x})) \\ s.t. \ \ \mathbf{x}_L \le \mathbf{x} \le \mathbf{x}_U \end{cases} \tag{6.22}$$

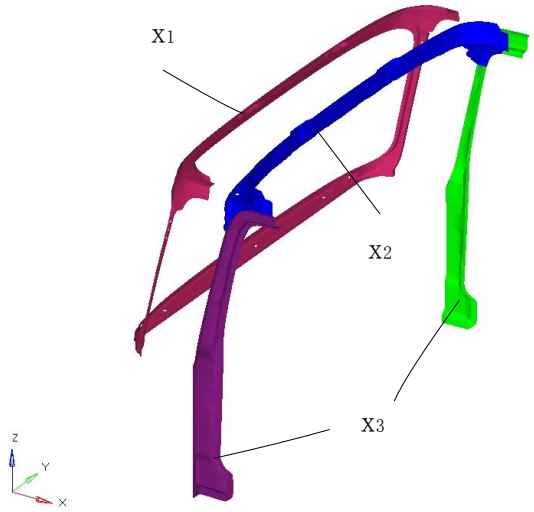

Fig. 6.15 Illustration of design variables

Table 6.10 Variable ranges

Design variables	*Varying ranges*	
	Lower bounds	*Upper bounds*
x_1 (mm)	0.7	2.0
x_2 (mm)	0.7	1.5
x_3 (mm)	0.7	1.0

Fig. 6.15 and Table 6.10 present three thickness design variables and their dimensional ranges to be optimized in this study. With regard to uncertainties, Grujicic et al. [45] pointed out the importance of considering variations in material properties to predict the fatigue performance of vehicle components. Thus, we would like to restrict

our attention on uncertainties induced by the material properties in this RDO problem. Specifically, the ultimate tensile strength (σ_b), elastic modulus (E) and density (ρ), which can be affected by rolling process [14], are chosen as the noise factors to take into account the uncertainties. Their fluctuations are in the ranges of E = [200 GPa, 220 GPa], ρ = [7700 kg/m^3, 7900 kg/m^3], and σ_b = [300 MPa, 340 MPa], respectively, which are from the statistical data in the ASM Metals Handbook [267].

The entire design procedure is described in the flowchart seen in Fig. 6.16. In the cross product array, the noise factors (i.e., material uncertainties) are arranged in outer array as in Table 6.11, which is sampled by orthogonal array, while the control factors (i.e., thickness design variables) are arranged in the inner array, which is generated by Optimal Latin Hypercube Sampling (OLHS). The results of cross product array are summarized in Table 6.12, where the first 30 designs are the training points and the last five are the assessment points. This study extends the conventional dual response surface model to the general dual surrogate model for fitting the mean and standard deviation of the fatigue life. Table 6.13 shows the error assessment of different dual surrogate models and it is found the dural Kriging models perform the best both in the global and local metrics.

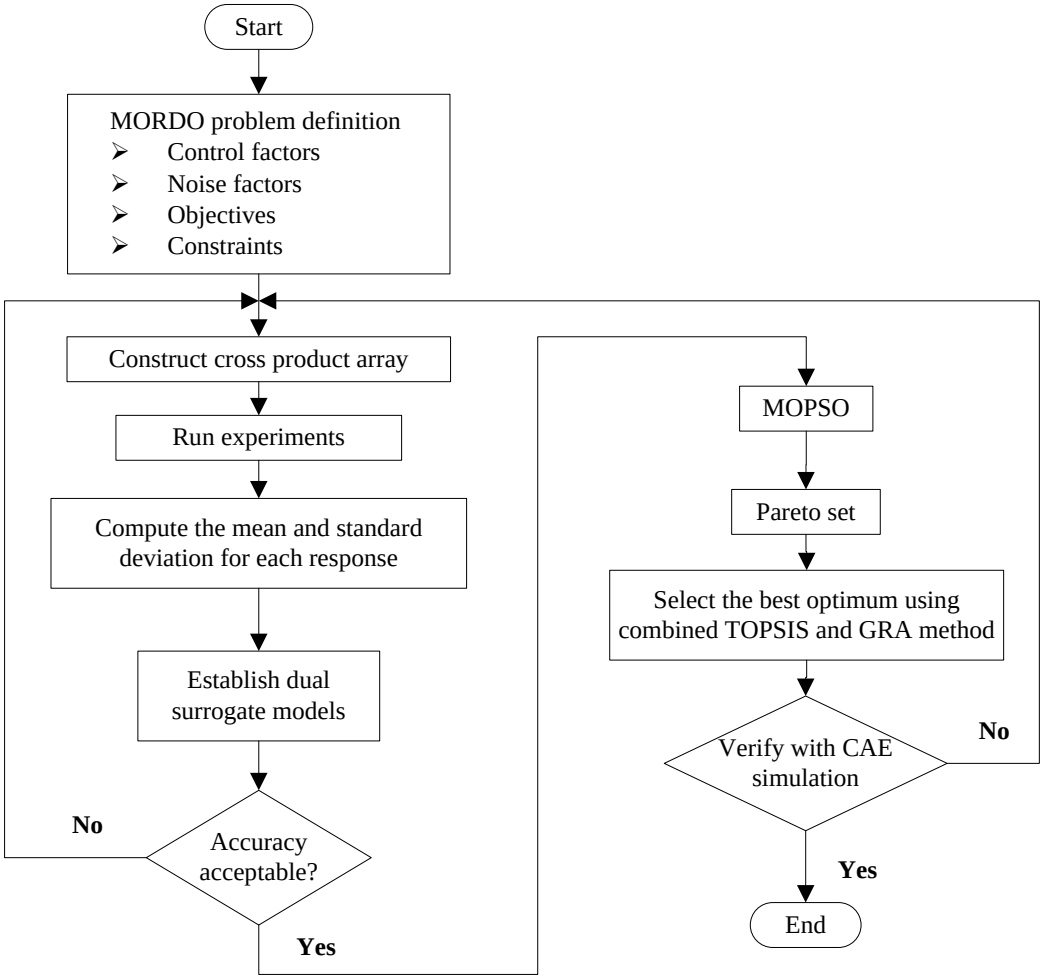

Fig. 6.16 Flowchart of optimisation process

Table 6.11 Outer array for the noise factors

No.	E (GPa)	ρ (kg/m^3)	σ_b (MPa)
1	200	7700	300
2	200	7900	340
3	220	7700	340
4	220	7900	300
5	210	7800	320

Table 6.12 Results of cross product array

	No.	x_1	x_2	x_3	F_μ	F_σ
Training points	1	1.69	0.76	0.95	4.12	0.0618
	2	1.96	1.31	0.82	4.75	0.0974
	3	1.91	1.11	0.97	4.74	0.0964
	4	1.60	1.22	0.91	4.53	0.0888
	5	1.10	0.98	0.83	4.11	0.0947
	6	0.97	0.73	0.88	3.72	0.0512
	7	1.87	1.17	0.73	4.63	0.0921
	8	0.74	1.25	0.80	3.42	0.0644
	9	1.37	1.14	0.79	4.31	0.0919
	10	1.82	0.81	0.77	4.31	0.0680
	11	1.15	1.33	0.87	4.12	0.0956
	12	0.92	1.09	0.72	3.78	0.0759
	13	1.33	1.36	0.99	4.23	0.0849
	14	1.46	1.00	1.00	4.38	0.0842
	15	1.06	1.20	0.96	4.04	0.0853
	16	0.79	0.87	0.78	3.46	0.0710
	17	1.73	1.03	0.86	4.56	0.0898
	18	0.70	1.06	0.90	3.32	0.0629
	19	1.19	0.78	0.74	3.99	0.0787
	20	1.42	1.50	0.84	4.35	0.0899
	21	0.88	0.92	0.98	3.78	0.0655
	22	1.51	0.70	0.81	3.94	0.0642

	23	0.83	1.42	0.93	3.70	0.0734
	24	1.64	1.39	0.75	4.54	0.0935
	25	2.00	0.89	0.89	4.57	0.0736
	26	1.55	0.95	0.71	4.41	0.0919
	27	1.78	1.44	0.94	4.69	0.0952
	28	1.28	0.84	0.92	4.09	0.0744
	29	1.24	1.28	0.70	4.23	0.1006
	30	1.01	1.47	0.76	3.99	0.0589
Assessment	31	2.00	1.30	1.00	4.85	0.1036
points	32	1.35	0.70	0.93	3.85	0.0660
	33	1.03	1.50	0.85	4.02	0.0581
	34	1.68	1.10	0.70	4.50	0.0905
	35	0.70	0.90	0.78	3.24	0.0636

Table 6.13 Accuracy assessment of different dual surrogate models

DSM	*Response*	R^2	*RAAE*	*RMAE*
DPRS	$F_\mu(\mathbf{x})$	0.9536	0.2006	0.2821
	$F_\sigma(\mathbf{x})$	0.7761	0.4212	0.6727
DKRG	$F_\mu(\mathbf{x})$	**0.9980**	**0.0374**	**0.0737**
	$F_\sigma(\mathbf{x})$	**0.9530**	**0.1775**	**0.3808**
DRBF	$F_\mu(\mathbf{x})$	0.9963	0.0586	0.0742
	$F_\sigma(\mathbf{x})$	0.6299	0.4276	1.2603

6.4.1.2 Optimisation results

Table 6.14 Robust design results with single objective optimisation

Description		Design 1	Design 2	Design 3				
				α= 0	α= 0.25	α= 0.50	α= 0.75	α= 1
Design variables	x_1	0.97	1.80	0.96	0.96	0.96	2.00	2.00
	x_2	0.73	1.21	0.70	0.70	0.70	0.86	1.50
	x_3	1.00	1.00	1.00	1.00	1.00	1.00	1.00
Fatigue life	$F_\mu(\mathbf{x})$	3.74	4.72	3.68	3.68	3.67	4.56	4.90
	$F_\sigma(\mathbf{x})$	0.050	0.083	0.0486	0.0486	0.0487	0.0703	0.100

The results of single objective optimisation are summarized in Table 6.14, where objective weight α as in Eq. (6.21) is assigned five values evenly distributed in [0, 1] for Design 3. For Design 1 (Eq. (6.19)) and Design 2 (Eq. (6.20)), the design achieve the optimum by pushing the design onto the bound of each constraint (i.e., $F_\sigma(\mathbf{x})$= 0.050 and $F_\mu(\mathbf{x})$= 4.72, respectively). Note that the constraints $F_{\sigma 0}$ and $F_{\mu 0}$ in Eqs. (6.19) and (6.20) can actively affect the optimums. In practical application, it is, however, difficult to define a constraint prior to optimisation.

For Design 3, when the weighting factor α= 0 or 1, the optimisation problems become to minimize the standard deviation or maximize the mean value of the fatigue life, respectively. That is to say that at these two cases, the optimisations solve for F_σ^* and F_μ^* in Eq. (6.21), respectively. Furthermore, when α increases from 0 to 1 evenly, the optimums obtained do not distribute evenly in the solution space. Specifically, the optimum almost remains unchanged when α changes from 0 to 0.50, whilst it changes

noticeably when α increases from 0.50 to 1.

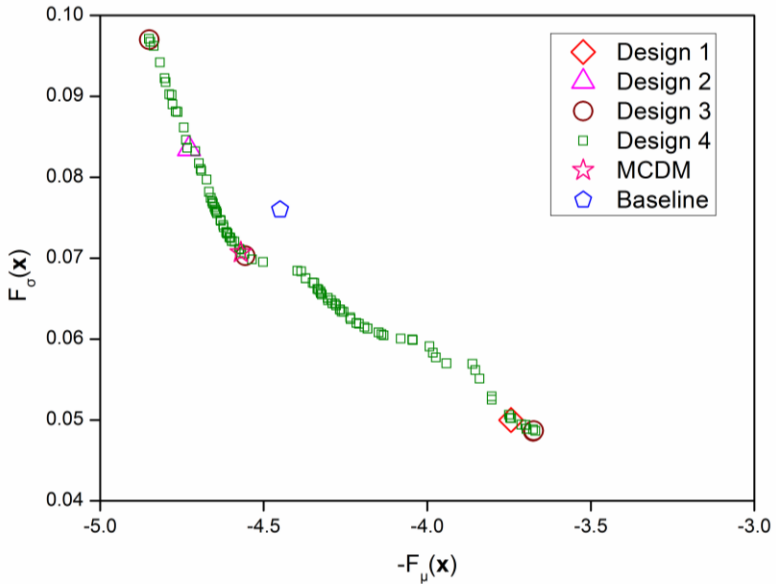

Fig. 17 Pareto frontier of fatigue mean and standard deviation

Fig. 6.17 plots the Pareto frontier of MOPSO obtained from Design 4, together with the results of the single objective optimisations and the baseline design. Obviously, MOPSO generates a well-distributed Pareto frontier over the entire design space, and each point represents a non-dominated solution. It can be seen that the optimal values of $F_\mu(\mathbf{x})$ and $F_\sigma(\mathbf{x})$ strongly conflict with each other, indicating that there is no any other point in the Pareto frontier that allows minimizing these two objectives concurrently without compromising one from another.

It is noted that while Designs 1 and 2 yield only one single point in the Pareto frontier, indicating one special Pareto solution, Design 3 can produce a number of solutions by changing the value of the weighting factor α. Nevertheless, some solutions from Design 3 (e.g., the solutions from α= 0 to 0.50) may distribute in one small region rather than spread over the Pareto space uniformly. Moreover, as a type of weighted cost function, Design 3 is effective only if the Pareto frontier is convex when it is used to

generate a Pareto frontier [268]. Obviously, Fig. 6.17 indicates that the convexity could be problematic in some region of the design space. Therefore, the adoption of MOPSO appears essential in this case.

6.4.2 MCDM

6.4.2.1 Decision model for MCDM

Often a multiobjective optimisation needs to cope with some conflicting objectives, typically forming a Pareto frontier from MOPSO. In order to rank the solutions in Pareto frontier and choose the best possible compromise, TOPSIS induced by Hwang and Yoon [269] and grey relational analysis (GRA) introduced by Deng [270] are integrated into this paper. The process of this hybrid method to determine the best compromise solution is presented as follows:

Step 1. Input **S** and **w** (i.e., **S** forms the Pareto frontier), where the component s_{ij} is the jth objective value at the ith alternative Pareto point, component w_j is the weight of the jth objective, and weight vector **w** must satisfy $\sum_{j=1}^{2} w_j = 1$. In this study, the weights are determined using the entropy method [271].

Step 2. Normalize **S** to be $\widehat{\mathbf{S}}$ according to Eq. (6.23).

$$\widehat{s}_{ij} = \frac{\max\limits_{\forall j} s_{ij} - s_{ij}}{\max\limits_{\forall j} s_{ij} - \min\limits_{\forall j} s_{ij}} \quad \text{for } i = 1, 2, \ldots, \tau \text{ and } j = 1, 2. \tag{6.23}$$

Step 3. Determine the ideal solution s^+ and the negative ideal solution s^- using Eqs. (12) and (13), respectively,

$$s^+ = (\max_{\forall i} \widehat{s}_{i1}, \max_{\forall i} \widehat{s}_{i2}) \tag{6.24}$$

$$s^{-} = (\min_{\forall i} \hat{s}_{i1}, \min_{\forall i} \hat{s}_{i2}) \tag{6.25}$$

Step 4. Calculate the grey relation coefficient of each alternative to the ideal $\gamma(s_j^{+}, \hat{s}_{ij})$ and the negative ideal solution $\gamma(s_j^{-}, \hat{s}_{ij})$ by taking s^{+} and s^{-} as the referential sequence and each alternative to be the comparative sequence:

$$\gamma(s_j^{+}, \hat{s}_{ij}) = \frac{\min_{\forall i} \min_{\forall j} \left| s_j^{+} - \hat{s}_{ij} \right| + \zeta \max_{\forall i} \max_{\forall j} \left| s_j^{+} - \hat{s}_{ij} \right|}{\left| s_j^{+} - \hat{s}_{ij} \right| + \zeta \max_{\forall i} \max_{\forall j} \left| s_j^{+} - \hat{s}_{ij} \right|} \tag{6.26}$$

$$\gamma(s_j^{-}, \hat{s}_{ij}) = \frac{\min_{\forall i} \min_{\forall j} \left| s_j^{-} - \hat{s}_{ij} \right| + \zeta \max_{\forall i} \max_{\forall j} \left| s_j^{-} - \hat{s}_{ij} \right|}{\left| s_j^{-} - \hat{s}_{ij} \right| + \zeta \max_{\forall i} \max_{\forall j} \left| s_j^{-} - \hat{s}_{ij} \right|} \tag{6.27}$$

where ζ is the distinguished coefficient ($0 \leq \zeta \leq 1$). In this study, $\zeta = 0.5$ [272].

Step 5. Determine the grade of the grey relation of each alternative to s^{+} and s^{-} by using Eqs. (16) and (17)

$$\gamma(s^{+}, \hat{s}_i) = \sum_{j=1}^{2} w_j \gamma(s_j^{+}, \hat{s}_{ij}) \tag{6.28}$$

$$\gamma(s^{-}, \hat{s}_i) = \sum_{j=1}^{2} w_j \gamma(s_j^{-}, \hat{s}_{ij}) \tag{6.29}$$

Step 6. Find the relative closeness C_i of the distance that an alternative is close to the ideal solution, which is defined in Eq. (6.30):

$$C_i = \frac{\gamma(s^{+}, \hat{s}_i)}{\gamma(s^{-}, \hat{s}_i)} \tag{6.30}$$

Step 7. Rank the priority of alternatives in a descending order of C_i and choose the best possible compromise solution.

It can be noted that the difference of the above integrated method from conventional TOPSIS lies in its introduction of the grey relation coefficient (i.e., $\gamma(s_j^{+}, \hat{s}_{ij})$ and

$\gamma(s_j^-, \hat{s}_{ij})$) of grey relation model to replace the general distance. Meanwhile, the conventional grey relation is revised in order to reflect the impact of decision-making theory. As a result, this method is considered to be able to acquire a satisfactory compromise solution for an MCDM problem [273].

6.4.2.2 MCDM result

After acquiring the Pareto set from MOPSO, the decision maker often needs to determine a compromise solution for accomplishing the assignment. By using the TOPSIS based on GRA, we rank these 100 Pareto solutions and select the best compromise, which is listed in Table 6.15 together with the baseline design. It can also be seen that the simulation results agree well with the DSM results, and more importantly, the optimal solution (signified with star in Fig. 6.16) selected by integrating TOPSIS with GRA not only improves the performance and robustness of the fatigue life simultaneously compared with the baseline, but also provides a proper compromise between performance and robustness compared with other Pareto points.

Table 6.15 Comparisons of the baseline and the best compromise designs

Description		*Baseline*	*Optimized (MCDM)*	
			DSM	*Simulation*
Design variables	x_1	1.5 mm	1.87 mm	
	x_2	1.5 mm	0.82 mm	
	x_3	1.5 mm	1.00 mm	
Fatigue life	$F_\mu(\mathbf{x})$	4.45	4.57	4.54

$F_\sigma(\mathbf{x})$	0.0755	0.0707	0.069

Note that in real-life engineering, design problems could be more complex, where more design variables and uncertainty types might be involved. In this study, while only three design variables and their material uncertainties were considered, the proposed DCM based multiobjective optimisation method combined with TOPSIS-based GRA procedure can be potentially extended to such more complicated problems

6.5 Summary

While various uncertainties are inevitably present in real-life optimisations, conventional deterministic optimisations could probably lead to the violation of constraints and the instability of performances. Therefore, nondeterministic optimisation methods were introduced to solve the automotive design problems. (a) A multiobjective reliability-based optimisation for design of a door was investigated. Based on analysis and design responses surface models, the structural mass was minimized and the vertical sag stiffness was maximized subjected to the probabilistic constraint. The results revealed that the Pareto frontier is divided into sensitive region and insensitive region with respect to uncertainties, and the decision maker is recommended to select a solution from the insensitive region. Furthermore, the reduction of uncertainties can help improve the reliability but will increase the manufacturing cost, and the tradeoff between the reliability target and performance should be made. (b) A multiobjective uncertain optimisation of the foam-filled double cylindrical structure was conducted by considering randomness in the foam density and wall thicknesses. Multiobjective particle swarm optimisation and Monte Carlo simulation were integrated in the optimisation. The results

proved that while the performances of the objectives are sacrificed slightly, the nondeterministic optimisation can enhance the robustness of the objectives and maintain the reliability of the constraint. (c) A multiobjective robust optimisation of the truck cab was performed by considering the uncertainty in material properties. The general version of dual response surface model, namely dual surrogate model, was proposed to approximate the means and standard deviations of the performances. Then, the multiobjective particle optimisation was used to generate the well-distributed Pareto frontier. Finally, a hybrid multi-criteria decision making model was proposed to select a best compromise solution considering both the fatigue performance and its robustness.

Chapter 7 Conclusions and future work

7.1 Conclusions

The conclusions are as follows:

(1) To excavate the potential of crash energy absorbers, the concept of functionally graded structure was introduced and multiobjective designs were implemented to this novel type of structures. First, note that the severe deformation takes place in the tubal corners, multi-cell tubes with a lateral thickness gradient were proposed to better enhance the crashworthiness. The results of crashworthiness analyses and optimisation showed that these functionally graded multi-cell tubes are preferable to a uniform multi-cell tube. Then, functionally graded foam filled tubes with different gradient patterns were analyzed and optimized subject to lateral impact and the results demonstrated that these structures can still behave better than uniform foam filled structures under lateral loading, which will broaden the application scope of functionally graded structures. Finally, dual functionally graded structures, i.e. functionally graded foam filled tubes with functionally graded thickness walls, were proposed and different combinations of gradients were compared. The results indicated that placing more material to tubal corners and the maximum density to the outmost layer are beneficial to achieve the best performance.

(2) To make full use of training data, multiple ensembles of surrogate models were proposed to maximize the fatigue life of a truck cab, while the panel thicknesses were taken as design variables and the structural mass the constraint. Meanwhile, particle swarm optimisation was integrated with sequential quadratic programming to avoid the premature convergence. The results illustrated that the hybrid particle swarm optimisation and ensembles of surrogates enable to attain a more competent solution for fatigue

optimisation.

(3) As the conventional surrogate based optimisation largely depends on the number of initial sample data, sequential surrogate modeling was proposed to practical applications in automotive industry. (a) To maximize the fatigue life of spot-welded joints, an expected improvement based sequential surrogate modeling method was utilized. The results showed that by using this method the performance can be significantly improved with only a relatively small number of finite element analyses. (c) A multiojective sequential surrogate modeling method was proposed to address a multiobjective optimisation of a foam-filled double cylindrical structure. By adding the sequential points and updating the Kriging model adaptively, more accurate Pareto solutions are generated.

(4) While various uncertainties are inevitably present in real-life optimisations, conventional deterministic optimisations could probably lead to the violation of constraints and the instability of performances. Therefore, nondeterministic optimisation methods were introduced to solve the automotive design problems. (a) A multiobjective reliability-based optimisation for design of a door was investigated. Based on analysis and design responses surface models, the structural mass was minimized and the vertical sag stiffness was maximized subjected to the probabilistic constraint. The results revealed that the Pareto frontier is divided into sensitive region and insensitive region with respect to uncertainties, and the decision maker is recommended to select a solution from the insensitive region. Furthermore, the reduction of uncertainties can help improve the reliability but will increase the manufacturing cost, and the tradeoff between the reliability target and performance should be made. (b) A multiobjective uncertain

optimisation of the foam-filled double cylindrical structure was conducted by considering randomness in the foam density and wall thicknesses. Multiobjective particle swarm optimisation and Monte Carlo simulation were integrated in the optimisation. The results proved that while the performances of the objectives are sacrificed slightly, the nondeterministic optimisation can enhance the robustness of the objectives and maintain the reliability of the constraint. (c) A multiobjective robust optimisation of the truck cab was performed by considering the uncertainty in material properties. The general version of dual response surface model, namely dual surrogate model, was proposed to approximate the means and standard deviations of the performances. Then, the multiobjective particle optimisation was used to generate the well-distributed Pareto frontier. Finally, a hybrid multi-criteria decision making model was proposed to select a best compromise solution considering both the fatigue performance and its robustness.

(5) Regarding the surrogate modelling, the conventional surrogate models, ensembles of surrogates, and sequential surrogate models were investigated. From the study, the conventional surrogate models are accurate enough for the small-scale crashworthiness optimisation problem and stiffness optimisation problem; the ensembles of surrogates are suitable for the large-scale problem (> 10 variables), to make full use of information from multiple surrogates and thus obtain a more competent optimum; the sequential surrogate models are suitable for the crashworthiness problems with uncertain factors, in order to adaptively increase the accuracy of surrogate modeling and guarantee the effective of the uncertainty-based optimisation.

7.2 Novelties

During this PhD study, the following ideas are considered innovative:

(1) Surrogate modeling and multiobjective optimisation were integrated to address the design problems of novel functionally graded structures, aiming to develop more advanced automotive energy absorbers.

(2) The ensembles of surrogates and hybrid particle swarm optimisation were proposed for design of a truck cab, which could make full use of training points and has a strong searching capacity.

(3) Sequential surrogate modeling methods were introduced to several optimisation problems in automotive industry so that the optimisations are less dependent on the number of initial training points and both the efficiency and accuracy are improved.

(4) The surrogate based optimisation method was implemented to address various uncertainties in real life applications. Furthermore, a hybrid multi-criteria decision making model was proposed to make the best compromise between the performance and robustness.

7.3 Future work

Though substantial work has been done for the optimisation of body structures, a lot of work remains to be explored. (1). The energy absorber needs to be optimisation in the context of the whole vehicle system. That to to say, all the components should be integrated to work as a whole to achieve the best crashworthiness performance. (2). Regarding the multiobjective sequential optimisation, the multiobjective version of EI criterion should be further studied to make full use of the predicted uncertainty information. (3). Dual surrogate models should be further investigated to account for the uncertainty in both design variables and noise factors.

References

[1] 高云凯. 汽车车身结构分析: 北京理工大学出版社; 2006.

[2] Fang H, Rais-Rohani M, Liu Z, Horstemeyer MF. A comparative study of metamodeling methods for multiobjective crashworthiness optimisation. Computers & Structures. 2005;83:2121-36.

[3] Zhu P, Zhang Y, Chen GL. Metamodel-based lightweight design of an automotive front-body structure using robust optimisation. Proceedings of the Institution of Mechanical Engineers Part D-Journal of Automobile Engineering. 2009;223:1133-47.

[4] Forsberg J, Nilsson L. Evaluation of response surface methodologies used in crashworthiness optimisation. International Journal of Impact Engineering. 2006;32:759-77.

[5] Pan F, Zhu P. Lightweight design of vehicle front-end structure: contributions of multiple surrogates. International Journal of Vehicle Design. 2011;57:124-47.

[6] Zhu P, Zhang Y, Chen G. Metamodeling development for reliability-based design optimisation of automotive body structure. Computers in Industry. 2011;62:729-41.

[7] Shi L, Yang RJ, Zhu P. A method for selecting surrogate models in crashworthiness optimisation. Structural and Multidisciplinary Optimisation. 2012;46:159-70.

[8] Shi L, Yang R-J, Zhu P. An adaptive response surface method for crashworthiness optimisation. Engineering Optimisation. 2013;45:1365-77.

[9] Song X, Sun G, Li G, Gao W, Li Q. Crashworthiness optimisation of foam-filled tapered thin-walled structure using multiple surrogate models. Struct Multidisc Optim. 2013;47:221-31.

[10] Fang J, Gao Y, Sun G, Zhang Y, Li Q. Parametric analysis and multiobjective optimisation for functionally graded foam-filled thin-wall tube under lateral impact. Computational Materials Science. 2014;90:265-75.

[11] Zerpa LE, Queipo NV, Pintos S, Salager J-L. An optimisation methodology of alkaline–surfactant–polymer flooding processes using field scale numerical simulation and multiple surrogates. J Petrol Sci Eng. 2005;47:197-208.

[12] Goel T, Haftka RT, Shyy W, Queipo NV. Ensemble of surrogates. Struct Multidiscip O. 2007;33:199-216.

[13] Acar E, Rais-Rohani M. Ensemble of metamodels with optimized weight factors. Struct Multidiscip O. 2009;37:279-94.

[14] Acar E. Various approaches for constructing an ensemble of metamodels using local measures. Struct Multidiscip O. 2010;42:879-96.

[15] Pan F, Zhu P. Design optimisation of vehicle roof structures: benefits of using multiple surrogates. International Journal of Crashworthiness. 2011;16:85-95.

[16] Zhou XJ, Ma YZ, Li XF. Ensemble of surrogates with recursive arithmetic average. Struct Multidiscip O. 2011;44:651-71.

[17] Zhou X, Ma Y, Tu Y, Feng Y. Ensemble of Surrogates for Dual Response Surface Modeling in Robust Parameter Design. Quality and Reliability Engineering International. 2012:n/a-n/a.

[18] Forrester AIJ, Keane AJ. Recent advances in surrogate-based optimisation. Progress in Aerospace Sciences. 2009;45:50-79.

[19] Fang JG, Gao YK, Sun GY, Zhang YT, Li Q. Parametric analysis and multiobjective optimisation for functionally graded foam-filled thin-wall tube under lateral impact. Comp Mater Sci. 2014;90:265-75.

[20] Chen Z, Qiu H, Gao L, Li X, Li P. A local adaptive sampling method for reliability-based design optimisation using Kriging model. Struct Multidisc Optim. 2014;49:401-16.

[21] Schonlau M. Computer experiments and global optimisation: University of Waterloo; 1998.

[22] Hamza K, Shalaby M. A framework for parallelized efficient global optimisation with application to vehicle crashworthiness optimisation. Engineering Optimisation. 2014;46:1200-21.

[23] Viana FA, Haftka RT, Watson LT. Efficient global optimisation algorithm assisted by multiple surrogate techniques. Journal of Global Optimisation. 2013;56:669-89.

[24] Keane AJ. Statistical Improvement Criteria for Use in Multiobjective Design Optimisation. AIAA Journal. 2006;44:879-91.

[25] Shimoyama K, Shinkyu J, Obayashi S. Kriging-surrogate-based optimisation considering expected hypervolume improvement in non-constrained many-objective test problems. Evolutionary Computation (CEC), 2013 IEEE Congress on2013. p. 658-65.

[26] Couckuyt I, Deschrijver D, Dhaene T. Fast calculation of multiobjective probability of improvement and expected improvement criteria for Pareto optimisation. J Glob Optim. 2014;60:575-94.

[27] Yang BS, Yeun YS, Ruy WS. Managing approximation models in multiobjective optimisation. Struct Multidiscip O. 2002;24:141-56.

[28] Johnson ME, Moore LM, Ylvisaker D. Minimax and maximin distance designs. Journal of statistical planning and inference. 1990;26:131-48.

[29] Youn BD, Choi KK, Yang RJ, Gu L. Reliability-based design optimisation for crashworthiness of vehicle side impact. Struct Multidisc Optim. 2004;26:272-83.

[30] Fu Y, Sahin KH. Better Optimisation of Nonlinear Uncertain Systems (BONUS) for vehicle structural design. Annals of Operations Research. 2004;132:69-84.

[31] Sinha K. Reliability-based multiobjective optimisation for automotive crashworthiness and occupant safety. Structural and Multidisciplinary Optimisation. 2007;33:255-68.

[32] Yang RJ, Akkerman A, Anderson DF, Faruque OM, Gu L. Robustness optimisation for vehicular crash simulations. Computing in Science & Engineering. 2000;2:8-13.

[33] Gu L, Yang RJ, Tho CH, Makowski M, Faruque O, Li Y. Optimisation and robustness for crashworthiness of side impact. International Journal of Vehicle Design. 2001;26:348-60.

[34] Zhang S, Zhu P, Chen W, Arendt P. Concurrent treatment of parametric uncertainty and metamodeling uncertainty in robust design. Struct Multidisc Optim. 2013;47:63-76.

[35] Zhang S, Zhu P, Chen W. Crashworthiness-based lightweight design problem via new robust design method considering two sources of uncertainties. Proceedings of the Institution of Mechanical Engineers Part C-Journal of Mechanical Engineering Science. 2013;227:1381-91.

[36] Zhu P, Pan F, Chen W, Viana FAC. Lightweight design of vehicle parameters under crashworthiness using conservative surrogates. Computers in Industry. 2013;64:280-9.

[37] Acar E, Solanki K. System reliability based vehicle design for crashworthiness and effects of various uncertainty reduction measures. Structural and Multidisciplinary Optimisation. 2009;39:311-25.

[38] Bohidar SK, Sharma R, Mishra PR. Functionally Graded Materials: A Critical Review. International Journal of Research. 2014;1:289-301.

[39] Song CY, Lee J. Reliability-based design optimisation of knuckle component using conservative method of moving least squares meta-models. Probabilist Eng Mech. 2011;26:364-79.

[40] d'Ippolito R, Hack M, Donders S, Hermans L, Tzannetakis N, Vandepitte D. Improving the fatigue life of a vehicle knuckle with a reliability-based design optimisation approach. J Stat Plan Infer. 2009;139:1619-32.

[41] Hyeon Ju B, Chai Lee B. Reliability-based design optimisation using a moment method and a kriging metamodel. Engineering Optimisation. 2008;40:421-38.

[42] Daskilewicz MJ, German BJ, Takahashi TT, Donovan S, Shajanian A. Effects of disciplinary uncertainty on multi-objective optimisation in aircraft conceptual design. Structural and Multidisciplinary Optimisation. 2011;44:831-46.

[43] Deb K, Padmanabhan D, Gupta S, Mall AK. Reliability-based multi-objective optimisation using evolutionary algorithms. Evolutionary multi-criterion optimisation: Springer; 2007. p. 66-80.

[44] Boessio ML, Morsch IB, Awruch AM. Fatigue lifetime estimation of commercial vehicles. J Sound Vib. 2006;291:169-91.

[45] Grujicic M, Arakere G, Bell WC, Marvi H, Yalavarthy HV, Pandurangan B, et al. Reliability-Based Design Optimisation for Durability of Ground Vehicle Suspension System Components. J Mater Eng Perform. 2010;19:301-13.

[46] Youn BD, Choi KK. A new response surface methodology for reliability-based design optimisation. Computers & structures. 2004;82:241-56.

[47] Sun GY, Li GY, Zhou SW, Li HZ, Hou SJ, Li Q. Crashworthiness design of vehicle by using multiobjective robust optimisation. Struct Multidiscip O. 2011;44:99-110.

[48] Koch PN, Yang RJ, Gu L. Design for six sigma through robust optimisation. Struct Multidisc Optim. 2004;26:235-48.

[49] Lönn D, Fyllingen Ø, Nilssona L. An approach to robust optimisation of impact problems using random samples and meta-modelling. International Journal of Impact Engineering. 2010;37:723-34.

[50] http://www.nhtsa.gov/

[51] http://www.stats.gov.cn/

[52] Liao X, Li Q, Yang X, Zhang W, Li W. Multiobjective optimisation for crash safety design of vehicles using stepwise regression model. Structural and multidisciplinary optimisation. 2008;35:561-9.

[53] Wang H, Li E, Li GY. Probability-based least square support vector regression metamodeling technique for crashworthiness optimisation problems. Computational Mechanics. 2011;47:251-63.

[54] Su R, Gui L, Fan Z. Multi-objective optimisation for bus body with strength and rollover safety constraints based on surrogate models. Struct Multidiscip O. 2011;44:431-41.

[55] Bojanowski C, Kulak RF. Multi-objective optimisation and sensitivity analysis of a paratransit bus structure for rollover and side impact tests. International Journal of Crashworthiness. 2011;16:665-76.

[56] 高云凯, 张朋, 吴锦妍, 王婧人. 基于 Kriging 模型的大客车侧翻安全性多目标优化. 同济大学学报: 自然科学版. 2012;40:1882-7.

[57] Marsolek J, Reimerdes HG. Energy absorption of metallic cylindrical shells with induced non-axisymmetric folding patterns. International Journal of Impact Engineering. 2004;30:1209-23.

[58] 黄金陵. 汽车车身设计: 机械工业出版社; 2007.

[59] Santis, F. De, The modelling of the vehicle frontal structure and the numerical simulation of the crash-test, Master's thesis, Politecnico di Torino, Facoltá di Ingegneria, Corso di specializzazione in Ingegneria Meccanica, Italy, Torino, 1996.

[60] Soto CA. Structural topology optimisation for crashworthiness. International Journal of Crashworthiness. 2004;9:277-83.

[61] Cho Y-B, Bae C-H, Suh M-W, Sin H-C. Maximisation of crash energy absorption by crash trigger for vehicle front frame using the homogenisation method. International Journal of Vehicle Design. 2008;46:23-50.

[62] Zhang Y, Zhu P, Chen G. Lightweight design of automotive front side rail based on robust optimisation. Thin-Walled Structures. 2007;45:670-6.

[63] Farkas L, Moens D, Donders S, Vandepitte D. Optimisation study of a vehicle bumper subsystem with fuzzy parameters. Mechanical Systems and Signal Processing. 2012;32:59-68.

[64] Belingardi G, Beyene AT, Koricho EG. Geometrical optimisation of bumper beam profile made of pultruded composite by numerical simulation. Composite Structures. 2013;102:217-25.

[65] 高云凯, 张玉婷, 方剑光. 基于混合元胞自动机的铝合金保险杠横梁设计. 同济大学学报: 自然科学版. 2015;43:456-61.

[66] Hanssen AG, Stobener K, Rausch G, Langseth M, Keller H. Optimisation of energy absorption of an A-pillar by metal foam insert. International Journal of Crashworthiness. 2006;11:231-41.

[67] Marklund PO, Nilsson L. Optimisation of a car body component subjected to side impact. Struct Multidisc Optim. 2001;21:383-92.

[68] Pan F, Zhu P, Zhang Y. Metamodel-based lightweight design of B-pillar with TWB structure via support vector regression. Computers & Structures. 2010;88:36-44.

[69] Alexander J. An approximate analysis of the collapse of thin cylindrical shells under axial loading. The Quarterly Journal of Mechanics and Applied Mathematics. 1960;13:10-5.

[70] Wierzbicki T, Abramowicz W. On the Crushing Mechanics of Thin-Walled Structures. J Appl Mech-T Asme. 1983;50:727-34.

[71] Abramowicz W, Jones N. Dynamic axial crushing of square tubes. Int J Impact Eng. 1984;2:179-208.

[72] Abramowicz W, Jones N. Dynamic progressive buckling of circular and square tubes. Int J Impact Eng. 1986;4:243-70.

[73] Zarei HR, Kroger M. Multiobjective crashworthiness optimisation of circular aluminum tubes. Thin-Walled Structures. 2006;44:301-8.

[74] Kurtaran H, Eskandarian A, Marzougui D, Bedewi NE. Crashworthiness design optimisation using successive response surface approximations. Computational Mechanics. 2002;29:409-21.

[75] Lee SH, Kim HY, Oh SI. Cylindrical tube optimisation using response surface method based on stochastic process. Journal of Materials Processing Technology. 2002;130:490-6.

[76] Wang H, Li GY, Li E. Time-based metamodeling technique for vehicle crashworthiness optimisation. Computer Methods in Applied Mechanics and Engineering. 2010;199:2497-509.

[77] Marzbanrad J, Ebrahimi MR. Multi-Objective Optimisation of aluminum hollow tubes for vehicle crash energy absorption using a genetic algorithm and neural networks. Thin-Walled Structures. 2011;49:1605-15.

[78] Lanzi L, Castelletti LML, Anghileri M. Multi-objective optimisation of composite absorber shape under crashworthiness requirements. Composite Structures. 2004;65:433-41.

[79] Ghamarian A, Zarei H. Crashworthiness investigation of conical and cylindrical end-capped tubes under quasi-static crash loading. International Journal of Crashworthiness. 2012;17:19-28.

[80] Yamazaki K, Han J. Maximization of the crushing energy absorption of tubes. Structural Optimisation. 1998;16:37-46.

[81] Allahbakhsh HR, Saemi J, Hourali M. Design optimisation of square aluminium damage columns with crashworthiness criteria. Mechanika. 2011:187-92.

[82] Liu Y. Optimum design of straight thin-walled box section beams for crashworthiness analysis. Finite Elements in Analysis and Design. 2008;44:139-47.

[83] Redhe M, Forsberg J, Jansson T, Marklund PO, Nilsson L. Using the response surface methodology and the D-optimality criterion in crashworthiness related problems. Struct Multidisc Optim. 2002;24:185-94.

[84] Jansson T, Nilsson L, Redhe M. Using surrogate models and response surfaces in structural optimisation – with application to crashworthiness design and sheet metal forming. Struct Multidisc Optim. 2003;25:129-40.

[85] Kaya N, Oeztuerk F. Multi-objective crashworthiness design optimisation of thin-walled tubes. International Journal of Vehicle Design. 2010;52:54-63.

[86] Liu Y. Crashworthiness design of multi-corner thin-walled columns. Thin-Walled Structures. 2008;46:1329-37.

[87] Hou S, Li Q, Long S, Yang X, Li W. Design optimisation of regular hexagonal thin-walled columns with crashworthiness criteria. Finite Elements in Analysis and Design. 2007;43:555-65.

[88] Liu Y. Thin-walled curved hexagonal beams in crashes - FEA and design. International Journal of Crashworthiness. 2010;15:151-9.

[89] Liu Y. Crashworthiness design of thin-walled curved beams with box and channel cross sections. International Journal of Crashworthiness. 2010;15:413-23.

[90] Chiandussi G, Avalle M. Maximisation of the crushing performance of a tubular device by shape optimisation. Computers & Structures. 2002;80:2425-32.

[91] Avalle M, Chiandussi G. Optimisation of a vehicle energy absorbing steel component with experimental validation. International Journal of Impact Engineering. 2007;34:843-58.

[92] Hou S, Han X, Sun G, Long S, Li W, Yang X, et al. Multiobjective optimisation for tapered circular tubes. Thin-Walled Structures. 2011;49:855-63.

[93] Avalle M, Chiandussi G, Belingardi G. Design optimisation by response surface methodology: application to crashworthiness design of vehicle structures. Struct Multidisc Optim. 2002;24:325-32.

[94] Liu Y. Design optimisation of tapered thin-walled square tubes. International Journal of Crashworthiness. 2008;13:543-50.

[95] Qi C, Yang S, Dong F. Crushing analysis and multiobjective crashworthiness optimisation of tapered square tubes under oblique impact loading. Thin-Walled Structures. 2012;59:103-19.

[96] Acar E, Guler MA, Gerceker B, Cerit ME, Bayram B. Multi-objective crashworthiness optimisation of tapered thin-walled tubes with axisymmetric indentations. Thin-Walled Structures. 2011;49:94-105.

[97] Zhang Y, Sun G, Xu X, Li G, Li Q. Multiobjective crashworthiness optimisation of hollow and conical tubes for multiple load cases. Thin-Walled Structures. 2014;82:331-42.

[98] Fang J, Gao Y, Sun G, Xu C, Li Q. Fatigue optimisation with combined ensembles of surrogate modeling for a truck cab. Journal of Mechanical Science and Technology. 2014;28:1-9.

[99] Najafi A, Rais-Rohani M. Sequential coupled process-performance simulation and multi-objective optimisation of thin-walled tubes. Materials & Design. 2012;41:89-98.

[100] Najafi A, Acar E, Rais-Rohani M. Multi-objective robust design of energy-absorbing components using coupled process–performance simulations. Engineering Optimisation. 2014;46:146-64.

[101] Xiang YJ, Wang Q, Fan ZJ, Fang HB. Optimal crashworthiness design of a spot-welded thin-walled hat section. Finite Elements in Analysis and Design. 2006;42:846-55.

[102] Tang L, Wang H, Li G, Xu F. Adaptive heuristic search algorithm for discrete variables based multi-objective optimisation. Struct Multidisc Optim. 2013;48:821-36.

[103] Abramowicz W, Wierzbicki T. Axial crushing of multicorner sheet metal columns. Journal of Applied Mechanics. 1989;56:113-20.

[104] Hou S, Zhang Z, Yang X, Yin H, Li Q. Crashworthiness optimisation of new thin-walled cellular configurations. Engineering Computations. 2014;31:4-.

[105] Zhang X, Cheng G, Wang B, Zhang H. Optimum design for energy absorption of bitubal hexagonal columns with honeycomb core. International Journal of Crashworthiness. 2008;13:99-107.

[106] Tran T, Hou S, Han X, Tan W, Nguyen N. Theoretical prediction and crashworthiness optimisation of multi-cell triangular tubes. Thin-Walled Structures. 2014;82:183-95.

[107] Hou S, Li Q, Long S, Yanga X, Li W. Multiobjective optimisation of multi-cell sections for the crashworthiness design. International Journal of Impact Engineering. 2008;35:1355-67.

[108] Sun G, Li G, Stone M, Li Q. A two-stage multi-fidelity optimisation procedure for honeycomb-type cellular materials. Computational Materials Science. 2010;49:500-11.

[109] Yin H, Wen G, Gan N. CRASHWORTHINESS DESIGN FOR HONEYCOMB STRUCTURES UNDER AXIAL DYNAMIC LOADING. International Journal of Computational Methods. 2011;8:863-77.

[110] Li M, Deng Z, Liu R, Guo H. Crashworthiness design optimisation of metal honeycomb energy absorber used in lunar lander. International Journal of Crashworthiness. 2011;16:411-9.

[111] Esfahlani SS, Shirvani H, Shirvani A, Nwaubani S, Mebrahtu H, Chirwa C. Hexagonal honeycomb cell optimisation by way of meta-model techniques. International Journal of Crashworthiness. 2013;18:264-75.

[112] Borvik T, Hopperstad OS, Reyes A, Langseth M, Solomos G, Dyngeland T. Empty and foam-filled circular aluminium tubes subjected to axial and oblique quasi-static loading. Int J Crashworthines. 2003;8:481-94.

[113] Seitzberger M, Rammerstorfer FG, Gradinger R, Degischer HP, Blaimschein M, Walch C. Experimental studies on the quasi-static axial crushing of steel columns filled with aluminium foam. Int J Solids Struct. 2000;37:4125-47.

[114] Santosa SP, Wierzbicki T, Hanssen AG, Langseth M. Experimental and numerical studies of foam-filled sections. Int J Impact Eng. 2000;24:509-34.

[115] Ahmad Z, Thambiratnam DP. Crushing response of foam-filled conical tubes under quasi-static axial loading. Mater Design. 2009;30:2393-403.

[116] Seitzberger M, Rammerstorfer FG, Degischer HP, Gradinger R. Crushing of axially compressed steel tubes filled with aluminium foam. Acta Mech. 1997;125:93-105.

[117] Reyes A, Hopperstad O, Hanssen A, Langseth M. Modeling of material failure in foam-based components. Int J Impact Eng. 2004;30:805-34.

[118] Zarei HR, Kroeger M. Crashworthiness optimisation of empty and filled aluminum crash boxes. International Journal of Crashworthiness. 2007;12:255-64.

[119] Zarei HR, Kroeger M. Optimisation of the foam-filled aluminum tubes for crush box application. Thin-Walled Structures. 2008;46:214-21.

[120] Toksoy AK, Güden M. The optimisation of the energy absorption of partially Al foam-filled commercial 1050H14 and 6061T4 Al crash boxes. International Journal of Crashworthiness. 2011;16:97-109.

[121] Hou S, Li Q, Long S, Yang X, Li W. Crashworthiness design for foam filled thin-wall structures. Materials & Design. 2009;30:2024-32.

[122] Zhang Y, Sun G, Li G, Luo Z, Li Q. Optimisation of foam-filled bitubal structures for crashworthiness criteria. Materials & Design. 2012;38:99-109.

[123] Yin H, Wen G, Liu Z, Qing Q. Crashworthiness optimisation design for foam-filled multi-cell thin-walled structures. Thin-Walled Structures. 2014;75:8-17.

[124] Bi J, Fang H, Wang Q, Ren X. Modeling and optimisation of foam-filled thin-walled columns for crashworthiness designs. Finite Elements in Analysis and Design. 2010;46:698-709.

[125] Kim HS. Analysis of crash response of aluminium foam-filled front side rail of a passenger car. International Journal of Crashworthiness. 2001;6:189-207.

[126] Kim HS, Chen W, Wierzbicki T. Weight and crash optimisation of foam-filled three-dimensional "S" frame. Computational Mechanics. 2002;28:417-24.

[127] Villa A, Strano M, Mussi V. Optimisation of Design and Manufacturing Process of Metal Foam Filled Anti-Intrusion Bars. 14th International Conference on Material Forming Esaform, 2011 Proceedings. 2011;1353:1656-61.

[128] Zarei H, Kroeger M. Optimum honeycomb filled crash absorber design. Materials & Design. 2008;29:193-204.

[129] Yin H, Wen G, Hou S, Chen K. Crushing analysis and multiobjective crashworthiness optimisation of honeycomb-filled single and bitubular polygonal tubes. Materials & Design. 2011;32:4449-60.

[130] Paz J, Díaz J, Romera L, Costas M. Crushing analysis and multi-objective crashworthiness optimisation of GFRP honeycomb-filled energy absorption devices. Finite Elements in Analysis and Design. 2014;91:30-9.

[131] Kinsey B, Liu Z, Cao J. A novel forming technology for tailor-welded blanks. Journal of Materials Processing Technology. 2000;99:145-53.

[132] Zhu P, Shi YL, Zhang KZ, Lin ZQ. Optimum design of an automotive inner door panel with a tailor-welded blank structure. Proceedings of the Institution of Mechanical Engineers Part D-Journal of Automobile Engineering. 2008;222:1337-48.

[133] Xu F, Sun G, Li G, Li Q. Crashworthiness design of multi-component tailor-welded blank (TWB) structures. Struct Multidisc Optim. 2013;48:653-67.

[134] Shi Y, Zhu P, Shen L, Lin Z. Lightweight design of automotive front side rails with TWB concept. Thin-Walled Structures. 2007;45:8-14.

[135] Ramakrishna S. Microstructural design of composite materials for crashworthy structural applications. Materials & Design. 1997;18:167-73.

[136] Zarei H, Kroeger M, Albertsen H. An experimental and numerical crashworthiness investigation of thermoplastic composite crash boxes. Composite Structures. 2008;85:245-57.

[137] Duan S, Tao Y, Han X, Yang X, Hou S, Hu Z. Investigation on structure optimisation of crashworthiness of fiber reinforced polymers materials. Composites Part B-Engineering. 2014;60:471-8.

[138] Sun G, Li G, Hou S, Zhou S, Li W, Li Q. Crashworthiness design for functionally graded foam-filled thin-walled structures. Materials Science and Engineering a-Structural Materials Properties Microstructure and Processing. 2010;527:1911-9.

[139] Yin H, Wen G, Hou S, Qing Q. Multiobjective crashworthiness optimisation of functionally lateral graded foam-filled tubes. Materials & Design. 2013;44:414-28.

[140] Yin H, Wen G, Fang H, Qing Q, Kong X, Xiao J, et al. Multiobjective crashworthiness optimisation design of functionally graded foam-filled tapered tube based on dynamic ensemble metamodel. Materials & Design. 2014;55:747-57.

[141] Mohammadiha O, Beheshti H. Optimisation of functionally graded foam-filled conical tubes under axial impact loading. Journal of Mechanical Science and Technology. 2014;28:1741-52.

[142] Zhang X, Wen Z, Zhang H. Axial crushing and optimal design of square tubes with graded thickness. Thin-Walled Structures. 2014;84:263-74.

[143] Sun G, Xu F, Li G, Li Q. Crashing analysis and multiobjective optimisation for thin-walled structures with functionally graded thickness. International Journal of Impact Engineering. 2014;64:62-74.

[144] 杜永昌, 管迪华. 汽车道路动态试验模拟控制系统的研究与开发. 汽车技术. 1999:16-8.

[145] 周鋐, 冯展辉, 周炜. 远程参数控制技术在轿车车身结构动强度试验中的应用. 汽车技术. 2001;1.

[146] 彭为, 靳晓雄, 周鋐, 金锋. 基于力控制的轿车后桥道路模拟试验研究. 中国工程机械学报. 2004:239-44.

[147] 彭为. 典型地区道路与 EVP 道路载荷谱当量关系及轿车后桥寿命数字化预测研究 [D]: 上海: 同济大学; 2004.

[148] Wannenburg J, Heyns PS, Raath AD. Application of a fatigue equivalent static load methodology for the numerical durability assessment of heavy vehicle structures. Int J Fatigue. 2009;31:1541-9.

[149] Koh SK. Fatigue analysis of an automotive steering link. Eng Fail Anal. 2009;16:914-22.

[150] He BY, Wang SX, Gao F. Failure analysis of an automobile damper spring tower. Eng Fail Anal. 2010;17:498-505.

[151] 孙凌玉, 吕振华. 利用计算机仿真技术预测车身零件疲劳寿命. 汽车工程. 2001;23:389-91.

[152] 高云凯, 李翠, 崔玲, 高冬. 燃料电池大客车车身疲劳寿命仿真分析. 汽车工程. 2010;32:7-12.

[153] Haiba M, Barton D, Brooks P, Levesley M. The development of an optimisation algorithm based on fatigue life. International Journal of Fatigue. 2003;25:299-310.

[154] Kim B-S, Koschel W. Shape Optimisation of a Front Suspension Fork According to the Axiom of Constant Stress. SAE Technical Paper; 1999.

[155] Friedman K, Mobrem M. Vehicle structural design utilizing optimized finite element modeling. SAE Technical Paper; 1998.

[156] Kang BS, Choi WS, Park GJ. Structural optimisation under equivalent static loads transformed from dynamic loads based on displacement. Computers & Structures. 2001;79:145-54.

[157] Krishna MM. Chassis Cross-Member Design Using Shape Optimisation-A Case Study. SAE Technical Paper; 1998.

[158] Krishna MM, Carifo J. Optimisation of an Engine Cradle in Frequency Domain. SAE Technical Paper; 2000.

[159] Ma Z-D, Kikuchi N, Cheng H-C. Topological design for vibrating structures. Computer methods in applied mechanics and engineering. 1995;121:259-80.

[160] Zhao C, Steven G, Xie Y. Evolutionary optimisation of maximizing the difference between two natural frequencies of a vibrating structure. Structural optimisation. 1997;13:148-54.

[161] Jang C-S, Yoo Y-D, Jeon J-W, Choi B-L, Jung E-W. Design of a light weight suspension component using CAE. SAE Technical Paper; 1998.

[162] Chang K-H, Choi KK, Tsai C-S, Chen C-J, Choi BS, Yu X. Design sensitivity analysis and optimisation tool (DSO) for shape design applications. Computing Systems in Engineering. 1995;6:151-75.

[163] Kang BJ, Sin HC, Kim JH. Optimal shape design of the front wheel lower control arm considering dynamic effects. Int J Automot Techn. 2007;8:309-17.

[164] Mrzyglod M, Zielinski AP. Parametric structural optimisation with respect to the multiaxial high-cycle fatigue criterion. Struct Multidiscip O. 2007;33:161-71.

[165] Song XG, Jung JH, Son HJ, Park JH, Lee KH, Park YC. Metamodel-based optimisation of a control arm considering strength and durability performance. Computers & Mathematics with Applications. 2010;60:976-80.

[166] Kim JK, Kim YJ, Yang WH, Park YC, Lee KH. Structural design of an outer tie rod for a passenger car. Int J Automot Techn. 2011;12:375-81.

[167] Hsu YL, Hsu MS. Weight reduction of aluminum disc wheels under fatigue constraints using a sequential neural network approximation method. Comput Ind. 2001;46:167-79.

[168] Schafer C, Finke E. Shape optimisation by design of experiments and finite element methods-an application of steel wheels. Struct Multidiscip O. 2008;36:477-91.

[169] Ping Z, Jun H, Jin M. Fatigue life analysis of the autobody in a sports utility vehicle and its improvement using the homogenization method. P I Mech Eng D-J Aut. 2008;222:2291-305.

[170] Adl AH, Panahi MS. Multi-Objective Optimal Design of a Passenger Car's Body. ASME Conference Proceedings. 2010;2010:277-86.

[171] Lee TH, Jung JJ. Metamodel-based shape optimisation of connecting rod considering fatigue life. Key Eng Mat. 2006;306-308:211-6.

[172] Ho S, Lee YL, Kang HT, Wang CJ. Optimisation of a crankshaft rolling process for durability. Int J Fatigue. 2009;31:799-808.

[173] Kaya N, Karen I, Ozturk F. Re-design of a failed clutch fork using topology and shape optimisation by the response surface method. Mater Design. 2010;31:3008-14.

[174] Jin R, Chen W, Sudjianto A. An efficient algorithm for constructing optimal design of computer experiments. Journal of statistical planning and inference. 2005;134:268-87.

[175] Montgomery DC. Desing and analysis of experiments. Jonh Wiley & Sons, New York, EUA. 1996.

[176] Draper NR, Smith H. Applied regression analysis 2nd ed. 1981.

[177] Hardy RL. Multiquadric equations of topography and other irregular surfaces. Journal of geophysical research. 1971;76:1905-15.

[178] Sacks J, Welch WJ, Mitchell TJ, Wynn HP. Design and analysis of computer experiments. Statistical science. 1989;4:409-23.

[179] Eberhart R, Kennedy J. A new optimizer using particle swarm theory. Micro Machine and Human Science, 1995 MHS'95, Proceedings of the Sixth International Symposium on: IEEE; 1995. p. 39-43.

[180] Kennedy J, Eberhart R. Particle swarm optimisation. Neural Networks, 1995 Proceedings, IEEE International Conference on1995. p. 1942-8 vol.4.

[181] Coello CAC, Pulido GT, Lechuga MS. Handling multiple objectives with particle swarm optimisation. Evolutionary Computation, IEEE Transactions on. 2004;8:256-79.

[182] Raquel CR, Naval Jr PC. An effective use of crowding distance in multiobjective particle swarm optimisation. Proceedings of the 2005 conference on Genetic and evolutionary computation: ACM; 2005. p. 257-64.

[183] Sun G, Li G, Gong Z, He G, Li Q. Radial basis functional model for multi-objective sheet metal forming optimisation. Engineering Optimisation. 2011;43:1351-66.

[184] Fang J, Gao Y, Sun G, Zhang Y, Li Q. Crashworthiness design of foam-filled bitubal structures with uncertainty. International Journal of Non-Linear Mechanics. 2014;67:120-32.

[185] Liew K, Lei Z, Zhang L. Mechanical analysis of functionally graded carbon nanotube reinforced composites: A review. Composite Structures. 2015;120:90-7.

[186] Habibi MK, Lu Y. Crack Propagation in Bamboo's Hierarchical Cellular Structure. Scientific reports. 2014;4.

[187] Cadman J, Chang C-C, Chen J, Chen Y, Zhou S, Li W, et al. Bioinspired lightweight cellular materials-understanding effects of natural variation on mechanical properties. Materials Science and Engineering: C. 2013;33:3146-52.

[188] Jiang Y, Zhao J, Liao E-Y, Dai R-C, Wu X-P, Genant HK. Application of micro-CT assessment of 3-D bone microstructure in preclinical and clinical studies. Journal of bone and mineral metabolism. 2005;23:122-31.

[189] Li C, Weng G. Antiplane crack problem in functionally graded piezoelectric materials. Journal of Applied Mechanics. 2002;69:481-8.

[190] Lin D, Li Q, Li W, Zhou S, Swain MV. Design optimisation of functionally graded dental implant for bone remodeling. Composites Part B: Engineering. 2009;40:668-75.

[191] Evangelista F, Roesler J, Paulino G. Numerical simulations of fracture resistance of functionally graded concrete materials. Transportation Research Record: Journal of the Transportation Research Board. 2009;2113:122-31.

[192] Yang R-J, Fu Y, Li G. Application of tailor rolled blank in vehicle front end for frontal impact. SAE Technical Paper; 2007.

[193] Li G, Xu F, Sun G, Li Q. A comparative study on thin-walled structures with functionally graded thickness (FGT) and tapered tubes withstanding oblique impact loading. International Journal of Impact Engineering. 2015;77:68-83.

[194] 孙光永. 薄板结构成形与耐撞性优化设计关键技术研究 [D]: 长沙: 湖南大学; 2011.

[195] Kim HS. New extruded multi-cell aluminum profile for maximum crash energy absorption and weight efficiency. Thin-Walled Structures. 2002;40:311-27.

[196] Zhang X, Cheng GD, Zhang H. Theoretical prediction and numerical simulation of multi-cell square thin-walled structures. Thin Wall Struct. 2006;44:1185-91.

[197] Zhang X, Cheng G. A comparative study of energy absorption characteristics of foam-filled and multi-cell square columns. International Journal of Impact Engineering. 2007;34:1739-52.

[198] Alavi Nia A, Parsapour M. An investigation on the energy absorption characteristics of multi-cell square tubes. Thin Wall Struct. 2013;68:26-34.

[199] Hou SJ, Li Q, Long SY, Yanga XJ, Li W. Multiobjective optimisation of multi-cell sections for the crashworthiness design. Int J Impact Eng. 2008;35:1355-67.

[200] Song J, Guo F. A comparative study on the windowed and multi-cell square tubes under axial and oblique loading. Thin-Walled Structures. 2013;66:9-14.

[201] Tang Z, Liu S, Zhang Z. Analysis of energy absorption characteristics of cylindrical multi-cell columns. Thin Wall Struct. 2013;62:75-84.

[202] Zhang X, Zhang H. Energy absorption of multi-cell stub columns under axial compression. Thin Wall Struct. 2013;68:156-63.

[203] Tran T, Hou S, Han X, Nguyen N, Chau M. Theoretical prediction and crashworthiness optimisation of multi-cell square tubes under oblique impact loading. International Journal of Mechanical Sciences. 2014;89:177-93.

[204] Bai Z, Guo H, Jiang B, Zhu F, Cao L. A study on the mean crushing strength of hexagonal multi-cell thin-walled structures. Thin-Walled Structures. 2014;80:38-45.

[205] Liu S-T, Tong Z-Q, Tang Z-L, Zhang Z-H. Design optimisation of the S-frame to improve crashworthiness. Acta Mech Sin. 2014;30:589-99.

[206] Hong W, Fan H, Xia Z, Jin F, Zhou Q, Fang D. Axial crushing behaviors of multi-cell tubes with triangular lattices. International Journal of Impact Engineering. 2014;63:106-17.

[207] Chen W, Wierzbicki T. Relative merits of single-cell, multi-cell and foam-filled thin-walled structures in energy absorption. Thin-Walled Structures. 2001;39:287-306.

[208] Najafi A, Rais-Rohani M. Mechanics of axial plastic collapse in multi-cell, multi-corner crush tubes. Thin-Walled Structures. 2011;49:1-12.

[209] Ahmad Z, Thambiratnam DP. Dynamic computer simulation and energy absorption of foam-filled conical tubes under axial impact loading. Computers & Structures. 2009;87:186-97.

[210] Santosa S, Wierzbicki T. Effect of an ultralight metal filler on the bending collapse behavior of thin-walled prismatic columns. International Journal of Mechanical Sciences. 1999;41:995-1019.

[211] Shahbeyk S, Vafai A, Estekanchi H. A parametric study of the bending crash performance of empty and metal foam-filled box-beams. International Journal of Crashworthiness. 2004;9:643-52.

[212] Zarei H, Kröger M. Bending behavior of empty and foam-filled beams: Structural optimisation. International Journal of Impact Engineering. 2008;35:521-9.

[213] Guo L, Yu J. Dynamic bending response of double cylindrical tubes filled with aluminum foam. International Journal of Impact Engineering. 2011;38:85-94.

[214] Kieback B, Neubrand A, Riedel H. Processing techniques for functionally graded materials. Materials Science and Engineering: A. 2003;362:81-106.

[215] Gupta N. A functionally graded syntactic foam material for high energy absorption under compression. Materials Letters. 2007;61:979-82.

[216] Brothers AH, Dunand DC. Mechanical properties of a density-graded replicated aluminum foam. Materials Science and Engineering: A. 2008;489:439-43.

[217] Matsumoto Y, Brothers A, Stock S, Dunand D. Uniform and graded chemical milling of aluminum foams. Materials Science and Engineering: A. 2007;447:150-7.

[218] Nouraei H. Nonlinear FEA of the Crush Behaviour of Functionally Graded Foam-filled Columns 2011.

[219] Deshpande VS, Fleck NA. Isotropic constitutive models for metallic foams. J Mech Phys Solids. 2000;48:1253-83.

[220] Hanssen AG, Hopperstad OS, Langseth M, Ilstad H. Validation of constitutive models applicable to aluminium foams. Int J Mech Sci. 2002;44:359-406.

[221] Reyes A, Hopperstad OS, Berstad T, Hanssen AG, Langseth M. Constitutive modeling of aluminum foam including fracture and statistical variation of density. Eur J Mech a-Solid. 2003;22:815-35.

[222] J. Fang, Y. Gao, G. Sun, J. Chen, Q. Li. Design of Functionally Graded Foam-filled Thin-wall Structures with Functionally Graded Thickness for Crashworthiness Criteria. Submitted to Composites Part B. JCOMB-D-15-00004

[223] Lee Y, Wierzbicki T. Effect of material distribution on axial and bending response of extruded aluminum profiles. Impact and Crashworthiness Lab Report. 2001;56.

[224] Jin R, Chen W, Simpson TW. Comparative studies of metamodelling techniques under multiple modelling criteria. Struct Multidiscip O. 2001;23:1-13.

[225] Clarke SM, Griebsch JH, Simpson TW. Analysis of Support Vector Regression for Approximation of Complex Engineering Analyses. ASME Conference Proceedings. 2003;2003:535-43.

[226] Ely GR, Seepersad CC. A Comparative Study of Metamodeling Techniques for Predictive Process Control of Welding Applications. Proceedings of the Asme International Manufacturing Science and Engineering Conference, Vol 1. 2009:395-407.

[227] Kim B-S, Lee Y-B, Choi D-H. Comparison study on the accuracy of metamodeling technique for non-convex functions. J Mech Sci Technol. 2009;23:1175-81.

[228] Sanchez E, Pintos S, Queipo N. Toward an optimal ensemble of kernel-based approximations with engineering applications. Struct Multidiscip O. 2008;36:247-61.

[229] Bishop CM. Neural networks for pattern recognition: Oxford university press; 1995.

[230] Viana FAC, Haftka RT, Steffen V. Multiple surrogates: how cross-validation errors can help us to obtain the best predictor. Struct Multidiscip O. 2009;39:439-57.

[231] Victoire TAA, Jeyakumar AE. Hybrid PSO-SQP for economic dispatch with valve-point effect. Electr Pow Syst Res. 2004;71:51-9.

[232] Fang J, Gao Y, Sun G, Xu C, Li Q. Multiobjective robust design optimisation of fatigue life for a truck cab. Reliability Engineering & System Safety. 2015;135:1-8.

[233] Bonte MHA, Fourment L, Do TT, van den Boogaard AH, Huetink J. Optimisation of forging processes using Finite Element simulations. Struct Multidiscip O. 2010;42:797-810.

[234] Ertas AH, Sonmez FO. Design optimisation of spot-welded plates for maximum fatigue life. Finite Elem Anal Des. 2011;47:413-23.

[235] Deng X, Chen W, Shi G. Three-dimensional finite element analysis of the mechanical behavior of spot welds. Finite Elem Anal Des. 2000;35:17-39.

[236] Pan N, Sheppard S. Spot welds fatigue life prediction with cyclic strain range. Int J Fatigue. 2002;24:519-28.

[237] Mahadevan S, Ni K. Damage tolerance reliability analysis of automotive spot-welded joints. Reliab Eng Syst Safe. 2003;81:9-21.

[238] Wang RJ, Shang DG. Low-cycle fatigue life prediction of spot welds based on hardness distribution and finite element analysis. Int J Fatigue. 2009;31:508-14.

[239] Ertas AH, Vardar O, Sonmez FO, Solim Z. Measurement and Assessment of Fatigue Life of Spot-Weld Joints. J Eng Mater-T Asme. 2009;131.

[240] Tovo R, Livieri P. A numerical approach to fatigue assessment of spot weld joints. Fatigue Fract Eng M. 2011;34:32-45.

[241] Zhang Y, Taylor D. Optimisation of spot-welded structures. Finite Elem Anal Des. 2001;37:1013-22.

[242] Chae SW, Kwon KY, Lee TS. An optimal design system for spot welding locations. Finite Elem Anal Des. 2002;38:277-94.

[243] Ertas AH, Sonmez FO. Optimisation of spot-weld joints. P I Mech Eng C-J Mec. 2009;223:545-55.

[244] Ellyin F, Valaire B. High-strain multiaxial fatigue. Journal of Engineering Materials and Technology. 1982;104:165.

[245] Fang J, Gao Y, Sun G, Zhang Y, Li Q. Crashworthiness design of foam-filled bitubal Structures with uncertainty. International Journal of Non-Linear Mechanics. 2014.

[246] Mirfendereski L, Salimi M, Ziaei-Rad S. Parametric study and numerical analysis of empty and foam-filled thin-walled tubes under static and dynamic loadings. Int J Mech Sci. 2008;50:1042-57.

[247] Guo L-w, Yu J-l. Experimental investigations on the quasi-static axial crushing of foam-filled double square columns. Journal of Experimental Mechanics. 2010;3:009.

[248] Helton JC, Johnson JD, Sallaberry CJ, Storlie CB. Survey of sampling-based methods for uncertainty and sensitivity analysis. Reliability Engineering & System Safety. 2006;91:1175-209.

[249] Tu J, Choi KK, Park YH. A new study on reliability-based design optimisation. Journal of Mechanical Design. 1999;121:557-64.

[250] Khakhali A, Nariman-zadeh N, Darvizeh A, Masoumi A, Notghi B. Reliability-based robust multi-objective crashworthiness optimisation of S-shaped box beams with parametric uncertainties. International Journal of Crashworthiness. 2010;15:443-56.

[251] Lonn D, Bergman G, Nilsson L, Simonsson K. Experimental and finite element robustness studies of a bumper system subjected to an offset impact loading. International Journal of Crashworthiness. 2011;16:155-68.

[252] Gu X, Sun G, Li G, Mao L, Li Q. A Comparative study on multiobjective reliable and robust optimisation for crashworthiness design of vehicle structure. Struct Multidisc Optim. 2013;48:669-84.

[253] Shi L, Zhu P, Yang R-J, Lin S-P. Adaptive sampling-based RBDO method for vehicle crashworthiness design using Bayesian metric and stochastic sensitivity analysis with independent random variables. International Journal of Crashworthiness. 2013;18:331-42.

[254] Vining GG, Myers RH. Combining Taguchi and response surface philosophies: a dual response approach. Journal of quality technology. 1990;22.

[255] Shin J-K, Lee K-H, Song S-I, Park G-J. Automotive door design with the ULSAB concept. using structural optimisation. Structural and Multidisciplinary Optimisation. 2002;23:320-7.

[256] Song S, Park G. Multidisciplinary optimisation of an automotive door with a tailored blank. Proceedings of the Institution of Mechanical Engineers, Part D: Journal of Automobile Engineering. 2006;220:151-63.

[257] Lee K-H, Kang D. Structural optimisation of an automotive door using the kriging interpolation method. Proceedings of the Institution of Mechanical Engineers, Part D: Journal of Automobile Engineering. 2007;221:1525-34.

[258] Cui X, Wang S, Hu SJ. A method for optimal design of automotive body assembly using multi-material construction. Materials & Design. 2008;29:381-7.

[259] Qu X, Haftka R. Reliability-based design optimisation using probabilistic sufficiency factor. Structural and Multidisciplinary Optimisation. 2004;27:314-25.

[260] Venkataraman S. Reliability optimisation using probabilistic sufficiency factor and correction response surface. Engineering Optimisation. 2006;38:671-85.

[261] Randrianalisoa J, Coquard R, Baillis D. Microscale direct calculation of solid phase conductivity of voronoi's foams. J Porous Media. 2013;16:411-26.

[262] Shahbeyk S, Vafai A, Petrinic N. Axial crushing of metal foam-filled square columns: Foam density distribution and impactor inclination effects. Thin Wall Struct. 2005;43:1818-30.

[263] Kaufman M, Balabanov V, Giunta A, Grossman B, Mason W, Burgee S, et al. Variable-complexity response surface approximations for wing structural weight in HSCT design. Computational Mechanics. 1996;18:112-26.

[264] Moradi M. Structural applications of metal foams considering material and geometrical uncertainty. 2011.

[265] Sun G, Song X, Baek S, Li Q. Robust optimisation of foam-filled thin-walled structure based on sequential Kriging metamodel. Structural and Multidisciplinary Optimisation. 2014;49:897-913.

[266] Fang J, Gao Y, Sun G, Zhang Y, Li Q. Crashworthiness design of foam-filled bitubal Structures with uncertainty. International Journal of Non-Linear Mechanics.

[267] ASM International. Handbook Committee. ASM handbook. 10th ed. Materials Park, OH: ASM International; 1990.

[268] Athan TW, Papalambros PY. A note on weighted criteria methods for compromise solutions in multi-objective optimisation. Eng Optimiz. 1996;27:155-76.

[269] Wang C, Yoon K. Multiple attribute decision making. Berlin: Spring-verlag. 1981.

[270] Ju-Long D. Control problems of grey systems. Systems & Control Letters. 1982;1:288-94.

[271] Lin C-T, Chang C-W, Chen C-B. The worst ill-conditioned silicon wafer slicing machine detected by using grey relational analysis. The International Journal of Advanced Manufacturing Technology. 2006;31:388-95.

[272] Deng J. The Fundamentals of grey theory. Huazhong University of Science and Technology Press, Wuhan. 2002.

[273] Chen M-F, Tzeng G-H. Combining grey relation and TOPSIS concepts for selecting an expatriate host country. Mathematical and Computer Modelling. 2004;40:1473-90.

Publications

Published journal article:

[1] **Fang J**, Gao Y, Sun G, Li Q. Multiobjective reliability-based optimisation for design of a vehicle door. *Finite Elements in Analysis and Design*. 2013;67:13-21.(**SCI** 000314910200002) **Impact factor: 2.017. Science Direct Top 25 Hottest Paper: No. 3 in Jan. to Dec. 2013 and Top 25 Most Cited Paper)**

[2] **Fang J**, Gao Y, An X, Sun G, Chen J, Li Q. Design of transversely-graded foam and wall thickness structures for crashworthiness criteria. *Composites Part B: Engineering*. Published online 24 Feburary 2016. **Impact factor: 2.983**

[3] **Fang J**, Gao Y, Sun G, Xu C, Li Q. Multiobjective robust design optimisation of fatigue life for a truck cab. *Reliability Engineering & System Safety*. 2015;135:1-8.(**SCI** 000348555600001) **Impact factor: 2.410**

[4] **Fang J**, Gao Y, Sun G, Zhang Y, Li Q. Parametric analysis and multiobjective optimisation for functionally graded foam-filled thin-wall tube under lateral impact. *Computational Materials Science*. 2014;90:265-75.(**SCI** 000336656200033) **Impact factor: 2.131**

[5] **Fang J**, Gao Y, Sun G, Li Q. Dynamic crashing behavior of new extrudable multi-cell tubes with a functionally graded thickness. *International Journal of Mechanical Sciences*. 2015;103:63-73.(**SCI** 000366233000007) **Impact factor: 2.034**

[6] **Fang J**, Gao Y, Sun G, Zhang Y, Li Q. Crashworthiness design of foam-filled bitubal structures with uncertainty. *International Journal of Non-Linear Mechanics*. 2014;67:120–32.(**SCI** 000347022100015) **Impact factor: 1.977**

[7] **Fang J**, Gao Y, Sun G, Xu C, Li Q. Fatigue optimisation with combined ensembles of surrogate modeling for a truck cab. *Journal of Mechanical Science and Technology*. 2014;28:1-9.(**SCI** 000345415300032) **Impact factor: 0.838**

[8] **Fang J**, Gao Y, Sun G, Xu C, Zhang Y, Li Q. Optimisation of spot-welded joints combined artificial bee colony algorithm with sequential kriging optimisation. *Advances in Mechanical*

Engineering. 2014;2014.(**SCI** 000340363100001) **Impact factor: 0.575**

[9] **Fang J**, Gao Y, Sun G, Li Q. Development of a novel identification platform for automotive dampers. *International Journal of Vehicle Design*. 2014;66:272-96.(**SCI** 000345246100004) **Impact factor: 0.405**

[10] **Fang J**, Gao Y, Wang J, Wang Y. Multi-objective shape optimisation of body-in-white based on mesh morphing technique. *Journal of Mechanical Engineering*. 2013;48:119-26.(EI: 13741676)

[11] Gao Y, **Fang J**, Xie M. Durability analysis and evaluation of a frame-type heavy truck cab. *Journal of Tongji University. Natural Science* 40 (5), 723-728.(EI: 14260192)